Joana Margarida Franco Dantas

Mestre em Bioquímica Estrutural e Funcional

Characterization of extracellular electron transfer networks in *Geobacter sulfurreducens*, a key bacterium for bioremediation and bioenergy applications

Dissertação para obtenção do Grau de Doutora em
Biotecnologia

Orientador: Prof. Doutor Carlos A. Salgueiro, Professor
Auxiliar com Agregação, Faculdade de Ciências e
Tecnologia, Universidade Nova de Lisboa

Júri:

Presidente:	Prof. Doutor Fernando Jorge da Silva Pina
Arguentes:	Prof. Doutor Douglas Vinson Laurents Prof. Doutor Brian James Goodfellow
Vogais:	Doutora Sofia Rocha Pauleta Prof. Doutor Carlos Frederico de Gusmão Campos Geraldes

FACULDADE DE
CIÊNCIAS E TECNOLOGIA
UNIVERSIDADE NOVA DE LISBOA

Dezembro 2017

Universidade Nova de Lisboa

Joana Margarida Franco Dantas

Mestre em Bioquímica Estrutural e Funcional

Characterization of extracellular electron transfer networks in *Geobacter sulfurreducens*, a key bacterium for bioremediation and bioenergy applications

Dissertação para obtenção do Grau de Doutora em Biotecnologia

Orientador: Prof. Doutor Carlos A. Salgueiro, Professor Auxiliar com Agregação,
Faculdade de Ciências e Tecnologia, Universidade Nova de Lisboa

FACULDADE DE
CIÊNCIAS E TECNOLOGIA
UNIVERSIDADE NOVA DE LISBOA

Dezembro 2017

Characterization of extracellular electron transfer networks in *Geobacter sulfurreducens*, a key bacterium for bioremediation and bioenergy applications

“Copyright”

Joana Margarida Franco Dantas
Faculdade de Ciências e Tecnologia
Universidade Nova de Lisboa

Agradecimentos

O trabalho apresentado nesta tese envolveu a participação direta ou indireta de várias pessoas a quem gostaria de expressar os meus agradecimentos. Em especial gostaria de agradecer:

Ao Prof. Doutor Carlos Salgueiro, excelente orientador que providenciou todas as condições para desenvolver todo o trabalho descrito nesta tese, bem como pelo magnifico exemplo de respeito e dedicação pela investigação científica e pelos seus alunos captando sempre o melhor de cada um. Agradeço também por todo o conhecimento transmitido, pelo companheirismo, paciência, pela disponibilidade que sempre manifestou e pelos momentos de descontração, assim como pela confiança e estímulo para prosseguir e nunca desistir, mesmo em situações complicadas.

À Doutora Marta Bruix, pelo acesso ao espectrómetro de Ressonância Magnética Nuclear (RMN) Bruker Avance 800 utilizado em algumas das experiências desta tese, bem como pela ajuda na interpretação dos resultados e todo o conhecimento transmitido. Agradeço ainda pelo excelente exemplo de dedicação, determinação e paixão pela investigação científica.

Ao Doutor P. Raj Pokkuluri e Doutor O. Kokhan pelo trabalho na determinação da estrutura de raios-X do citocromo PccH e em alguns cálculos de *docking*, bem como pela disponibilidade demonstrada na interpretação dos resultados experimentais.

À Prof. Doutora Teresa Catarino pela ajuda incansável na realização, interpretação e discussão das experiências de cinética, bem como disponibilidade para utilização do equipamento de *stopped-flow* e da câmara anaeróbica no ITQB.

Ao Prof. Doutor David L. Turner agradeço a sua ajuda nos cálculos da estrutura do OmcF no estado reduzido, bem como pelas discussões cruciais para a interpretação de alguns resultados experimentais.

À Prof. Doutora Isabel Couto pela ajuda e disponibilidade em questões relacionadas com biologia molecular.

À Doutora Leonor Morgado, por todas as discussões profícuas, pela partilha de conhecimento, pelo trabalho de equipa, pelo perfeccionismo demonstrado e dedicação pela investigação científica, bem como pelos momentos de lazer e boa disposição.

A todos os meus colegas de laboratório, bem como estudantes de licenciatura e mestrado que foram passando pelo Lab 6.11 durante os últimos anos, pelo dinamismo, diversidade, simpatia, boa disposição, admirável capacidade de trabalho e com os quais também aprendi imenso.

À Faculdade de Ciências e Tecnologia da Universidade NOVA de Lisboa (FCT-UNL), à Unidade de Ciências Biomoleculares Aplicadas (UCIBIO) e ao Laboratório Associado Rede de Química e Tecnologias (REQUIMTE), por terem fornecido os recursos necessários para desenvolver este trabalho.

À Fundação para a Ciência e Tecnologia pelo suporte e financiamento, através da bolsa de doutoramento, SFRH/BD/89701/2012, e pelos projetos PTDC/BBB-BQB/3554/2014 e UID/Multi/04378/2013 co-financiados por ERDF através de fundos nacionais, no âmbito do Acordo de Parceria PT2020 (POCI-01-0145-FEDER-007728).

Ao Laboratório de RMN da FCT-UNL, integrado na Rede Nacional de RMN e financiado pela Fundação para a Ciência e Tecnologia através do projeto, RECI/BBB-BQB/0230/2012, pelo acesso aos espectrómetros de RMN.

À minha família, em especial aos meus pais e irmão, bem como a todos os meus amigos pelo apoio incondicional, preocupação e por me acompanharem e estarem sempre presentes ao longo da minha vida. Por fim, gostaria de deixar um agradecimento muito especial ao Daniel Duarte, por me acompanhar nestes desafios sempre com um grande sorriso e por tudo o que representa para mim.

Resumo

As bactérias do género *Geobacter* têm despertado interesse devido ao seu impacto no meio ambiente e às suas aplicações biotecnológicas, incluindo a biorremediação de contaminantes orgânicos e inorgânicos, produção de bioenergia e bioeletrónica. Além da capacidade de transferência de eletrões para aceitadores terminais, estas bactérias conseguem também aceitar eletrões de elétrodos, um processo que é atualmente explorado na área da eletrossíntese microbiana. Estas aplicações baseiam-se num processo de troca de eletrões entre as células e o seu exterior, designado de transferência extracelular de eletrões (TEE). No entanto, os mecanismos subjacentes a estes processos encontram-se ainda em discussão. Com base em estudos genéticos e proteómicos identificaram-se citocromos do tipo *c* essenciais no processo de TEE, localizados na membrana interna, periplasma e membrana externa da bactéria *G. sulfurreducens*. Nesta Tese vão ser estudados alguns destes citocromos, tais como, o MacA, associado à membrana interna, os citocromos periplasmáticos PpcA-E e PccH, e o citocromo OmcF localizado na membrana externa.

As interações moleculares entre as proteínas PpcA-E e os seus possíveis parceiros redox, nomeadamente, MacA, PccH e um análogo dos ácidos húmicos, foram avaliadas por espectroscopia de ressonância magnética nuclear (RMN), cinética e *docking*. A afinidade entre cada complexo redox foi determinada por experiências de perturbação de desvio químico. Estes resultados demonstraram que as moléculas formam complexos reversíveis de baixa afinidade, compatíveis com uma transferência de eletrões rápida e seletiva, tipicamente observada entre parceiros redox.

A técnica de RMN foi igualmente utilizada para determinar a estrutura em solução do citocromo OmcF no estado reduzido, as alterações conformacionais dependentes da variação de pH e a sua dinâmica em solução.

O citocromo PccH foi estudado a nível bioquímico e estrutural, recorrendo às técnicas de dicroísmo circular, espectroscopia de UV-visível e RMN. Com base na sua estrutura, determinada por cristalografia de raios-X, demonstrou-se que esta é única entre os citocromos monohémicos do tipo *c*. De igual modo, os potenciais de redução, determinados por titulações redox a diferentes valores de pH, são invulgarmente baixos em comparação com outros valores descritos para este tipo de proteínas. Considerando as suas características estruturais e funcionais o citocromo PccH representa uma nova subclasse de citocromos monohémicos.

Os resultados obtidos e descritos nesta Tese constituem um importante contributo para a compreensão dos mecanismos de transferência eletrónica na bactéria *G. sulfurreducens*.

Palavras-chave: Transferência eletrónica, *Geobacter sulfurreducens*, Proteínas hémicas, RMN, Interações de proteínas, Estrutura de proteínas

Abstract

Geobacter bacteria have awakened significantly attention because of their impact on natural environments and biotechnological applications that include the bioremediation of organic and inorganic contaminants, bioenergy production and bioelectronics. In addition to electron transfer towards extracellular terminal acceptors, *Geobacter* cells can also accept electrons from electrodes, in current-consuming biofilms, a process that is currently explored in microbial electrosynthesis. These practical applications rely on an efficient transfer of electrons between the cell and its exterior, a process designated extracellular electron transfer (EET). However, the precise mechanisms underlying EET processes are still under debate. Genetic and proteomics studies have identified several *c*-type cytochromes as key components for EET in *G. sulfurreducens*. These proteins are located at the inner-membrane (IM), periplasm and outer-membrane (OM). Examples of such cytochromes include the IM-associated cytochrome MacA, periplasmic cytochromes PpcA-E and PccH, as well as, the OM cytochrome OmcF, which were studied in this Thesis.

Molecular interactions between PpcA-E and their putative redox partners, including a humic substance analogue molecule, MacA or PccH, were probed by NMR spectroscopy, stopped-flow kinetics and molecular docking. For the interacting pairs, their binding affinity was also determined by NMR chemical shift perturbation experiments. The results obtained showed that the interacting molecules establish reversible low-binding affinity complexes in specific regions of the proteins to warrant a rapid and selective electron transfer, a typical feature observed for electron transfer reactions between redox partners.

In addition, NMR spectroscopy was also used to determine the solution structure of OmcF in the reduced state, its pH-dependent conformational changes and backbone dynamics.

A biochemical and structural characterization of the cytochrome PccH was also carried out using circular dichroism, UV-visible and NMR spectroscopic techniques. The structure of PccH determined by X-ray crystallography showed that it is unique among the monoheme *c*-type cytochromes. The reduction potentials determined for PccH at different pH values by visible redox titrations are unusually low compared to those reported for other monoheme *c*-type cytochromes. Considering the structural and functional features of PccH it was proposed that this protein represents a first characterized example of a new subclass of monoheme *c*-type cytochromes.

Overall, the results obtained constitute an important contribute to the current understanding of the *G. sulfurreducens* extracellular electron transfer mechanisms.

Keywords: Electron transfer; *Geobacter sulfurreducens*; Heme proteins, NMR; Protein interactions; Protein structure

Table of contents

List of figures

1. Introduction

2. Materials and methods

3. Molecular interaction studies between the triheme cytochromes from *G. sulfurreducens* and the redox active humic substances analog

4. NMR interaction studies between inner membrane-associated and periplasmic cytochromes

5. Solution structure and dynamics of the outer membrane cytochrome OmcF

6. Biochemical and structural characterization of PccH

7. Future perspectives

8. Conclusions

A. Appendix

List of tables

1. Introduction

2. Materials and methods

3. Molecular interaction studies between the triheme cytochromes from *G. sulfurreducens* and the redox active humic substances analog

4. NMR interaction studies between inner membrane-associated and periplasmic cytochromes

5. Solution structure and dynamics of the outer membrane cytochrome OmcF

6. Biochemical and structural characterization of PccH

7. **Future perspectives**

A. **Appendix**

Abbreviations, symbols and constants

2xYT	2x Yeast extract – tryptone
AH_2QDS	Anthrahydroquinone-2,6,-disulphonate
Amp	Ampicillin
AQDS	Anthraquinone-2,6-disulphonate
BMRB	Biological Magnetic Resonance Data Bank
Ccm	Cytochrome *c* maturation
CD	Circular dichroism
Clo	Chloramphenicol
COSY	Correlation spectroscopy
DMRB	Dissimilatory metal reducing bacteria
E_{app}	Macroscopic apparent midpoint reduction potential
e_{app}	Microscopic apparent midpoint reduction potential
EDTA	Ethylenediamine tetraacetic acid
EET	Extracellular electron transfer
EXSY	Exchange spectroscopy
HMQC	Heteronuclear multiple quantum coherence
HP	MacA high potential heme
HS	Humic substances
HSQC	Heteronuclear single quantum coherence
IM	Inner membrane
Imc	Inner membrane cytochrome
IPTG	Isopropyl-β-D-thiogalactopyranoside
IUPAC-IUB	International Union of Pure and Applied Chemistry and International Union of Biochemistry
K_d	Equilibrium dissociation constant
LB	Luria-bertani medium
Lols	lower distance limits
Lov	lower limit volume
LP	MacA low potential heme
MALDI-TOF-MS	Matrix-assisted laser desorption−ionization time-of-flight mass spectrometry
Mac	Membrane associated cytochrome
MFC	Microbial fuel cells
MHC	Multiheme cytochromes *c*
MW	Molecular weight
NHE	Normal hydrogen electrode
NMR	Nuclear magnetic resonance
NOE	Nuclear Overhauser effect
NOESY	Nuclear Overhauser effect spectroscopy
OD_{600}	Optical density at 600 nm
OM	Outer membrane
Omc	Outer membrane cytochrome
PCR	Polymerase chain reaction
PDB	Protein data bank
pI	Isolectric point
Ppc	Periplasmic cytochrome
$PpcA_{ox}$	Periplasmic cytochrome A in the oxidized form
$PpcA_{red}$	Periplasmic cytochrome A in the reduced form

Ppm	Parts per million
rmsd	Root mean square deviation
Rpm	Rotations per minute
S^2	Order parameter
SDS-PAGE	Sodium dodecyl sulfate – polyacrylamide gel electrophoresis
T_1	Longitudinal relaxation
T_2	Transverse relaxation
TOCSY	Total correlation spectroscopy
TMBZ	Tetramethylbenzidine
Tris	Tris – tris(hydroxymethyl)aminomethane
Upls	Upper distance limits
Upv	Upper limit volume
UV-visible	Ultraviolet-visible
δ	Chemical shift
τ_c	Correlation time
τ_m	Global rotational diffusion correlation time
$\Delta\delta_{comb}$	Combined chemical shift

Amino acid abbreviations

Alanine	Ala	A
Arginine	Arg	R
Asparagine	Asn	N
Aspartate	Asp	D
Cysteine	Cys	C
Glutamate	Glu	E
Glutamine	Gln	Q
Glycine	Gly	G
Histidine	His	H
Isoleucine	Ile	I
Leucine	Leu	L
Lysine	Lys	K
Methionine	Met	M
Phenylalanine	Phe	F
Proline	Pro	P
Serine	Ser	S
Threonine	Thr	T
Tryptophan	Trp	W
Tyrosine	Tyr	Y
Valine	Val	V

1

INTRODUCTION

1. Introduction

Dissimilatory metal reduction is a widespread process that occurs in the major groups of Bacteria and is fundamental for the geochemistry of aquatic sediments, submerged soils, and terrestrial subsurfaces [1, 2]. Unlike other respiratory pathways, where the final electron acceptor is a freely diffusible gas or a readily soluble molecule that can be reduced inside the cell, dissimilatory metal reducing bacteria (DMRB) can sustain their energy requirements by coupling the oxidative metabolism of organic compounds to the reduction of extracellular metals [2].

The respiratory reduction of extracellular electron acceptors can be achieved by two broad mechanisms that involve direct or indirect reduction [3, 4]. In the first case, direct electron transfer is achieved by the contact between redox proteins located at the surface of the bacteria or via electrically conductive appendages that have been called biological nanowires (Fig 1.1). In the indirect mechanism, reduction of acceptors can be mediated by small redox-active molecules that are either secreted by the cell into the environment (endogenous electron shuttles) or are already available in the environment (exogenous electron shuttles) or mediated by bacterial-produced organic ligands (also designated as chelators), which solubilize metals prior to their reduction (Fig 1.1).

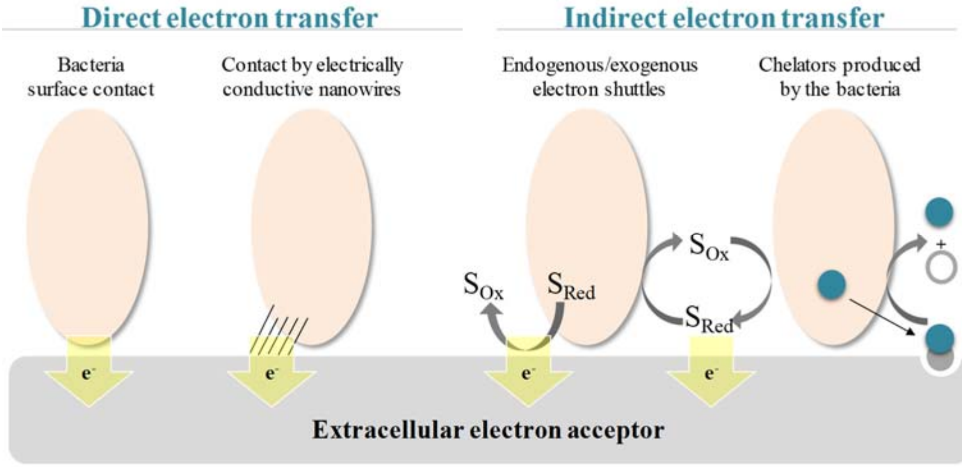

Fig 1.1 Schematic representation of bacterial direct and indirect electron transfer mechanisms to the extracellular electron acceptors. S_{Ox} and S_{Red} correspond to oxidized and reduced electron shuttles, respectively. The action of chelators is illustrated by circles: blue (chelator); gray (insoluble acceptor); white (solubilized acceptor) [5]. This figure was adapted from [5].

DMRB have attracted significant attention because of their respiratory characteristics offering an important role in the environmental recycling and removal of metal contaminants from groundwater [2]. Furthermore, some of these microorganisms (*e.g. Desulfuromonas acetoxidans*, *Geobacter sulfurreducens*, *Geobacter metallireducens*, *Rhodoferax ferrireducens*, *Desulfobulbus propionicus*, *Enterococcus gallinarum*, *Shewanella putrefaciens* and *Shewanella oneidensis* [6]) belong to the group of exoelectrogens, as they can also couple their oxidative metabolism to the electron transfer toward electrode surfaces from which electric current can be harvested in microbial fuel cells (MFC) [7, 8]. Particularly in the case of *Geobacter* species, highly cohesive protein filaments with metallic-like conductivity can be produced, offering the possibility to design microbial-based electronic sensors and other devices [9].

Currently much research is focused on alternative and renewable energy sources to offset world-wide concerns regarding global warming and fossil energy depletion [10]. Understanding the electron transfer processes by which exoelectrogens can couple the oxidation of organic compounds to the electron transfer to electrodes is a crucial step to allow the optimization of current production by MFC. Although, the present MFC power densities are too low to be considered as a viable alternative energy source, substantial improvements have been made in the last few years [11]. Given the broad range of biotechnological applications covered by DMRB it is important to understand the functional mechanism of their respiratory pathways. This would allow the scientific community to improve and optimize DMRB-based practical applications. Of these, the most studied DMRB belong to the Shewanellaceae and Geobacteraceae families, particularly *S. oneidensis* and *G. sulfurreducens*. The work developed and presented in this Thesis is focused on the structural and functional characterization of electron transfer components from *G. sulfurreducens* and for this reason the current knowledge of this bacterium is summarized in the next sections.

1.1 The *Geobacter sulfurreducens* bacteria

The *G. sulfurreducens* bacteria are comma-shaped rods are Gram-negative and can be found in contaminated soils and sediments where Fe(III) is an important respiratory terminal electron acceptor. However, their respiratory capability is not confined to iron reduction since they can also utilize a large diversity of electron donors and acceptors making them important agents in several biogeochemical cycles [12]. The important discoveries associated with *G. sulfurreducens* bacteria are summarized in Fig 1.2.

G. sulfurreducens bacteria display a remarkably respiratory versatility. They can utilize acetate, lactate, formate, anthrahydroquinone-2,6-disulphonate (AH_2QDS) or hydrogen, as electron donors, and fumarate, sulphur, malate, Co(III), Cr(VI), Mn(IV) oxides, U(VI), Tc(VII), anthraquinone-2,6-disulphonate (AQDS), among others, as electron acceptors [12, 13]. This respiratory capability can be used for several practical applications. For example, at physiological conditions, degradation of hydrocarbon contaminants in soils and the reduction of soluble metals (*e.g.* U(VI), Cr(VI)) to insoluble precipitates in contaminated aquifers (U(IV), Cr(III), respectively) facilitates the bioremediation of these pollutants [12, 14]. Moreover, these bacteria can be used to develop bioenergy applications as they grow on several electrode surfaces [12].

G. sulfurreducens was the first *Geobacter* species to have its genome fully sequenced, it is amenable to genetic manipulation and has been used as a model organism [15, 16]. This bacterium was previously classified as a strict anaerobe, but it has been verified that it can also grow in presence of low atmospheric oxygen levels [17, 18]. *G. sulfurreducens* tolerated exposure to oxygen for at least one day and grew with oxygen as the sole electron acceptor until concentrations of 10% in headspace. Additionally, the analysis of its genome revealed the presence of genes encoding typical enzymes for oxygen detoxification, such as catalase, cytochrome *c* oxidase or superoxide dismutase [18]. The analysis of the genome sequence of *G. sulfurreducens* revealed that it encodes 111 cytochromes *c*, 73 of which are multiheme cytochromes [15].

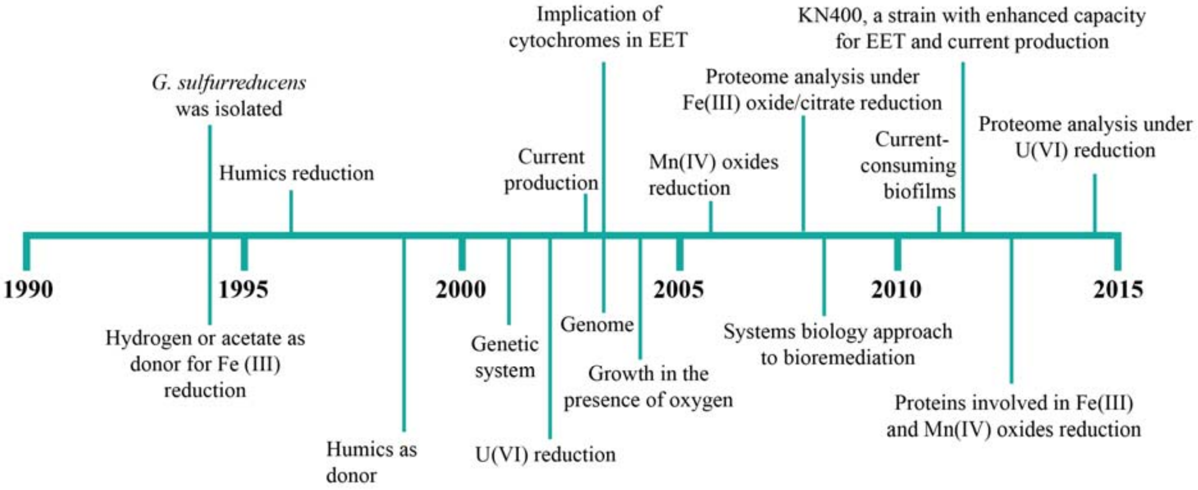

Fig 1.2 Time line of the important discoveries associated with *Geobacter sulfurreducens*. The time line presented in this figure was adapted from [12].

1.2 Cytochromes

Cytochromes are important proteins involved in a diversity of biological functions including electron transfer, oxygen transport and storage, catalysis, gas sensing and gene regulation [19]. The functional diversity of cytochromes is further extended by combining heme groups with other cofactors, including flavins and/or metal ions (*e.g.* molybdenum or copper). Different variables related with the type of heme groups and neighbor amino acids, modulate this functional versatility, namely (i) the ability of the protein environment to tune heme reactivity, (ii) the number and nature of protein-donated axial ligands to iron, (iii) the heme solvent exposure, (iv) the heme accessibility to exogenous ligands, (v) the distribution of polar and charged groups in the heme neighborhood, and (vi) specific properties of the heme-binding site in the protein [19, 20].

Proteins containing one or more heme groups are one of the most studied classes of biomolecules, due to their range of cellular biological functions. Usually, the cytochromes are named accordingly to their heme type letter, in italic, and a number in subscript depending on some intrinsic characteristics related to the protein axial ligands coordination, number of heme groups, optical or functional properties [21]. For example, the cytochrome c_{551}, involved in dissimilative denitrification of *Pseudomonas aeruginosa*, is a monoheme cytochrome axially coordinated by one histidine and one methionine that shows a band in the optical spectra with absorption maximum at 551 nm (α band) in the reduced state [22].

Cytochromes *c* are heme proteins containing a *c*-type heme and often function as electron carriers. In most cases, the polypeptide chain of these proteins is covalently bound to one or several *c*-type heme groups through thioether linkages established with the sulfhydryl groups of two cysteine residues in a conserved binding motif sequence CXXCH, where the X represents any amino acid (Fig 1.3) [19, 23]. This sequence is highly variable and all amino acids have been found in the "XX" segment in nature, except for the amino acid cysteine. In some cases, this segment can be larger and contain up to 15 amino acids (*e.g.* cytochrome MccA from *Wolinella succinogenes*) [19, 24].

The heme group displays a central role in the functional modulation of these proteins. It is constituted by four pyrrole subunits connected by methane bridges (protoporphyrin IX) and in the center, the iron ion is equatorially coordinated by four nitrogen atoms (Fig 1.3). The Iron (0) is a transition metal with 26 electrons arranged in the electronic configuration $1s^2 2s^2 2p^6 3s^2 3p^6 3d^6 4s^2$, where the normal number correspond to the orbitals (s, p and d) and the superscripts represent the electron occupancies. This configuration is also represented as $[Ar]3d^6 4s^2$, to emphasize that it is the occupancy of the higher energy 4s and 3d orbitals, superimposed on an argon core, that determines the electronic properties and the chemical behavior of the heme iron. Generally, in electron transfer cytochromes, the iron exists in the ferrous (Fe(II)) and ferric (Fe(III)) states, with the electronic configurations $[Ar]3d^6 4s^0$ and $[Ar]3d^5 4s^0$, respectively. Iron(IV) ($[Ar]3d^4 4s^0$) is a less common state but often found in catalytic cycles of some enzymes, such as catalases or peroxidases [23].

The description of high and low spin states relates to the distribution of the electrons in the five 3d orbitals (two orbitals e_g with higher energy and three t_{2g} with lower energy, according to Crystal Field Theory [25]). Each orbital holds a maximum of two electrons, and the energy separation between the e_g and t_{2g} orbitals is influenced by the ligands coordinated to the iron ion. The iron ion is in the high spin state if the d-orbital splitting is smaller than the pairing energy (weak crystal field) and therefore the electrons remain mostly unpaired in the orbitals (e_g and t_{2g}). Conversely, if the d-orbital splitting is larger compared to the pairing energy (strong crystal field), the electrons enter the t_{2g} orbitals and pair to produce the low spin state. Porphyrin is a strong ligand that places the iron ion close to a state where small energy differences between the axial ligand components of the field can cause the change of spin state [23]. Therefore, the determination of the spin state of a heme protein is important, because it provides information about the nature of the heme axial ligands and their stereochemistry. The heme spin state can be probed by a variety of spectroscopic techniques [26].

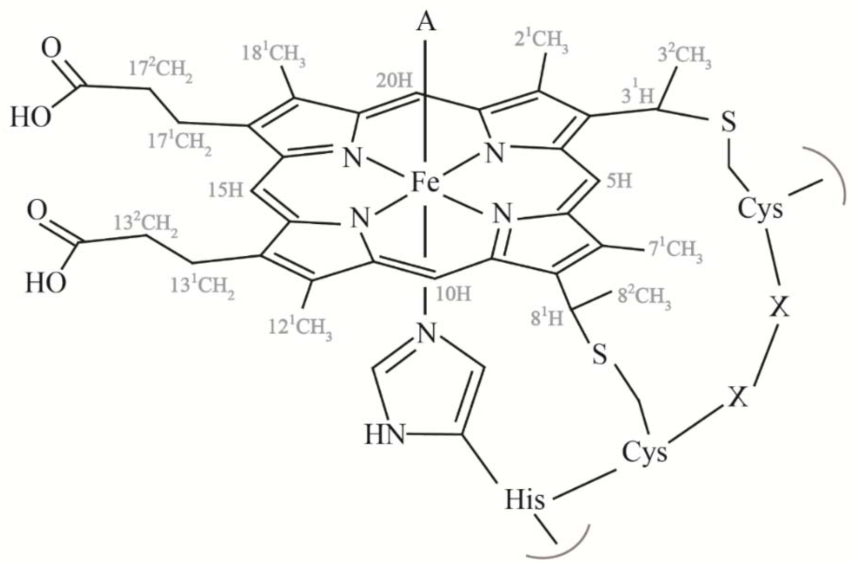

Fig 1.3 Schematic representation of a *c*-type heme and the correspondent polypeptide binding motif. The axial coordination position labeled with A can be free or occupied by ligands such the side chain of methionine, histidine, asparagine or tyrosine residues, which are the most common. The IUPAC nomenclature for tetrapyrroles is illustrated in gray [27]. This figure was adapted from [5].

As depicted in Fig 1.3, four out the six heme iron coordination positions are equatorially occupied by nitrogen atoms. In most cases, one of the two axial coordination positions of cytochromes *c* is occupied by the side chain of a histidine in the binding motif sequence, which is also designated as proximal ligand. On the contrary, the distal ligand is more variable and can be the side chain of a (i) methionine, which predominates in monoheme cytochromes *c*, (ii) histidine, particularly in multiheme cytochromes *c* or (iii) asparagine or tyrosine, although less frequently [21, 28]. The distal position of the heme can be also transiently vacant, as observed in cytochromes with enzymatic activity [5, 21, 28].

When the distal ligand is histidine or methionine residues, a strong crystal field and thus, a low spin state is observed. In contrast, if the side chain of asparagine, tyrosine or a water molecule bind the heme iron distal position, a high spin state will be observed [23]. Additionally, the identification of the iron axial coordination is important, because it determines the protein function, in most cases. Generally, the heme proteins involved in electron transfer reactions have both axial positions occupied and hold histidine or methionine residues as distal ligands. On the contrary, in the case of heme proteins with enzymatic activity that use a subtract molecule as heme axial ligand, an alternation between the iron penta- and hexa-coordinated forms is observed (*e.g.* peroxidases, catalases) [5, 23]. The heme redox potential is also strongly dependent on the nature of the axial ligands. For example, the side chain methionine sulfur is a good electron acceptor and favors the electron-rich reduced state resulting in a more positive redox potential compared to bis-histidinyl coordinated heme groups [29, 30].

1.3 Multiheme cytochromes

Multiheme cytochromes *c* (MHC) are crucial components of several biological processes where they drive electron transfer pathways. However, MHC can also display enzymatic activity [31, 32] or participate in signal transduction events [33]. In these complex cytochromes, the heme groups are arranged along the polypeptide chain and extend the protein global working redox potential ranges, because of the contribution of each individual heme redox potential. Additionally, these proteins might be able to receive or donate multiple electrons in a cooperative way, a process that can be modulated by the intrinsic properties of neighboring hemes (redox interactions) or protonatable centers (redox-Bohr effect) [34]. As well, these proteins can also putatively work as electron biocapacitors and contribute to the enhancement of the bacterial electron-storage capacity [35-37]. Typically, the heme iron-iron distances between adjacent hemes in MHC do not exceed 16 Å. This allows a fast electronic exchange between the redox centers, a crucial feature to assure efficient redox reactions [3, 28, 38]. The high number of hemes in these proteins not only provides the cell with a remarkable electron storage capacity but also allows them to transfer electrons through large distances without the need for successive binding events. For the reasons presented above, the precise tuning of the heme redox potentials in MHC is of crucial importance. These are affected by several factors that include: (i) the differences in the free energy between the oxidized and reduced states resulting from molecular interaction changes; (ii) the modulation of the electrostatic interactions within the protein or with the solvent; (iii) the heme solvent accessibility; (iv) the extent to which the heme group is distorted from planarity; (v) the protonation state of the heme propionate groups; (vi) the type of axial ligands and heme iron coordination [23, 39-45]. In most of the cases, MHC have a lower amino acid residue to heme ratio compared to monoheme cytochromes and, therefore, are more solvent exposed [23, 41]. The heme solvent exposure and its axial coordination (typically His-His) strongly contribute to the lower redox potential values generally observed in MHC.

1.4 Extracellular electron transfer pathways in *G. sulfurreducens*

The strategic localization of cytochromes from *G. sulfurreducens* at the bacterial inner membrane (IM), periplasm or outer membrane (OM) allows the transfer of electrons from intracellular carriers (*e.g.* NADH) to extracellular acceptors in a process termed extracellular electron transfer (EET). Previous proteomic studies revealed that 79 *c*-type cytochromes from *G. sulfurreducens* were expressed during growth on Fe(III) citrate or Fe(III) oxide electron acceptors, using acetate as electron donor [46]. The proteomic analysis and concomitant phenotypes of *G. sulfurreducens* mutant strains with gene encoding the studied cytochromes are summarized in Table 1.1.

Table 1.1 Analysis of proteome and phenotypes of different deletion mutant strains of *G. sulfurreducens* for cells grown in the presence of the acetate (electron donor) and Fe(III) oxide or Fe(III) citrate (electron acceptor). "IM" stands for inner membrane, "P" for periplasm and "OM" for outer membrane.

Locus ID	**Gene name**	**Predicted cellular location**	**Analysis of the proteome**	**Phenotype during growth on the electron acceptors**		**Ref**
				Fe(III) oxide	**Fe(III) citrate**	
GSU0274	*cbcL*	IM	-	Impaired growth	Increased growth rate	[47]
GSU0364	*ppcB*	P	Detected in Fe(III) citrate and Fe(III) oxide cultures	No phenotype	Impaired growth	[46, 48]
GSU0365	*ppcC*	P	Detected in Fe(III) citrate and Fe(III) oxide cultures	No phenotype	Impaired growth	[46, 48]
GSU0466	*macA*	IM-associated	More abundant during growth with Fe(III) oxides *vs* Fe(III) citrate. Involved in the regulation of OmcB	Impaired growth	Impaired growth	[46, 48]
GSU0612	*ppcA*	P	Detected in Fe(III) citrate and Fe(III) oxide cultures	No phenotype	Impaired growth	[46, 48, 49]
GSU0618	*omcE*	OM	More abundant during growth with Fe(III) oxide *vs* Fe(III) citrate	Impaired growth	No phenotype	[48, 50]
GSU1024	*ppcD*	P	More abundant during growth with Fe(III) oxides *vs* Fe(III) citrate	No phenotype	Increased Fe(III) reduction	[46, 48]
GSU1760	*ppcE*	P	Detected in Fe(III) citrate cultures	No phenotype	Increased growth rate	[46, 48]
GSU1996	-	P	More abundant during growth with Fe(III) citrate *vs* Fe(III) oxide	-	-	[46]
GSU2076	*omcZ*	OM	More abundant during growth with Fe(III) citrate *vs* Fe(III) oxide	No phenotype	No phenotype	[46, 48, 51]
GSU2432	*omcF*	OM	Involved in the regulation of OmcB, OmcC and OmcS	Impaired growth	Impaired growth	[48, 52, 53]
GSU2504	*omcS*	OM	More abundant during growth with Fe(III) oxides *vs* Fe(III) citrate	No growth	No phenotype	[48, 50, 54]
GSU2731	*omcC*	OM	More abundant during growth with Fe(III) oxides *vs* Fe(III) citrate	No phenotype	No phenotype	[48, 55]
GSU2737	*omcB*	OM	Detected in Fe(III) citrate and Fe(III) oxide cultures	Impaired growth	Impaired growth	[48, 55]
GSU3259	*imcH*	IM	-	Increased growth rate	No growth	[56]

The electron transfer mechanisms in *G. sulfurreducens* and the proteins implicated in each pathway are still under investigation. It is consensual that NADH electrons are transferred to the quinone pool via an IM NADH dehydrogenase. However, from this point the electron transfer mechanism(s) toward the final electron acceptors are still under debate.

The first studies envisioned that the IM-associated diheme cytochrome MacA (GSU0466, the naming scheme of the genome is in accordance with http://www.genome.jp/kegg/genome.html) with 35 kDa molecular weight, might be part of an electron transport chain moving electrons from the inner membrane, through the periplasmic cytochromes, to the outer surface of the cell [57, 58]. Proteomic studies revealed that MacA is more abundant during growth with Fe(III) oxides *vs* Fe(III) citrate (Table 1.1) [46]. Then, gene knock-out studies implicated the deletion of *macA* in the inhibition of the expression of the *omcB* gene. Expression of the outer membrane cytochrome OmcB in the *macA*-deficient mutant restored the capacity for Fe(III) reduction [53]. Additionally, the similarity in expression patterns and mutant phenotypes between MacA and OmcB suggests that they may function in the same or similar routes of electron transfer [48]. Cytochrome MacA was also identified as a peroxidase and capable of exchange electrons with the periplasmic *c*-type cytochrome PpcA [59].

More recently, it was suggested that depending upon the redox potential of the final electron acceptor different proteins are involved in the quinone pool regeneration [47, 56]. At least, two different routes were identified in response to the amount of energy available in a metal or electrode distant from the cell [56]. This is supported by several studies that revealed a complex transcriptional response by *G. sulfurreducens* to different electron acceptors [46, 54, 60, 61]. Indeed, the large number of *c*-type cytochromes [15] and the examination that no single deletion eliminates electron transfer to all electron acceptors further confirm the complexity of the EET in *G. sulfurreducens* [48, 62].

Studies examining electron transfer from *G. sulfurreducens* to poised graphite electrodes demonstrated that at least two IM proteins are implicated in two different EET pathways, i) CbcL-dependent pathway, for potentials below -100 mV *vs* NHE (Fe(III)- oxides, such as ferrihydrite), and ii) ImcH-dependent pathway, for electrodes poised at redox potentials above -100 mV *vs* NHE (Fe(III) citrate, Fe(III)-EDTA) [47, 56]. These observations confirmed that at least another quinone oxidoreductase is active in the bacteria to support growth at low redox potentials even when the *imcH* gene is deleted [56].

The CbcL protein (GSU0274) contains a HydC/FdnI diheme *b*-type cytochrome linked to a 9-heme periplasmic cytochrome *c* domain [47]. On the other hand, the cytochrome ImcH (GSU3259) was predicted to contain up to three transmembrane helices (depending on processing of a putative signal-anchor), a region of NapC/NirT homology, and up to 7 heme *c*-type heme binding motifs [56]. For Fe(III) oxides the redox potential decreases as Fe(II) accumulates triggering the utilization of electron transfer pathways that support lower cell yield and slower growth rates, but still allow some respiration.

With this new perspective, *G. sulfurreducens* bacterium can also be used as a redox sensor to report the redox potential of an extracellular electron acceptor and represents an array of thermodynamic opportunities, where these bacteria rapidly alter their respiratory strategy to take advantage of the available extracellular electron acceptor [63]. However, the electron transfer pathways from the reduced quinone pool to the final electron acceptor are still far from being understood.

In the currently proposed model for *G. sulfurreducens*, the electrons from IM cytochromes are then transferred to periplasmic *c*-type cytochromes. The most studied periplasmic cytochrome is PpcA (GSU0612) that belongs to a family composed by five low molecular weight (~10 kDa) periplasmic triheme cytochromes with approximately 70 residues each. The other four cytochromes of this family are designated PpcB (GSU0364), PpcC (GSU0365), PpcD (GSU1024), PpcE (GSU1760) and share 77 % (PpcB), 62 % (PpcC), 57 % (PpcD) and 65 % (PpcE) amino acid sequence identity with PpcA. Genetic studies revealed that these cytochromes are involved in different electron transfer pathways. PpcA was detected in *G. sulfurreducens* cultures that grow in presence of Fe(III) citrate and Fe(III) oxide [46]. Deletion of the gene encoding for PpcA affected the reduction of Fe(III) and U(VI) [49, 64]. Genes encoding for PpcB and PpcC belong to the same locus and the double deletion of these genes affected U(VI) reduction. Both cytochromes were detected in Fe(III) citrate and Fe(III) oxide cultures [46, 64]. PpcD is more abundant during growth with Fe(III) oxides *vs* Fe(III) citrate [46]. The deletion of its gene affected the reduction of U(VI) [64]. PpcE was only detected in cultures with Fe(III) citrate and its deletion also affected U(VI) reduction [46, 64]. Due to the cellular location of these five cytochromes it was proposed that they are the likely reservoir of electrons destined for the cell outer surface and bridge the electron transfer between the cytoplasm and the cell exterior [49, 60].

Also located in the periplasm of *G. sulfurreducens,* the dodecaheme cytochrome GSU1996 (42.3 kDa) is composed by four similar triheme domains, designated A, B, C and D (see section 1.4.1.1). and the 12-heme groups might allow the cytochrome to act as a periplasmic electron capacitor [36, 37].

To reduce extracellular compounds, electrons are transferred from the periplasm to the OM proteins. As suggested for *S. oneidensis*, it is proposed that in *G. sulfurreducens*, the electrons reach the cellular exterior through porin-cytochrome trans-outer membrane complexes. The complexes OmaB-OmbB-OmcB and OmaC-OmbC-OmcC in *G. sulfurreducens* may have similar functions to the ones described for the MtrA-MtrB-MtrC complex in *S. oneidensis* [65]. These complexes consist of a porin-like OM protein (OmbB or OmbC), a periplasmic octaheme cytochrome *c* (OmaB or OmaC) and an OM dodecaheme cytochrome *c* (OmcB or OmcC). Studies revealed that these complexes are directly involved in the reduction of Fe(III) citrate and ferrihydrite by *G. sulfurreducens* [55].

OmcF (GSU2432) is the smallest monoheme cytochrome *c* (11 kDa) and it was predicted to be localized at the OM of *G. sulfurreducens* [15]. The deletion of the *omcF* gene impaired Fe(III) citrate reduction and affected the expression of the OM cytochromes OmcB, OmcC and OmcS [52]. The deletion of *omcF* resulted in a loss of expression of *omcB* and *omcC*, and overexpression of *omcS*, during growth on Fe(III) citrate [66]. More recent studies demonstrated that a *omcF*-deficient strain was unable to grow in presence of Fe(III) oxide and showed a significant decrease in current production [48, 66].

OmcS (47 kDa) and OmcZ (30 kDa) are extracellular *c*-type cytochromes from *G. sulfurreducens* containing six and eight heme groups, respectively [51, 67]. It was demonstrated that OmcS is associated with conductive pili [67] and OmcZ is well suited for promoting electron transfer in current-producing *G. sulfurreducens* biofilms [68]. The deletion of the gene encoding OmcS cytochrome affected the bacterial growth in the presence of Fe(III) oxides (Table 1.1). It was also observed that OmcS is more abundant during growth with Fe(III) oxides *vs* Fe(III) citrate (Table 1.1). The opposite effect was observed for OmcZ (Table 1.1) and also, *in vitro* studies demonstrated that OmcZ transfers electrons to a diversity of potential extracellular electron acceptors, such as Fe(III) citrate, U(VI), Cr(VI), Au(III), Mn(IV) oxide, and AQDS, but not Fe(III) oxide [46, 51].

OmcE (GSU0618) is a tetraheme *c*-type cytochrome (26 kDa) located in the exterior of the OM of the bacterium. This cytochrome is more abundant during growth with Fe(III) oxide than in cells grown on Fe(III) citrate (Table 1.1). Previous studies revealed that the *omcE*-deficient mutant did slowly adapt to reduce Fe(III) oxide suggesting that one or more, as undetermined yet, components can partially compensate for the loss of OmcE [50].

1.4.1 Characterization of cytochromes *c*

Since the publication of *G. sulfurreducens* genome sequence and the development of an expression system to overproduce MHC [15, 69], several efforts to optimize the expression constructs, as well as the host strains, have been undertaken to increase the protein expression yields, a crucial step to assist the structural and functional characterization of *G. sulfurreducens* cytochromes (Fig 1.4).

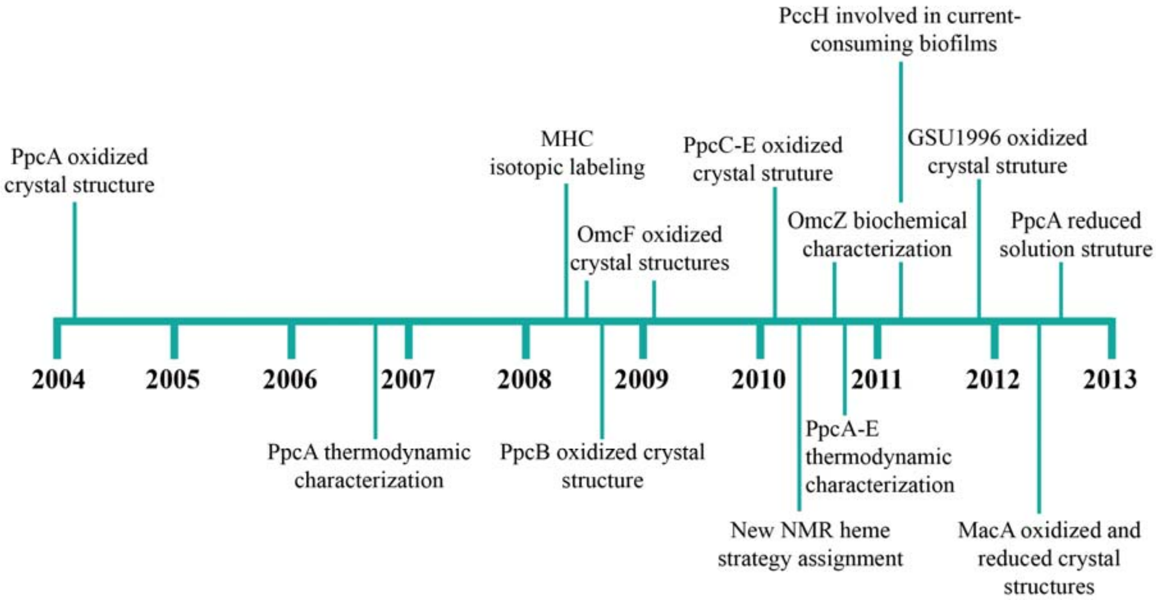

Fig 1.4 Time line of important discoveries related with the *G. sulfurreducens* cytochromes addressed in this Thesis.

1.4.1.1 Structural characterization

Three-dimensional structures of biological macromolecules can be determined by X-ray crystallography and NMR at near atomic resolution. The structures obtained by NMR represent the average over oriented molecules in solution, whereas diffraction data represent an average over molecules arranged in a periodic crystal lattice. Despite their similarities and differences, X-ray crystallography and NMR are well established complementary high-resolution methods to analyze protein structure-function relationships.

Structures of heme proteins are extremely under-represented in structural databases (~4%, data from Protein Data Bank, http://www.rcsb.org/pdb/, 2017), which constitute a severe bottleneck in the elucidation of their structural–functional relationships. Further, structures of heme proteins determined by NMR are very few (~1%). Mostly because of the presence of heme groups, which not only contribute with their proton-containing groups (four methyl groups, four meso protons, two thioether protons, two thioether methyls and two propionates; see Fig 1.3), but also affect the polypeptide chain NMR signals, particularly in the paramagnetic state, due to the magnetic properties of the heme iron that further spread and broaden the signals [70, 71].

Particularly in the case of MHC, advances in expression protocols that allowed their isotopic labeling in a more cost-effective manner together with the implementation of methodologies, that simplify the assignment of NMR signals have contributed to improve the structural characterization of these proteins [69, 70, 72-76].

Out of cytochromes found in *Geobacter*, PpcA was the first structurally characterized by X-ray crystallography in the oxidized state [77]. In the following years the crystal structures of the other four periplasmic triheme cytochromes PpcB-E belonging to the PpcA-family were also determined in the oxidized state [78, 79]. More recently, the solution structures of PpcA in the reduced and oxidized forms were also determined by NMR [80, 81]. The structures of these cytochromes are similar (Fig 1.5) but important local variations are observed. In these proteins, an antiparallel β-sheet is conserved at the N-terminal of all structures, and is followed by distinct helical regions in the different proteins. The heme core structures are similar, with hemes I and IV roughly parallel to each other and with both nearly perpendicular to heme III [77-80]. Within the five structures, in general heme I shows the highest solvent exposure, while heme III is the lowest exposed. On the other hand, heme IV shows the largest positive electrostatic surface due to the considerable number of neighboring lysine residues, except for PpcE. This positively charged surface around heme IV is the most conserved region, while the lowest similarity region is located near heme I [79]. The spatial arrangement of the hemes is superimposable with those of the structurally homologous tetraheme cytochromes c_3, with the sole difference being the absence of heme II and the corresponding polypeptide segment. For this reason, the three heme groups in triheme cytochromes are numbered I, III and IV [82]. All members of the PpcA-family contain three low-spin heme groups with His–His axial coordination [79].

Structures for other *G. sulfurreducens* cytochromes were also determined by X-ray crystallography, namely those of cytochromes OmcF [83, 84] and GSU1996, both in the oxidized state [36], and MacA in the reduced, oxidized and intermediate states [59] (Fig 1.5).

Two structures for OmcF were determined and published nearly at the same time [83, 84]. The first one was obtained for the cytochrome crystalized with a strep-tag II fusion protein at the N-terminal [83] and the second one was obtained only for the mature protein, which is represented in the Fig 1.5 [84]. Analysis of the crystal structure and UV-visible spectral features of OmcF showed that the heme group is in the low-spin state and has His–Met axial coordination.

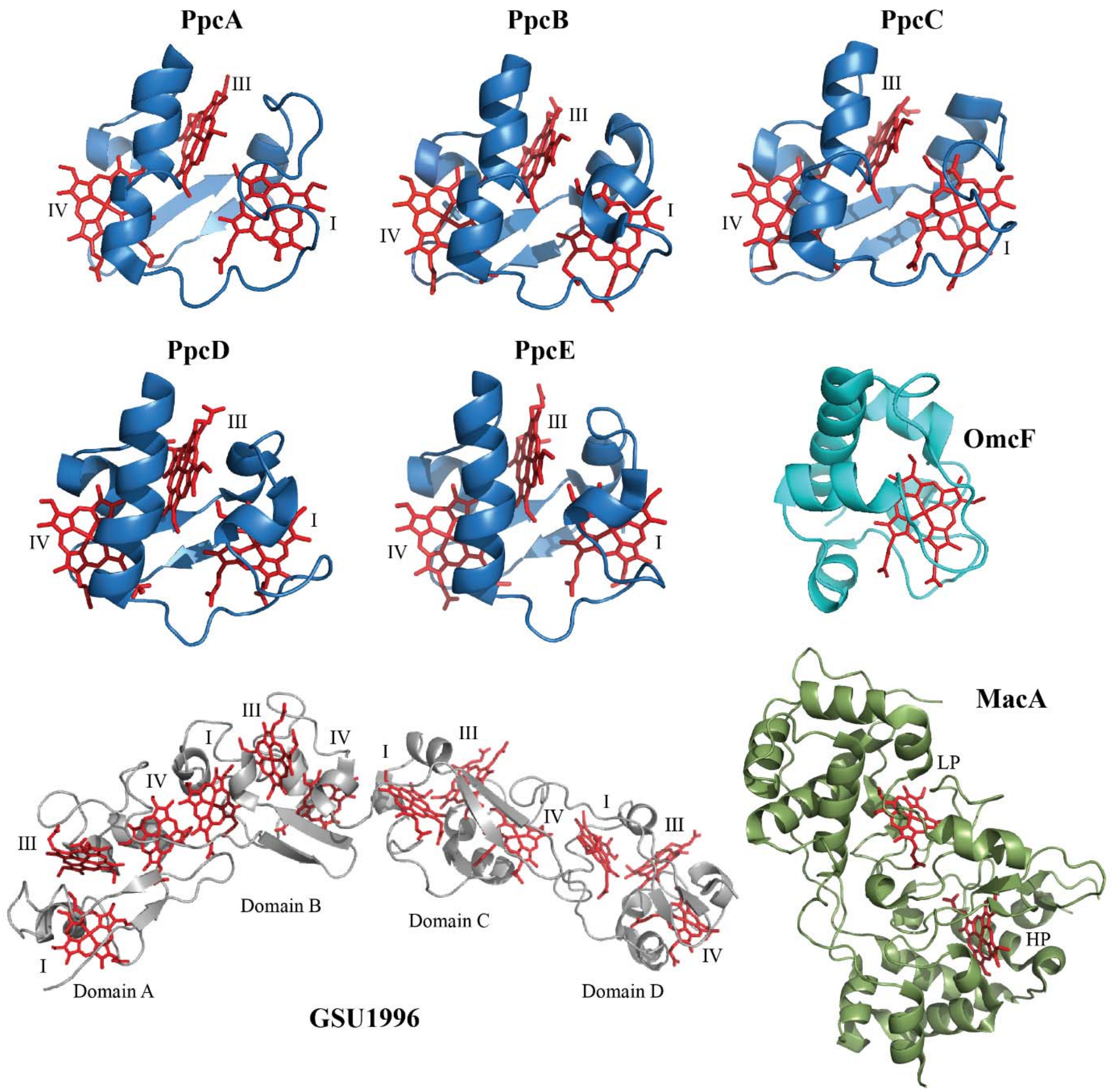

Fig 1.5 Structures of *G. sulfurreducens* cytochromes obtained in the oxidized state. The solution structure of PpcA (lowest energy; PDB ID: 2MZ9 [81] and the crystal structures of PpcB (chain A, PDB ID: 3BXU [78]), PpcC (PDB ID: 3H33 [79]), PpcD (chain A, PDB ID: 3H4N [79]), and PpcE (PDB ID: 3H34 [79]) are represented in blue. Crystal structures of OmcF (PDB ID: 3CU4 [84]), GSU1996 (PDB ID: 3OV0 [36]) and MacA (PDB ID: 4AAL [59]) are represented in cyan, gray and green, respectively. Roman numerals indicate the hemes (in red) in their order of attachment to the CXXCH motif in the polypeptide chain. The structures were drawn using the PyMOL molecular graphics system [85]. This figure was adapted from [5].

GSU1996 is a “nanowire” of hemes that may function as a capacitor to enhance the periplasmic bacterial electron-storage capability. It is organized in four similar domains (A-D) each containing three hemes and connected by a flexible linker. Each domain has structural homology to triheme cytochromes, differing only in heme IV, which contains His-Met axial coordination [36].

MacA forms two globular domains, each holding a *c*-type heme group. The hemes are named as high potential (HP) and low potential (LP), because of the electric potential difference between them. The LP heme is located at the N-terminal domain whereas the C-terminal domain harbors the HP one.

1.4.1.2 Thermodynamic characterization

In the same way, the presence of several heme groups constitutes the major bottleneck in the detailed thermodynamic characterization of MHC. For monoheme cytochromes only the reduced and oxidized states may coexist in solution. However, for MHC several one-electron reversible transfer steps convert the fully reduced state into the fully oxidized one, yielding additional intermediate oxidation stages (Fig 1.6). Therefore, when the values of redox potentials of each heme group are not sufficiently different, the global redox potentials measured by voltammetry or potentiometric redox titrations are macroscopic in nature and only describe the overall redox behavior of the MHC [68, 84, 86, 87]. Although these parameters contain information on the working functional ranges of these cytochromes, in most cases they are insufficient to provide mechanistic information on the electron transfer pathways. This can only be achieved when the fractional contribution of each possible microstate during the oxidation of the protein is obtained.

In the case of monoheme cytochromes the reduction potential of the heme can be obtained directly from the Nernst equation. In this case, the e_{app} value *(i.e.* the point at which the oxidized and reduced fractions of the protein are equal) corresponds to the reduction potential of the heme. However, this is not the case for MHC. The characterization of the redox properties of multiheme cytochromes is complex due to the co-existence of several heme groups. In fact, the several one-electron reversible transfer steps connecting the fully reduced and the fully oxidized states establish different redox stages, each grouping microstates with the same number of oxidized hemes. As an example, for a triheme cytochrome, three consecutive reversible steps of one-electron transfer convert the fully reduced state (stage 0, S_0) in the fully oxidized state (stage 3, S_3), and thus four different redox stages can be defined (Fig 1.6). Additionally, within each microstate, the group responsible for the redox-Bohr effect can be protonated or deprotonated, leading to a total of 16 microstates (Fig 1.6).

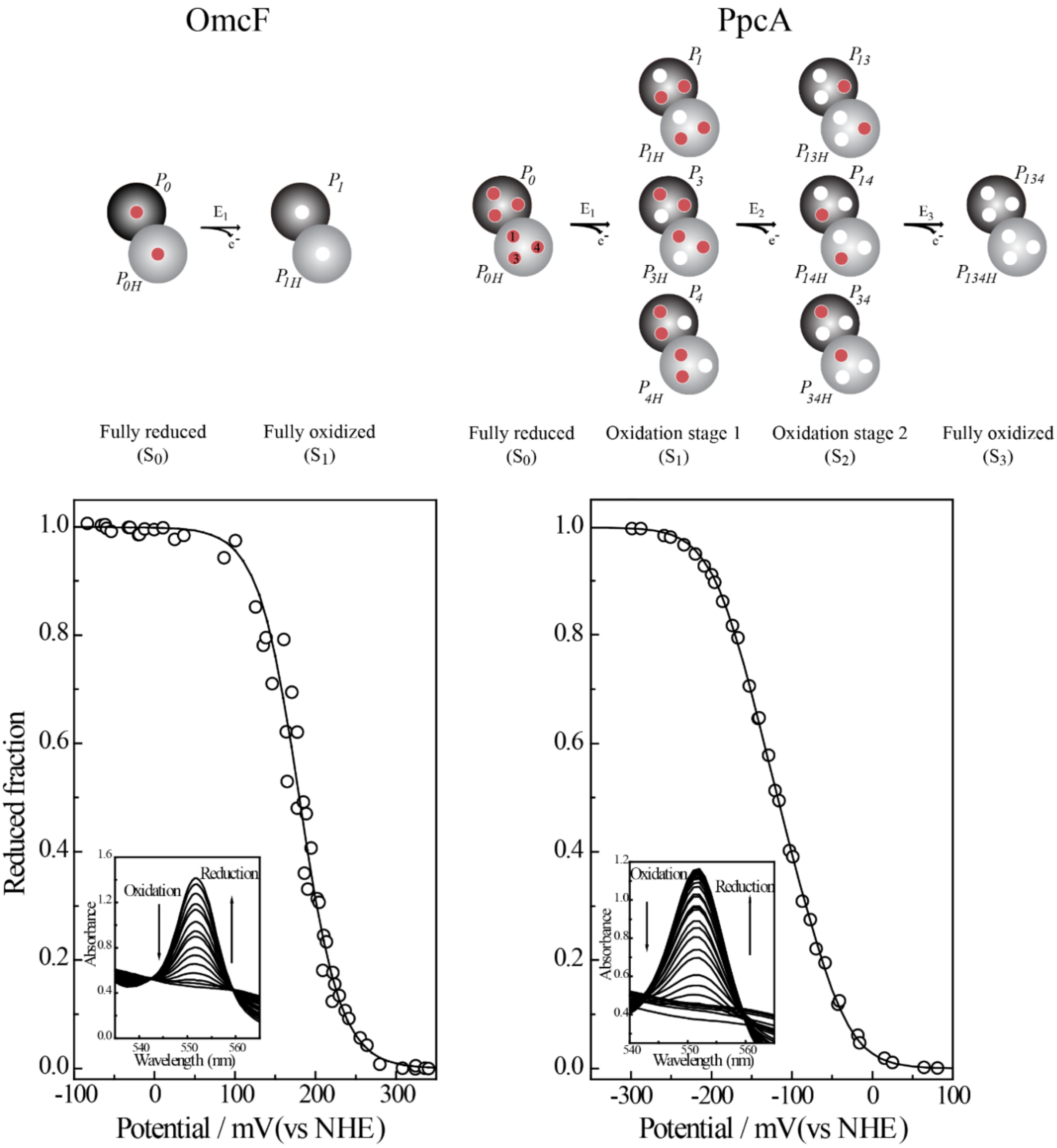

Fig 1.6 Electronic distribution scheme and potentiometric redox titrations followed by visible spectroscopy for monoheme (OmcF) and triheme (PpcA) cytochromes. The inner circles represent heme groups, which can either be reduced (red circles) or oxidized (white circles). The microstates are grouped per the number of oxidized hemes in each oxidation stage, connected by consecutive one-electron redox steps. P_{0H} and P_0 represent the reduced protonated and deprotonated microstates, respectively. P_{ijkH} and P_{ijk}, indicate, respectively, the protonated and deprotonated microstates, where i, j, and k represent the heme(s) that are oxidized in that particular microstate. In the lower panels, potentiometric redox titrations followed by visible spectroscopy of OmcF and PpcA (pH 7) are indicated. Solid lines indicate the result of the fits for the Nernst equation (OmcF) and for a model of three consecutive reversible redox steps between the different oxidation stages (PpcA) [78, 84]. This figure was adapted from [88].

In MHC containing neighboring heme groups, the reduction potential of each heme is most often modulated by redox interactions with other hemes and by the solution pH (redox-Bohr interactions).

Thus, to completely characterize the redox centers in a MHC it is necessary to determine the heme reduction potentials, the redox interactions and the properties of the redox-Bohr center(s). To calculate these thermodynamic parameters, it is necessary to monitor the stepwise oxidation of each heme oxidation at several pH values. This information can be achieved by NMR spectroscopy, which allows probing the individual heme oxidation profiles due to the different spectral signatures of the NMR spectra of low spin MHC in the reduced and oxidized states.

In conditions of fast intramolecular electron exchange (between the different microstates within the same oxidation stage) and slow intermolecular electron exchange (between different oxidation stages) on the NMR time scale [78], the heme oxidation fraction can be determined from the chemical shifts of the heme substituents in the different oxidation stages. Combining the information from redox titrations monitored by UV-visible spectroscopy and this NMR data it is possible to determine the absolute thermodynamic parameters and evaluate the contribution of each microstate and their relevance to the electron transfer mechanism.

This strategy was firstly described in the study of tetraheme cytochrome c_3 from *Desulfovibrio vulgaris* (13 kDa) by Turner and co-workers [89]. The increase in the protein molecular weight and/or the number of hemes leads to a decrease of the NMR spectral quality, as a result of signal overlapping, and usually impairs the monitoring of the individual heme oxidation profiles. To date, the detailed thermodynamic characterization of multiheme cytochromes has been limited to proteins containing up to four heme groups and 64 kDa molecular weight [90]. Therefore, the redox characterization of larger multiheme proteins can only be accomplished at the macroscopic level. This characterization was already performed for some cytochromes from *G. sulfurreducens* (Table 1.2).

Overall, the E_{app} values determined for *G. sulfurreducens* cytochromes listed in Table 1.2 span from −220 to +180 mV and are consistent with the axial coordination of the heme groups. In fact, cytochromes with His–His axially coordinated hemes have negative values, whereas a positive value was only observed for OmcF whose heme has His–Met axial coordination. Despite the presence of four hemes with His-Met axial coordination in GSU1996 the E_{app} value is negative. From the analysis of Table 1.2 it is also observed that the redox-active potential windows of the cytochromes correlate with their number of hemes. This indicates that the hemes are not redox equivalent and provides a rationalization for the involvement of several MHC in the same electron transfer pathway. An exception is observed for the dodecaheme cytochrome GSU1996, which has a comparable redox window to PpcA-family cytochromes. This feature can be explained by the structural architecture of the redox centers in cytochrome GSU1996.

Table 1.2 Data set of *G. sulfurreducens* *c*-type cytochromes participating in extracellular electron transfer pathways. E_{app} stands for the midpoint reduction potential correspondent to the point at which the oxidized and reduced fractions are equal, and 'NHE' for normal hydrogen electrode. The potential window was determined from potentiometric redox curves considering 1-99% range for protein reduction/oxidation. The redox potential values were determined at pH 7.

Protein	Heme axial ligands	E_{app} (mV) *vs* NHE	Potential window (mV)
MacA	His-Met	-188 [59]	250
GSU1996	His-His; His-Met	-124 [91]	320
PpcA	His-His	-117 [78]	285
PpcB	His-His	-137 [78]	270
PpcC	His-His	-143 [91]	265
PpcD	His-His	-132 [92]	275
PpcE	His-His	-134 [92]	280
OmcZ[a]	Not determined	-220 [68]	405
OmcF	His-Met	+180 [84]	240
OmcS	His-His	-212 [86]	320

[a] OmcZ is present in large ($OmcZ_L$ = 50 kDa) and small ($OmcZ_s$ = 30 kDa) forms. The data presented refer to $OmcZ_s$, which is the predominant extracellular form of OmcZ and retains the eight heme groups.

Except for PpcC, which presented multiple conformations in solution that impaired the monitorization of its heme oxidation profiles, the complete thermodynamic parameters were determined for the triheme cytochromes from PpcA-family (Tables 1.3 and 1.4) [92, 93]. The heme reduction potentials are negative, differ from each other, and cover different functional ranges. These reduction potentials are strongly modulated by heme-heme interactions and by interactions with protonated groups (the redox-Bohr effect), yielding different cooperative networks for each protein.

Table 1.3 Heme reduction potentials and pairwise interactions (mV) of the fully reduced and protonated forms of PpcA, PpcB, PpcD and PpcE [92].

	Heme redox potentials			Redox interactions			Redox-Bohr interactions		
	I	III	IV	I-III	I-IV	III-IV	I-H	III-H	IV-H
PpcA	-154	-138	-125	27	16	41	-32	-31	-58
PpcB	-150	-166	-125	17	8	32	-16	-9	-38
PpcD	-156	-139	-149	46	3	14	-28	-23	-53
PpcE	-167	-175	-116	27	5	22	-12	2	-13

The macroscopic pK_a values associated with the redox-Bohr center in each of the four oxidation stages are indicated in Table 1.4. The larger redox-Bohr effect is observed for PpcA and PpcD, 2.1 and 1.8 pH units, respectively. The ΔpK_a value is lower for PpcB and much smaller for PpcE (1.1 and 0.3 pH units, respectively) [92].

Table 1.4 Macroscopic pK_a values of the redox-Bohr center for PpcA, PpcB, PpcD, and PpcE at each stage of oxidation [92].

	pK_a			
Oxidation stage	**PpcA**	**PpcB**	**PpcD**	**PpcE**
0	8.6	7.4	8.7	7.7
1	8.0	7.1	8.1	7.6
2	7.2	6.8	7.4	7.5
3	6.5	6.3	6.9	7.4
ΔpK_a	2.1	1.1	1.8	0.3

1.5 Current-consuming biofilms

As previously described in section 1.4, electron transfer towards extracellular terminal acceptors is one of the most remarkable features of the bacterium *G. sulfurreducens*. However, it was recently discovered that *G. sulfurreducens* cells can also accept electrons from electrodes, in current-consuming biofilms [94]. In this process, the reducing power provided by an electrode, maintained at a sufficient negative electrochemical potential, can be used by the cells to synthesize valuable organic compounds, thus opening new perspectives in the field of bioremediation and biofuel production [95, 96]. To develop these applications, understanding the mechanisms by which microorganisms can accept electrons from electrodes are essential. These mechanisms are still poorly understood and to shed light on this, Strycharz and co-workers [97] used microarray analysis to compare gene transcript abundance in current-consuming *versus* current-producing *G. sulfurreducens* biofilms. In the first case, *G. sulfurreducens* cells mediate the transfer of electrons from a graphite cathode poised at -293 mV to the terminal electron acceptor fumarate (+30 mV). In the second case, a graphite anode poised at +507 mV was used as extracellular electron acceptor for the oxidation of acetate (-280 mV) (the redox potentials refer to NHE). The results showed that genes encoding for OM cytochromes (*e.g.* OmcZ) or PilA that are essential for efficient current-producing cells, had a much lower abundance in current-consuming biofilms [97]. On the contrary, a putative periplasmic *c*-type cytochrome PccH (GSU3274) clearly showed the largest transcript abundance [97]. Deletion of gene *pccH* completely inhibited electron transfer from electrodes, but had no influence on electron transfer to electrodes [97]. Overall, this study suggested that the routes for electron transfer from electrodes to *G. sulfurreducens* cells may be different than the ones for current production.

1.6 Objectives and Thesis outline

The structural and functional characterization of cytochromes from *G. sulfurreducens* is crucial to understand the EET mechanisms and to engineer improved forms of these electron transfer components that ultimately will contribute to increase the bacterial respiratory rates. This is the main goal of this Thesis. The Thesis is divided in eight Chapters. A general introduction is presented in Chapter 1, followed by the description of the experimental procedures in Chapter 2. Chapter 3 describes the backbone resonance NMR assignment of the periplasmic triheme cytochromes (PpcA-E, except for PpcC) in the oxidized state followed by the mapping of the molecular interaction between each protein and the humic substance analogue, AQDS. The molecular interactions between the IM-associated cytochrome MacA and the periplasmic cytochrome PpcA were also probed by NMR spectroscopy and are described in Chapter 4. The backbone and side chain NMR assignment of the OmcF in the fully reduced state together with its solution structure, backbone dynamics and pH-dependent conformational changes are described in the Chapter 5. Then, Chapter 6 is dedicated to the functional and structural characterization of PccH, a key cytochrome for electron transfer from electrodes to the bacterium *G. sulfurreducens*. Chapter 7 describes the experiments that support the ongoing studies that pave the way for the future experiments to be carried out at the host laboratory (Heme Proteins Research Group, UCIBIO-Requimte, Chemistry Department of FCT-UNL). These will include (i) the solution structure determination of PpcD in the reduced form, (ii) NMR interactions studies between the triheme periplasmic cytochromes and putative redox partners and (iii) the functional and structural characterization of the OM cytochromes OmaB, OmcS and OmcE. Finally, Chapter 8 presents an overall discussion on the results obtained together with some concluding remarks.

1.7 References

1. Nealson KH & Saffarini D (1994) Iron and manganese in anaerobic respiration: environmental significance, physiology, and regulation. *Annu Rev Microbiol* **48**, 311-343.

2. Lovley DR (1993) Dissimilatory metal reduction. *Annu Rev Microbiol* **47**, 263-290.

3. Breuer M, Rosso KM, Blumberger J & Butt JN (2015) Multi-haem cytochromes in *Shewanella oneidensis* MR-1: structures, functions and opportunities. *J R Soc Interface* **12**, 20141117.

4. Hernandez ME & Newman DK (2001) Extracellular electron transfer. *Cell Mol Life Sci* **58**, 1562-1571.

5. Salgueiro CA & Dantas JM (2016) Multiheme cytochromes. In *Protein folding and structure*. Gomes CM, ed, pp. 39. Springer-Verlag Berlin Heidelberg.

6. Erable B, Duteanu NM, Ghangrekar MM, Dumas C & Scott K (2010) Application of electro-active biofilms. *Biofouling* **26**, 57-71.

7. Kumar R, Singh L, Wahid ZA & Din MFM (2015) Exoelectrogens in microbial fuel cells toward bioelectricity generation: a review. *Int J Energ Res* **39**, 1048-1067.

8. Logan BE, Hamelers B, Rozendal R, Schroder U, Keller J, Freguia S, Aelterman P, Verstraete W & Rabaey K (2006) Microbial fuel cells: methodology and technology. *Environ Sci Technol* **40**, 5181-5192.

9. Lovley DR (2012) Electromicrobiology. *Annu Rev Microbiol* **66**, 391-409.

10. Franks AE, Malvankar N & Nevin KP (2010) Bacterial biofilms: The powerhouse of a microbial fuel cell. *Biofuels* **1**, 589-604.

11. Ren H, Tian H, Gardner CL, Ren TL & Chae J (2016) A miniaturized microbial fuel cell with three-dimensional graphene macroporous scaffold anode demonstrating a record power density of over 10 000 W m^{-3}. *Nanoscale* **8**, 3539-3547.

12. Lovley DR, Ueki T, Zhang T, Malvankar NS, Shrestha PM, Flanagan KA, Aklujkar M, Butler JE, Giloteaux L, Rotaru AE*, et al.* (2011) *Geobacter*: the microbe electric's physiology, ecology, and practical applications. *Adv Microb Physiol* **59**, 1-100.

13. Speers AM & Reguera G (2012) Electron donors supporting growth and electroactivity of *Geobacter sulfurreducens* anode biofilms. *Appl Environ Microbiol* **78**, 437-444.

14. Lovley DR, Holmes DE & Nevin KP (2004) Dissimilatory Fe(III) and Mn(IV) reduction. *Adv Microb Physiol* **49**, 219-286.

15. Methé BA, Nelson KE, Eisen JA, Paulsen IT, Nelson W, Heidelberg JF, Wu D, Wu M, Ward N, Beanan MJ*, et al.* (2003) Genome of *Geobacter sulfurreducens*: metal reduction in subsurface environments. *Science* **302**, 1967-1969.

16. Coppi MV, Leang C, Sandler SJ & Lovley DR (2001) Development of a genetic system for *Geobacter sulfurreducens*. *Appl Environ Microbiol* **67**, 3180-3187.

17. Caccavo F, Jr., Lonergan DJ, Lovley DR, Davis M, Stolz JF & McInerney MJ (1994) *Geobacter sulfurreducens* sp. nov., a hydrogen- and acetate-oxidizing dissimilatory metal-reducing microorganism. *Appl Environ Microbiol* **60**, 3752-3759.

18. Lin WC, Coppi MV & Lovley DR (2004) *Geobacter sulfurreducens* can grow with oxygen as a terminal electron acceptor. *Appl Environ Microb* **70**, 2525-2528.

19. Bowman SEJ & Bren KL (2008) The chemistry and biochemistry of heme *c*: functional bases for covalent attachment. *Nat Prod Rep* **25**, 1118-1130.

20. Chapman SK, Daft S & Munro AW (2005) Heme: The most versatile redox centre in biology? In *Metal Sites in Proteins and Models*. pp. 39-70. Springer Berlin Heidelberg.

21. Bertini I, Cavallaro G & Rosato A (2006) Cytochrome *c*: occurrence and functions. *Chem Rev* **106**, 90-115.

22. Cutruzzola F, Arese M, Ranghino G, van Pouderoyen G, Canters G & Brunori M (2002) *Pseudomonas aeruginosa* cytochrome c_{551}: probing the role of the hydrophobic patch in electron transfer. *J Inorg Biochem* **88**, 353-361.

23. Moore GR & Pettigrew GW (1990) *Cytochromes c : evolutionary, structural and physicochemical aspects*. Springer-Verlag, Berlin.

24. Hartshorne RS, Kern M, Meyer B, Clarke TA, Karas M, Richardson DJ & Simon J (2007) A dedicated haem lyase is required for the maturation of a novel bacterial cytochrome *c* with unconventional covalent haem binding. *Mol Microbiol* **64**, 1049-1060.

25. Van Vleck JH (1932) Theory of the variations in paramagnetic anisotropy among different salts of the iron group. *Phys Rev* **41**, 208-215.

26. Walker FA (1999) Magnetic spectroscopic (EPR, ESEEM, Mössbauer, MCD and NMR) studies of low-spin ferriheme centers and their corresponding heme proteins. *Coordin Chem Rev* **185-186**, 471-534.

27. Moss GP (1988) Nomenclature of tetrapyrroles. Recommendations 1986 IUPAC-IUB Joint Commission on Biochemical Nomenclature (JCBN). *Eur J Biochem* **178**, 277-328.

28. Smith LJ, Kahraman A & Thornton JM (2010) Heme proteins-diversity in structural characteristics, function, and folding. *Proteins* **78**, 2349-2368.

29. Pettigrew GW & Moore GR (1987) Cytochromes *c*: biological aspects. In *Molecular Biology*. pp. 282. Springer-Verlag Heidelberg, Berlin.

30. Banci L, Bertini I, Rosato A & Varani G (1999) Mitochondrial cytochromes *c*: a comparative analysis. *J Biol Inorg Chem* **4**, 824-837.

31. Brausemann A, Seidel J, Wüst A & Einsle O (2015) Multiheme peroxidases. In *Heme peroxidases*. Raven E & Dunford B, eds. Royal Society of Chemistry, RSC Publ, Cambridge.

32. Gordon EHJ, Pealing SL, Chapman SK, Ward FB & Reid GA (1998) Physiological function and regulation of flavocytochrome c_3, the soluble fumarate reductase from *Shewanella putrefaciens* NCIMB 400. *Microbiology* **144**, 937-945.

33. Pokkuluri PR, Pessanha M, Londer YY, Wood SJ, Duke NEC, Wilton R, Catarino T, Saigueiro CA & Schiffer M (2008) Structures and solution properties of two novel periplasmic sensor domains with *c*-type heme from chemotaxis proteins of *Geobacter sulfurreducens*: Implications for signal transduction. *J Mol Biol* **377**, 1498-1517.

34. Xavier AV (1986) Energy transduction coupling mechanisms in multiredox center proteins. *J Inorg Biochem* **28**, 239-243.

35. Esteve-Núñez A, Sosnik J, Visconti P & Lovley DR (2008) Fluorescent properties of *c*-type cytochromes reveal their potential role as an extracytoplasmic electron sink in *Geobacter sulfurreducens*. *Environ Microbiol* **10**, 497-505.

36. Pokkuluri PR, Londer YY, Duke NE, Pessanha M, Yang X, Orshonsky V, Orshonsky L, Erickson J, Zagyanskiy Y, Salgueiro CA*, et al.* (2011) Structure of a novel dodecaheme cytochrome *c* from *Geobacter sulfurreducens* reveals an extended 12 nm protein with interacting hemes. *J Struct Biol* **174**, 223-233.

37. Fernandes AP, Nunes TC, Paquete CM & Salgueiro CA (2017) Interaction studies between periplasmic cytochromes provide insights into extracellular electron transfer pathways of *Geobacter sulfurreducens*. *Biochem J* **474**, 797-808.

38. Page CC, Moser CC, Chen X & Dutton PL (1999) Natural engineering principles of electron tunnelling in biological oxidation-reduction. *Nature* **402**, 47-52.

39. Das DK & Medhi OK (1998) The role of heme propionate in controlling the redox potential of heme: square wave voltammetry of protoporphyrinato IX iron (III) in aqueous surfactant micelles. *J Inorg Biochem* **70**, 83-90.

40. Ma JG, Zhang J, Franco R, Jia SL, Moura I, Moura JJ, Kroneck PM & Shelnutt JA (1998) The structural origin of nonplanar heme distortions in tetraheme ferricytochromes c_3. *Biochemistry* **37**, 12431-12442.

41. Tezcan FA, Winkler JR & Gray HB (1998) Effects of ligation and folding on reduction potentials of heme proteins. *J Am Chem Soc* **120**, 13383-13388.

42. Liu Y, Moenne-Loccoz P, Hildebrand DP, Wilks A, Loehr TM, Mauk AG & Ortiz de Montellano PR (1999) Replacement of the proximal histidine iron ligand by a cysteine or tyrosine converts heme oxygenase to an oxidase. *Biochemistry* **38**, 3733-3743.

43. de Lacroix de Lavalette A, Barucq L, Alric J, Rappaport F & Zito F (2009) Is the redox state of the c_i heme of the cytochrome b_6f complex dependent on the occupation and structure of the Q_i site and *vice versa*? *J Biol Chem* **284**, 20822-20829.

44. Armstrong FA (1997) Evaluations of reduction potential data in relation to coupling, kinetics and function. *J Biol Inorg Chem* **2**, 139-142.

45. Gunner MR, Alexov E, Torres E & Lipovaca S (1997) The importance of the protein in controlling the electrochemistry of heme metalloproteins: Methods of calculation and analysis. *J Biol Inorg Chem* **2**, 126-134.

46. Ding YH, Hixson KK, Aklujkar MA, Lipton MS, Smith RD, Lovley DR & Mester T (2008) Proteome of *Geobacter sulfurreducens* grown with Fe(III) oxide or Fe(III) citrate as the electron acceptor. *Biochim Biophys Acta* **1784**, 1935-1941.

47. Zacharoff L, Chan CH & Bond DR (2016) Reduction of low potential electron acceptors requires the CbcL inner membrane cytochrome of *Geobacter sulfurreducens*. *Bioelectrochemistry* **107**, 7-13.

48. Aklujkar M, Coppi MV, Leang C, Kim BC, Chavan MA, Perpetua LA, Giloteaux L, Liu A & Holmes DE (2013) Proteins involved in electron transfer to Fe(III) and Mn(IV) oxides by *Geobacter sulfurreducens* and *Geobacter uraniireducens*. *Microbiology* **159**, 515-535.

49. Lloyd JR, Leang C, Hodges Myerson AL, Coppi MV, Cuifo S, Methe B, Sandler SJ & Lovley DR (2003) Biochemical and genetic characterization of PpcA, a periplasmic *c*-type cytochrome in *Geobacter sulfurreducens*. *Biochem J* **369**, 153-161.

50. Mehta T, Coppi MV, Childers SE & Lovley DR (2005) Outer membrane *c*-type cytochromes required for Fe(III) and Mn(IV) oxide reduction in *Geobacter sulfurreducens*. *Appl Environ Microbiol* **71**, 8634-8641.

51. Inoue K, Leang C, Franks AE, Woodard TL, Nevin KP & Lovley DR (2011) Specific localization of the *c*-type cytochrome OmcZ at the anode surface in current-producing biofilms of *Geobacter sulfurreducens*. *Env Microbiol Rep* **3**, 211-217.

52. Kim BC, Leang C, Ding YHR, Glaven RH, Coppi MV & Lovley DR (2005) OmcF, a putative *c*-type monoheme outer membrane cytochrome required for the expression of other outer membrane cytochromes in *Geobacter sulfurreducens*. *J Bacteriol* **187**, 4505-4513.

53. Kim BC & Lovley DR (2008) Investigation of direct *vs*. indirect involvement of the *c*-type cytochrome MacA in Fe(III) reduction by *Geobacter sulfurreducens*. *FEMS Microbiol Lett* **286**, 39-44.

54. Nevin KP, Kim BC, Glaven RH, Johnson JP, Woodard TL, Methe BA, Didonato RJ, Covalla SF, Franks AE, Liu A*, et al.* (2009) Anode biofilm transcriptomics reveals outer surface components essential for high density current production in *Geobacter sulfurreducens* fuel cells. *PLoS One* **4**, e5628.

55. Liu Y, Fredrickson JK, Zachara JM & Shi L (2015) Direct involvement of *ombB*, *omaB*, and *omcB* genes in extracellular reduction of Fe(III) by *Geobacter sulfurreducens* PCA. *Front Microbiol* **6**, 1075.

56. Levar CE, Chan CH, Mehta-Kolte MG & Bond DR (2014) An inner membrane cytochrome required only for reduction of high redox potential extracellular electron acceptors. *MBio* **5**, e02034.

57. Butler JE, Kaufmann F, Coppi MV, Nunez C & Lovley DR (2004) MacA, a diheme *c*-type cytochrome involved in Fe(III) reduction by *Geobacter sulfurreducens*. *J Bacteriol* **186**, 4042-4045.

58. Lovley DR (2006) Bug juice: harvesting electricity with microorganisms. *Nat Rev Microbiol* **4**, 497-508.

59. Seidel J, Hoffmann M, Ellis KE, Seidel A, Spatzal T, Gerhardt S, Elliott SJ & Einsle O (2012) MacA is a second cytochrome *c* peroxidase of *Geobacter sulfurreducens*. *Biochemistry* **51**, 2747-2756.

60. Ding YH, Hixson KK, Giometti CS, Stanley A, Esteve-Nunez A, Khare T, Tollaksen SL, Zhu W, Adkins JN, Lipton MS*, et al.* (2006) The proteome of dissimilatory metal-reducing microorganism *Geobacter sulfurreducens* under various growth conditions. *Biochim Biophys Acta* **1764**, 1198-1206.

61. Holmes DE, Chaudhuri SK, Nevin KP, Mehta T, Methe BA, Liu A, Ward JE, Woodard TL, Webster J & Lovley DR (2006) Microarray and genetic analysis of electron transfer to electrodes in *Geobacter sulfurreducens*. *Environ Microbiol* **8**, 1805-1815.

62. Rollefson JB, Levar CE & Bond DR (2009) Identification of genes involved in biofilm formation and respiration via mini-Himar transposon mutagenesis of *Geobacter sulfurreducens*. *J Bacteriol* **191**, 4207-4217.

63. Levar CE, Hoffman CL, Dunshee AJ, Toner BM & Bond DR (2017) Redox potential as a master variable controlling pathways of metal reduction by *Geobacter sulfurreducens*. *ISME J* **3**, 741-752.

64. Shelobolina ES, Coppi MV, Korenevsky AA, DiDonato LN, Sullivan SA, Konishi H, Xu H, Leang C, Butler JE, Kim BC*, et al.* (2007) Importance of *c*-type cytochromes for U(VI) reduction by *Geobacter sulfurreducens*. *BMC Microbiol* **7**, 16.

65. Liu Y, Wang Z, Liu J, Levar C, Edwards MJ, Babauta JT, Kennedy DW, Shi Z, Beyenal H, Bond DR*, et al.* (2014) A trans-outer membrane porin-cytochrome protein complex for extracellular electron transfer by *Geobacter sulfurreducens* PCA. *Environ Microbiol Rep* **6**, 776-785.

66. Kim BC, Postier BL, Didonato RJ, Chaudhuri SK, Nevin KP & Lovley DR (2008) Insights into genes involved in electricity generation in *Geobacter sulfurreducens* via whole genome microarray analysis of the OmcF-deficient mutant. *Bioelectrochemistry* **73**, 70-75.

67. Leang C, Qian X, Mester T & Lovley DR (2010) Alignment of the *c*-type cytochrome OmcS along pili of *Geobacter sulfurreducens*. *Appl Environ Microbiol* **76**, 4080-4084.

68. Inoue K, Qian XL, Morgado L, Kim BC, Mester T, Izallalen M, Salgueiro CA & Lovley DR (2010) Purification and characterization of OmcZ, an outer-surface, octaheme *c*-type cytochrome essential for optimal current production by *Geobacter sulfurreducens*. *Appl Environ Microb* **76**, 3999-4007.

69. Londer YY, Pokkuluri PR, Tiede DM & Schiffer M (2002) Production and preliminary characterization of a recombinant triheme cytochrome c_7 from *Geobacter sulfurreducens* in *Escherichia coli*. *Biochim Biophys Acta* **1554**, 202-211.

70. Morgado L, Fernandes AP, Londer YY, Bruix M & Salgueiro CA (2010) One simple step in the identification of the cofactors signals, one giant leap for the solution structure determination of multiheme proteins. *Biochem Biophys Res Commun* **393**, 466-470.

71. Paixão VB, Vis H & Turner DL (2010) Redox linked conformational changes in cytochrome c_3 from *Desulfovibrio desulfuricans* ATCC 27774. *Biochemistry* **49**, 9620-9629.

72. Londer YY, Pokkuluri PR, Erickson J, Orshonsky V & Schiffer M (2005) Heterologous expression of hexaheme fragments of a multidomain cytochrome from *Geobacter sulfurreducens* representing a novel class of cytochromes *c*. *Protein Expr Purif* **39**, 254-260.

73. Londer YY, Pokkuluri PR, Orshonsky V, Orshonsky L & Schiffer M (2006) Heterologous expression of dodecaheme "nanowire" cytochromes *c* from *Geobacter sulfurreducens*. *Protein Expr Purif* **47**, 241-248.

74. Fernandes AP, Couto I, Morgado L, Londer YY & Salgueiro CA (2008) Isotopic labeling of *c*-type multiheme cytochromes overexpressed in *E. coli*. *Protein Expr Purif* **59**, 182-188.

75. Fonseca BM, Tien M, Rivera M, Shi L & Louro RO (2012) Efficient and selective isotopic labeling of hemes to facilitate the study of multiheme proteins. *Biotechniques* **52**, 1-7.

76. Shi L, Lin JT, Markillie LM, Squier TC & Hooker BS (2005) Overexpression of multi-heme *c*-type cytochromes. *Biotechniques* **38**, 297-299.

77. Pokkuluri PR, Londer YY, Duke NE, Long WC & Schiffer M (2004) Family of cytochrome c_7-type proteins from *Geobacter sulfurreducens*: structure of one cytochrome c_7 at 1.45 Å resolution. *Biochemistry* **43**, 849-859.

78. Morgado L, Bruix M, Orshonsky V, Londer YY, Duke NE, Yang X, Pokkuluri PR, Schiffer M & Salgueiro CA (2008) Structural insights into the modulation of the redox properties of two *Geobacter sulfurreducens* homologous triheme cytochromes. *Biochim Biophys Acta* **1777**, 1157-1165.

79. Pokkuluri PR, Londer YY, Yang X, Duke NE, Erickson J, Orshonsky V, Johnson G & Schiffer M (2010) Structural characterization of a family of cytochromes c_7 involved in Fe(III) respiration by *Geobacter sulfurreducens*. *Biochim Biophys Acta* **1797**, 222-232.

80. Morgado L, Paixão VB, Schiffer M, Pokkuluri PR, Bruix M & Salgueiro CA (2012) Revealing the structural origin of the redox-Bohr effect: the first solution structure of a cytochrome from *Geobacter sulfurreducens*. *Biochem J* **441**, 179-187.

81. Morgado L, Bruix M, Pokkuluri PR, Salgueiro CA & Turner DL (2017) Redox- and pH-linked conformational changes in triheme cytochrome PpcA from *Geobacter sulfurreducens*. *Biochem J* **474**, 231-246.

82. Pessanha M, Londer YY, Long WC, Erickson J, Pokkuluri PR, Schiffer M & Salgueiro CA (2004) Redox characterization of *Geobacter sulfurreducens* cytochrome c_7: physiological relevance of the conserved residue F15 probed by site-specific mutagenesis. *Biochemistry* **43**, 9909-9917.

83. Lukat P, Hoffmann M & Einsle O (2008) Crystal packing of the c_6-type cytochrome OmcF from *Geobacter sulfurreducens* is mediated by an N-terminal Strep-tag II. *Acta Crystallogr D Biol Crystallogr* **64**, 919-926.

84. Pokkuluri PR, Londer YY, Wood SJ, Duke NE, Morgado L, Salgueiro CA & Schiffer M (2009) Outer membrane cytochrome *c*, OmcF, from *Geobacter sulfurreducens*: high structural similarity to an algal cytochrome c_6. *Proteins* **74**, 266-270.

85. DeLano WL (2002) The PyMOL molecular graphics system. In http://wwwpymolorg.

86. Qian X, Mester T, Morgado L, Arakawa T, Sharma ML, Inoue K, Joseph C, Salgueiro CA, Maroney MJ & Lovley DR (2011) Biochemical characterization of purified OmcS, a *c*-type cytochrome required for insoluble Fe(III) reduction in *Geobacter sulfurreducens*. *Biochim Biophys Acta* **1807**, 404-412.

87. Salgueiro CA (2012) The multifaceted role of cytochromes c_7 in metal reduction - a structural and functional overview. *Global J Biochem* **3**, 1-15.

88. Dantas JM, Morgado L, Aklujkar M, Bruix M, Londer YY, Schiffer M, Pokkuluri PR & Salgueiro CA (2015) Rational engineering of *Geobacter sulfurreducens* electron transfer components: a foundation for building improved *Geobacter*-based bioelectrochemical technologies. *Front Microbiol* **6**, 752.

89. Turner DL, Salgueiro CA, Catarino T, Legall J & Xavier AV (1996) NMR studies of cooperativity in the tetrahaem cytochrome c_3 from *Desulfovibrio vulgaris*. *Eur J Biochem* **241**, 723-731.

90. Pessanha M, Rothery EL, Miles CS, Reid GA, Chapman SK, Louro RO, Turner DL, Salgueiro CA & Xavier AV (2009) Tuning of functional heme reduction potentials in *Shewanella* fumarate reductases. *Biochim Biophys Acta* **1787**, 113-120.

91. Santos TC, Silva MA, Morgado L, Dantas JM & Salgueiro CA (2015) Diving into the redox properties of *Geobacter sulfurreducens* cytochromes: a model for extracellular electron transfer. *Dalton Trans* **44**, 9335-9344.

92. Morgado L, Bruix M, Pessanha M, Londer YY & Salgueiro CA (2010) Thermodynamic characterization of a triheme cytochrome family from *Geobacter sulfurreducens* reveals mechanistic and functional diversity. *Biophys J* **99**, 293-301.

93. Morgado L, Bruix M, Londer YY, Pokkuluri PR, Schiffer M & Salgueiro CA (2007) Redox-linked conformational changes of a multiheme cytochrome from *Geobacter sulfurreducens*. *Biochem Biophys Res Commun* **360**, 194-198.

94. Gregory KB, Bond DR & Lovley DR (2004) Graphite electrodes as electron donors for anaerobic respiration. *Environ Microbiol* **6**, 596-604.

95. Nevin KP, Woodard TL, Franks AE, Summers ZM & Lovley DR (2010) Microbial electrosynthesis: feeding microbes electricity to convert carbon dioxide and water to multicarbon extracellular organic compounds. *MBio* **1**, e00103-00110.

96. Rabaey K & Rozendal RA (2010) Microbial electrosynthesis - revisiting the electrical route for microbial production. *Nat Rev Microbiol* **8**, 706-716.

97. Strycharz SM, Glaven RH, Coppi MV, Gannon SM, Perpetua LA, Liu A, Nevin KP & Lovley DR (2011) Gene expression and deletion analysis of mechanisms for electron transfer from electrodes to *Geobacter sulfurreducens*. *Bioelectrochemistry* **80**, 142-150.

2

MATERIALS AND METHODS

2. Materials and methods

This Chapter describes the general protocols used to produce the proteins studied under the scope of this Thesis (PpcA-E, OmcF and PccH). Particularly, it focuses on the construction of the expression vectors, heterologous expression of the proteins, purification process, purity evaluation and UV-visible analysis, except for the diheme cytochrome MacA that was kindly provided by Prof. Oliver Einsle (Freiburg, Germany). The more specific experimental protocols used in the study of each protein or set of proteins will be presented in detail in the following Chapters (Chapters 3-6).

2.1 Expression vectors and site directed mutagenesis

The expression vectors containing the gene sequence for PpcA-E and OmcF mature proteins were prepared by the collaborative group at Argonne National Laboratory, Lemont, Illinois, USA. The expression vectors containing the gene sequence for PccH and PccH mutants were prepared in this work. The cloning protocol used in this work is described below.

The DNA sequence for mature PpcA was previously cloned in plasmid pCK32, a pUC derivative containing the *lac* promoter and the OmpA leader sequence [1]. In the case of OmcF, the DNA sequence encoding for the mature protein was cloned in plasmid pLBM4 [2]. This plasmid was made based on pCKN5 (an intermediate plasmid used to design pVA203). Vector pVA203 [3] was used to clone the gene sequences for mature PpcB-E [4, 5]. Vectors pCKN5 and pVA203 derived from pCK32 have a *NotI* site introduced at the end of the leader peptide coding sequence and thus allow cloning without adding extra residues at the N-terminus of targets [6].

The plasmid containing the *pccH* gene sequence is also a pVA203 derivative and was designated pCS3274. This gene was amplified with primers containing restriction sites for the enzymes *EcoRI* (5’-CCTTTGAATTCTCAGTACGTGACCGTGATGG-3’) and *NotI* (5’-CTACCGCGGCCGCTGGCGAGGTGACCTATC-3’). Fragment size (420 bp) was confirmed by 0.8% agarose gel electrophoresis. Ligation was carried out with an insert:vector molar ratio of 5:1, overnight, at 16 °C. The ligation product was transformed into *E. coli* DH5α competent cells prepared by the calcium chloride method [7] and plated for selection in LB medium supplemented with 100 µg/mL ampicillin (Amp). The resulting colonies were screened by colony PCR with pCK32 primers (pCK32_fw: 5’-GGCTCGTATGTTGTGTGGAA-3’ and pCK32_rv: 5’-AAGGGAAGAAAGCGAAAGGA-3’), and those with a PCR product of the correct size were grown in liquid LB supplemented with Amp for plasmid extraction and sequencing. Plasmid pEC86 that contains the cytochrome *c* maturation gene cluster *ccmABCDEFGH* [8] and a chloramphenicol (Clo) selection marker (NZYTech), was a kind gift from Dr. Thöny-Meyer (Zürich, Switzerland). All the other plasmids contain an Amp selection marker (NZYTech).

For mutagenesis, QuikChange Site-Directed Mutagenesis Kit (NZYTech) was used in accordance with the manufacturer's instructions to prepare the PccH mutants. To identify the putative methionine axially coordinated to the heme, each methionine residue in the sequence of cytochrome PccH (M46, M48, M67 and M84) was independently replaced by alanine (PccHM46A, PccHM48A, PccHM67A and PccHM84A). Oligonucleotides were designed by the QuikChange Primer Design program (Agilent Technologies) and the PccH expression vector was used as a template. An overview of the Site-Directed Mutagenesis method is indicated in Fig 2.1.

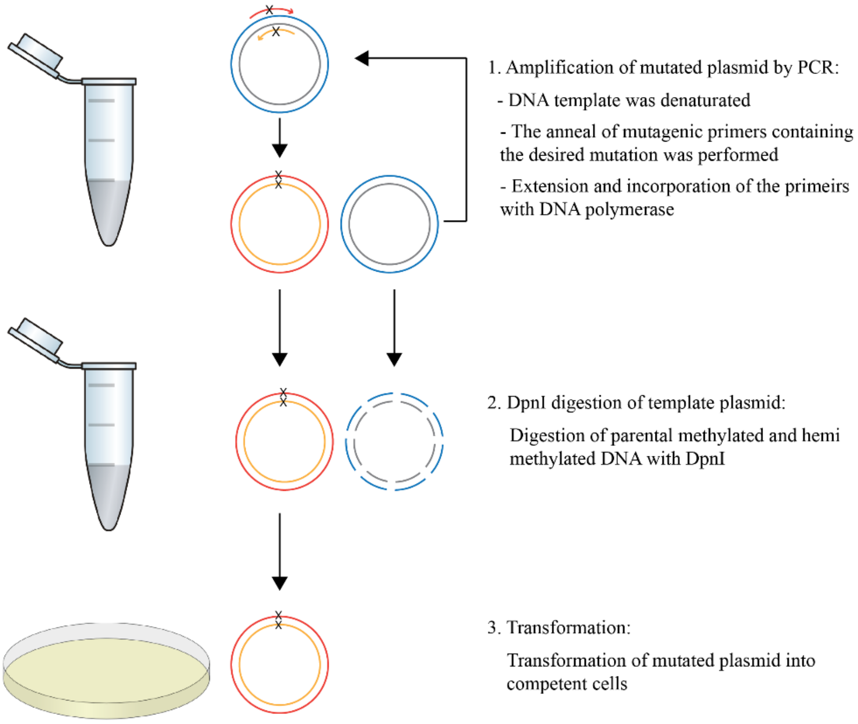

Fig 2.1 Overview of the Site-Directed mutagenesis method. Plasmid template and mutated are represented by blue/gray and red/orange colors. The primers are represented by red and orange arrows. The "X" represent local of the desired mutation. Adapted from *http://www.genomics.agilent.com/article.jsp?pageId=388.*

After that, competent cells of *Escherichia coli*, strain DH5α were transformed with each plasmid containing the gene sequence for each protein mutant. Briefly, the solution containing the host and the expression vector was placed in ice for 30 min, followed by a period of 1 min at 42ºC and again a period of 1 min in ice. Then, Luria-Bertani medium (LB) liquid medium (5 g/L yeast extract (NZYTech), 10 g/L tryptone (VWR) and 10 g/L NaCl (Panreac)) was added to the cells and was left to grow aerobically during 60 min, at 37ºC and 200 rpm. Cells were inoculated in LB medium containing 15 g/L agar (VWR) and supplemented with 100 µg/mL Amp, and were left overnight at 37ºC. Positive and negative controls were always carried out. Then, a transformed colony was transferred to LB medium, supplemented with the same concentration of Amp. The cells were left to grow aerobically, at 37ºC and 200 rpm, overnight. The plasmids were then isolated following a standard protocol NZYMiniPrep (NZYTech). The presence of the desired gene sequence or the mutations were confirmed by DNA sequencing performed by STAB Vida.

2.2 Heterologous expression

An overview of the production of either unlabeled or ^{13}C, ^{15}N uniformly labelled proteins is provided in Fig 2.2. The heterologous expression of each protein was performed using *E. coli* strain BL21(DE3), harboring the plasmid pEC86 [8]. These competent cells are then co-transformed with the expression plasmid, described in the previous section, containing the gene sequence encoding for each protein.

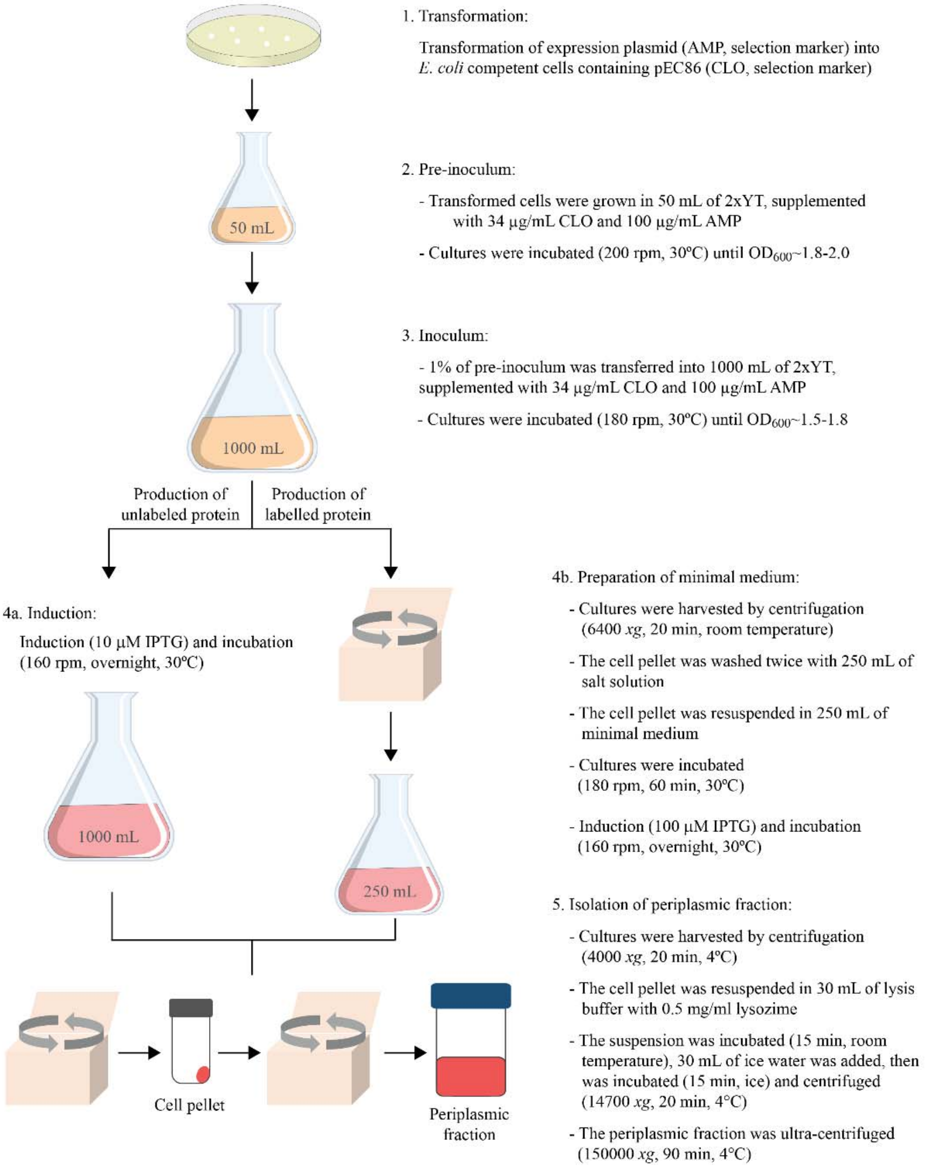

1. Transformation:

Transformation of expression plasmid (AMP, selection marker) into *E. coli* competent cells containing pEC86 (CLO, selection marker)

2. Pre-inoculum:

- Transformed cells were grown in 50 mL of 2xYT, supplemented with 34 µg/mL CLO and 100 µg/mL AMP
- Cultures were incubated (200 rpm, 30ºC) until OD_{600}~1.8-2.0

3. Inoculum:

- 1% of pre-inoculum was transferred into 1000 mL of 2xYT, supplemented with 34 µg/mL CLO and 100 µg/mL AMP
- Cultures were incubated (180 rpm, 30ºC) until OD_{600}~1.5-1.8

4a. Induction:

Induction (10 µM IPTG) and incubation (160 rpm, overnight, 30ºC)

4b. Preparation of minimal medium:

- Cultures were harvested by centrifugation (6400 *x*g, 20 min, room temperature)
- The cell pellet was washed twice with 250 mL of salt solution
- The cell pellet was resuspended in 250 mL of minimal medium
- Cultures were incubated (180 rpm, 60 min, 30ºC)
- Induction (100 µM IPTG) and incubation (160 rpm, overnight, 30ºC)

5. Isolation of periplasmic fraction:

- Cultures were harvested by centrifugation (4000 *x*g, 20 min, 4ºC)
- The cell pellet was resuspended in 30 mL of lysis buffer with 0.5 mg/ml lysozime
- The suspension was incubated (15 min, room temperature), 30 mL of ice water was added, then was incubated (15 min, ice) and centrifuged (14700 *x*g, 20 min, 4ºC)
- The periplasmic fraction was ultra-centrifuged (150000 *x*g, 90 min, 4ºC)

Fig 2.2 Overview of the production and isolation scheme for the unlabeled and ^{13}C, ^{15}N labelled proteins.

Transformed *E. coli* cells were grown in 50 mL of 2x Yeast extract – Tryptone (2xYT) liquid medium (10 g/L yeast extract, 16 g/L tryptone, and 5 g/L NaCl) supplemented with 34 µg/mL Clo and 100 µg/mL Amp, both from NZYTech. Cultures were grown aerobically to optical density at 600 nm (OD_{600}) ~1.8-2.0, at 30°C and 200 rpm, overnight. After that cells were transferred from 50 mL pre-inoculum to the inoculum of 1L of 2xYT medium supplemented with the same concentrations of Clo and Amp (Fig 2.2). All the steps described above are analogous to produce labeled or unlabeled proteins. From this step forward, production of unlabeled and labelled proteins was carried out through two different processes and are described in the following sections and in the Fig 2.2.

2.2.1 Unlabeled protein expression

The cultures were grown aerobically until OD_{600}~1.5-1.8, at 30ºC and 180 rpm. The protein expression was then induced with 10 µM of isopropyl-β-D-thiogalactopyranoside (IPTG) from NZYTech. After induction, cells were left overnight, at 30°C and 160 rpm (Fig 2.2).

2.2.2 ^{13}C, ^{15}N uniformly labeled protein expression

After cultures reaching an OD_{600}~1.5-1.8, 1L of 2xYT growth media were harvested by centrifugation at 6400 *xg* during 20 min. The cell pellet was then washed twice with 250 mL of a salt solution containing 110 mM KH_2PO_4 (Honeywell Riedel-de Haen), 240 mM Na_2HPO_4 (VWR), and 43 mM NaCl (Panreac). Then, cells were resuspended in 250 mL of minimal media containing 22 mM KH_2PO_4, 48 mM Na_2HPO_4, 8.6 mM NaCl, 20 mg/L biotin (Sigma), 2 mM $MgSO_4.7H_2O$ (Panreac), 0.1 mM $CaCl_2$ (Sigma-Aldrich), 5 µM $MnCl_2.4H_2O$ (Baker's), 10 µM $FeSO_4.7H_2O$ (Merck), 20 mg/L vitamin B1 (Merck), 2 g/L ^{13}C-Glucose (Sigma) as carbon source, 1 g/L $^{15}NH_4Cl$ (CIL isotopes) as nitrogen source and 1 mM of the heme precursor δ-aminolevulinic acid (Sigma). The minimal media was supplemented with the same concentrations of both antibiotics and then the cultures where incubated at 30ºC and 200 rpm, during 60 min. The labeled protein expression was then induced with 100 µM IPTG. After induction, cells were left overnight, at 30°C and 160 rpm (Fig 2.2).

2.3 Isolation of the periplasmic fraction

Cells were harvested and the periplasmic fraction was isolated by centrifugation at 4000 *xg* for 20 min at 4°C. The cell *pellet* was gently resuspended in 30 mL of lysis buffer (20% sucrose (Fisher scientific), 100 mM Tris-HCl (NZYTech and Carlo ERBA) pH 8.0 and 0.5 mM EDTA (Sigma) containing 0.5 mg/mL of lysozyme (Fluka), per liter of initial cell culture. The suspension was incubated 15 min at room temperature, then 30 mL of ice water was added and then, incubated on ice during 15 min. After that, the suspension was centrifuged at 14700 *xg* for 20 min at 4°C. The supernatant constituted the periplasmic fraction, which was ultra-centrifuged at 150000 *xg* for 90 min at 4°C and then dialyzed against the adequate buffer to perform the following purification steps (Fig 2.2).

2.4 Protein purification

All produced proteins were purified by cation exchange and molecular exclusion chromatography. The isoelectric point (pI) and molecular weight (MW) for each cytochrome produced and purified in this Thesis are indicated in Table 2.1.

Table 2.1 Isolectric point (pI) and molecular weight (MW) of mature proteins targeted in this Thesis. pI and MW were predicted with the pI/Mw tool program on the ExPASy Server (http://web.expasy.org/compute_pi) using the amino acid sequence of each mature cytochrome.

Cytochrome	Number of hemes	Number of residues	pI	MW (Da)[a]
PpcA	3	71	9.20	9570 [9]
PpcB	3	71	8.98	9564
PpcC	3	72	8.83	9647
PpcD	3	72	8.96	9562
PpcE	3	70	9.51	9661
OmcF	1	85	7.83	9275 [2]
PccH	1	129	8.84	15452 (this work)
PccHM46A	1	129	8.84	15393
PccHM48A	1	129	8.84	15393
PccHM67A	1	129	8.84	15393
PccHM84A	1	129	8.84	15393

[a] Except for PpcA, OmcF and PccH, whose values were determined by mass spectrometry, the total molecular weight was determined from the amino acid sequence of the mature protein plus 616 Da of each heme group [10].

The precise experimental conditions used to purify each protein were adapted in accordance with the features listed in Table 2.1. For cation exchange chromatography, 2x5mL Econo-Pac High S cartridges (Bio-Rad) were equilibrated with 10 mM Tris-HCl pH 8.5 (PpcA, PpcE) or pH 8.0 (PpcB, PpcD, PccH, and PccH mutants). All proteins were eluted with a 0-300 mM NaCl gradient at a flow rate of 1 mL/min. In the case of OmcF, the cationic columns were equilibrated with 20 mM sodium acetate (Panreac) pH 5 and the protein was eluted with a 0-1 M NaCl gradient at a flow rate of 1 mL/min.

For molecular exclusion chromatography, the red colored fractions obtained in the cation exchange chromatographic step were concentrated to 1 mL and then injected in a XK 16/70 column (GE Healthcare) packed with Superdex 75 (GE Healthcare), with molecular weight range between 3 and 70 kDa. The column was equilibrated with 20 mM sodium acetate pH 5 containing 100 mM NaCl (for OmcF) or with 100 mM sodium phosphate buffer, pH 8.0 (for the other cytochromes). Proteins were eluted at a flow rate of 1 mL/min. Both chromatographic methods were monitored with an ÄKTA Prime Plus Chromatography System (GE Healthcare).

2.5 Protein purity evaluation

The protein purity was evaluated by SDS-PAGE using a Mini-PROTEAN® Electrophoresis System (Bio-Rad). Samples containing loading buffer in equal volume, were loaded in the 5% and 15% acrylamide stacking and resolving gel, respectively. Samples was subjected to 120 V during 90 min. The markers Precision Plus Protein™ Dual Xtra Prestained Protein Standards (Bio-Rad) or NZYColour Protein Marker II (NZYTech) with MW ranges 11-245 kDa (for PccH and its mutants) and 2-250 kDa (for the other cytochromes). Protein bands were revealed with tetramethylbenzidine (TMBZ) [11] or Coomassie Brilliant blue staining [12]. Coomassie Brilliant blue (Merck) is an anionic protein dye that stains almost all proteins, with a detection limit of ~0.1–0.5 μg protein, resulting in dark blue bands. Otherwise, with TMBZ (Acros Organics) staining, heme proteins can be detected, using TMBZ as a chromogenic electron donor and H_2O_2 as an electron acceptor, which gives rise to light blue bands.

2.6 UV-visible analysis, quantification and molar extinction coefficient

UV-visible absorption spectra were acquired for all proteins in the oxidized and reduced states. These spectral features were used for protein quantification, identification of the heme spin state and heme axial ligands.

The spectra were acquired at room temperature, on an UV–visible scanning spectrophotometer Ultraspec 2100pro (Amersham Biosciences, Switzerland) using quartz cuvettes with 1 cm path length. In the UV-visible spectra of oxidized low spin cytochromes, a band at 695 nm is characteristic of His-Met iron coordination, which is absent in hemes with His-His coordination [13]. Amongst all proteins studied in this Thesis, the band at 695 nm was only observed for cytochromes PccH and OmcF. Fully reduction of samples was achieved by adding sodium dithionite (Sigma) in small increments from a 2 M stock.

The concentration of purified cytochrome PccH was determined using the Pierce BCA Protein Assay Kit (Thermo Scientific), using horse-heart cytochrome *c* as standard [14]. UV-visible spectra were recorded in the range 350-700 nm, for both oxidized and reduced samples to determine the molar extinction coefficient. For the other proteins, the concentration was determined by measuring the absorbance of the reduced cytochrome α band at ~552 nm, using the molar extinction coefficient of each cytochrome. For PpcA-E, OmcF and PccH cytochromes, the molar extinction coefficient values were 97.5 [9], 23.8 [15] and 32.5 $mM^{-1}cm^{-1}$ (this work), respectively. The final yields of each protein produced and purified are provided in Table 2.2.

Table 2.2 Final yields of each cytochrome produced and purified during the time course of this Thesis.

Cytochrome	**Final yield (mg/per liter of culture)**	
	2xYT medium	**Minimal medium**
PpcA	2.70	2.00
PpcB	2.39	1.07
PpcC	1.27	1.20
PpcD	1.68	2.04
PpcE	2.55	1.66
OmcF	8.00	5.00
PccH	4.70	-
PccHM46A	11.70	-
PccHM48A	1.26	-
PccHM67A	8.61	-
PccHM84A	0.03	-

2.7 References

1. Londer YY, Pokkuluri PR, Tiede DM & Schiffer M (2002) Production and preliminary characterization of a recombinant triheme cytochrome c_7 from *Geobacter sulfurreducens* in *Escherichia coli*. *Biochim Biophys Acta* **1554**, 202-211.

2. Pokkuluri PR, Londer YY, Wood SJ, Duke NE, Morgado L, Salgueiro CA & Schiffer M (2009) Outer membrane cytochrome *c*, OmcF, from *Geobacter sulfurreducens*: high structural similarity to an algal cytochrome c_6. *Proteins* **74**, 266-270.

3. Pokkuluri PR, Londer YY, Duke NE, Erickson J, Pessanha M, Salgueiro CA & Schiffer M (2004) Structure of a novel c_7-type three-heme cytochrome domain from a multidomain cytochrome *c* polymer. *Protein Sci* **13**, 1684-1692.

4. Pokkuluri PR, Londer YY, Yang X, Duke NE, Erickson J, Orshonsky V, Johnson G & Schiffer M (2010) Structural characterization of a family of cytochromes c_7 involved in Fe(III) respiration by *Geobacter sulfurreducens*. *Biochim Biophys Acta* **1797**, 222-232.

5. Morgado L, Bruix M, Orshonsky V, Londer YY, Duke NE, Yang X, Pokkuluri PR, Schiffer M & Salgueiro CA (2008) Structural insights into the modulation of the redox properties of two *Geobacter sulfurreducens* homologous triheme cytochromes. *Biochim Biophys Acta* **1777**, 1157-1165.

6. Londer YY, Pokkuluri PR, Orshonsky V, Orshonsky L & Schiffer M (2006) Heterologous expression of dodecaheme "nanowire" cytochromes *c* from *Geobacter sulfurreducens*. *Protein Expr Purif* **47**, 241-248.

7. Sambrook J & Russell DW (2001) *Molecular cloning : a laboratory manual*. 3rd edn. Cold Spring Harbor Laboratory Press, Cold Spring Harbor, N.Y.

8. Arslan E, Schulz H, Zufferey R, Kunzler P & Thony-Meyer L (1998) Overproduction of the *Bradyrhizobium japonicum c*-type cytochrome subunits of the *cbb*$_3$ oxidase in *Escherichia coli*. *Biochem Biophys Res Commun* **251**, 744-747.

9. Seeliger S, Cord-Ruwisch R & Schink B (1998) A periplasmic and extracellular *c*-type cytochrome of *Geobacter sulfurreducens* acts as a ferric iron reductase and as an electron carrier to other acceptors or to partner bacteria. *J Bacteriol* **180**, 3686-3691.

10. Thony-Meyer L (1997) Biogenesis of respiratory cytochromes in bacteria. *Microbiol Mol Biol Rev* **61**, 337-376.

11. Thomas PE, Ryan D & Levin W (1976) An improved staining procedure for the detection of the peroxidase activity of cytochrome P-450 on sodium dodecyl sulfate polyacrylamide gels. *Anal Biochem* **75**, 168-176.

12. Brunelle JL & Green R (2014) Coomassie blue staining. *Methods Enzymol* **541**, 161-167.

13. Pettigrew GW & Moore GR (1987) Cytochromes *c*: biological aspects. In *Molecular Biology*. pp. 282. Springer-Verlag Heidelberg, Berlin.

14. Smith PK, Krohn RI, Hermanson GT, Mallia AK, Gartner FH, Provenzano MD, Fujimoto EK, Goeke NM, Olson BJ & Klenk DC (1985) Measurement of protein using bicinchoninic acid. *Anal Biochem* **150**, 76-85.

15. Lukat P, Hoffmann M & Einsle O (2008) Crystal packing of the c_6-type cytochrome OmcF from *Geobacter sulfurreducens* is mediated by an N-terminal Strep-tag II. *Acta Crystallogr D Biol Crystallogr* **64**, 919-926.

3

MOLECULAR INTERACTION STUDIES BETWEEN THE TRIHEME CYTOCHROMES FROM *G. SULFURREDUCENS* AND THE REDOX ACTIVE HUMIC SUBSTANCES ANALOG[1]

---

[1] Partially reproduced from Dantas JM, Morgado L, Catarino T, Kokhan O, Pokkuluri PR, Salgueiro CA (2014) Evidence for interaction between the triheme cytochrome PpcA from *Geobacter sulfurreducens* and anthrahydroquinone-2,6-disulfonate, an analog of the redox active components of humic substances, Biochim Biophys Acta 1837, 750-760 (doi: 10.1016/j.bbabio.2014.02.004) and Dantas JM, Kokhan O, Pokkuluri PR, Salgueiro CA (2015) Molecular interaction studies revealed the bifunctional behavior of triheme cytochrome PpcA from *Geobacter sulfurreducens* toward the redox active analog of humic substances, Biochim Biophys Acta 1847, 1129-1138 (doi: 10.1016/j.bbabio.2015.06.004), in accordance with the Editors' Copyright Policy.

3. Molecular interaction studies between the triheme cytochromes from *G. sulfurreducens* and the redox active humic substances analog

The bacterium *G. sulfurreducens* displays an extraordinary respiratory versatility underpinning the diversity of electron donors and acceptors that can be used to sustain anaerobic growth, as stated in the Chapter 1. This versatility was also observed toward humic substances (HS), which are natural organic matter formed by the decomposition of plant, animal, and microbial tissues, which are widely distributed in terrestrial and aquatic environments [1, 2]. All known humic-reducing microorganisms are capable of transferring electrons (and protons) to AQDS, reducing it to anthrahydroquinone-2,6-disulfonate (AH_2QDS) [2, 3]. These molecules are considered HS analogues and are commonly used to investigate bacterial humic respiration mechanisms. AQDS can be used by *G. sulfurreducens* as terminal electron acceptor, but the bacterium also can use as electron donor the reduced form of AQDS [4, 5]. Such bi-directional utilization of HS confers competitive advantages to these bacteria in Fe(III) enriched environments.

Gene knockout experiments carried out in *G. sulfurreducens* suggested that the humic (or AQDS) respiration uses multiple routes for electron transfer [6]. However, the molecular mechanisms or electron transfer pathways of respiration underlying the use of these compounds is presently unknown. Compared to microbial reduction of AQDS, less information is available on the use of AH_2QDS as electron donor. Several studies have demonstrated that different anaerobic bacteria can oxidize reduced HS, or analogs, in the presence of suitable electron acceptors [4, 7, 8]. In this case, the organisms obtain carbon from other limited but readily degradable sources, such as acetate, and simply use AH_2QDS as an energy source [9]. This capability provides these organisms a potential competitive advantage over other heterotrophs that require organic compounds as both carbon and energy sources and, therefore, need significantly higher concentrations of carbon compounds to grow [9].

Recently, experiments carried out for *G. sulfurreducens* cells suggested that the periplasmic triheme cytochrome PpcA may transfer electrons directly to AQDS or HS that are able to traverse the OM [10]. Voordeckers and co-workers [6] showed that a quintuple mutant with the simultaneous deletion of genes coding for OM cytochromes OmcB, OmcE, OmcS, OmcT and OmcZ yielded nearly complete inhibition of AQDS or HS reduction. Interestingly, the deletion of the individual genes only partially inhibited AQDS or HS reduction, which suggests that distinct OM cytochromes can contribute to the reduction of HS and also, could exist multiple routes for transfer of electrons to these acceptors [6]. Nevertheless, all the proteins identified so far to be involved in AQDS and HS reduction in *G. sulfurreducens* are *c*-type multiheme cytochromes [6, 10]. In addition to this, as it was also pointed out, the fact that several multiheme cytochromes appear to be capable of transfer electrons to AQDS and HS suggested that the reduction of quinone moieties by these molecules is not very specific, indicating all these cytochromes might have similar structural and functional features that allow them to form an effective redox-complex and warrant electron transfer to the acceptors [6]. Therefore, the molecular interaction studies involving periplasmic triheme cytochromes and HS analogues could provide suitable models of interaction in the absence of the purified OM cytochromes, which have proven difficult to obtain in necessary quantities for detailed physicochemical studies.

In this Chapter, UV–visible, stopped-flow kinetics, NMR experiments and molecular docking calculations were used to investigate whether the HS analogue and the PpcA-family can function as redox partners and to fingerprint the regions involved in the interaction between these cytochromes and AQDS or AH_2QDS. As mentioned in the Chapter 1, the PpcA-family is composed by five periplasmic cytochromes c_7 located in the *G. sulfurreducens* periplasm and with high sequence identity (Fig 3.1).

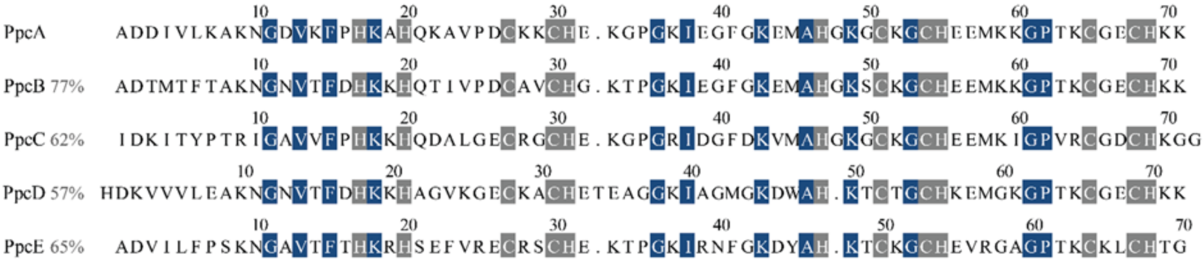

PpcA ADDIVLKAKNGDVKFPHKAHQKAVPDCKKCHE.KGPGKIEGFGKEMAHGKGCKGCHEEMKKGPTKCGECHKK

PpcB 77% ADTMTFTAKNGNVTFDHKKHQTIVPDCAVCHG.KTPGKIEGFGKEMAHGKSCKGCHEEMKKGPTKCGECHKK

PpcC 62% IDKITYPTRIGAVVFPHKKHQDALGECRGCHE.KGPGRIDGFDKVMAHGKGCKGCHEEMKIGPVRCGDCHKGG

PpcD 57% HDKVVVLEAKNGNVTFDHKKHAGVKGECKACHETEAGGKIAGMGKDWAH.KTCTGCHKEMGKGPTKCGECHKK

PpcE 65% ADVILFPSKNGAVTFTHKRHSEFVRECRSCHE.KTPGKIRNFGKDYAH.KTCKGCHEVRGAGPTKCKLCHTG

Fig 3.1 Alignment of the amino acid sequences of periplasmic triheme cytochromes from *G. sulfurreducens*. The conserved residues in the proteins are boxed: heme attached (gray) and non-heme attached residues (blue). The sequence identity for each cytochrome in relation to PpcA is also indicated.

The results of these experiments allowed to present for the first time biochemical and biophysical evidence for a molecular interaction between the periplasmic cytochromes and a putative redox partner, an important step for understanding the humic respiratory pathways in *G. sulfurreducens*.

3.1 Results and discussion

The results, and concomitant discussion, of the interaction studies between the cytochromes from the PpcA-family (except for PpcC) and the HS analogue are presented in this section. The interactions were firstly probed by stopped flow kinetic experiments (section 3.1.1), then by NMR chemical shift perturbation experiments (sections 3.1.2.1, 3.1.3.1 and 3.1.4.2) and verified by molecular docking calculations (sections 3.1.2.2, 3.1.3.2 and 3.1.4.3). The NMR studies were firstly carried out for PpcA in the oxidized and reduced forms (sections 3.1.2 and 3.1.3) for which the assignments of the backbone and side chains were already available [11-13]. The results obtained for PpcA prompt us to extend the NMR interaction studies also to PpcB, PpcD and PpcE in the oxidized state, whose results are described in section 3.1.4.

3.1.1 Equilibrium and kinetic studies probed by UV–visible spectroscopy

The different UV-visible absorption spectral signatures were used to investigate the extent in which the triheme cytochromes were reduced by AH_2QDS or oxidized by AQDS at equilibrium. Using the UV-visible absorption spectra of PpcA as an example, this cytochrome displays the typical features of a hexacoordinated *c*-type cytochrome containing hemes in the low spin state (Fig 3.2). In the oxidized form, the spectrum is dominated by the Soret band with a maximum at 406 nm. After reduction with sodium dithionite, three bands are observed at 417 nm (Soret band), 522 nm (β band) and 552 nm (α band), typical of low spin ferrous *c*-type hemes. On the other hand, the UV-visible absorption spectrum of AQDS displays an absorption band with a maximum at 325 nm, whereas that of AH_2QDS shows two bands with maxima at 385 nm and 410 nm (Fig 3.2B).

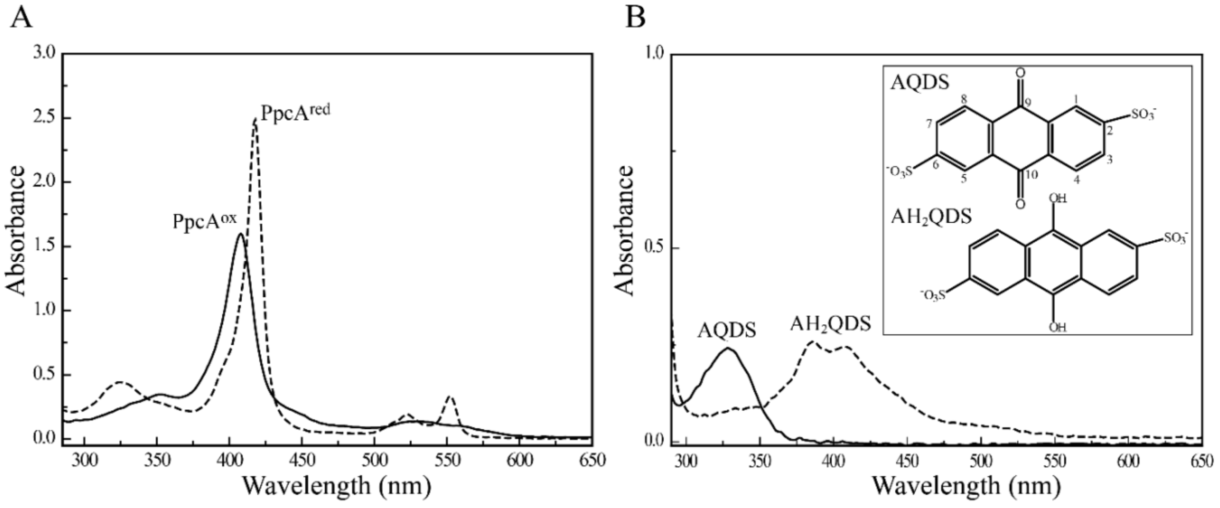

Fig 3.2 UV–visible absorption spectra of PpcA (A) and AQDS/AH_2QDS (B). The continuous and dashed lines correspond to the oxidized and reduced forms, respectively. The spectra were obtained at 25 °C and pH 7. The concentration of PpcA and AQDS or AH_2QDS were 3 µM and 31 µM, respectively. Structures of AQDS and AH_2QDS are indicated in the inset and were drawn with program ChemDraw Ultra 12.0 [14].

The other members of the PpcA-family display similar UV–visible absorption spectra as the ones obtained for PpcA. The maximum absorption bands for all members of the family and for AQDS and AH_2QDS are indicated in the Table 3.1.

Table 3.1 UV-visible maximum absorption bands in the electronic absorption spectra of cytochromes PpcA, PpcB, PpcD, PpcE, AQDS and AH_2QDS in oxidized and reduced forms.

		UV-visible maximum absorption bands (nm)					
		PpcA	PpcB	PpcD	PpcE	AQDS	AH_2QDS
Oxidized	Soret	406	408	409	408		
	others					325	
Reduced	Soret	417	417	418	418		
	β-band	522	522	523	523		
	α-band	552	552	553	553		
	others						410; 385

The effect of the addition of an oxidized PpcA sample ($PpcA_{ox}$) to a solution containing AH_2QDS was first monitored by UV–visible spectroscopy (Fig 3.3A) and the reverse experiment by adding AQDS to a sample of reduced PpcA ($PpcA_{red}$) (Fig 3.3B). The UV–visible spectra obtained after the addition of an equimolar amount of $PpcA_{ox}$ to a solution containing AH_2QDS showed the features of reduced cytochrome, as confirmed by the typical α and β bands (see blue line in Fig 3.3A). In the UV–visible spectrum of AH_2QDS before addition of $PpcA_{ox}$ (dashed line in Fig 3.3A), the typical band of sodium dithionite, with an absorption maximum at 315 nm, is not present, confirming that reduction of PpcA is achieved only via oxidation of AH_2QDS. Although the features of the reduced form are present, it is important to stress that the cytochrome is not fully reduced, neither could it be, because the equimolar concentration of redox partners does not correspond to an equimolar concentration of electrons, since the reduced quinone is a two-electron donor whereas the oxidized cytochrome needs three electrons to become fully reduced. In fact, the value of the absorbance at 552 nm shows that the PpcA is less than 50% reduced in this experiment. In the reverse experiment, the addition of equimolar AQDS to $PpcA_{red}$, results in only *ca.* 20% of oxidation of the cytochrome, and even after the addition of a 40× molar excess of AQDS, the percentage of oxidation of the cytochrome is not larger than 50%, as shown by the UV–visible spectra (see blue lines in Fig 3.3B). These results show that, at equilibrium, the electron transfer occurs preferentially from the reduced quinone to the oxidized cytochrome, as expected based on their reduction potentials (see below).

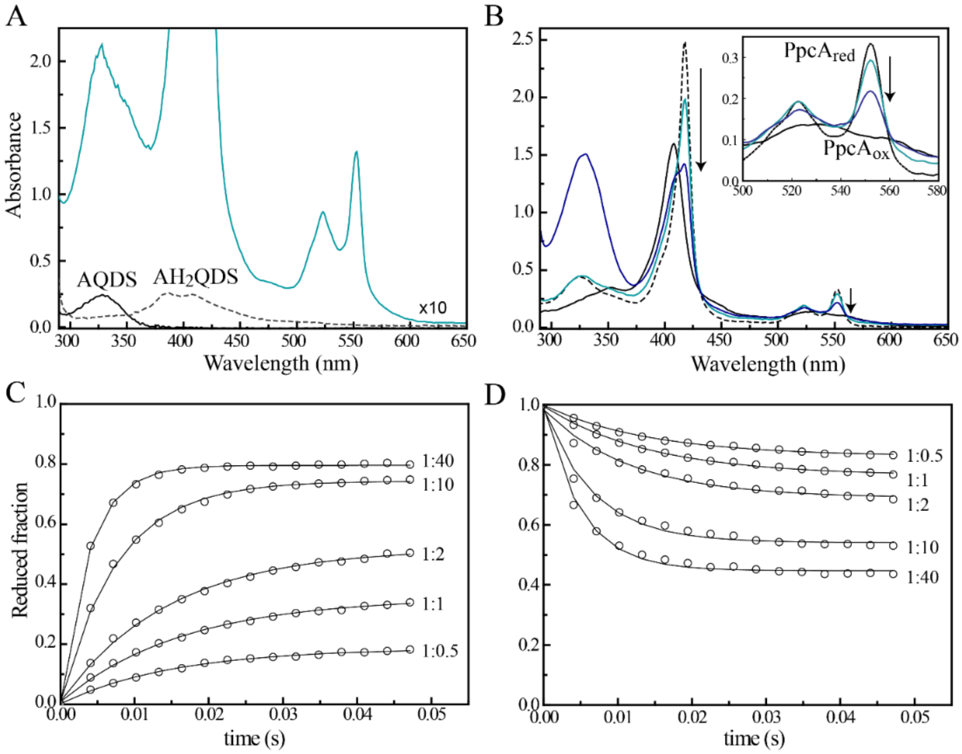

Fig 3.3 Assays of AH2QDS oxidation coupled to PpcA reduction (left panels) and AQDS reduction coupled to PpcA oxidation (right panels) at 25 °C and pH 7. (A) UV-visible spectra of AQDS (continuous black line) and AH2QDS (dashed line). As an example the spectrum obtained for a ratio $PpcA_{ox}$:AH2QDS 1:1 is indicated (continuous blue line) in this experiment the concentrations were both 3 µM. (B) UV-visible spectra of $PpcA_{ox}$ (continuous black line) and $PpcA_{red}$ (dashed black line). As an example the spectra obtained for $PpcA_{red}$:AQDS ratios of 1:1 and 1:40 are indicated by blue lines. In these experiments, the concentration of PpcA was 3 µM and the concentration of AQDS was varied. The arrow points to increasing concentrations of AQDS. In the inset an enlarged scale of the spectra between 500 nm and 580 nm is showed for clarity. Panels (C) and (D) represent the fast electron transfer between AH2QDS and $PpcA_{ox}$ and between $PpcA_{red}$ and AQDS, respectively. The traces were recorded at λ=552 nm and normalized using the absorbance of the fully reduced and the fully oxidized cytochrome at the same wavelength. The time scale was corrected for the dead time of the stopped-flow apparatus. Cytochrome to quinone molar ratios of 1:0.5, 1:1, 1:2, 1:10 and 1:40 were used in both reductive (panel C) and oxidative (panel D) experiments. The solid lines are the result of the fit of the data with a single exponential, using the tool Solver from Microsoft Excel. The final concentration of protein was 3 µM in all experiments.

The stopped-flow technique was used to obtain kinetic information on the reaction between reduced quinone and oxidized PpcA, PpcB, PpcD and PpcE, and on the reverse reaction, between oxidized quinone and the reduced proteins (Table 3.2). The experiments were carried out for the different cytochrome to quinone molar ratios. As an example, normalized kinetic traces for the reductive and oxidative experiments are presented for PpcA in Fig 3.3C and D, respectively, and the result of the fit of the data for all cytochromes with single exponentials is shown in Table 3.2. Up to 1:2 cytochrome to quinone ratio, the observed rate constants are constant, and very similar for the reductive and oxidative experiments $k_{obs} \approx 70\ s^{-1}$. For the larger ratios, 1:10 and 1:40, the observed rate constant increases in an approximately linear fashion and the amplitudes, which were increasing with increasing ratios, tend to stabilize. In the reductive experiments, a slow phase ($k_{obs} \approx 1\ s^{-1}$) with significant amplitude (>10% of the total reaction) seems to be associated with the transfer of the third electron, leading to the full reduction of the protein. In the oxidative experiments, a slow phase ($k_{obs} \approx 3$ s^{-1}) is also visible, but it does not seem so significant, possibly because oxidation never progresses beyond 64%. The extent of the overall reaction, observed both in the reductive and in the oxidative kinetic experiments, is in good agreement with the results obtained in the UV-visible equilibrium experiments, confirming that thermodynamic equilibration is reached in a short time scale.

For the two lower molar ratios of cytochromes to AQDS the extension of the reaction increases but the rate constants are maintained both for the reductive and the oxidative reactions. The reduction rate constants obtained are similar for PpcB, PpcD and PpcE (*ca.* 20 s^{-1}) but lower than the rate constant obtained for PpcA (Table 3.2). The oxidation rates, however, differ significantly when we compare different cytochromes: PpcB displays the smaller rate constant (*ca.* 20 s^{-1}) and PpcD and PpcE have higher rate constants (*ca.* 200 s^{-1}). It follows that, like PpcA, PpcB has similar rate constants for the reduction and oxidation by AQDS, whereas for PpcD and PpcE the oxidation is *ca.* 10 times faster than the reduction. It should be noted that there is a large error associated with the higher rate constants because a significant part of the reaction is lost in the dead time of the apparatus and the rate is obtained through extrapolation to the reference value at time zero. Therefore, the experiments done with high molar ratios of cytochrome to AQDS are useful to obtain the limiting values for the extension of the reaction but the rate constants are not reliable.

In general terms PpcA, PpcB, PpcD and PpcE display a similar behavior in the reaction with AQDS, which agrees with their similar thermodynamic and structural properties. All of them reach 100% reduction with a 10-fold excess of reduced AQH_2DS and in all of them the oxidation stops after transfer of two electrons from the cytochrome to AQDS, even for a larger excess of oxidizing agent.

Table 3.2 Rate constants (s^{-1}) obtained from the fit of normalized stopped-flow kinetic data with exponentials. The values for the percentage of total reduction and total oxidation of cytochromes were calculated from the spectra recorded at the end of the reaction, using standard spectra for the fully reduced and fully oxidized states. The concentration of PpcA, PpcB, PpcD and PpcE after mixing was 3 μM, in all experiments. The data were acquired at 25 °C and pH 7. *k_{fast} of the fit with 2 exponentials.

Reduction	PpcB		PpcD		PpcE		PpcA	
[AH_2QDS] (μM)	k_{obs} (s^{-1})	Total reduction (%)	k_{obs} (s^{-1})	Total reduction (%)	k_{obs} (s^{-1})	Total reduction (%)	k_{obs} (s^{-1})	Total reduction (%)
3	13±3	63	-	2	16±1	15	50±3	36
6	15±3	100	14±1	33	23±1	43	52±3	56
30	74±8	100	55±5	79	133±7*	90	126±15	>85
120	320±100	100	177±19*	97	477±100*	100	291±25*	>95

Oxidation	PpcB		PpcD		PpcE		PpcA	
[AQDS] (μM)	k_{obs} (s^{-1})	Total oxidation (%)	k_{obs} (s^{-1})	Total oxidation (%)	k_{obs} (s^{-1})	Total oxidation (%)	k_{obs} (s^{-1})	Total oxidation (%)
3	20±3	27	185±11*	46	110±22*	28	58±6	26
6	23±4	36	229±64*	46	150±16*	33	65±12	35
30	217±48*	51	448±75*	59	350±50*	45	131±27	49
120	400±100*	64	700±100*	68	550±100*	62	245±63*	64

Thermodynamic considerations explain these observations, since the reduction potential of AQDS (-184 mV *versus* NHE [15]) is lower than the macroscopic reduction potential of any of the cytochromes (Table 3.3). Nevertheless, the relative rate constants and the extension of the fast electron transfer for similar concentrations of the redox partners can be discussed. Although the reduction rate constants are of the same order of magnitude, PpcA has a slightly higher rate constant that might be related to the slightly higher driving force. However, the extension of the fast phase is higher for PpcB and this may be a consequence of electrons entering the cytochrome through the heme with highest reduction potential (Table 3.3). Fast intramolecular electron transfer to hemes I and III, leaves heme IV free to receive more electrons. Extending this line of thinking to PpcE makes us propose heme I for the main entrance gate for electrons in this cytochrome since its kinetic behavior is similar to that of PpcD. A kinetic behavior similar to PpcB, would be expected if heme IV were the main entrance point in PpcE. The same reasoning applies to the oxidation reaction where the behavior of PpcE is again closer to that of PpcD than to PpcB. With respect to oxidation by AQDS, we can divide the cytochromes in two groups: PpcA and PpcB display similar rate constants for the reductive and oxidative reactions whereas PpcD and PpcE display oxidative rate constants *ca*. 10 times higher than the respective reductive rate constants.

Rate constants for electron transfer between proteins and small molecules are mainly determined by driving force, electrostatic interactions, and solvent accessibility. The driving force is less favorable in the oxidative reaction (uphill in all cases) and, apart from surface charge alterations related to redox-Bohr effects, in this case electrostatic interactions are not expected to be very different in the reductive and the oxidative reactions. Thus, we may speculate that the large rate constants determined for the oxidation of PpcD and PpcE by AQDS are the result of local conformational changes that increase the accessibility of the quinone to the heme in the reduced cytochromes.

Table 3.3 Global (E_{app}) and heme midpoint reduction potentials of cytochromes PpcA, PpcB, PpcD and PpcE from *G. sulfurreducens* (pH 7) [16]. The redox potential values are relative to NHE. The standard errors are given in parentheses.

Cytochrome	E_{app} (mV)	Heme I (mV)	Heme III (mV)	Heme IV (mV)
PpcA	-117 (5)	-147 (5)	-104 (5)	-111 (5)
PpcB	-137 (5)	-146 (3)	-156 (3)	-119 (3)
PpcD	-132 (5)	-150 (6)	-96 (6)	-151 (6)
PpcE	-134 (5)	-154 (4)	-161 (4)	-96 (5)

3.1.2 PpcA$_{ox}$-AQDS interaction studies

3.1.2.1 NMR chemical shift perturbation experiments

Many biochemical and biophysical techniques allow detecting protein–protein or protein-ligand interactions. However, to properly map the molecular interaction interfaces would require a method for detailed atomic-resolution. NMR is suitable for such identification since it can detect even transient interactions resulting from relatively short lifetime complexes (for a review see [17]). Multidimensional isotope edited-NMR spectroscopy is a powerful technique to probe conformational changes in the chemical environment of a nucleus and has been used to study redox complexes, providing a wealth of information about the nature of complex interfaces. Complex formation gives rise to changes in the chemical environment of the nuclei at the interface, such that their chemical shift (δ) differs in the bound and free forms. However, the study of molecular interactions involving heme proteins is complex by the significant differences in the NMR spectra of their reduced and oxidized forms. To overcome this effect, the analysis at the atomic level of the interacting regions in electron transfer complexes is typically carried out with both partners in the same oxidation state. There are plenty of examples in the literature that illustrate the power of this approach for obtaining physiological and structural insights into the details of interactions between redox partners [18-21]. The above scenario also applies to cytochrome PpcA, which is diamagnetic in the reduced form ($S = 0$) and paramagnetic in the oxidized form ($S= 1/2$). Therefore, the unpaired electron of each heme iron exerts significant paramagnetic shifts on the heme signals and nearby residues, yielding different NMR spectra. Consequently, the same type of signal is differently affected by the paramagnetic centers, showing different levels of broadness and are spread all over the entire NMR spectral window (for a review see [22]). To illustrate this effect, the 2D ^{1}H ^{15}N HSQC (heteronuclear single quantum coherence) spectra obtained for PpcA$_{red}$ and PpcA$_{ox}$ are indicated in Fig 3.4. These spectra provide information on the polypeptide backbone and side chain NH signals and are in the front line to map the interaction regions in the interface of molecular complexes.

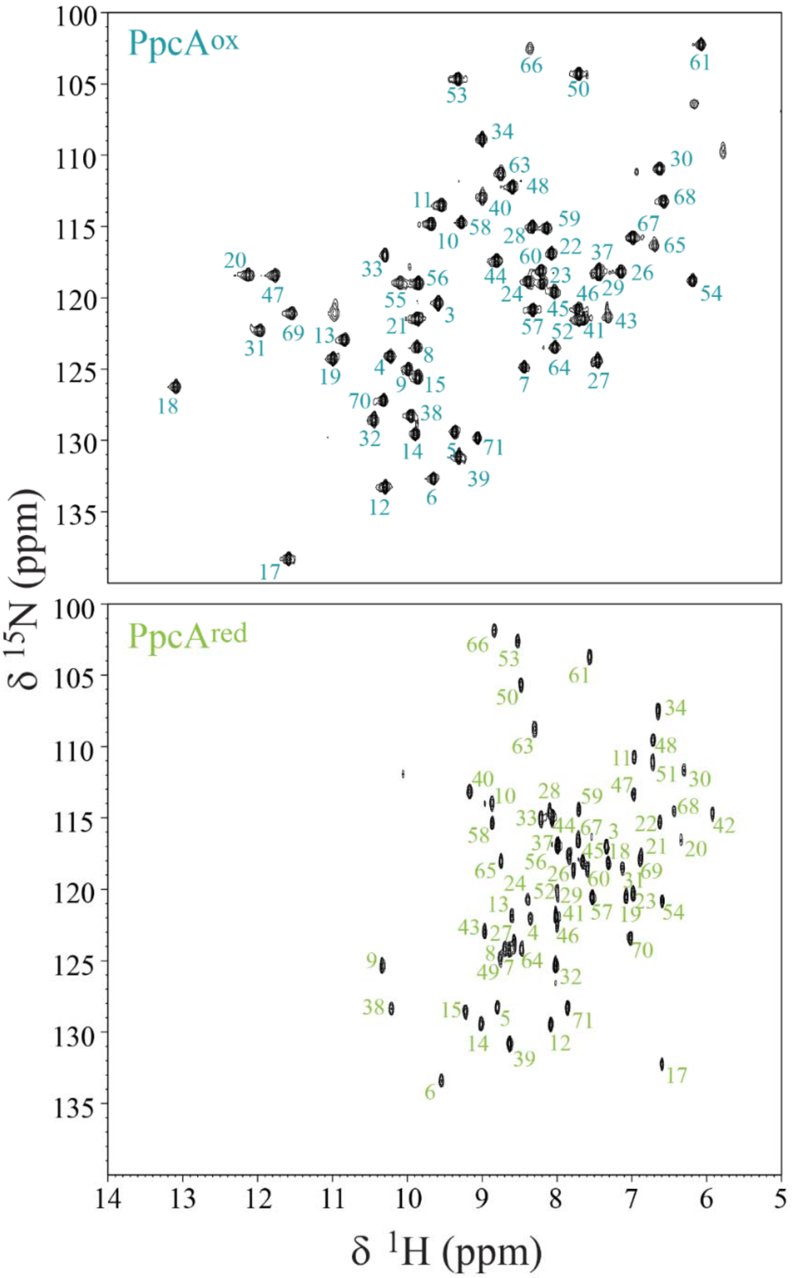

Fig 3.4 Region of the backbone NH signals in the 2D ^{1}H ^{15}N HSQC NMR spectra of PpcA in the oxidized (PpcA$_{ox}$ - upper spectrum) and reduced (PpcA$_{red}$ - lower spectrum) state at 298 K and pH 7.1.

In the present work, the molecular interactions between cytochrome PpcA and AQDS were first investigated by measuring the chemical shift perturbation of the backbone NH signals of PpcA$_{ox}$. The assignment of PpcA$_{ox}$ resonances was previously determined at pH 5.5 [13] and in this work, was reassigned at pH 7.1, except for residues Ala^1, Asp^2, Gly^{36}, Gly^{42}, Lys^{49} and Cys^{51}. The backbone NH signals at the N-terminal residues are usually not observable due to fast exchange with solvent. The backbone NH signals of Gly^{36} and Gly^{42} were not observable, most probably due to signal broadness caused by the nearby hemes I and IV paramagnetic iron atoms, since they were not detected also at low pH values. However, the backbone amide signals of Lys^{49} and Cys^{51} were not observed due to their rapid solvent exchange at pH 7.1, since these signals are observed at pH 5.5. The chemical shift perturbations of the backbone NH signals of PpcA$_{ox}$ with increasing amounts of AQDS were monitored by recording a series of 2D ^{1}H, ^{15}N HSQC NMR spectra (Fig 3.5).

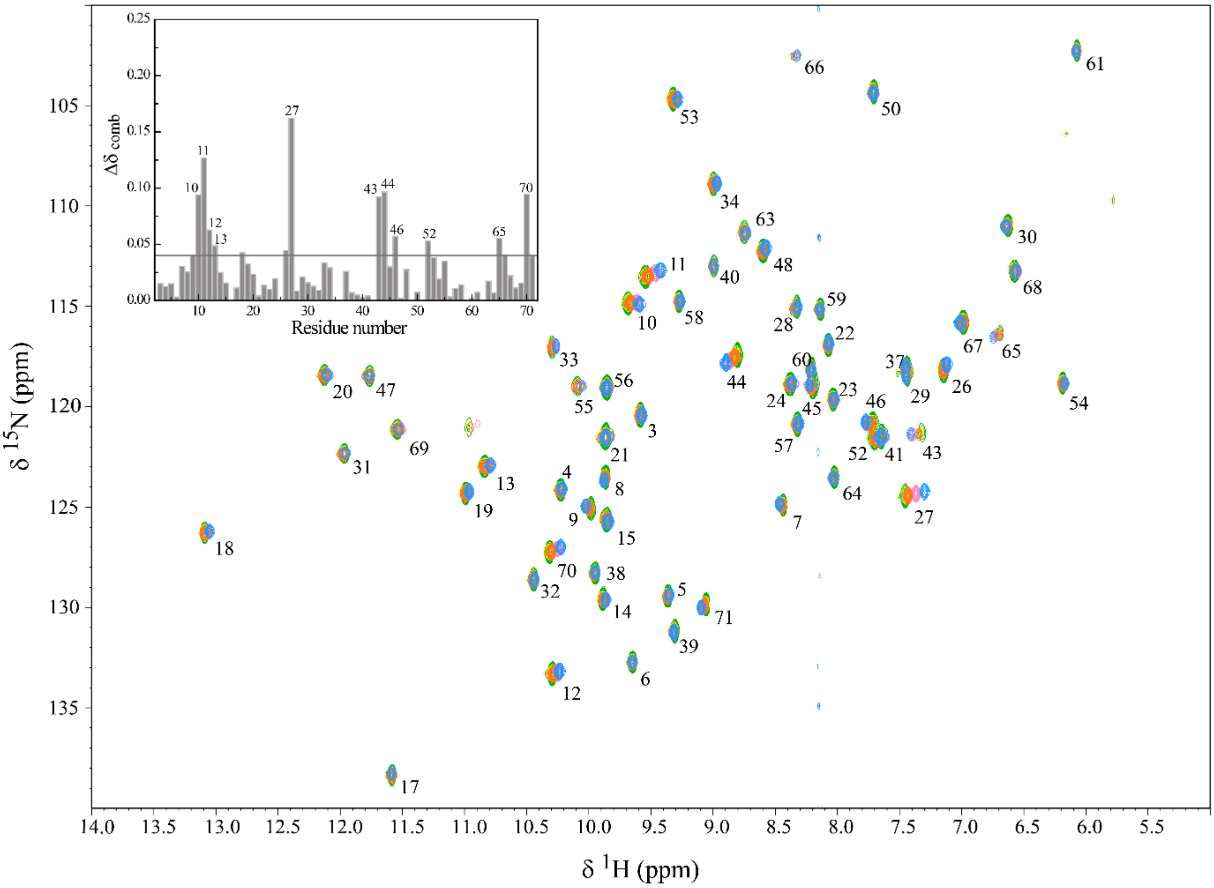

Fig 3.5 Overlay of the 2D ^{1}H, ^{15}N HSQC NMR spectra of ^{15}N-enriched PpcA$_{ox}$ (0.5 mM) in the presence of increasing amounts of AQDS, at 298 K. The contours of the signals in the reference spectrum are shown in green while in the spectral overlay, the concentration of AQDS increases from green to blue contours. To clarity of the figure, only the spectra acquired with 0.8; 4.0; 15.8 and 39.6 mM AQDS are shown. The assignments of NH signals are indicated. Samples were prepared in 45 mM sodium phosphate buffer pH 7 with 100 mM final ionic strength. The insets show the plot of the combined chemical shift changes determined from the directly observed ^{1}H and ^{15}N chemical shifts, in accordance with the Eq. (1). The horizontal line in the inset was determined with the standard deviation to zero value, σ^0_{corr} (see section 3.3.1.3).

The NH signals showing highest chemical shift perturbation are those in the polypeptide segment Asn^{10} to Val^{13}, Lys^{43}, Glu^{44}, Ala^{46}, Lys^{52}, Cys^{65} and Lys^{70}, all residues located near heme IV with one exception of residue Cys^{27} which is near heme I. Analysis of the chemical shift perturbation as a function of AQDS concentration yielded hyperbolic binding curves which were fitted to a 1:1 model considering fast exchange conditions (Fig 3.6).

The K_d values obtained from the fitting of the ligand-induced chemical shift perturbation curves (Fig 3.6) are in the millimolar range and suggest the formation of a low affinity complex. These values are of the same magnitude as those obtained for the binding of calixarene to cytochrome *c* C102T from *Saccharomyces cerevisiae* [23-25]. The low-binding affinity complex and the specific interaction in the proximity of heme IV suggest a rapid and selective electron transfer between the quinone molecule and PpcA, a typical feature in electron transfer reactions between redox partners [18, 26, 27].

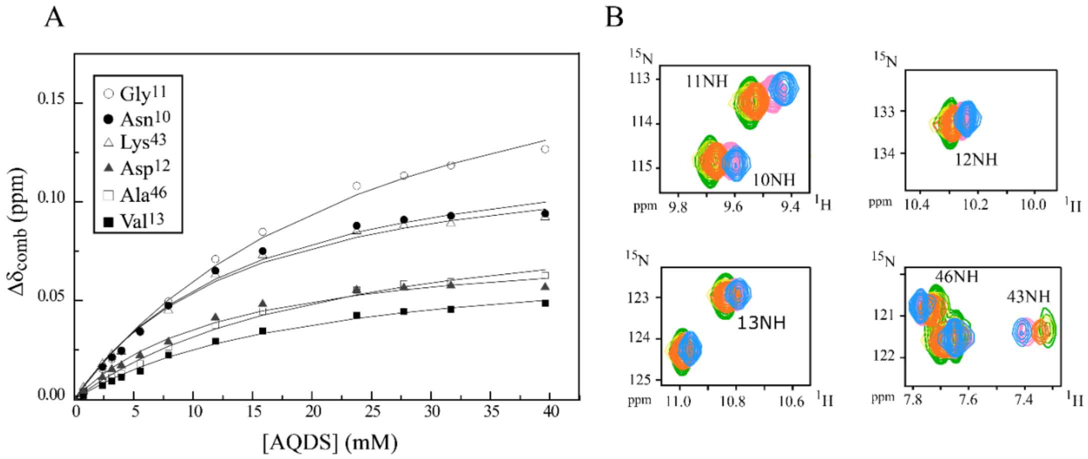

Fig 3.6 Binding isotherms for $PpcA_{ox}$-AQDS interaction (A) and selected regions from overlaid 2D ^{1}H, ^{15}N HSQC NMR spectra (B). (A) Labels indicate the NH signals that were monitored in the chemical shift perturbation experiments (for clarity of the figure NH signals of Glu^{44}, Lys^{52}, Cys^{65} and Lys^{70} are not shown). Each data set was fit to a 1:1 binding model considering fast exchange conditions (solid lines). An average K_d value was calculated as 18 ± 5 mM from the titration curves. (B) Expansion of each NMR spectrum. The amount of AQDS increases from green to blue contours.

The most affected residues are highlighted on the three-dimensional structure of PpcA, except for Cys^{27} (Fig 3.7). The chemical shift perturbation of the NH group of a single residue Cys^{27} located near heme I most probably represents secondary effects of AQDS binding in the region of heme IV. In fact, previous ^{15}N NMR relaxation experiments carried out on PpcA have shown that Cys^{27} is in the most flexible region of the polypeptide chain and also shows the highest sensitivity to conformational exchange processes in the microsecond–millisecond time scale [12].

As shown by the equilibrium and kinetic studies probed by UV–visible spectroscopy, $PpcA_{ox}$ can be fully reduced in the presence of AH_2QDS. However, the three heme groups of PpcA provide three distinct entry gates for the electrons. Therefore, it is expected that the donor and at least one of the heme groups of PpcA are near for an effective electron transfer. Under this scenario, we then moved to study the effect of the interaction between AQDS and the $PpcA_{ox}$ on the heme group NMR signals. PpcA is one of the smallest *c*-type cytochromes described so far with a high ratio of hemes to amino acids (approximately 1 heme per 24 amino acids). Thus, any perturbation caused by the binding of an extraneous molecule to PpcA is expected to affect the NMR signals of the heme substituents. Each heme has four heme methyls and their ^{1}H NMR signals are found in less crowded regions of the 1D ^{1}H NMR spectrum of $PpcA_{ox}$. For this reason, they constitute excellent probes for monitoring the chemical shift perturbations on PpcA$_{ox}$ heme groups. Consequently, in the present work the interactions between AQDS and PpcA$_{ox}$ were further evaluated by monitoring the chemical shift perturbation on the PpcA$_{ox}$ heme methyl signals on the 1D ^{1}H NMR spectra.

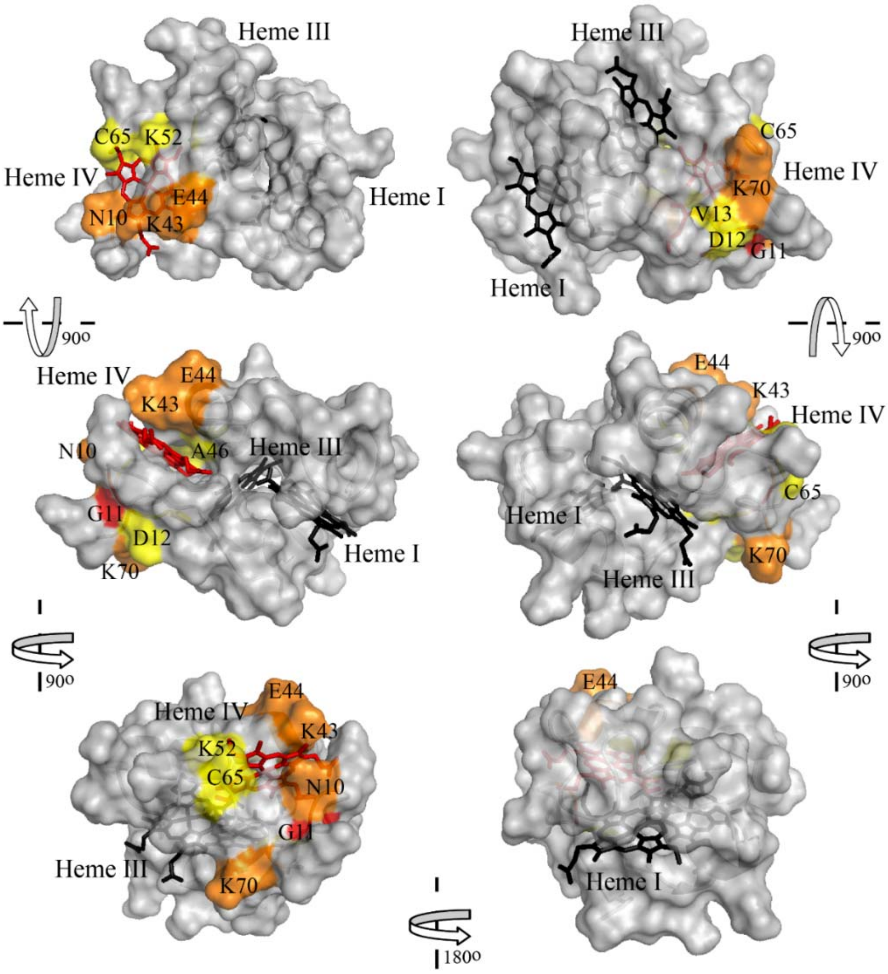

Fig 3.7 Surface map of significantly perturbed residues in PpcA upon AQDS binding. The molecular surface was generated in PyMOL [28] by using the PpcA structure (PDB ID: 2LDO [12]). Residues for which the amide resonances experienced small ($\Delta\delta_{comb}$ > 0.04 ppm), medium ($\Delta\delta_{comb} \geq 0.07$ ppm) or large ($\Delta\delta_{comb} \geq 0.10$ ppm) shifts are colored yellow, orange and red, respectively. Heme IV is shown in red and hemes I and III are shown in black. The left and right panels are related by a 180° rotation. Upper images are related to lower images by 90° rotations as indicated.

The low-field regions of the 1D ^{1}H NMR spectra, acquired during the titration of PpcA$_{ox}$ with increasing amounts of AQDS, are indicated in Fig 3.8. The analysis of the chemical shift perturbation clearly shows that signals of heme IV methyls are the most affected (Fig 3.8). This data further confirms the interaction of AQDS with PpcA$_{ox}$.

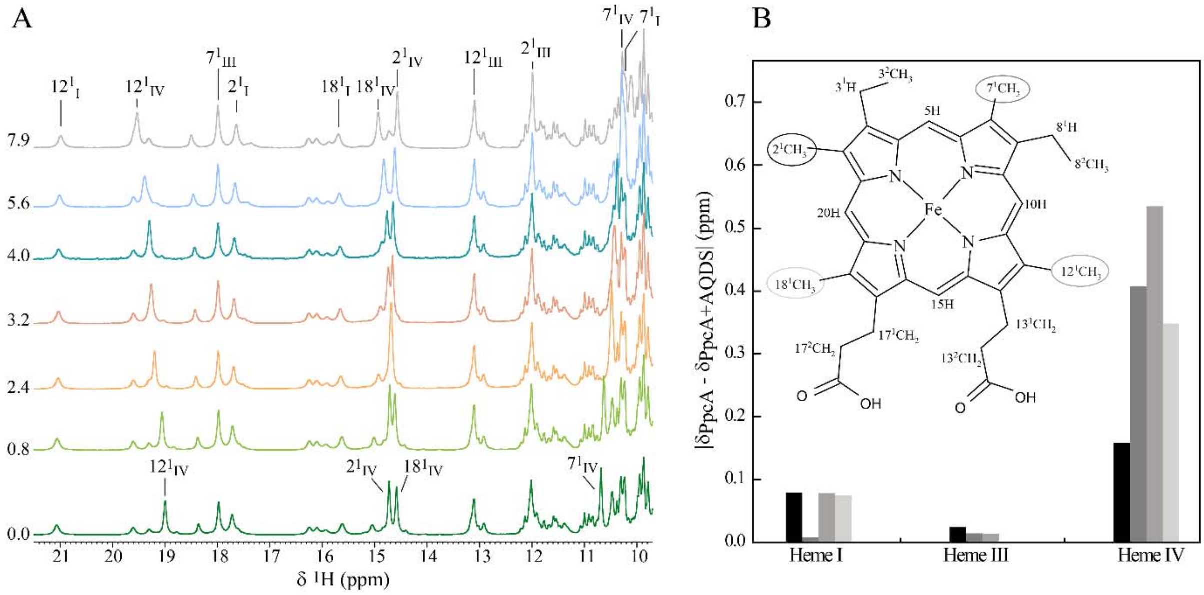

Fig 3.8 ¹H chemical shift changes of the heme methyls of PpcA$_{ox}$, at 298 K. (A) Expansions of the low-field region of 1D ¹H NMR spectra obtained for PpcA$_{ox}$ in presence of increasing amounts of AQDS. The heme methyl signals (2^1CH_3, 7^1CH_3, 12^1CH_3 and 18^1CH_3) following the IUPAC nomenclature [29] are labeled, except heme methyl $18^1CH_3^{III}$ whose signal appears at a chemical shift of approximately 1 ppm. The value of AQDS concentration (mM) used in each experiment is indicated on the left of each spectrum. Samples were prepared in 45 mM sodium phosphate buffer pH 7 with 100 mM final ionic strength. (B) Variation of the heme methyl group chemical shifts $|\delta_{PpcA}-\delta_{PpcA+AQDS}|$. The shifts were taken from the PpcA spectra obtained in the absence (δ_{PpcA}) and in the presence of 7.9 mM AQDS ($\delta_{PpcA+AQDS}$). The bars represent the ¹H chemical shift variations of methyl groups in the following order from left to right: 2^1CH_3, 7^1CH_3, 12^1CH_3 and 18^1CH_3. The diagram of a heme *c* is shown in the inset.

For the electron transfer between AQDS and PpcA$_{ox}$ to occur at physiologically relevant rates, at least one PpcA heme group and the donor must be in close proximity. Therefore, the larger magnitude observed in the chemical shift perturbation of the heme IV methyl signals compared with that observed in the backbone NH signals indicates that the data is consistent. All three heme groups of PpcA are considerably exposed to the solvent, with heme I showing the largest exposure [12, 30]. Therefore, the selective interaction between AQDS and heme IV of PpcA$_{ox}$ must be driven by other factors than simple heme exposure. The location of several lysine residues around heme IV confers a highly positively charged surface near this heme group. Interestingly, the crystal structure of PpcA$_{ox}$ (PDB ID 1OS6) showed that the lysine residues located near heme IV form an anion binding region, where two sulfate ions (SO_4^{2-}) were observed [30]. Thus, the two negative charges of AQDS conferred by the two sulfonate ions (see inset on Fig 3.2B) are likely to drive AQDS toward heme IV. Therefore, considering the net positive charge of PpcA around heme IV and the negatively charged AQDS, electrostatic interactions are expected to contribute favorably to the binding affinity of the PpcA–AQDS redox complex. In the crystal structure, one sulfate ion is H-bonded to the His^{47} Nδ_1 and is close to Lys^{43} (3.4 Å) and Lys^{52} (4.8 Å). Therefore, based on the chemical shift perturbation data, AQDS could bind on the distal site of heme IV between Lys[43] and Lys[52]. However, if this is the case it would be expected that the ring of His[47] will be reoriented, due to the larger volume of AQDS molecule.

Unfortunately, the ring proton signals of the heme axial histidines are extremely broad due to the paramagnetic effect of the unpaired electron of the iron ion in PpcA$_{ox}$. Therefore, to probe any change in the geometry of the heme axial ligands, we analyzed the chemical shift perturbation on the βCH$_2$ protons of all axial ligands of PpcA$_{ox}$ (Fig 3.9). From this analysis, βCH$_2$ protons of His[47] are clearly the most affected, suggesting a reorientation of His[47] in presence of AQDS. Moreover, the heme methyl chemical shifts depend on the relative orientation of the heme axial ring planes [31]. Therefore, the larger perturbation observed in the heme IV methyl chemical shifts (Fig 3.8) further confirms the alteration on the geometry of heme IV axial ligands in presence of AQDS.

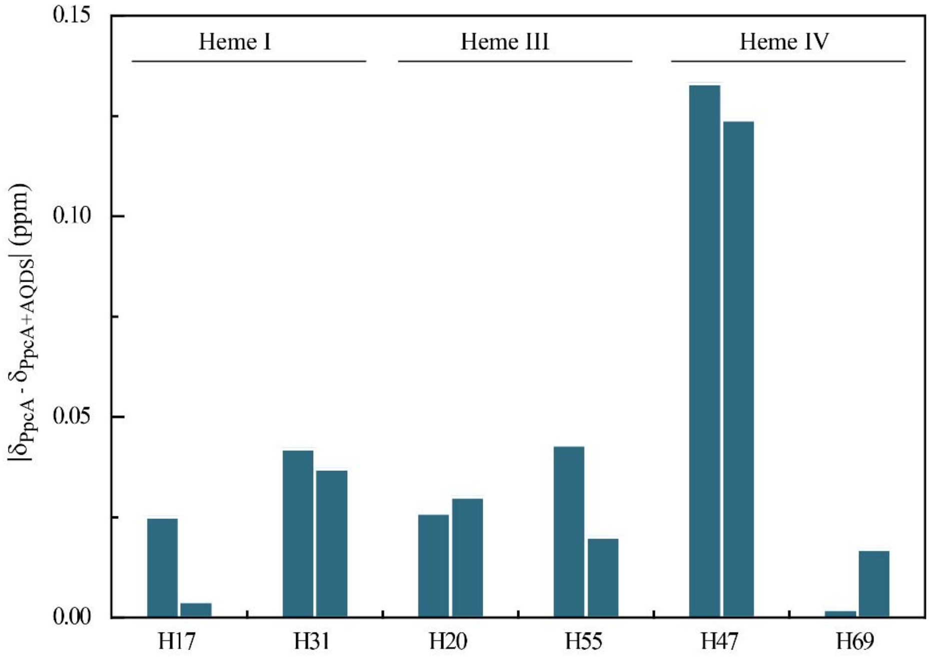

Fig 3.9 ^{1}H chemical shift changes $|\delta_{PpcA} - \delta_{PpcA+AQDS}|$ in the βCH$_2$ groups of the heme axial histidines. The shifts were taken from the 2D ^{1}H, ^{1}H NOESY NMR spectra (80 ms, mixing-time) acquired for 0.5 mM samples of PpcA prepared in ^2H_2O in the absence (δ_{PpcA}) and in the presence of 7.9 mM AQDS ($\delta_{PpcA+AQDS}$) at 25 °C and pH 7.1.

The interaction between PpcA$_{ox}$ and AQDS was further investigated by observing the pattern of the AQDS signals in the 1D ^{1}H NMR spectra in the absence and presence of the protein (Fig 3.10). The 1D ^{1}H NMR spectrum of free AQDS (Fig 3.10A) shows three signals at 8.43, 8.16, 8.13 ppm that correspond to the three pairs of equivalent protons (H1/H5; H3/H7; H4/H8). The protons H1/H5 are considerably less shielded compared to the other pairs due to the electron-withdrawing effect of the sulfonate ion and correspond to the signal at 8.43 ppm. The two very close doublets centered at 8.16 and 8.13 ppm were assigned to the pairs of protons H3/H7 and H4/H8, respectively. In the presence of the protein, the pattern of AQDS signals is clearly affected, confirming the interaction between $PpcA_{ox}$ and AQDS (*cf.* spectra expansions A and B in Fig 3.10). The broadness and displacement observed in the AQDS signals clearly confirmed the existence of a molecular interaction between the protein and the quinone.

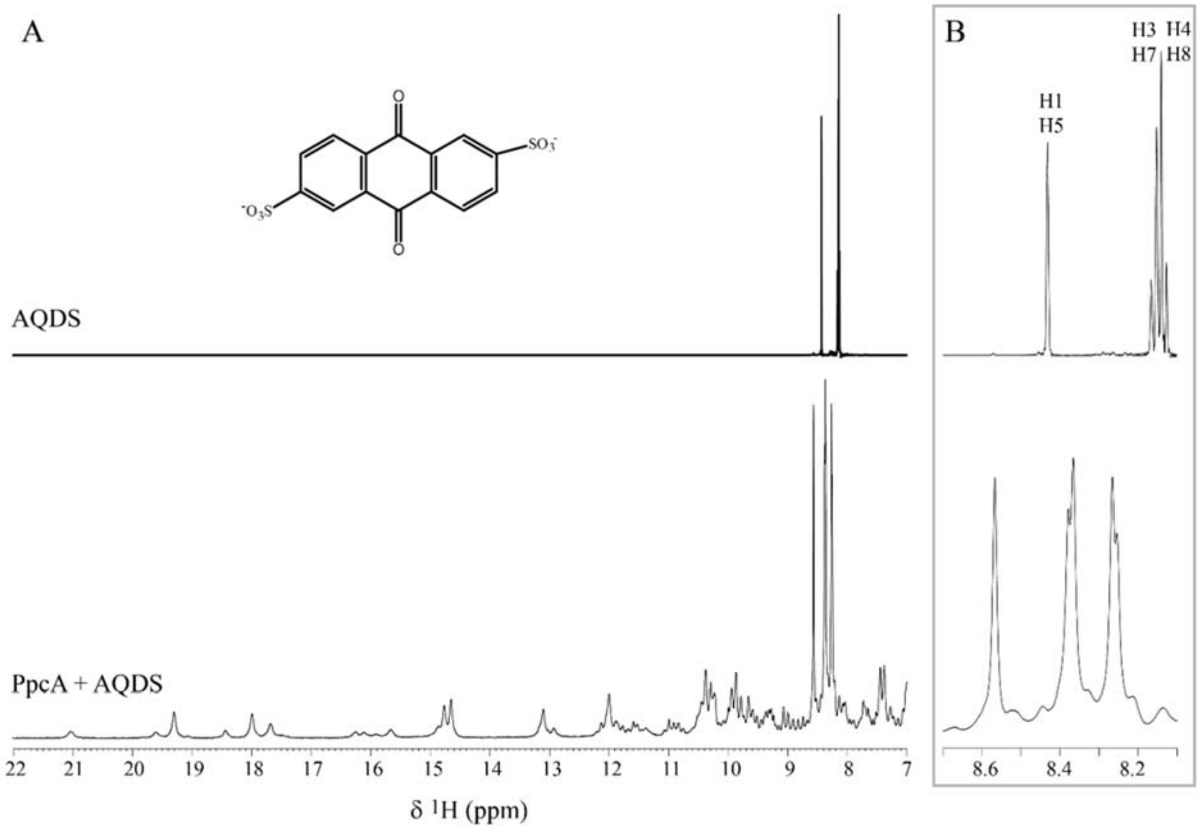

Fig 3.10 ^{1}H chemical shift changes of the AQDS signals in presence of $PpcA_{ox}$, at 298 K. (A) 1D ^{1}H NMR spectral features of free AQDS (upper spectrum) and AQDS in the presence of $PpcA_{ox}$ (lower spectrum). (B) Expansion of the spectral region containing the proton signals of AQDS. The three pairs of equivalent protons (H1/H5; H3/H7 and H4/H8) are indicated. Samples were prepared in 45 mM sodium phosphate buffer pH 7 with 100 mM final ionic strength.

Finally, the comparison of 1D ^{1}H NMR spectra of $PpcA_{ox}$ obtained before and after removal of the ligand by ultrafiltration methods confirm that the interaction between the cytochrome and AQDS is fully reversible (Fig 3.11).

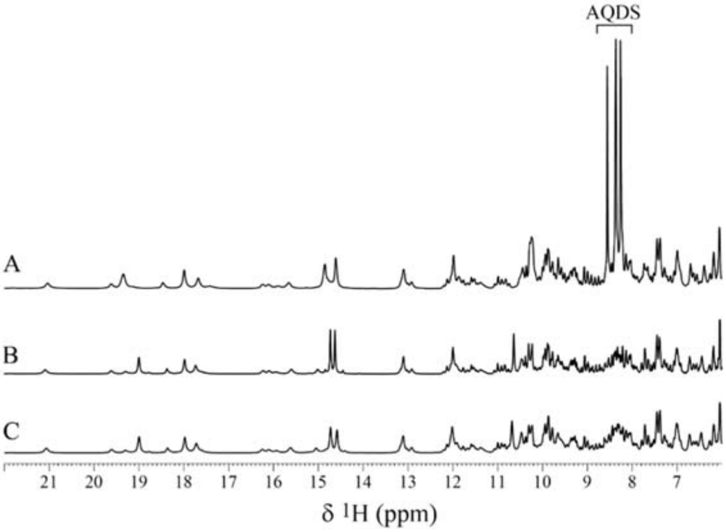

Fig 3.11 Reversibility of AQDS binding to PpcA$_{ox}$ monitored by 1D ^{1}H NMR, at 298 K. Samples were prepared in 45 mM sodium phosphate buffer pH 7 with 100 mM final ionic strength. A fingerprint region of the PpcA 1D ^{1}H NMR spectrum is shown: (A) PpcA in the presence of 0.8 mM AQDS; (B) PpcA prior to the addition of AQDS and (C) PpcA after removal of AQDS.

3.1.2.2 Molecular docking calculations

Docking was performed using the Anchor-and-Grow algorithm, implemented in Dock6.4 for binding of AH$_2$QDS to PpcA$_{ox}$. This model assumes that the protein is rigid but the ligand may have some flexibility, which in the case of AH$_2$QDS is only rotational flexibility of the sulfonate groups. Remarkably, the docking results showed that AH$_2$QDS binds near heme IV in six of the top ten complex models and mapped most residues showing significant NMR chemical shift perturbations (*cf.* Figs 3.7 and 3.12). The NMR data conclusions are also coincidental with the docking calculations, which indicate that the complex between PpcA and AH$_2$QDS is preferably formed near heme IV region (see Fig 3.12).

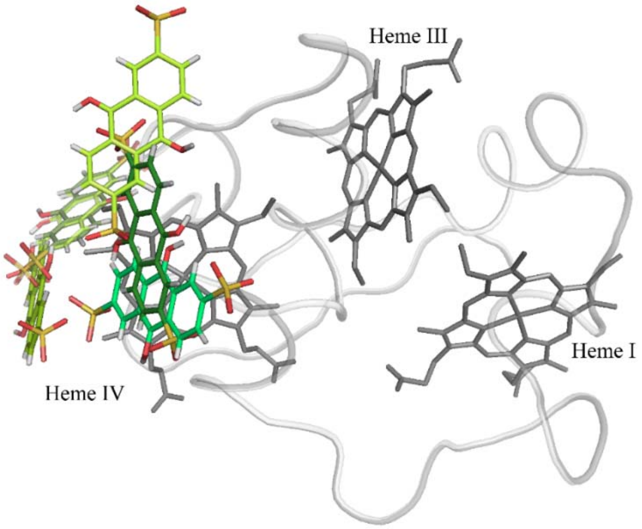

Fig 3.12 PpcA–AH$_2$QDS docked complexes calculated in DOCK 6.4 [32]. PpcA (oriented as in the first panel of Fig 3.7) is illustrated as a ribbon diagram with the heme groups shown in gray sticks. The six of the top 10 docking results for quinone binding near heme IV are shown.

3.1.3 PpcA$_{red}$- AH$_2$QDS interaction studies

3.1.3.1 NMR chemical shift perturbation experiments

In this section, the molecular interaction between PpcA$_{red}$ and the AH$_2$QDS was studied. A series of 2D ^{1}H,^{15}N HSQC NMR spectra were used to monitor this molecular interaction (Fig 3.13).

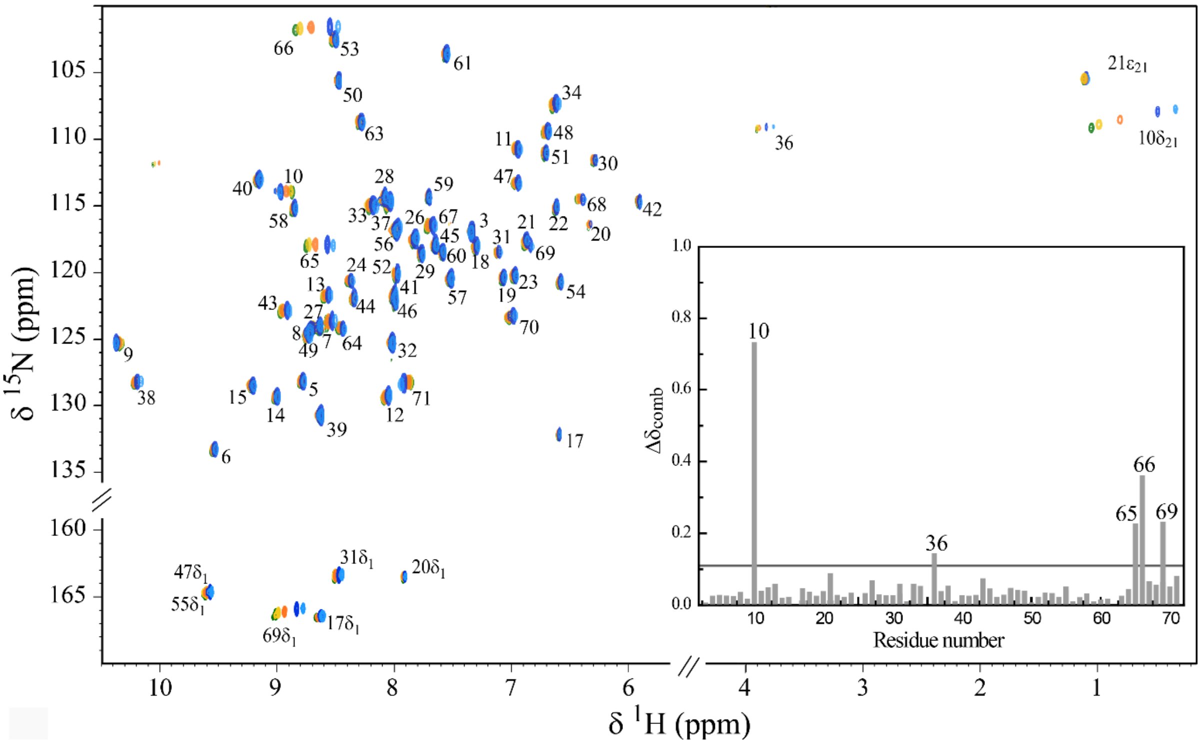

Fig 3.13 Overlay of the 2D ^{1}H, ^{15}N HSQC NMR spectra of ^{15}N-enriched PpcA (0.5 mM) in the presence of increasing amounts of AH$_2$QDS, at 298 K. The contours of the signals in the reference spectrum are shown in green. In the spectral overlay, the concentration of AH$_2$QDS increases from green to light blue contours. For clarity purposes, only the spectra acquired with 0.7 (yellow); 3.3 (orange); 13.0 (dark blue) and 32.5 mM (light blue) AH$_2$QDS are shown. The assignments of NH signals are indicated. Samples were prepared in 45 mM sodium phosphate buffer pH 7 with 100 mM final ionic strength. The inset shows the plot of the combined chemical shift changes determined from the directly observed ^{1}H and ^{15}N chemical shifts, in accordance with the Eq. (3.1). The horizontal line in the inset was determined with the standard deviation to zero value, σ^0_{corr} (see section 3.3.1.3).

The NH signals of PpcA have been previously assigned, except for the first two residues, Ala^1 and Asp^2 [11], and were used to monitor the chemical shift perturbations caused by the AH$_2$QDS. The inset in Fig 3.13 shows the combined chemical shift changes for each NH signal. The backbone NH signals of Cys^{65} and Gly^{66} and the side chain NH signals of Asn^{10}δ$_{21}$ and His^{69}δ$_1$ show the highest chemical shift perturbation. The backbone NH signal of Gly^{36} appears slightly above the cut off line. However, as previously shown, the proton signal of Gly^{36} is strongly up-field shifted due to the large ring current shifts caused by heme I [11]. In fact, this signal is observed at 3.90 ppm (see Fig 3.13), which clearly contrasts with the typical positions for these signals in non-heme proteins and with the other PpcA glycine NH signals in the range of 9 to 6 ppm. Therefore, any marginal reorganization on the polypeptide chain near Gly^{36} NH group is expected to affect its chemical shift. For electron transfer to occur between PpcA and any redox partner at physiologically relevant rates it is expected that at least one of the heme groups of the protein would be near the interacting partner. This sets the heme substituents as excellent targets for monitoring relevant interactions for electron transfer [33, 34]. Therefore, in the present work the interactions between AH$_2$QDS and PpcA were further evaluated by monitoring the chemical shift perturbation on the heme substituents by 2D ^{1}H, ^{1}H NOESY (nuclear Overhauser effect spectroscopy) experiments. The analysis of the chemical shift perturbation shows that the signals of heme IV are clearly the most affected and constitute additional evidence for a specific interaction between the quinol and the protein in the neighborhood of this heme (Fig 3.14).

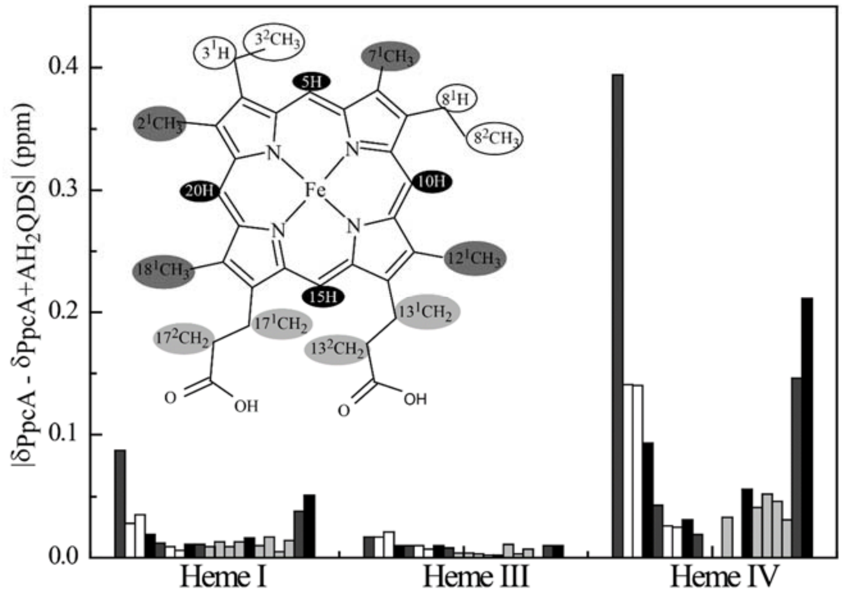

Fig 3.14 Variation of the ^{1}H chemical shift of the PpcA$_{red}$ heme substituents at 298 K. The diagram of a heme *c* labeled in accordance with the IUPAC nomenclature [29] is shown in the inset. The shifts were taken from the PpcA spectra obtained in the absence (δ_{PpcA}) and in the presence of AH$_2$QDS ($\delta_{PpcA-AH2QDS}$). The bars represent the ^{1}H chemical shift variations of thioether methines/thioether methyls, propionates αCH$_2$ protons, methyl groups and meso-protons, respectively. In each set of bars, the heme substituents are represented clockwise in the following order: 2^1CH_3, 3^1H, 3^2CH_3, 5H, 7^1CH_3, 8^1H, 8^2CH_3, 10H, 12^1CH_3, 13^1CH_2, 13^2CH_2, 15H, 17^1CH_2, 17^2CH_2, 18^1CH_3, 20H (see the inset). The heme propionate CH$_2$ groups are not equivalent yielding two distinct chemical shifts.

Particularly, the most perturbed heme signals are in the more solvent exposed heme edge and include the heme methyls $2^1CH_3^{IV}$ and $18^1CH_3^{IV}$, and the meso-proton $20H^{IV}$. Moreover, the chemical shifts of these methyls in the absence of AH$_2$QDS are 3.59 ppm and 3.33 ppm, for $2^1CH_3^{IV}$ and $18^1CH_3^{IV}$, respectively. On the other hand, in the presence of AH$_2$QDS the chemical shifts are nearly identical (3.20 ppm and 3.18 ppm, for $2^1CH_3^{IV}$ and $18^1CH_3^{IV}$, respectively) indicating that the chemical environment near these protons is similar in the presence of the quinol (Fig 3.15).

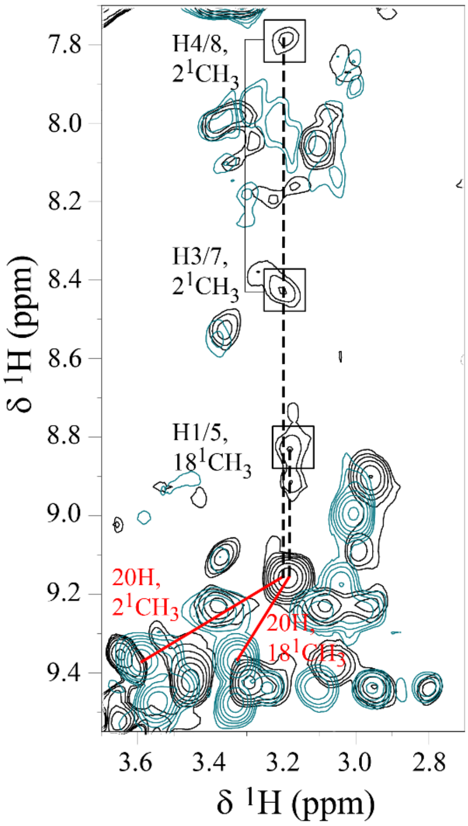

Fig 3.15 Selected region of 2D ^{1}H, ^{1}H NOESY NMR spectra of PpcA acquired at 298K in the absence (blue) and presence (black) of AH$_2$QDS. The spectra were acquired with 80 ms and the tr-NOE connectivities observed between the AH$_2$QDS and heme methyl $2^1CH_3^{IV}$ and $18^1CH_3^{IV}$ signals are indicated in black squares connected by dashed lines. The red lines indicate the positions of the cross-peaks 20H, $2^1CH_3^{IV}$ and 20H, $18^1CH_3^{IV}$ in both spectra (see also Fig 3.14). Samples were prepared in 45 mM sodium phosphate buffer pH 7 with 100 mM final ionic strength.

To further confirm the interaction between the reduced quinone and PpcA we also monitored the NMR signals of AH$_2$QDS. Small molecules, such as AH$_2$QDS, have short correlation times (τ_c) due to their fast tumbling in solution and, consequently, the intramolecular NOE connectivities have different sign relative to the diagonal signals (positive NOEs). On the other hand, when bound to a protein, a small molecule acquires the motional properties of the macromolecule and will have larger τ_c, and the NOE connectivities will have the same sign as the diagonal signals (negative NOEs). Therefore, the interaction of AH$_2$QDS with PpcA was also evaluated by the analysis of the 2D ^{1}H, ^{1}H NOESY spectra of PpcA acquired in the presence and absence of the ligand (Fig 3.16). The region of the 2D ^{1}H, ^{1}H NOESY spectrum of PpcA containing the AH$_2$QDS signals is indicated in Fig 3.16A. The sharp peaks corresponding to the quinol signals are easily identified at 8.84, 8.43, 7.79 ppm, which correspond to the three pairs of equivalent protons (H1/H5; H3/H7; H4/H8). The singlet at 8.84 ppm corresponds to the H1/H5 pair. The two doublets centered at 8.43 and 7.79 ppm correspond to the non-specifically assigned pairs H3/H7 and H4/H8. The cross-peaks between these two pairs have negative NOEs, a feature only observable if the τ_c of the small molecule increases upon binding to high molecular weight entity (Fig 3.16A).

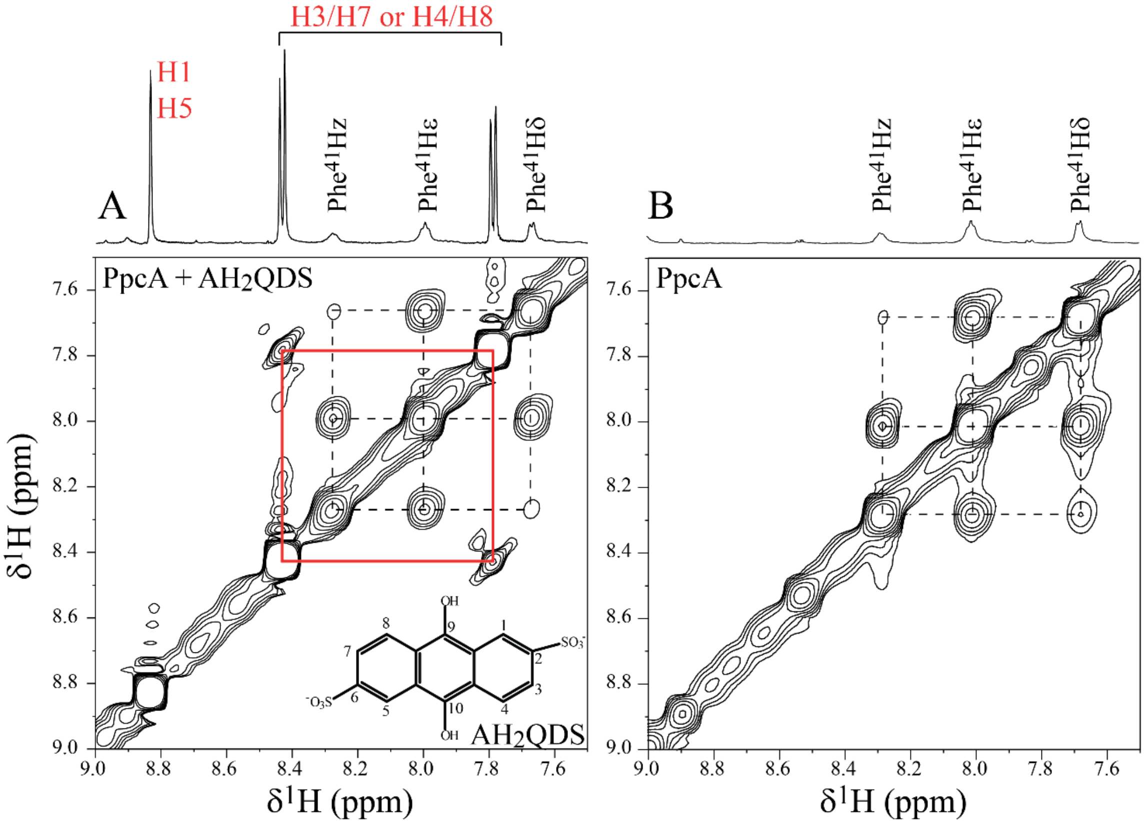

Fig 3.16 Selected region of 2D ^{1}H, ^{1}H NOESY NMR spectra (80 ms, mixing-time) of PpcA (0.5 mM) acquired in the presence (A) and absence (B) of AH$_2$QDS (2.5 mM). The corresponding 1D spectrum is represented at the top of each 2D ^{1}H, ^{1}H NOESY spectra. To be used as a guide between the two spectra, the signals of PpcA Phe^{41} aromatic ring protons are connected by black dashed lines. The solid red line connects the negative NOE observed between the quinol signals. Samples were prepared in 45 mM sodium phosphate buffer pH 7 with 100 mM final ionic strength.

In the region of the 2D ^{1}H, ^{1}H NOESY spectra indicated in Fig 3.15, the presence of transfer NOE (tr-NOE) connectivities between the AH$_2$QDS protons and the heme methyls $2^1CH_3^{IV}$ and $18^1CH_3^{IV}$ are illustrated (see black squares in Fig 3.15). These signals are also in phase with the diagonal of the spectrum, which constitutes additional evidence for interaction between the protein and the AH$_2$QDS at the most solvent exposed edge of heme IV. The residues showing the highest chemical shift perturbations caused by the AH$_2$QDS including heme IV are highlighted on the three-dimensional structure of PpcA (Fig 3.17).

After identifying that the region containing heme IV is involved in the formation of the complex between PpcA and AH$_2$QDS, we then analyzed the chemical shift perturbation of the most affected NH signals, as a function of quinol concentration. The increasing chemical shift perturbations indicated that the free and bound forms of PpcA$_{red}$ are in fast exchange on the NMR time scale. The average size of the chemical shift perturbation for PpcA:AH$_2$QDS complex is higher than the one previously reported for PpcA:AQDS (section 3.1.2.1). This indicates that PpcA and AQDS form an encounter complex consisting of a dynamic ensemble of orientations (very small perturbation, for a review see Ref. [18]). However, the higher average size of the chemical shift perturbation and the smaller number of affected residues suggest that complex formed by PpcA and AH_2QDS exists in fewer orientations, which indicates the formation of a more specific complex in solution.

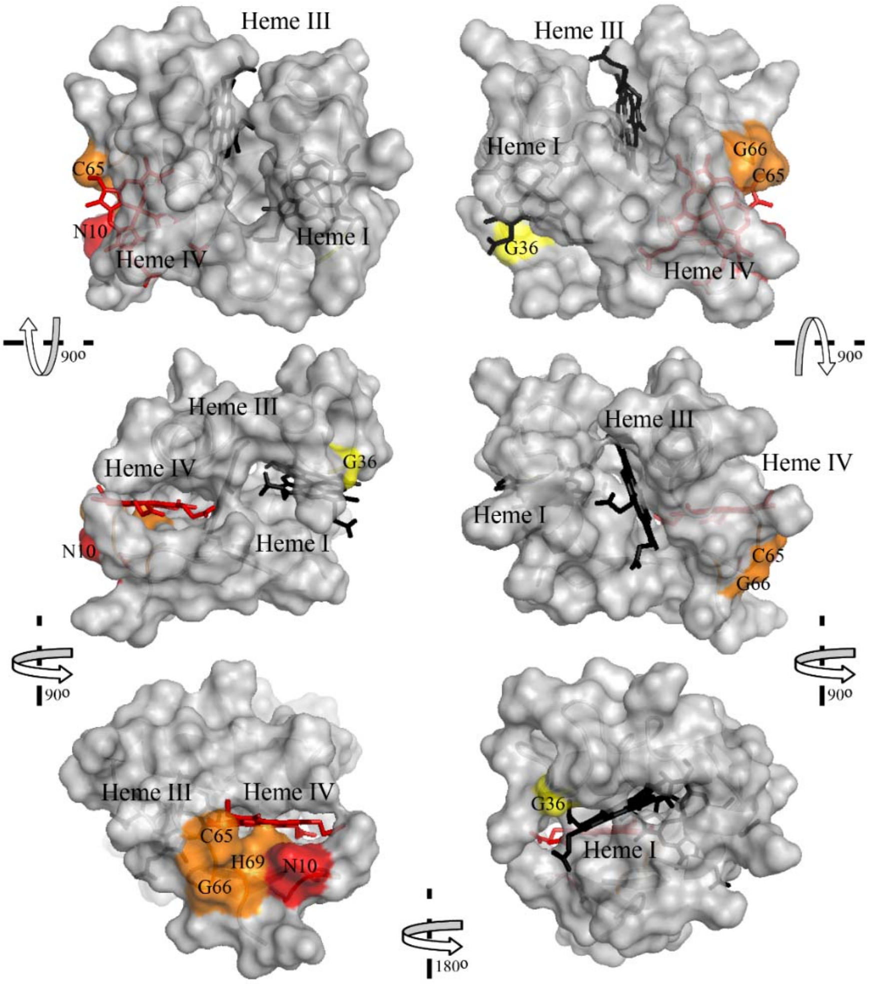

Fig 3.17 Chemical shift perturbation map of PpcA in presence of AH_2QDS. The molecular surface was generated in PyMOL [28] by using the PpcA structure (PDB ID: 2LDO [12]). Residues for which the amide resonances experienced small ($\Delta\delta_{comb} > 0.1$ ppm), medium ($\Delta\delta_{comb} \geq 0.2$ ppm) or large ($\Delta\delta_{comb} \geq 0.4$ ppm) shifts are colored yellow, orange and red, respectively. Heme IV is shown in red and hemes I and III are shown in black. The left and right panels are related by a 180° rotation. Upper images are related to lower images by 90° rotations as indicated.

The dependence of the chemical shift perturbation as a function of AH_2QDS concentration yielded hyperbolic binding curves, which were fitted to a 1:1 model considering fast exchange conditions (Fig 3.18).

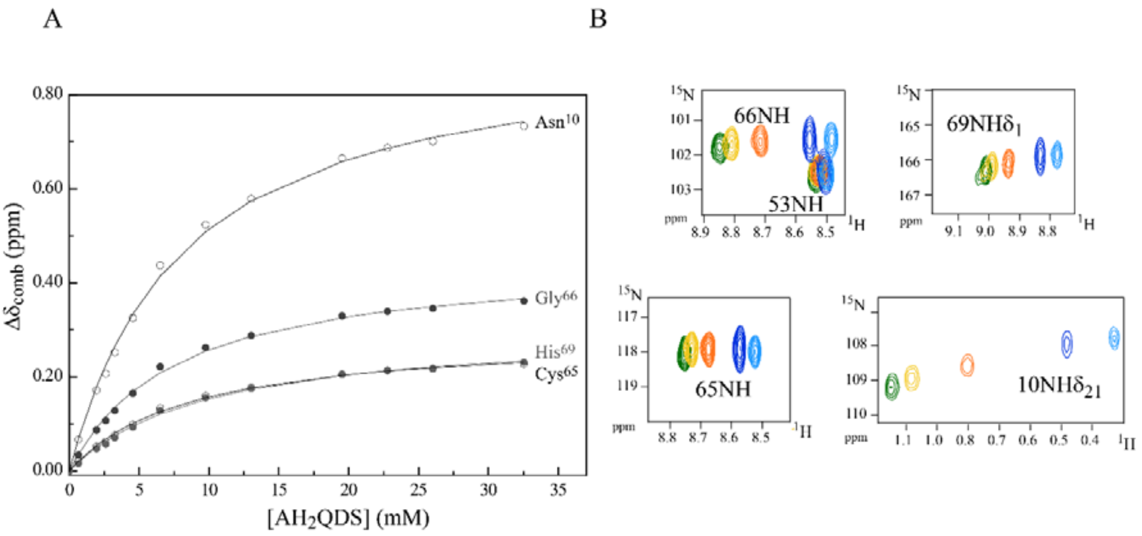

Fig 3.18 Binding isotherms for PpcA:AH$_2$QDS interaction (A) and selected regions from overlaid 2D ^{1}H,^{15}N HSQC NMR spectra (B). In panel A, labels indicate the NH signals that were monitored in the chemical shift perturbation experiments. Each data set was fit to a 1:1 binding model considering fast exchange conditions (solid lines). An average K_d value was calculated as 8 ± 1 mM from the titration curves. In the expansion of each NMR spectrum (panel B) the amount of AH$_2$QDS increases from green to light blue contours (see Fig 3.13).

The K_d value obtained from the fitting of the ligand-induced chemical shift perturbation curves are in the millimolar range and suggest the formation of a low affinity complex (Fig 3.18). In addition, the average K_d value obtained in this section (8±1mM) is also comparable to the one obtained for PpcA$_{ox}$ interacting with AQDS (18 ± 5mM, section 3.1.2.1) reinforcing the evidence obtained from the UV-visible and stopped flow studies (section 3.1.1), which suggested that the electron transfer proceeds in both directions at similar rates and that the thermodynamic equilibrium is reached in a short time scale (k_{obs} 1 s^{-1} for reductive experiments and k_{obs} 3 s^{-1} in the oxidative ones). Compared to AQDS, the smaller K_d value obtained for binding of AH$_2$QDS also corroborates the kinetic studies indicating that the extent of electron transfer is under thermodynamic control, *i.e.*, it is more favorable from AH$_2$QDS to PpcA$_{ox}$, than in the opposite direction (see section 3.1.1). The low-binding affinity complex and the specific interaction in the proximity of heme IV warrant a rapid and selective electron transfer between AH$_2$QDS and PpcA, a typical feature in electron transfer reactions between redox partners [18, 26, 27]. As previously mentioned, the region close to heme IV of the PpcA has a highly positive electrostatic surface [12]. These positively charged residues are expected to form an anion binding region and drive the negatively charged AH$_2$QDS molecule toward heme IV, thus contributing favorably to the binding affinity between the cytochrome and the quinol. Recently, molecular dynamics simulation of an anionic porphyrin, free base TPPS [meso-tetrakis(4-sulfonatophenyl)porphyrin], binding to PpcA also implicated the same positively charged surface near the heme IV [35].

3.1.3.2 Molecular docking calculations

The binding of quinol near heme IV is also coincidental with the docking calculations, which show that the six of the top 10 modeled complex structures, obtained with rigid protein–flexible ligand docking, were clustered near this heme (Fig 3.19A). One of those two sites corresponded to the area with the strongest observed NMR shifts. Top four docking complex structures with ligands located in this area were further refined with protein–flexible ligand docking simulations. They revealed that in addition to several non-polar interactions between the protein and the quinol ligand, lysine residues of the protein were reorienting toward sulfonates and hydroxyls of the bound quinol. In the best docking model of the complex, the quinol is stacked between the side chain of Lys^{71} and the main chain near Cys^{65} and Gly^{66} (Fig 3.19B). One of the quinol hydroxyl groups hydrogen bonds with the main chain O of His^{69} and with the side chain NZ of Lys^{71}. One of the sulfonate groups forms hydrogen bonds with NZ of Lys^{70} and main chain N of Lys^{71}. Side chain of Asn^{10} forms hydrogen bond with NZ of Lys^{71}. Side chain of Asn^{10} is in van der Waals contact with the heme IV atoms CHB (20H) and CMA ($18^1CH_3^{IV}$). The other sulfonate group is exposed to solvent and is near CMB of heme IV ($2^1CH_3^{IV}$).

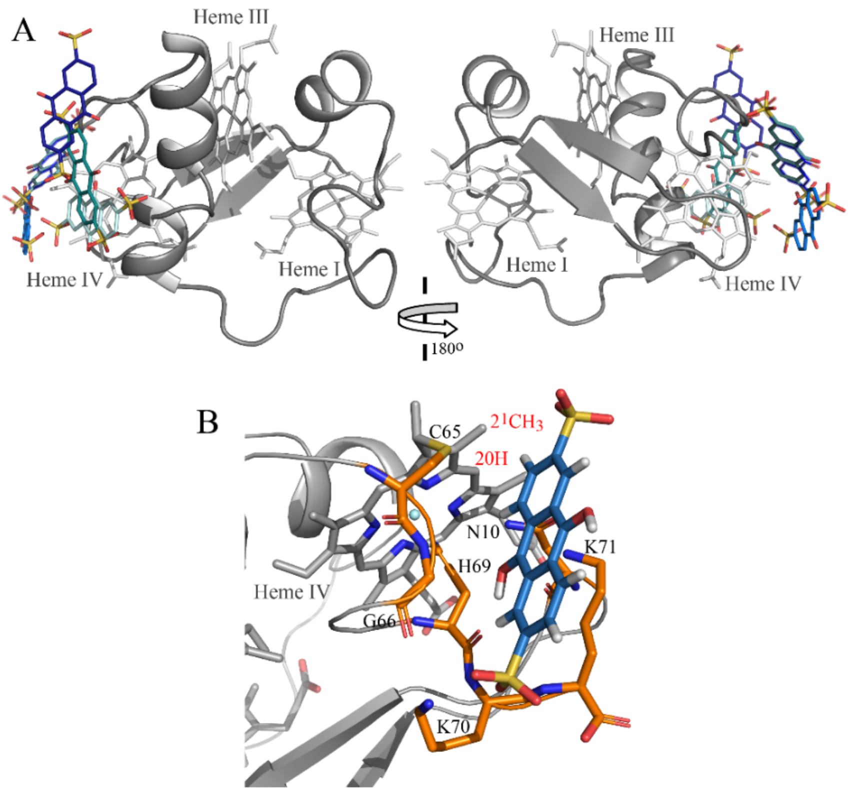

Fig 3.19 PpcA–AH_2QDS docked complexes calculated in DOCK 6.7 [32]. (A) PpcA is illustrated as a ribbon diagram with the heme groups shown in gray sticks. The left and right panels are related by a 180° rotation. The six of the top 10 docking results for quinol (shown in colored sticks) binding near heme IV are shown. (B) A close-up view of the best complex model obtained by protein–flexible ligand docking calculations. The heme IV and protein residues are shown as sticks in atom type colors, whereas the quinol is shown in the following colors: carbon, blue; oxygen, red; sulfur, yellow and hydrogens in gray. Part of the protein is shown as Cα cartoon in gray. Two of the heme atoms are labeled in red in accordance with the IUPAC nomenclature [29].

3.1.3.3 Effect of binding of HS on the thermodynamic properties of the redox centers in the cytochrome PpcA

Electron transfer between redox partners at rates compatible with metabolic processes requires bringing the redox centers of the donor and acceptor molecules to close proximity and in proper orientation. In addition, the reduction potentials must be such that they ensure favorable driving force, which is one of the main determinants of the electron transfer rates [36]. Therefore, to properly interpret the data obtained for PpcA in the presence of the HS analog, it is important to evaluate the impact on the redox properties of PpcA upon formation of the complex with this compound. To achieve this, we have undertaken a detailed thermodynamic characterization of PpcA in the presence of the quinol.

The thermodynamic parameters of the free protein were previously determined by fitting the pH dependence of the chemical shifts of heme methyls $12^1CH_3^I$, $7^1CH_3^{III}$ and $12^1CH_3^{IV}$, measured in different stages of oxidation, together with data from visible redox titrations obtained at pH 7 and 8 [37]. In the present work, the same set of heme methyl groups were used to characterize the redox properties of PpcA heme groups in the presence of the HS analog. 2D ^1H, ^1H EXSY (exchange spectroscopy) spectra were collected at different pH values and the chemical shifts of heme methyls $12^1CH_3^I$, $7^1CH_3^{III}$ and $12^1CH_3^{IV}$ were measured for the different oxidation stages. Examples of these spectra are given in Fig 3.20.

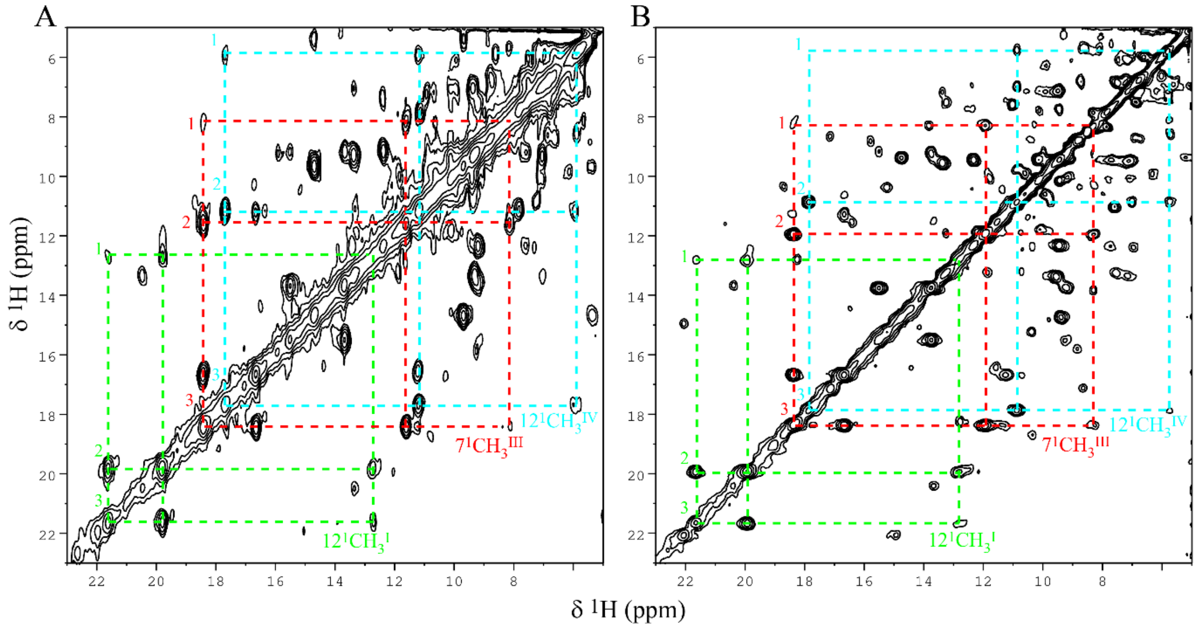

Fig 3.20 Expansions of 2D ^1H, ^1H EXSY NMR spectra obtained for PpcA in the absence (A) and the presence (B) of AH_2QDS (15 °C and pH 6). Cross-peaks resulting from intermolecular electron transfer between the oxidation stages 1-3 are indicated for the heme methyls $12^1CH_3^I$ (green dashed lines), $7^1CH_3^{III}$ (red dashed lines) and $12^1CH_3^{IV}$ (blue dashed lines). Roman and Arabic numbers indicate the hemes and the oxidation stages, respectively. To reduce crowding in the figure, the 2D ^1H, ^1H EXSY NMR spectra with cross-peaks to oxidation stage 0 are not shown.

The similarity between the spectra obtained for PpcA in the absence and presence of the quinol indicates that the formation of the complex did not decrease the spectral quality. Thus, as for the free protein, in the presence of quinol the following NMR features were observed: (i) slow inter- and fast intramolecular electron transfer among the redox equilibria are maintained allowing discrimination of the individual heme signals in different oxidation stages and (ii) fast exchange on the NMR time scale for the bound and unbound states so that a single signal is observed at a position that is weighted by their relative populations. Therefore, it was possible to monitor the oxidation profiles of the hemes by 2D ^{1}H, ^{1}H EXSY NMR in the presence of the quinol molecule. The chemical shifts of heme methyls $12^1CH_3^I$, $7^1CH_3^{III}$ and $12^1CH_3^{IV}$ measured for oxidation stages 1–3 in the pH range of 6.0–9.0 are indicated in Fig 3.21.

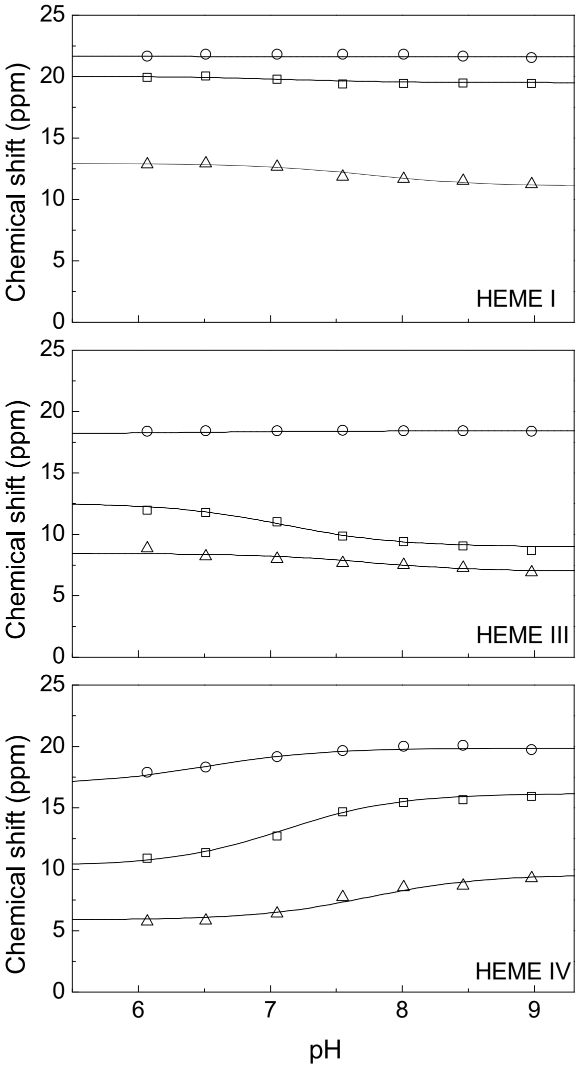

Fig 3.21 Fitting of the thermodynamic model to the experimental data for PpcA in the presence of AH_2QDS. The panels show the pH dependence of heme methyl chemical shifts at oxidation stages 1 (Δ), 2 (□), and 3 (○). The black solid lines are the result of the simultaneous fitting of the NMR and visible data.

To measure the impact of the bound quinol on the redox properties of the heme groups in PpcA a thermodynamic model was fitted to the pH dependence of the observed chemical shift of heme methyls, together with the data from visible redox titrations (see section 3.3.1.4). The thermodynamic parameters obtained from the fitting are indicated in Table 3.4.

Table 3.4 Thermodynamic parameters determined for PpcA in the presence of quinol. For comparison, the values previously obtained for the free protein PpcA [38] were also included. In each case, the fully reduced and protonated protein was taken as reference. Diagonal values (in bold) correspond to oxidation energies of the hemes and deprotonating energy of the redox-Bohr center. Off-diagonal values are the redox (heme–heme) and redox-Bohr (heme–proton) interaction energies. All energies are reported in meV, with standard errors given in parentheses.

	Energy (meV)			
	Heme I	**Heme III**	**Heme IV**	**Redox-Bohr center**
PpcA:AQDS				
Heme I	**-152 (4)**	25 (2)	13 (3)	-27 (4)
Heme III		**-137 (4)**	37 (2)	-22 (4)
Heme IV			**-119 (4)**	-54 (3)
Redox-Bohr center				**476 (7)**
PpcA				
Heme I	**-154 (5)**	28 (3)	17 (3)	-36 (5)
Heme III		**-140 (5)**	42 (3)	-31 (5)
Heme IV			**-120 (6)**	-62 (4)
Redox-Bohr center				**497 (9)**

The quality of the fittings obtained for the pH dependence of the NMR paramagnetic chemical shifts clearly shows that the experimental data is well described by the model (see solid lines in Fig 3.21). Overall, the results obtained showed that the quinol binding to PpcA had little effect on the reduction potential of the hemes in the fully reduced and protonated protein (Table 3.4). Also, the redox interactions remain essentially unaffected compared to the free cytochrome, indicating that the intramolecular dielectric environment and the heme core structure are essentially undisturbed by complex formation. On the other hand, as a result of the complex formation, the properties of the PpcA redox-Bohr center, previously assigned to heme IV propionate P_{13} [12, 37, 39] are more affected. However, the strongest redox-Bohr interactions with heme IV and the similar pH dependence of the heme methyl signals in the presence of the quinol indicate that the redox-Bohr center is the same (heme IV propionate P_{13}). To evaluate the effect of the quinol interaction on the heme redox properties at physiological pH, the oxidation curves of each heme and the molar fractions of each microstate were computed from the thermodynamic parameters listed in Table 3.4 and are represented in Fig 3.22. From the analysis of the individual heme oxidation curves, the e_{app} values of heme IV slightly decrease in the presence of the quinol and its oxidation occurs at earlier oxidation stages compared to that of heme III. Consequently, the positive redox interaction between hemes IV and III has a larger contribution in the midpoint reduction potential of the latter, which increases proportionally the heme IV oxidation fraction.

Thus, the last step of oxidation is even more dominated by the oxidation of heme III and the order of oxidation of the hemes is thus I–IV–III (see upper panels in Fig 3.22). As discussed above, this order of oxidation of the hemes is crucial to establish the preferred e^-/H^+ transfer pathway, which is a key feature of the PpcA functional mechanism [40-42].

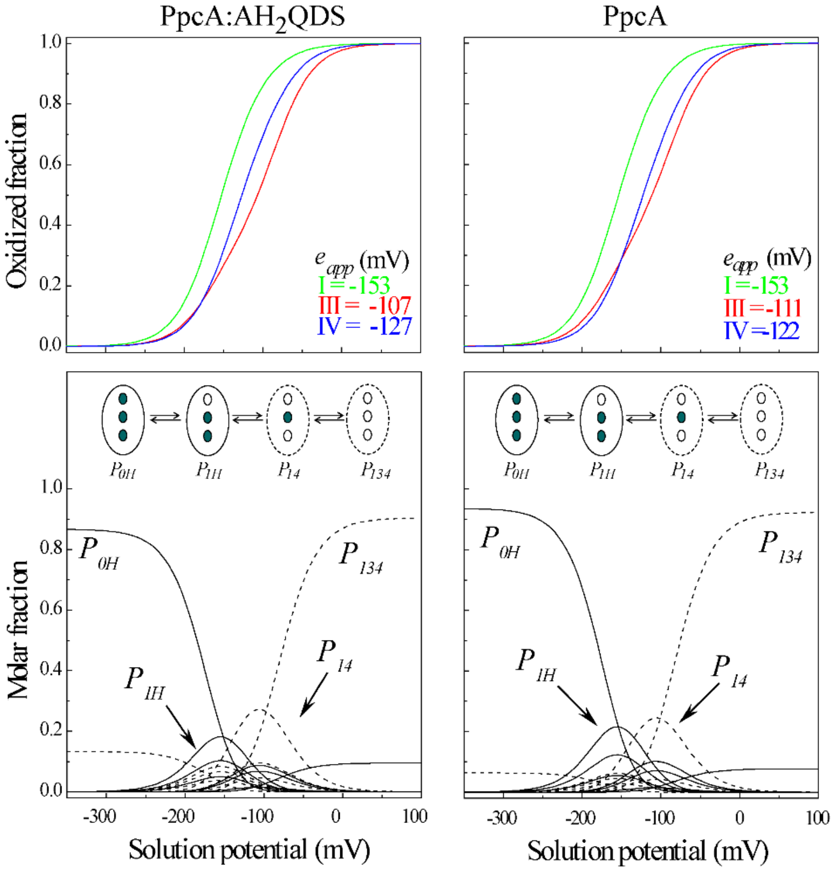

Fig 3.22 Oxidized fractions of the individual hemes (upper panels) and molar fractions of the 16 individual microstates (lower panels) for PpcA in the presence (left panels) and absence (right panels) of quinol at pH 7.5. The curves were calculated as a function of the solution reduction potential using the parameters listed in Table 3.4. In the upper panels, the heme e_{app} values (heme I - green; heme III - red; and heme IV - blue) are indicated. In the lower panels, solid and dashed lines indicate the protonated and deprotonated microstates, respectively. For clarity, only the relevant microstates in each oxidation stage are labeled. The inset shows the functional pathway for electron uptake and release coupled with protonation in PpcA. The solid lines indicate the protonated microstates. The dashed lines indicate the deprotonated microstates. Inner circles represent heme groups, which can be either reduced or oxidized and are colored blue or white, respectively. The dominant microstates in each oxidation stages are labeled. P_{0H} represents the reduced protonated microstate. P_{ijkH} and P_{ijk}, indicate respectively the protonated and deprotonated microstates, where i, j, and k represent the heme(s) that are oxidized in that particular microstate.

Therefore, to evaluate the effect of the presence of the quinol on the PpcA functional mechanism, the relative contribution of each of the 16 possible microstates was determined as a function of the solution potential (Fig 3.22 lower panels). Such study was previously undertaken for the free protein and a coherent electron transfer pathway coupled to proton transfer was identified [37]. The results obtained in the presence of the quinol showed that despite the changes observed in the heme oxidation profiles that are reflected in the higher contribution of the microstate P_{14} (see below), the protein is still able to perform a concerted e$^-$/H$^+$ transfer between oxidation stages 1 and 2. In fact, the oxidation stage 0 is dominated by the fully reduced and protonated microstate P_{0H} and stage 1 is dominated by the oxidation of heme I (P_{1H}) while keeping the redox-Bohr center protonated. Oxidation stage 2 is dominated by the oxidation of hemes I and IV and deprotonation of the acid–base center (P_{14}), that remains deprotonated in stage 3 upon full oxidation of heme III (P_{134}). Therefore, a route is defined for electron transfer in PpcA:quinol complex: $P_{0H} \leftrightarrow P_{1H} \leftrightarrow P_{14} \leftrightarrow P_{134}$ (same as in PpcA in the absence of the ligand [37, 38]) and the cytochrome retains the essential features of its functional mechanism.

In the previous section, it was shown that the heme IV region is involved in the complex formation between the PpcA and the quinol. Therefore, the reduction potential value of heme IV (−127 mV) determined in the presence of the quinol thermodynamically favors the reduction of the former and agrees with the UV-visible and stopped-flow kinetic experiments that showed that electron transfer proceeds in both directions at a similar rate but its extent is thermodynamically controlled, favoring the reduction of the cytochrome by the AH_2QDS.

3.1.4 Interaction studies between AQDS and PpcB, PpcD and PpcE cytochromes

Overall the results obtained for the detailed interactions studies between the HS analogue and PpcA in the oxidized and reduced states indicate that the protein interface region is the same in both redox states. Therefore, for the other PpcA-family members the interaction studies with HS analogue was carried out exclusively in the oxidized state. The dispersion of the protein signals in the oxidized state as a consequence of the heme unpaired electrons, as well as the experimental setup, does facilitate the study of the molecular interactions with HS analogue in this redox state. As for PpcA, the molecular interactions between the triheme cytochromes PpcB, PpcD and PpcE from *G. sulfurreducens* and AQDS were investigated by NMR spectroscopy using 2D ^{1}H,^{15}N HSQC NMR spectra. In order to assist this study, the backbone and side chain assignment of PpcB, PpcD and PpcE was firstly obtained as described in section 3.1.4.1.

3.1.4.1 Backbone and side chain assignment of PpcB, PpcD and PpcE cytochromes

2D ^{1}H,^{15}N HSQC and the series of 3D NMR experiments (3D CBCANH, 3D CBCA(CO)NH, 3D HNCA, 3D HN(CO)CA) were acquired for PpcB, PpcD and PpcE in oxidized state at different pH values to assure fully protonation of the redox-Bohr center (Fig A.1, Appendix). The assignment of the backbone resonances followed the same methodology described for PpcA (section 3.3.1.2) and is indicated in Tables A.1-3 (Appendix). The percentage of the assignment obtained is shown in Table A.4 (Appendix). These assignments were reassigned at pH 7 to probe the interaction between PpcB, PpcD and PpcE with the HS analogue (Fig 3.23). The NH signals of PpcB (except for residues Ala^1, Asp^2, Gly^{42} and Cys^{51}), PpcD (except for residues His^1, Asp^2 and Gly^{38}) and PpcE (except for residues Ala^1, Asp^2, Gly^{42} and Thr^{62}) are indicated in Fig 3.23. The backbone NH signals at the first N-terminal residues are usually not observable due to fast exchange with the solvent. The backbone NH signals of PpcB (Gly^{42} and Cys^{51}), PpcD (Gly^{38}) and PpcE (Gly^{42} and Thr^{62}) were not observed, most probably due to signal broadening caused by the nearby paramagnetic irons of heme groups, since they were also not detected at lower pH.

3.1.4.2 NMR chemical shift perturbation experiments

The effect of the addition of increasing amounts of AQDS on the backbone NH signals of the three cytochromes were monitored by recording a series of 2D ^{1}H,^{15}N HSQC NMR spectra (Fig 3.23). The inset in each NMR spectrum shows the combined chemical shift changes averaged for each NH signal.

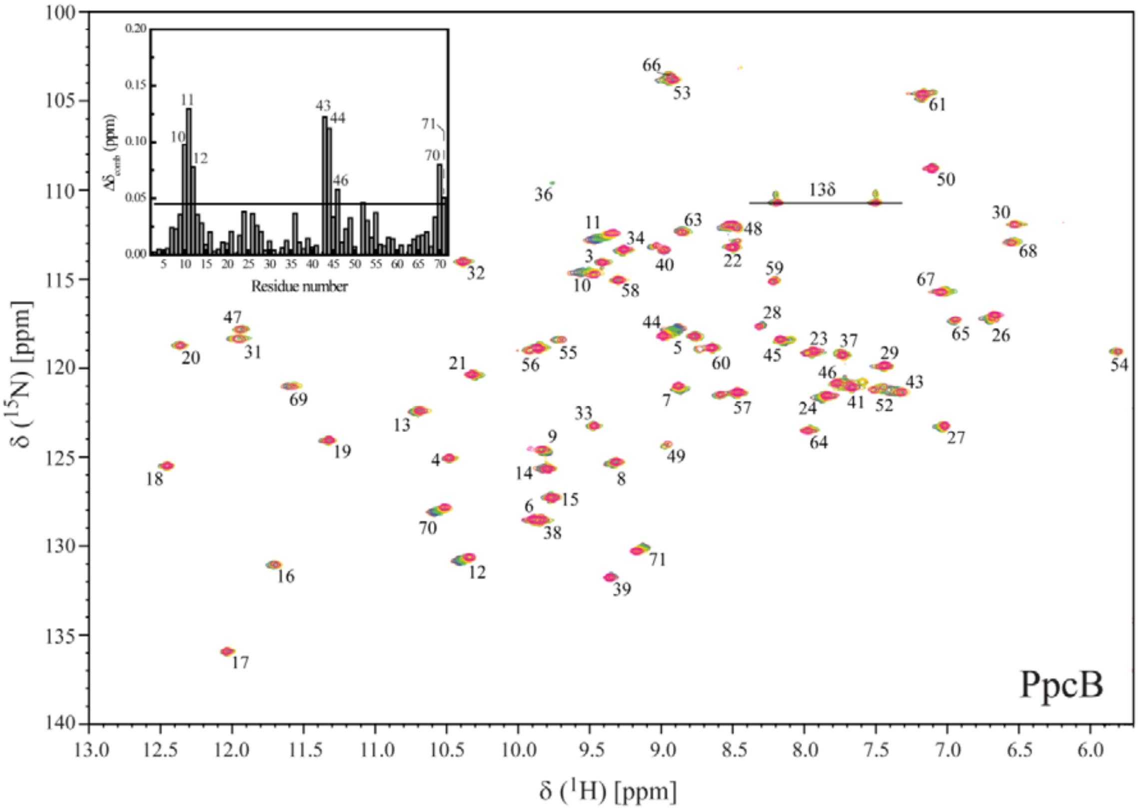

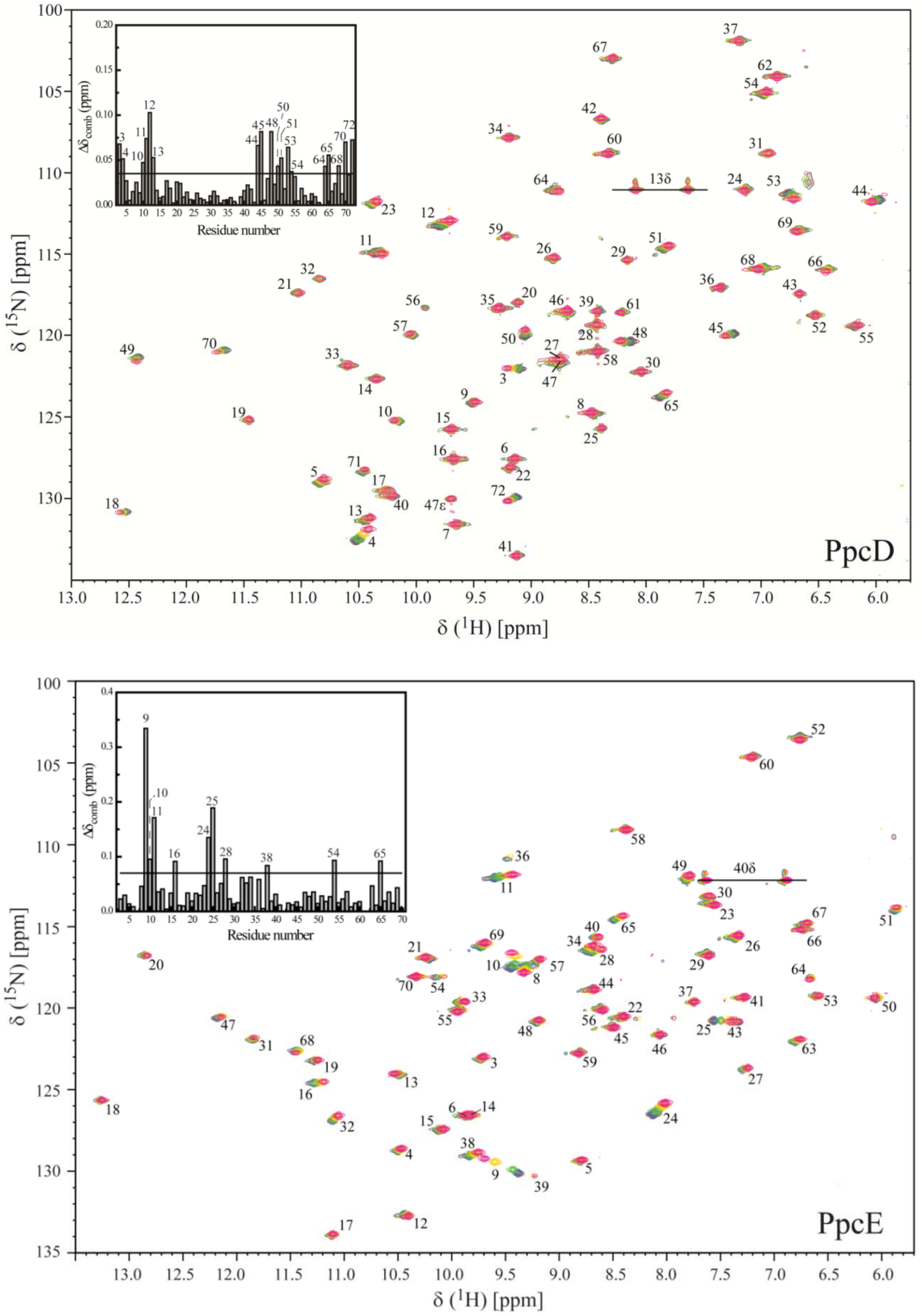

Fig 3.23 Overlay of the 2D ^1H,^{15}N HSQC NMR spectra of ^{13}C,^{15}N-enriched PpcB, PpcD and PpcE (0.8 mM) in the presence of increasing amounts of AQDS, at 298K. The contours of the signals in the reference spectrum are shown in orange while in the spectral overlay, the concentration of AQDS increases from blue to pink contours. The assignments of NH signals are indicated. Samples were prepared in 45 mM sodium phosphate buffer pH 7 with 100 mM final ionic strength. The insets show the plot of the combined chemical shift changes determined from the directly observed ^1H and ^{15}N chemical shifts, in accordance with Eq. 3.1. The horizontal line in the inset was determined with the standard deviation to zero value, σ_0^{corr} (see section 3.3.1.3).

The NH signals showing the highest chemical shift perturbation are listed in Table 3.5. In the case of PpcB protein, the NH signals showing highest chemical shift perturbation are those in the polypeptide segment Asn^{10} to Asn^{12}, Lys^{43}, Glu^{44}, Ala^{46}, Lys^{70}, and Lys^{71}, all residues located near heme IV. For PpcD protein, the NH signals showing highest chemical shift perturbation are those in the polypeptide segment Lys^{10} to Asn^{13}, Gly^{44}, Lys^{45}, Ala^{48}, Lys^{50}, Thr^{51}, Thr^{53}, Gly^{54}, Thr^{64}, Lys^{65}, Glu^{68}, His^{70} and Lys^{72}, all residues located near heme IV, except for Lys^{3} and Val^{4} located in the N-terminal and near heme I. On the other hand, in the case of PpcE protein, the NH signals showing highest chemical shift perturbation are in two distinct regions, one near heme IV including those in the polypeptide segment Lys^{9} to Gly^{11} and Lys^{65}, and the other near heme I including Thr^{16}, Val^{24}, Arg^{25}, Arg^{28}, Ile^{38} and His^{54}.

Table 3.5 Most affected NH signals in PpcB, PpcD and PpcE in the presence of AQDS (see Fig 3.23).

Cytochrome	Polypeptide backbone NH signals
PpcB	Asn^{10}, Gly^{11}, Asn^{12}, Lys^{43}, Glu^{44}, Ala^{46}, Lys^{70}, Lys^{71}
PpcD	Lys^{3}, Val^{4}, Lys^{10}, Asn^{11}, Gly^{12}, Asn^{13}, Gly^{44}, Lys^{45}, Ala^{48}, Lys^{50}, Thr^{51}, Thr^{53}, Gly^{54}, Thr^{64}, Lys^{65}, Glu^{68}, His^{70}, Lys^{72}
PpcE	Lys^{9}, Asn^{10}, Gly^{11}, Thr^{16}, Val^{24}, Arg^{25}, Arg^{28}, Ile^{38}, His^{54}, Lys^{65}

The residues showing the highest chemical shift perturbations caused by the AQDS are highlighted on the three-dimensional structure of each cytochrome (Fig 3.24).

Analysis of the chemical shift perturbation as a function of AQDS concentration for the most affected residues yielded hyperbolic binding curves which were fitted to a 1:1 model considering fast exchange conditions (Fig 3.25).

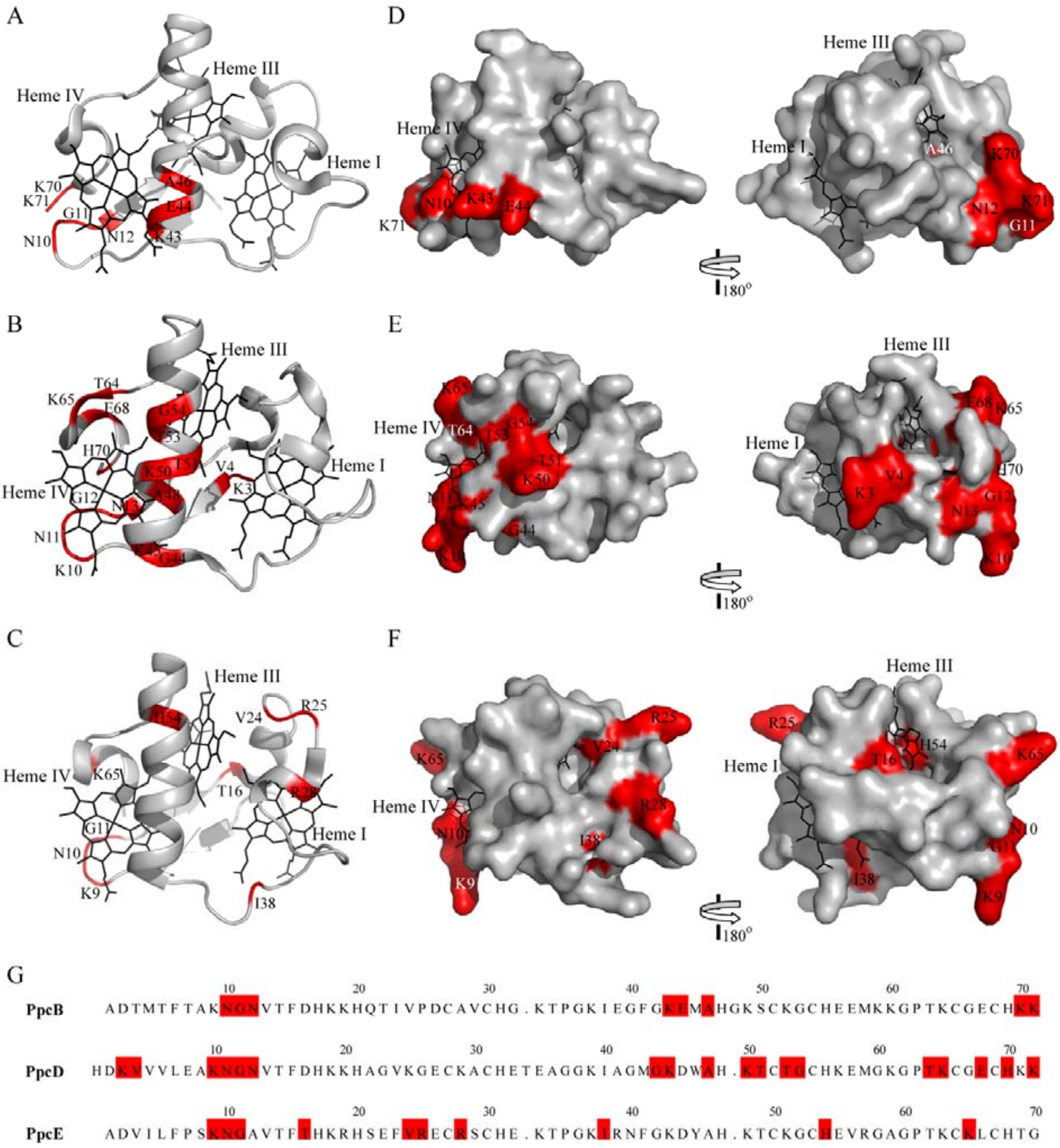

Fig 3.24 Chemical-shift perturbation map of PpcB, PpcD and PpcE in the presence of AQDS. The structural (panels A-C) and the molecular surface (panels D-F) maps were generated in PyMOL [28] using the structures of PpcB (PDB ID, 3BXU [39]) PpcD (PDB ID, 3H4N [43]) and PpcE (PDB ID, 3H34 [43]). The residues whose NH signals showed the weighted NMR chemical shift differences larger than the mean values are represented in red. In representation, the hemes are shown in black. The left and right molecular surfaces in panels (D-F) are related by a 180° rotation. The amino acid sequence alignment for the three cytochromes is shown in panel G using the same color code. The residues are numbered sequentially from the amino terminus to carboxyl terminus and could be different from that in the PDB deposited structures.

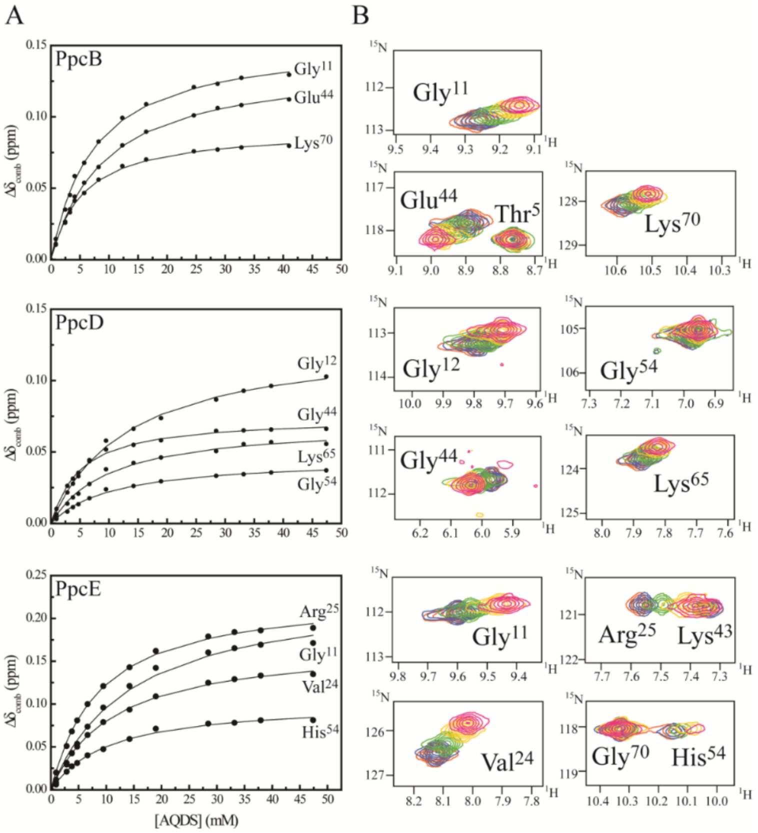

Fig 3.25 Binding isotherms for PpcB, PpcD and PpcE redox complex with AQDS (left panels) and selected regions from overlaid 2D ^{1}H,^{15}N HSQC NMR spectra (right panels). In the left panels, the labels indicate the NH signals that were monitored in the chemical shift perturbation experiments. For clarity one signal of each affected polypeptide region in each cytochrome is shown. Each data set was fit to a 1:1 binding model considering fast exchange conditions (solid lines). An average K_d value was calculated as 6 ± 2 mM; 8 ± 4 mM and 12 ± 6 mM from the titration curves for PpcB, PpcD and PpcE, respectively. In the expansion of each NMR spectrum (right panels) the amount of AQDS increases from blue to pink contours.

A dissociation constant (K_d) value was determined for NH signals showing the highest chemical shift perturbation (Table 3.6). In each protein, a small set of residues showed distinct and higher K_d values, compared to those located in the close vicinity to the heme groups, probably reflecting propagation of perturbations from the binding surfaces or local conformational changes rather than direct binding (Lys^{71} for PpcB; Lys^{10}, Thr^{51}, Glu^{68}, His^{70} and Lys^{72} for PpcD and Lys^{9} and Ile^{38} for PpcE). The average K_d values obtained, excluding the above set of residues, are of the same order of magnitude for all cytochromes (PpcB, 6 ± 2 mM; PpcD, 8 ± 4 mM and PpcE, 12 ± 6 mM) indicating that the proteins bind to AQDS with similar affinity. The K_d values obtained from the fitting of the ligand-induced chemical shift perturbation curves are in the milimolar range, suggesting the formation of a low affinity complex and are consistent with previously reported values for PpcA. Interestingly, the K_d values in all three cytochromes are similar to those previously determined for PpcA:AQDS complex (18 ± 5 mM), which provides a common functional pattern to these cytochromes showing that the low-binding affinity complex and the specific interaction in the proximity of hemes warrant a rapid and selective electron transfer to the quinone [18, 26, 27].

Table 3.6 Equilibrium dissociation constants (*K*$_d$) values calculated from the NH signals of PpcA, PpcB, PpcD and PpcE showing the highest chemical shift perturbation in presence of AQDS (298 K, pH 7 and 100 mM final ionic strength). The chemical shift difference between the free form and the complex form ($\Delta\delta_{max}$) are also indicated.

Protein	Residue	K_d (mM)	$\Delta\delta_{max}$ (ppm)
PpcA	Asn^{10}	14.3 ± 0.7	0.1
	Gly^{11}	25.6 ± 1.1	0.2
	Asp^{12}	21.6 ± 1.1	0.1
	Val^{13}	19.2 ± 0.5	0.1
	Cys^{27}	38.1 ± 0.4	0.3
	lys^{43}	13.5 ± 0.5	0.1
	Glu^{44}	27.4 ± 1.6	0.2
	Ala^{46}	12.3 ± 0.7	0.1
	Lys^{52}	6.3 ± 0.4	0.1
	Cys^{65}	84.4 ± 0.1	0.2
	Lys^{70}	21.9 ± 1.0	0.2
PpcB	Asn^{10}	3.5 ± 0.1	0.1
	Gly^{11}	6.8 ± 0.1	0.2
	Asn^{12}	6.2 ± 0.1	0.1
	Lys^{43}	5.3 ± 0.1	0.1
	Glu^{44}	8.6 ± 0.1	0.1
	Ala^{46}	5.4 ± 0.2	0.1
	Lys^{70}	5.0 ± 0.1	0.1
	Lys^{71}	20.2 ± 0.4	0.1
PpcD	Lys^{3}	96.5 ± 14.3	0.2
	Val^{4}	81.0 ± 8.0	0.1
	Lys^{10}	67.2 ± 4.7	0.1
	Asn^{11}	4.6 ± 0.2	0.1
	Gly^{12}	12.7 ± 0.3	0.1
	Asn^{13}	13.9 ± 0.4	0.1
	Gly^{44}	4.5 ± 0.1	0.1
	Lys^{45}	4.7 ± 0.1	0.1
	Ala^{48}	4.0 ± 0.1	0.1
	Lys^{50}	10.9 ± 0.2	0.1
	Thr^{51}	21.8 ± 0.8	0.1
	Thr^{53}	6.2 ± 0.1	0.1
	Gly^{54}	10.0 ± 0.3	0.1
	Thr^{64}	7.2 ± 0.3	0.1
	Lys^{65}	9.4 ± 0.3	0.1
	Glu^{68}	68.5 ± 7.5	0.1
	His^{70}	22.5 ± 1.7	0.1
	Lys^{72}	20.7 ± 0.8	0.1
PpcE	Lys^{9}	32.1 ± 3.2	0.6
	Asn^{10}	6.3 ± 0.2	0.1
	Gly^{11}	11.5 ± 0.4	0.2
	Thr^{16}	18.3 ± 0.7	0.1
	Val^{24}	9.0 ± 0.1	0.2
	Arg^{25}	6.8 ± 0.1	0.2
	Arg^{28}	18.6 ± 0.8	0.1
	Ile^{38}	31.9 ± 2.3	0.2
	His^{54}	8.2 ± 0.2	0.1
	Lys^{65}	17.5 ± 0.9	0.1

As shown by the stopped-flow kinetics measurements, the three cytochromes can be fully reduced in presence of AH_2QDS. However, the three hemes in each protein can provide distinct entry gates for the electrons. Thus, it is expected that the electron donor and at least one of the heme groups in each cytochrome are near, suggesting an effective electron transfer within the complex. Therefore, the NMR signals of heme substituents, which were previously assigned [44] are expected to be perturbed by the binding of the electron donor. Among all the heme substituents, the heme methyl groups are the best probes, since their signals are typically found in less crowded regions of the NMR spectra. Thus, we also investigated the effect of the AQDS addition on the heme methyl NMR signals of each protein by acquiring a series of 2D $^1H,^{13}C$ HMQC (heteronuclear multiple quantum coherence) spectra (Fig 3.26).

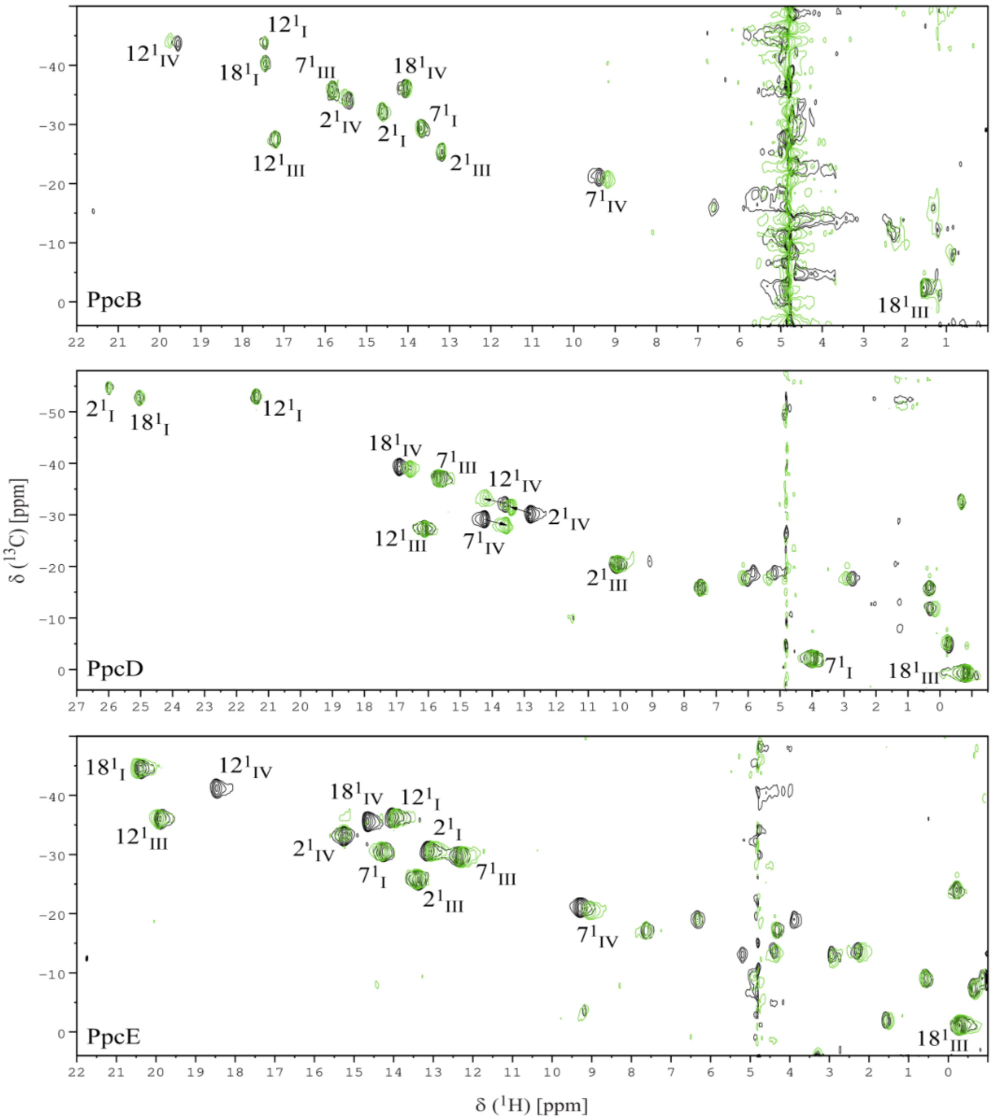

Fig 3.26 Selected regions of 2D $^1H,^{13}C$ HMQC of PpcB, PpcD and PpcE in the absence (black) and presence (green) of AQDS, at 298 K. The heme methyls of each cytochrome are labeled. Samples were prepared in 45 mM sodium phosphate buffer pH 7 with 100 mM final ionic strength.

The analysis of the chemical shift perturbation experiments clearly showed that the signals of heme IV methyls are the most affected in all the cytochromes (Fig 3.27). However, in the case of PpcE the chemical shift perturbations resulting from the addition of AQDS were not restricted to heme IV methyls and non-negligible effects were also observed for heme I methyl signals, and less pronounced effects on those of heme III (Fig 3.27). The increasing chemical shift perturbations, as a function of AQDS concentration, indicated that the free and bound forms of each cytochrome are in fast exchange on the NMR time scale. Though, for PpcE, broadening of heme IV NMR signals was observed suggesting an intermediate binding exchange regime for this cytochrome (Fig 3.26).

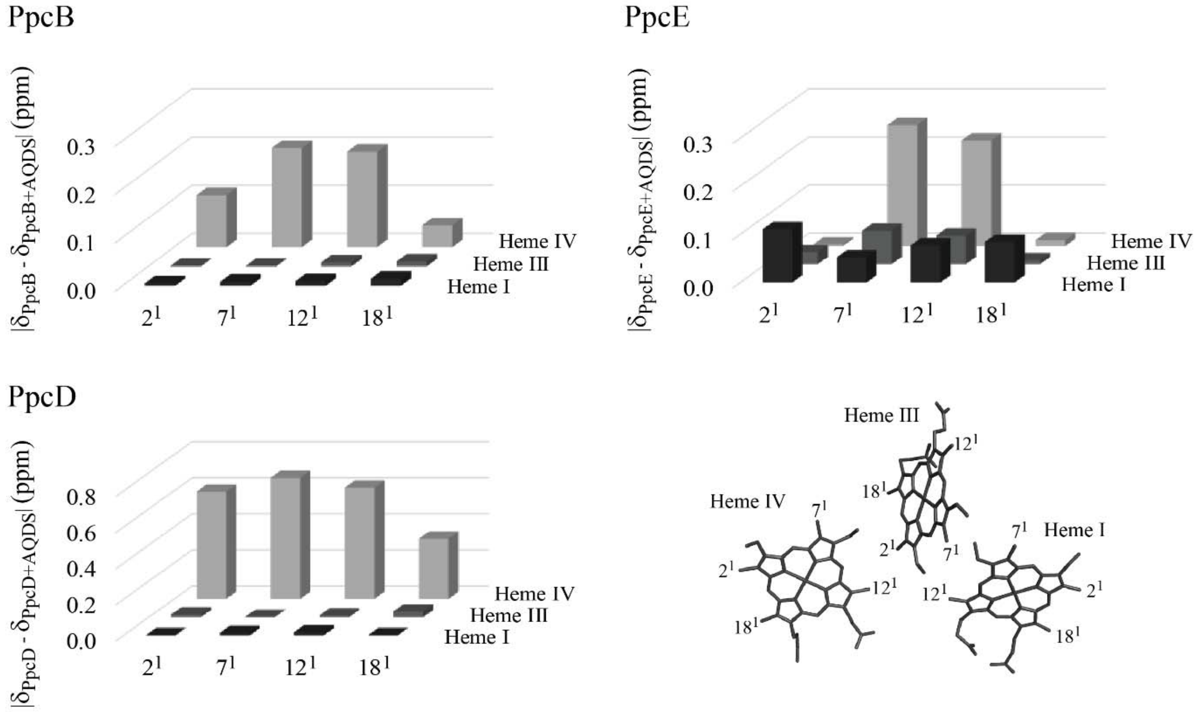

Fig 3.27 Variation of the ^{1}H chemical shift of the heme methyls of PpcB, PpcD and PpcE. The shifts were taken from spectra acquired in the absence ($\delta_{PpcB/D/E}$) and in the presence of AQDS ($\delta_{PpcB/D/E + AQDS}$). The bars represent the ^{1}H chemical shift variations of the heme methyl labeled accordingly to the IUPAC nomenclature for tetrapyrroles [29].

Analysis of the PpcA-E amino acid sequences and structures indicates that the region surrounding heme IV is the most conserved in this family [33]. Moreover, as previously reported, the analysis of the charged residues distribution in these proteins showed that the electrostatic surfaces are different, but had a positively charged surface near heme IV. Indeed, in the case of PpcA, PpcB, PpcD and PpcE 16, 13, 14 and 7 positively charged residues are close to heme IV, respectively and, on the other hand, 6, 4, 4 and 7 are in the heme I region, respectively. Interestingly, PpcE is the only member of PpcA-family with the positively charged residues equally distributed in the two affected regions.

As observed in Fig 3.10 (section 3.1.2.) for the experiments with PpcA in the presence of AQDS, the broadness and displacement is also observed in the AQDS signals in the presence of the cytochromes PpcB, PpcD and PpcE confirming the existence of a molecular interaction between these proteins and the quinone (Fig 3.28).

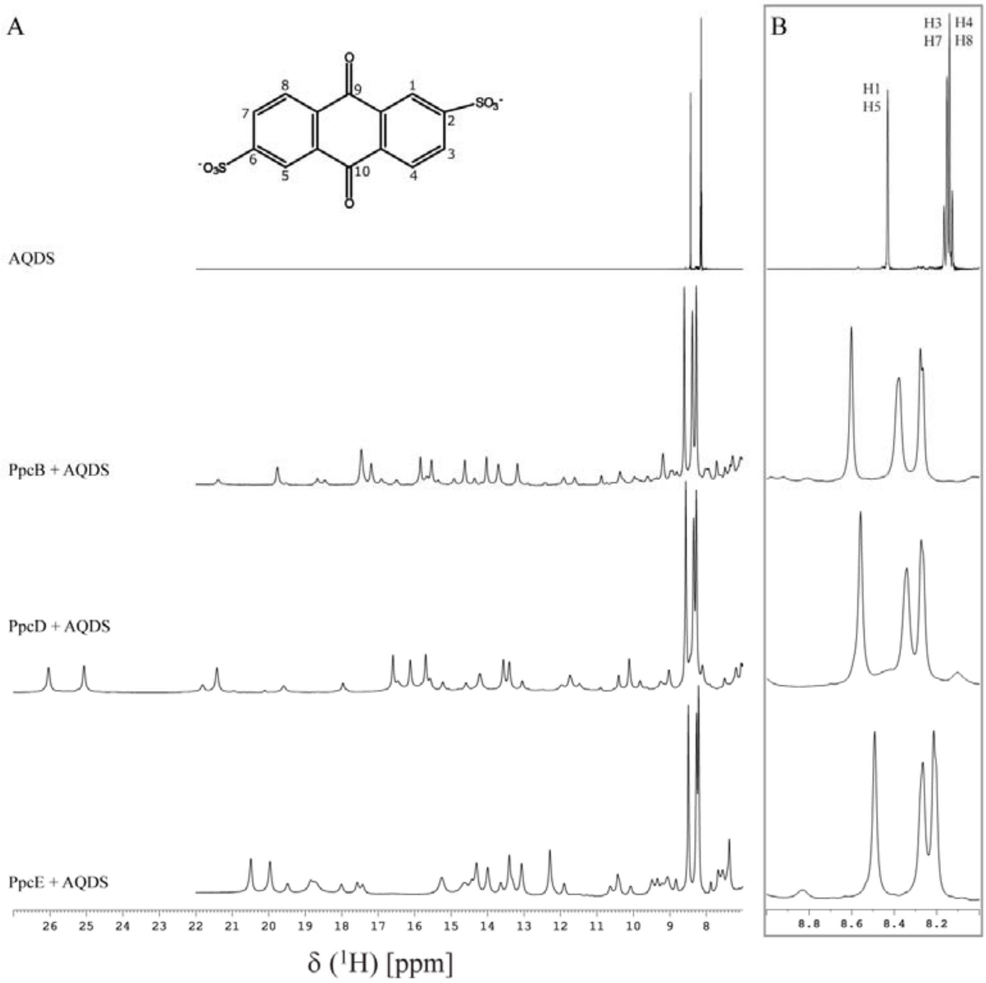

Fig 3.28 ^{1}H chemical shift changes of the AQDS signals in presence of PpcB, PpcD and PpcE, at 298 K. (A) 1D ^{1}H NMR spectral features of free AQDS (upper spectrum) and AQDS in the presence of cytochromes PpcB, PpcD and PpcE. (B) Expansion of the spectral region containing the proton signals of AQDS. Samples were prepared in 45 mM sodium phosphate buffer pH 7 with 100 mM final ionic strength.

3.1.4.3 Molecular docking calculations

The docking site predictions for PpcB with HADDOCK revealed a high score cluster of structures in which AQDS was centered near the edge of heme IV. The best docking model showed one AQDS sulfonate forming hydrogen bonds with side chain NZ atom of Lys^{71} (referred to the X-ray numbering, see Fig 3.29) whereas the other sulfonate forms a hydrogen bond with the side chain NZ atom of Lys^{43}. The aromatic core of AQDS formed van der Waals contacts with the well-exposed $2^{1}CH_3$ and $18^{1}CH_3$ methyl groups of heme IV (Fig 3.29A).

Similarly, to PpcB the docking site predictions for PpcD showed that AQDS was located near heme IV in the high score cluster of structures. The best docking model indicates that one AQDS sulfonate forms a hydrogen bond with NZ atom of Lys^{43} and NH atom of Lys^{48}, while the other sulfonate was seen forming hydrogen bonds with NZ atoms of Lys^{64} (Fig 3.29A). In addition, NH atom of Gly^{53} was located within 3.8Å from one of the quinone core oxygen atoms.

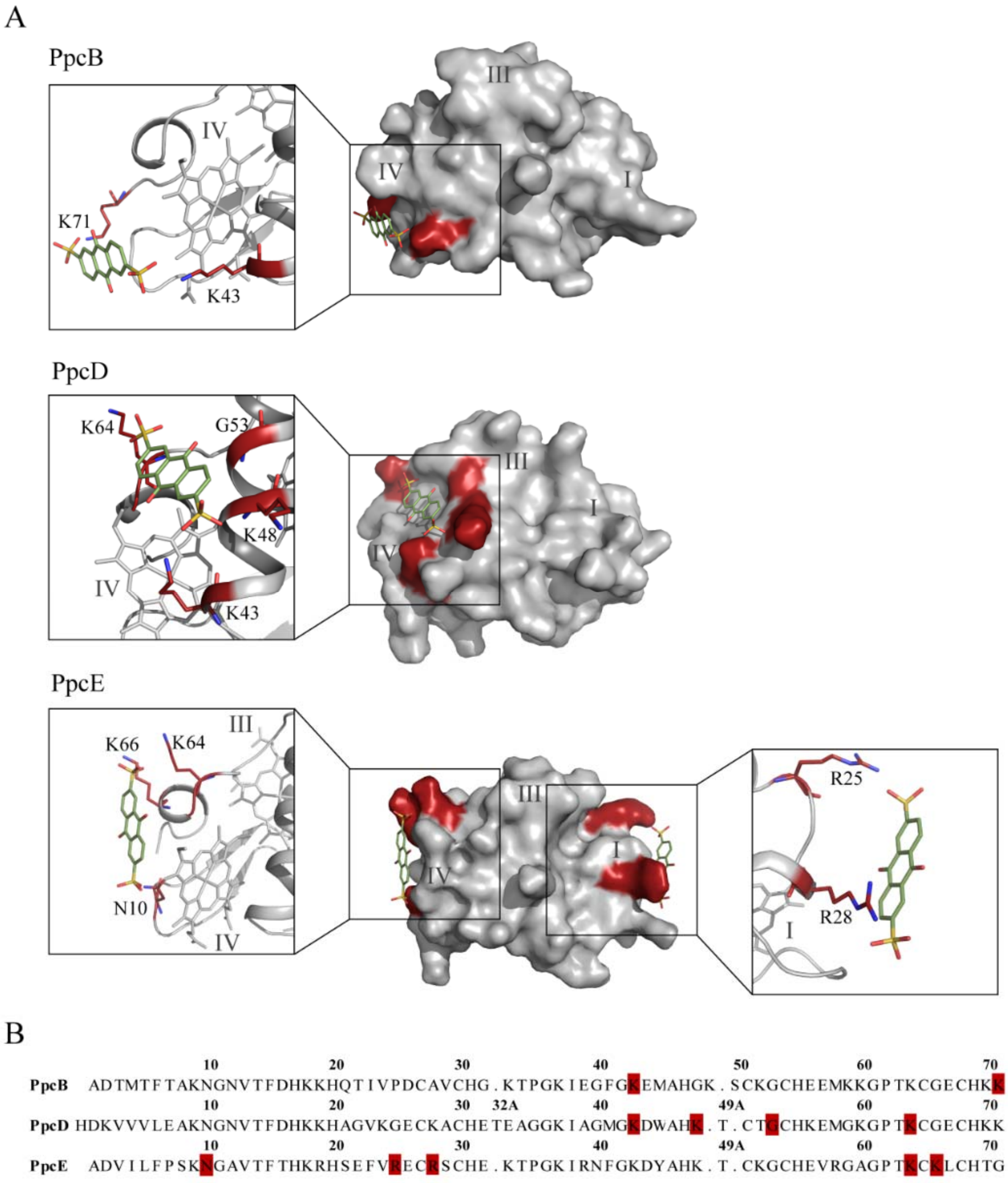

```
                10                  20                  30                      40                   50                  60                  70
PpcB   ADTMTFTAKNGNVTFDHKKHQTIVPDCAVCHG.KTPGKIEGFGKEMAHGK.SCKGCHEEMKKGPTKCGECHKK
                10                  20                  30   32A                40                   49A                 60                  70
PpcD HDKVVVLEAKNGNVTFDHKKHAGVKGECKACHETEAGGKIAGMGKDWAHK.T.CTGCHKEMGKGPTKCGECHKK
                10                  20                  30                      40                   49A                 60                  70
PpcE   ADVILFPSKNGAVTFTHKRHSEFVRECRSCHE.KTPGKIRNFGKDYAHK.T.CKGCHEVRGAGPTKCKLCHTG
```

Fig 3.29 Docked complexes between PpcB, PpcD and PpcE and AQDS calculated with HADDOCK 2.2 webserver. (A) Best docking models obtained for each cytochrome and AQDS. The structural and the molecular surface maps were generated in PyMOL [28] using the structures of PpcB (PDB ID, 3BXU [39]) PpcD (PDB ID, 3H4N [43]) and PpcE (PDB ID, 3H34 [43]). A close-up view of the best docking models. The hemes and protein residues are shown as sticks in atom type colors, whereas AQDS is shown in the following colors: carbon, green; oxygen, red and sulfur, yellow. Part of the protein is shown as Cα cartoon in grey. (B) The amino acid sequence alignment for the three cytochromes, numbered according to the structural alignment reported earlier [43].

Finally, for PpcE, the locations of residues with significant NMR chemical shift perturbations cover two distinct protein surface area with residues located both near hemes I and IV (Fig 3.24). This observation suggests the presence of two independent ligand binding sites on the PpcE surface, which was confirmed by the docking calculations. Docking calculations for PpcE were performed in separate for each set of residues and the highest scoring cluster of structures positioned the AQDS molecule near hemes I and IV (Fig 3.29A). The best docking model for residues placed near heme I indicate that two AQDS sulfonates form hydrogen bonds with Arg^{25} and Arg^{28} side chains, respectively (Fig 3.29A). On the other hand, the best docking model for residues placed near heme IV shows one of the sulfonate groups forms hydrogen bonds to NZ atoms of Lys^{64}, Lys^{66} (Fig 3.29A). The other sulfonate forms hydrogen bonds with the side chain atoms of Asn^{10} and is near the well-exposed 2^1CH_3 (2.3 Å) and 18^1CH_3 (4.7 Å) methyl groups of heme IV.

3.2 Conclusions

In this work, the extent of the electron transfer between the HS analogue, anthraquinone disulfonate, and four triheme cytochromes from the PpcA-family (PpcA, PpcB, PpcD and PpcE) at physiological pH was studied by stopped-flow kinetics. The electron transfer is under thermodynamic control favoring the reduction of the four cytochromes. The extent of reduction of each cytochrome correlates with their apparent macroscopic midpoint reduction potential (-117 mV for PpcA; -137 mV for PpcB; -132 mV – for PpcD; and -134 mV for PpcE).

Using NMR chemical shift perturbation experiments we also showed that the proteins establish a low affinity and reversible complex with AQDS, which is a typical feature in electron transfer reactions between redox partners. The NMR studies allowed to map the interface regions in redox-complex between AQDS and each cytochrome. The results obtained showed that the binding of the quinone is not random but instead defined by patches containing positively charged residues close to heme IV in all cytochromes, and in addition close to heme I in the case of PpcE. The common structural and functional features of the redox complexes established between a family of periplasmic triheme cytochromes and AQDS provides a model for the molecular interaction between OM multiheme cytochromes, such as OmcB, OmcE, OmcS, OmcT or OmcZ, that could directly interact with the humic substance analog at the cell surface. In summary, the present study revealed fundamental and crucial structural and functional features on the nature of the complex established between multiheme cytochromes and the HS analogue, which could pave the way to engineer microorganisms with optimal desirable properties toward this form of respiration.

3.3 Materials and methods

3.3.1 NMR studies

The NMR assignment of backbone and side chain was previously determined for PpcA, in both redox states [11-13]. In this Thesis, the assignment of the backbone signals was obtained for PpcB, PpcD and PpcE in the oxidized state. NMR spectroscopy was also used to probe protein-ligand interactions, between PpcA-family and HS analogue.

3.3.1.1 NMR samples preparation and experiments

For the NMR assignment of backbone, protein samples (1-2 mM) were prepared in 92%H_2O/ 8%^2H_2O. For PpcB, PpcD and PpcE samples were prepared in 45 mM sodium phosphate buffer with 100 mM NaCl, at pH 5.5, 5.9 and 6.5, respectively. For the protein-ligand interaction studies, samples of PpcA-E cytochromes (~0.5 mM) were prepared in phosphate buffer pH 7.1 with NaCl (100 mM final ionic strength) in 92%H_2O/8%^2H_2O (labeled sample) or ^2H_2O (unlabeled sample). For NMR redox titrations, protein samples (70 μM) were prepared in 80 mM phosphate buffer with 250 mM in 99% ^2H_2O and reduced as described previously [37, 39]. Briefly, the NMR tubes were sealed with a gas-tight serum cap and the air was flushed out from the sample. The samples were reduced directly in the NMR tube with gaseous hydrogen in the presence of catalytic amounts of hydrogenase from *Desulfovibrio vulgaris* (Hildenborough). Partially oxidized samples were obtained by first removing the hydrogen from the reduced sample with nitrogen and then adding controlled amounts of air into the NMR tube [37, 39].

All NMR experiments were acquired in a Bruker Avance III 600 spectrometer with a triple-resonance cryoprobe (TCI). ^1H chemical shifts are reported in parts per million (ppm) calibrated using the water signal as internal reference and the ^{15}N and ^{13}C chemical shifts calibrated through indirect referencing [45]. Before and after all 2D and 3D experiments, 1D ^1H NMR spectra were acquired to verify the protein integrity. The pH of the samples was measured before and after each set of NMR experiments to confirm that pH of the solution is maintained. Spectra were processed using TOPSPIN software (Bruker Biospin, Karlsruhe, Germany) and analyzed with program Sparky (T. D. Goddard and D. G. Kneller, SPARKY 3, University of California, San Francisco).

NMR acquisition parameters and experiments acquired for the backbone assignment of PpcB, PpcD and PpcE proteins are summarized in Table 3.7.

Table 3.7 NMR experiments and acquisition details for the PpcB, PpcD, PpcE backbone resonance assignment in the oxidized state. The NMR experiments acquired in Bruker Avance III 600 spectrometer are indicated. ‘ns’ stands for the number of scans.

Protein	NMR experiments	Complex points			Spectral width (Hz)			Frequency offset (Hz)			ns
		^{1}H	^{15}N	^{13}C	^{1}H	^{15}N	^{13}C	^{1}H	^{15}N	^{13}C	
PpcB	2D ^{1}H,^{15}N HSQC	2048	256	-	9615	2554	-	2819	7236	-	8
	2D ^{1}H,^{13}C HSQC	2048	-	256	24038	-	22636	2819	-	6036	4
	3D HNCA	2048	40	128	9615	2554	9054	2819	7236	9658	8
	3D HN(CO)CA	2048	40	128	9615	2554	9054	2819	7236	9658	8
	3D CBCANH	2048	40	128	9615	2554	12073	2819	7236	7545	16
	3D CBCA(CO)NH	2048	40	128	9615	2554	12073	2819	7236	7545	16
PpcD	2D ^{1}H,^{15}N HSQC	2048	256	-	11433	2189	-	2842	7115	-	8
	2D ^{1}H,^{13}C HSQC	2048	-	256	18029	-	12676	2842	-	6338	8
	3D HNCA	2048	40	128	10822	2189	9357	2842	7115	9658	8
	3D HN(CO)CA	2048	40	128	10822	2189	9357	2842	7115	9658	16
	3D CBCANH	2048	40	128	10822	2189	12676	2842	7115	6338	24
	3D CBCA(CO)NH	2048	40	128	10822	2189	12676	2842	7115	6338	16
PpcE	2D ^{1}H,^{15}N HSQC	2048	256	-	11433	2189	-	2822	7176	-	8
	2D ^{1}H,^{13}C HSQC	2048	-	256	18029	-	12676	2822	-	7092	8
	3D HNCA	2048	40	128	11433	2189	9357	2822	7176	9658	24
	3D HN(CO)CA	2048	40	128	11433	2189	9357	2822	7176	9658	24
	3D CBCANH	2048	40	128	11433	2189	12676	2822	7176	7092	32
	3D CBCA(CO)NH	2048	40	128	11433	2189	12676	2822	7176	7092	32

The effect of humic substance analog on the chemical shifts of reduced PpcA and oxidized PpcA, PpcB, PpcD, PpcE amide signals were monitored by the analysis of a series of 2D ^{1}H, ^{15}N HSQC spectra in the presence of increasing amounts of AQDS or AH$_2$QDS. To measure the impact of the interaction also on the AQDS NMR signals, 1D ^{1}H NMR spectra of AQDS in the presence and absence of PpcA were acquired. Heme substituent signals of (i) reduced PpcA were observed in the presence of AQDS and, (ii) oxidized PpcA, PpcB, PpcD, PpcE were observed in the presence of AH$_2$QDS. For that the following set of experiments was acquired (i) 2D ^{1}H,^{1}H TOCSY (total correlation spectroscopy) with 45 ms and 2D ^{1}H,^{1}H NOESY with 80 ms, and (ii) 2D ^{1}H, ^{13}C HMQC, 2D ^{1}H,^{1}H TOCSY (45 ms) and 2D ^{1}H,^{1}H NOESY (80 ms). To investigate the binding reversibility between cytochromes and AQDS, 1D ^{1}H NMR spectra were acquired for the cytochromes in the absence of AQDS and after removal of this molecule by ultrafiltration methods (Amicon Ultra, 3 kDa). All 1D ^{1}H NMR spectra in the present study were acquired by collecting 16 K data points with at least 64 scans.

The oxidation patterns of the heme groups of PpcA in the presence of the HS analog were monitored by 2D ^{1}H, ^{1}H EXSY. NMR spectra were acquired in partially oxidized samples in the pH range of 6.0–9.0, to unambiguously map the oxidation of the individual hemes throughout the redox titrations. All the spectra were acquired at 15 °C with a mixing time of 25 ms, with 2048 (F$_2$) x 256 (F$_1$) data points for a sweep width of 24038 Hz with 256 scans per increment.

3.3.1.2 Protein backbone assignment

In the 2D $^{1}H,^{15}N$ HSQC NMR spectra, a single NH signal is observed for each amino acid, except for N-terminal and proline. The N-terminal amino proton is not observed due to very rapid exchange with the solvent. Additionally, the amide signals of the asparagine and glutamine side chains and the amine signals from arginine, lysine, histidine and tryptophan side chains can also be observed in this experiment. Overall, the 2D ^{1}H, ^{15}N HSQC spectrum should contain at least one signal for each residue in the protein and, consequently, this spectrum provides an excellent high-resolution NMR "*fingerprint"* of the protein. Diverse information can be obtained from the analysis of these spectra, namely the protein folding, aggregation, dynamic regions and stability. Moreover, any chemical shift exchange caused by temperature, pH and ionic strength variation, or the presence of other proteins or ligands, can be probed by the NH signals in these NMR spectra.

One of the strategies to assign the signals in the 2D $^{1}H,^{15}N$ HSQC spectra is based on the sequential assignment using ^{13}C, ^{15}N isotopically labeled proteins and a set of 3D experiments (HNCA, HN(CO)CA, CBCANH and CBCA(CO)NH) to attribute the backbone atom (N, HN, Cα and Cβ), as illustrated in Fig 3.30.

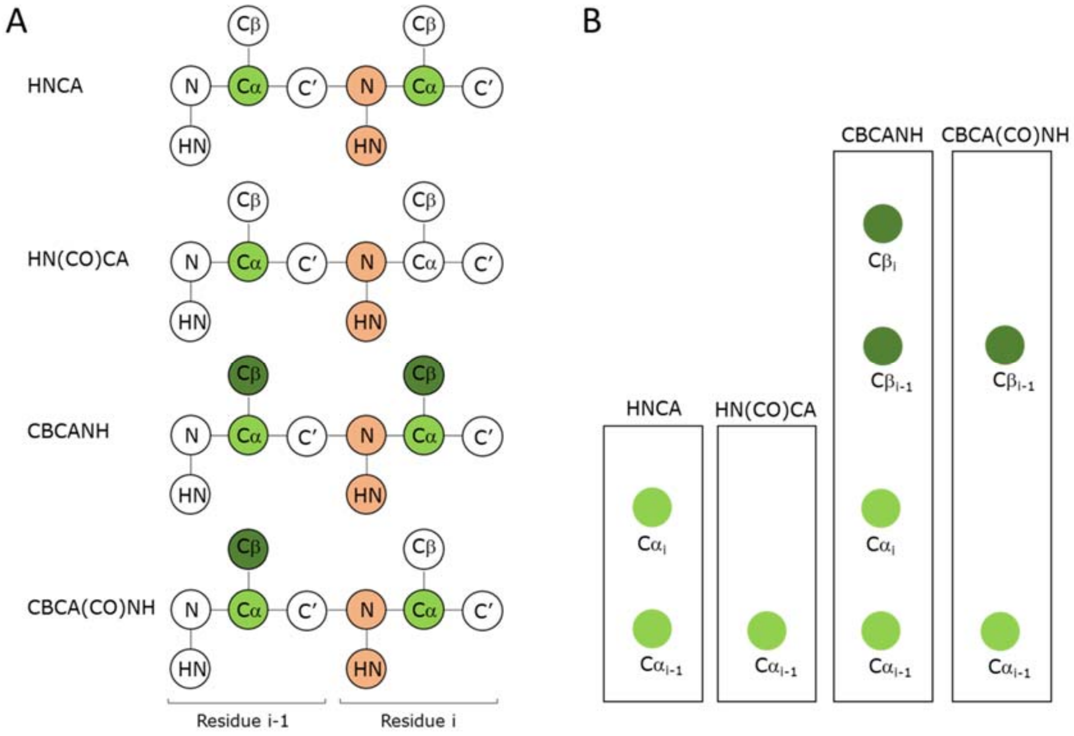

Fig 3.30 Strategy to specifically assign the backbone NH signals in 2D $^{1}H,^{15}N$ HSQC. (A) Correlations observed in 2D $^{1}H,^{15}N$ HSQC and 3D experiments HNCA, HN(CO)CA, CBCANH and CBCA(CO)NH and (B) backbone assignment strategy. A NH signal in 2D $^{1}H,^{15}N$ HSQC is selected (orange) and two Cα in HNCA are found (light green). After that, an identical Cα is found in HN(CO)CA, corresponding to the $C\alpha_{i-1}$. Then, an identical pair $C\alpha_{i}/C\alpha_{i-1}$ is identify in CBCANH and two Cβ are found (dark green). Lastly, an identical Cβ is found in CBCA(CO)NH, corresponding to the $C\beta_{i-1}$.

As described in Fig 3.30, a NH signal is selected in the 2D ^{1}H,^{15}N HSQC spectrum and the corresponding ^{1}H and ^{15}N chemical shifts represent a 2D NH plan. In the 3D experiments, this 2D NH plane is selected, and then, two pairs Cα/Cβ are identified, one is attributed to the residue (i) and the other to its antecessor (i-1). After that, the residue placed on the right of residue i (i+1), can be sequentially attributed, looking for a new 2D NH plan with one pair Cα/Cβ different ($C\alpha_{i+1}/C\beta_{i+1}$), and another pair Cα/Cβ identical to residue i ($C\alpha_i/C\beta_i$). The assignment of the protein backbone is obtained by repeating the strategy described.

3.3.1.3 Molecular interactions

To measure the impact of the interaction on NMR signals of a protein-ligand complex a series of 2D ^{1}H, ^{15}N HSQC were acquired and data was analyzed by a strategy proposed by Schumann and co-workers [46]. Briefly, the weighted average chemical shift ($\Delta\delta_{comb}$) of each backbone amide signal was calculated in accordance with Eq. 3.1.

$$\Delta\delta_{comb} = \sqrt{(\Delta\delta_H)^2 + (w_i\Delta\delta_i)^2} \qquad (3.1)$$

ΔδH is the chemical shift change in ppm in ^{1}H dimension, $\Delta\delta_i$ is the chemical shift change in ppm in ^{15}N or ^{13}C dimension and the term $w_i = |\gamma^{15}N|/|\gamma^1H|$ or $w_i = |\gamma^{13}C|/|\gamma^1H|$ compensates for the scaling differences between ^{15}N and ^{13}C, and ^{1}H chemical shifts [46]. The magnetogyric ratios of ^{1}H (γ^1H), ^{15}N (γ^{15}N) and ^{13}C (γ^{13}C) nucleus are 1.000, 0.102 and 0.251, respectively. To select the most affected signal(s) to be used in the calculation of the equilibrium dissociation constant (K_d), a cutoff value was determined iteratively with the standard deviation to zero value, σ_0^{corr}, in accordance with Eq. 3.2.

$$\sigma_0^{corr} = \sqrt{\frac{1}{N}\sum(\Delta\delta_{comb} - 0)^2} \qquad (3.2)$$

where N corresponds to the number of $\Delta\delta_{comb}$ values determined. In an initial step, a value of σ_0 is determined from all $\Delta\delta_{comb}$ values. The $\Delta\delta_{comb}$ exceeding three times the determined σ_0 are removed and a first corrected standard deviation σ_0^{corr} is obtained for the remaining $\Delta\delta_{comb}$ values. If there are $\Delta\delta_{comb}$ values larger than three times the new σ_0^{corr} value, they will be excluded and a new σ_0^{corr} will be determined. This process is repeated until no $\Delta\delta_{comb}$ value larger than three times that of the actual σ_0^{corr} remained, which is then taken as the cut-off criterion.

The binding curves for the interaction between the protein P and the ligand L were obtained by plotting the magnitude of the chemical shift change ($\Delta\delta_{comb}$) as function of ligand concentration. The data were fitted using the tool Solver from Microsoft Excel with $\Delta\delta_{comb}$ and ligand concentration as dependent and independent variables, respectively and, K_d and $\Delta\delta_{max}$, as the fit parameters considering fast exchange conditions at the binding site, in accordance with the following equilibrium: P + L↔PL (Eq. 3.3).

$$\Delta\delta_{comb} = (\Delta\delta_{P-L})\frac{([\mathrm{P}]+[\mathrm{L}]+K_d)-\sqrt{([\mathrm{P}]+[\mathrm{L}]+K_d)^2-4[\mathrm{P}][\mathrm{L}]}}{2[\mathrm{P}]} \qquad (3.3)$$

$\Delta\delta_{max}$ is the maximum chemical shift change, when [L] >> K_d and the binding site is saturated, [P] the total protein concentration and [L] the total ligand concentration.

3.3.1.4 Thermodynamic characterization

To determine the thermodynamic parameters of a MHC, it is necessary to monitor the oxidation profile of the hemes at several pH values by 2D ^{1}H, ^{1}H exchange spectroscopy (EXSY) experiments. This can only be achieved when the electron exchange is fast between the different microstates within the same oxidation stage (intramolecular) and slow between the different oxidation stages (intermolecular) on the NMR time scale [39]. The heme methyl resonances are the easiest identifiable NMR signals amongst the heme substituents, making them ideal candidates to monitor the stepwise oxidation of the hemes [47].

The paramagnetic shifts of the heme methyls are proportional to the oxidation fraction of an individual heme and, thus contain information that can be used to infer about the redox properties of each heme group [48, 49]. However, the NMR data *per se* are insufficient to determine the absolute thermodynamic parameters and need to be complemented with data from potentiometric redox titrations monitored by visible spectroscopy, obtained for at least for two different pH values [50].

3.3.2 Kinetic studies

Electron exchange between AQDS and the triheme cytochromes PpcA, PpcB, PpcD and PpcE was studied, in both directions, using stopped-flow kinetics. Sample preparation and kinetic experiments were performed at 25 °C under anaerobic conditions inside an anaerobic chamber Mbraun MB 150 I with circulation of nitrogen to avoid sample reoxidation. Rapid mixing kinetic experiments were carried out on a HI-TECH KinetAsyst SF-61 DX2 stopped-flow apparatus and the data were acquired with a diode array in the wavelength range of 350 to 700 nm.

Samples were prepared in phosphate buffer pH 7.1 with NaCl (100 mM final ionic strength). The buffer was prepared inside the anaerobic chamber with degassed water. The protein solutions (ca. 3 µM) were prepared by dilution of a stock solution in degassed buffer and the concentrations were determined from the absorbance of the reduced forms at λ=552 nm using an extinction coefficient of 97 500 M^{-1} cm^{-1} [51]. A concentrated AQDS (≥ 98% purity, Sigma) stock solution (120 µM) was prepared in degassed buffer inside the anaerobic chamber and the 30 µM, 6 µM, 3 µM, and 1.5 µM AQDS solutions were prepared by successive dilutions of the concentrated stock solution. Reduced solutions of AQDS and PpcA were obtained by adding a stoichiometric amount of sodium dithionite, after determining the concentration of the sodium dithionite solution from its absorbance at λ=315 nm using an extinction coefficient of 8000 M^{-1} cm^{-1} [52]. UV-visible spectra were acquired before and after addition of sodium dithionite to monitor the extent of the reduction and to confirm that there was no excess reducing agent in the solution. In the reductive experiments, each oxidized cytochrome was mixed with AH_2QDS in the stopped-flow apparatus and the reduction of the protein was followed in the full spectral range (350-700 nm). The signal at 552 nm was normalized using reference spectra for the fully oxidized and fully reduced forms and the time scale was corrected for the dead time of the apparatus. To obtain the observed rate constants for the reduction of the cytochrome by AH_2QDS, the normalized signal was fitted with one or two exponentials as necessary. In the oxidative experiments, each reduced cytochrome was mixed with AQDS in stopped-flow apparatus and the oxidation of the protein was followed in the full spectral range (350-700 nm). The signals at 552 nm were also normalized and corrected for the dead time and then fitted with one or two exponentials to obtain the observed rate constants for the oxidation of each cytochrome by the oxidized AQDS. The following cytochrome to quinone ratios: 1:1, 1:2, 1:10 and 1:40 were used in both types of experiments. For high cytochrome to quinone ratios the reaction is very fast and a significant part is lost in the dead time of the apparatus (3 ms). After correction of the time scale, the initial data point was taken from the oxidized or the reduced reference spectra, for the reductive or the oxidative experiments, respectively. All concentrations refer to after mixing values.

3.3.3 Molecular docking calculations

Docking calculations were performed with Anchor-and-Grow algorithm as implemented in DOCK 6.4 and 6.7 [32]. Atomic coordinates of PpcA were taken from the NMR structure of the protein (PDB ID: 2LDO [12]). Atomic coordinates for AQDS and AH_2QDS were taken from LUPBUT entry of the Cambridge Structural Database. Protein and ligand structures were prepared for docking calculations with UCSF Chimera 1.5.2 [53]. Hydrogens were added to protein to reflect the neutral pH and heme charges are that for an oxidized state from AMBER force field. Molecular docking simulations between PpcB, PpcD, PpcE triheme cytochrome and AQDS were performed using HADDOCK 2.2 web server [54]. The crystal structures of PpcB (PDB ID: 3BXU [39]); PpcD (PDB ID: 3H4N [43]) and PpcE (PDB ID: 3H34 [43]) were used, and atomic coordinates for AQDS were taken from LUPBUT entry of the Cambridge Structural Database. PpcB and PpcD structures contain two protein chains. For PpcD, only more complete chain B was used in docking calculations. In contrast, both chains A and B of PpcB were used in docking and generally produced similar results. All these steps were performed with the default settings using those residues with the strongest observed NMR perturbations as active (Table 3.5), unless specified otherwise.

3.4 References

1. Struyk Z & Sposito G (2001) Redox properties of standard humic acids. *Geoderma* **102**, 329-346.

2. Lovley DR, Coates JD, Blunt-Harris EL, Phillips EJP & Woodward JC (1996) Humic substances as electron acceptors for microbial respiration. *Nature* **382**, 445-448.

3. Coates JD, Ellis DJ, Blunt-Harris EL, Gaw CV, Roden EE & Lovley DR (1998) Recovery of humic-reducing bacteria from a diversity of environments. *Appl Environ Microbiol* **64**, 1504-1509.

4. Lovley DR, Fraga JL, Coates JD & Blunt-Harris EL (1999) Humics as an electron donor for anaerobic respiration. *Environ Microbiol* **1**, 89-98.

5. Strycharz SM, Glaven RH, Coppi MV, Gannon SM, Perpetua LA, Liu A, Nevin KP & Lovley DR (2011) Gene expression and deletion analysis of mechanisms for electron transfer from electrodes to *Geobacter sulfurreducens*. *Bioelectrochemistry* **80**, 142-150.

6. Voordeckers JW, Kim BC, Izallalen M & Lovley DR (2010) Role of *Geobacter sulfurreducens* outer surface *c*-type cytochromes in reduction of soil humic acid and anthraquinone-2,6-disulfonate. *Appl Environ Microbiol* **76**, 2371-2375.

7. Lovley DR, Fraga JL, Blunt-Harris EL, Hayes LA, Phillips EJP & Coates JD (1998) Humic substances as a mediator for microbially catalyzed metal reduction. *Acta hydrochim hydrobiol* **26**, 152-157.

8. Aulenta F, Maio VD, Ferri T & Majone M (2010) The humic acid analogue antraquinone-2,6-disulfonate (AQDS) serves as an electron shuttle in the electricity-driven microbial dechlorination of trichloroethene to cis-dichloroethene. *Bioresour Technol* **101**, 9728-9733.

9. Coates JD, Cole KA, Chakraborty R, O'Connor SM & Achenbach LA (2002) Diversity and ubiquity of bacteria capable of utilizing humic substances as electron donors for anaerobic respiration. *Appl Environ Microbiol* **68**, 2445-2452.

10. Lloyd JR, Leang C, Hodges Myerson AL, Coppi MV, Cuifo S, Methe B, Sandler SJ & Lovley DR (2003) Biochemical and genetic characterization of PpcA, a periplasmic *c*-type cytochrome in *Geobacter sulfurreducens*. *Biochem J* **369**, 153-161.

11. Morgado L, Paixão VB, Salgueiro CA & Bruix M (2011) Backbone, side chain and heme resonance assignments of the triheme cytochrome PpcA from *Geobacter sulfurreducens*. *Biomol NMR Assign* **5**, 113-116.

12. Morgado L, Paixão VB, Schiffer M, Pokkuluri PR, Bruix M & Salgueiro CA (2012) Revealing the structural origin of the redox-Bohr effect: the first solution structure of a cytochrome from *Geobacter sulfurreducens*. *Biochem J* **441**, 179-187.

13. Morgado L, Bruix M, Pokkuluri PR, Salgueiro CA & Turner DL (2017) Redox- and pH-linked conformational changes in triheme cytochrome PpcA from *Geobacter sulfurreducens*. *Biochem J* **474**, 231-246.

14. Cousins KR (2011) Computer review of ChemDraw Ultra 12.0. *J Am Chem Soc* **133**, 8388.

15. Clark WM (1960) *Oxidation-reduction potentials of organic systems*. Williams & Wilkins, Baltimore.

16. Santos TC, Silva MA, Morgado L, Dantas JM & Salgueiro CA (2015) Diving into the redox properties of *Geobacter sulfurreducens* cytochromes: a model for extracellular electron transfer. *Dalton Trans* **44**, 9335-9344.

17. Liu Z, Gong Z, Dong X & Tang C (2016) Transient protein-protein interactions visualized by solution NMR. *Biochim Biophys Acta* **1864**, 115-122.

18. Prudêncio M & Ubbink M (2004) Transient complexes of redox proteins: structural and dynamic details from NMR studies. *J Mol Recognit* **17**, 524-539.

19. Meschi F, Wiertz F, Klauss L, Blok A, Ludwig B, Merli A, Heering HA, Rossi GL & Ubbink M (2011) Efficient electron transfer in a protein network lacking specific interactions. *J Am Chem Soc* **133**, 16861-16867.

20. Sakamoto K, Kamiya M, Imai M, Shinzawa-Itoh K, Uchida T, Kawano K, Yoshikawa S & Ishimori K (2011) NMR basis for interprotein electron transfer gating between cytochrome *c* and cytochrome *c* oxidase. *Proc Natl Acad Sci USA* **108**, 12271-12276.

21. Yahata N, Saitoh T, Takayama Y, Ozawa K, Ogata H, Higuchi Y & Akutsu H (2006) Redox interaction of cytochrome c_3 with [NiFe] hydrogenase from *Desulfovibrio vulgaris* Miyazaki F. *Biochemistry* **45**, 1653-1662.

22. Morgado L, Fernandes AP, Londer YY, Bruix M & Salgueiro CA (2010) One simple step in the identification of the cofactors signals, one giant leap for the solution structure determination of multiheme proteins. *Biochem Biophys Res Commun* **393**, 466-470.

23. McGovern RE, Fernandes H, Khan AR, Power NP & Crowley PB (2012) Protein camouflage in cytochrome *c*-calixarene complexes. *Nat Chem* **4**, 527-533.

24. Gordo S, Martos V, Santos E, Menendez M, Bo C, Giralt E & de Mendoza J (2008) Stability and structural recovery of the tetramerization domain of p53-R337H mutant induced by a designed templating ligand. *Proc Natl Acad Sci USA* **105**, 16426-16431.

25. Martos V, Bell SC, Santos E, Isacoff EY, Trauner D & de Mendoza J (2009) Molecular recognition and self-assembly special feature: Calix[4]arene-based conical-shaped ligands for voltage-dependent potassium channels. *Proc Natl Acad Sci USA* **106**, 10482-10486.

26. Ubbink M (2004) Complexes of photosynthetic redox proteins studied by NMR. *Photosynth Res* **81**, 277-287.

27. Bashir Q, Scanu S & Ubbink M (2011) Dynamics in electron transfer protein complexes. *FEBS J* **278**, 1391-1400.

28. DeLano WL (2002) The PyMOL molecular graphics system. In http://wwwpymolorg.

29. Moss GP (1988) Nomenclature of tetrapyrroles. Recommendations 1986 IUPAC-IUB Joint Commission on Biochemical Nomenclature (JCBN). *Eur J Biochem* **178**, 277-328.

30. Pokkuluri PR, Londer YY, Duke NE, Long WC & Schiffer M (2004) Family of cytochrome c_7-type proteins from *Geobacter sulfurreducens*: structure of one cytochrome c_7 at 1.45 Å resolution. *Biochemistry* **43**, 849-859.

31. Turner DL, Salgueiro CA, Schenkels P, LeGall J & Xavier AV (1995) Carbon-13 NMR studies of the influence of axial ligand orientation on haem electronic structure. *Biochim Biophys Acta* **1246**, 24-28.

32. Lang PT, Brozell SR, Mukherjee S, Pettersen EF, Meng EC, Thomas V, Rizzo RC, Case DA, James TL & Kuntz ID (2009) DOCK 6: combining techniques to model RNA-small molecule complexes. *RNA* **15**, 1219-1230.

33. Fonseca BM, Paquete CM, Neto SE, Pacheco I, Soares CM & Louro RO (2013) Mind the gap: cytochrome interactions reveal electron pathways across the periplasm of *Shewanella oneidensis* MR-1. *Biochem J* **449**, 101-108.

34. Paquete CM, Fonseca BM, Cruz DR, Pereira TM, Pacheco I, Soares CM & Louro RO (2014) Exploring the molecular mechanisms of electron shuttling across the microbe/metal space. *Front Microbiol* **5**, 318.

35. Kokhan O, Ponomarenko N, Pokkuluri PR, Schiffer M & Tiede DM (2014) Multimerization of solution-state proteins by tetrakis(4-sulfonatophenyl)porphyrin. *Biochemistry* **53**, 5070-5079.

36. Marcus RA & Sutin N (1985) Electron transfers in chemistry and biology. *Biochim Biophys Acta - Reviews on Bioenergetics* **811**, 265-322.

37. Morgado L, Bruix M, Pessanha M, Londer YY & Salgueiro CA (2010) Thermodynamic characterization of a triheme cytochrome family from *Geobacter sulfurreducens* reveals mechanistic and functional diversity. *Biophys J* **99**, 293-301.

38. Dantas JM, Morgado L, Marques AC & Salgueiro CA (2014) Probing the effect of ionic strength on the functional robustness of the triheme cytochrome PpcA from *Geobacter sulfurreducens*: a contribution for optimizing biofuel cell's power density. *J Phys Chem B* **118**, 12416-12425.

39. Morgado L, Bruix M, Orshonsky V, Londer YY, Duke NE, Yang X, Pokkuluri PR, Schiffer M & Salgueiro CA (2008) Structural insights into the modulation of the redox properties of two *Geobacter sulfurreducens* homologous triheme cytochromes. *Biochim Biophys Acta* **1777**, 1157-1165.

40. Morgado L, Lourenço S, Londer YY, Schiffer M, Pokkuluri PR & Salgueiro CA (2014) Dissecting the functional role of key residues in triheme cytochrome PpcA: a path to rational design of *G. sulfurreducens* strains with enhanced electron transfer capabilities. *PLoS One* **9**, e105566.

41. Morgado L, Dantas JM, Simoes T, Londer YY, Pokkuluri PR & Salgueiro CA (2012) Role of Met58 in the regulation of electron/proton transfer in trihaem cytochrome PpcA from *Geobacter sulfurreducens*. *Biosci Rep* **33**, 11-22.

42. Dantas JM, Morgado L, Londer YY, Fernandes AP, Louro RO, Pokkuluri PR, Schiffer M & Salgueiro CA (2012) Pivotal role of the strictly conserved aromatic residue F15 in the cytochrome c_7 family. *J Biol Inorg Chem* **17**, 11-24.

43. Pokkuluri PR, Londer YY, Yang X, Duke NE, Erickson J, Orshonsky V, Johnson G & Schiffer M (2010) Structural characterization of a family of cytochromes c_7 involved in Fe(III) respiration by *Geobacter sulfurreducens*. *Biochim Biophys Acta* **1797**, 222-232.

44. Dantas JM, Saraiva IH, Morgado L, Silva MA, Schiffer M, Salgueiro CA & Louro RO (2011) Orientation of the axial ligands and magnetic properties of the hemes in the cytochrome c_7 family from *Geobacter sulfurreducens* determined by paramagnetic NMR. *Dalton Trans* **40**, 12713-12718.

45. Wishart DS, Bigam CG, Yao J, Abildgaard F, Dyson HJ, Oldfield E, Markley JL & Sykes BD (1995) ^{1}H, ^{13}C and ^{15}N chemical shift referencing in biomolecular NMR. *J Biomol NMR* **6**, 135-140.

46. Schumann FH, Riepl H, Maurer T, Gronwald W, Neidig KP & Kalbitzer HR (2007) Combined chemical shift changes and amino acid specific chemical shift mapping of protein-protein interactions. *J Biomol NMR* **39**, 275-289.

47. Salgueiro CA & Dantas JM (2016) Multiheme cytochromes. In *Protein folding and structure*. Gomes CM, ed, pp. 39. Springer-Verlag Berlin Heidelberg.

48. Salgueiro CA, Turner DL, Santos H, LeGall J & Xavier AV (1992) Assignment of the redox potentials to the four haems in *Desulfovibrio vulgaris* cytochrome c_3 by 2D-NMR. *FEBS Lett* **314**, 155-158.

49. Santos H, Moura JJ, Moura I, LeGall J & Xavier AV (1984) NMR studies of electron transfer mechanisms in a protein with interacting redox centres: *Desulfovibrio gigas* cytochrome c_3. *Eur J Biochem* **141**, 283-296.

50. Turner DL, Salgueiro CA, Catarino T, Legall J & Xavier AV (1996) NMR studies of cooperativity in the tetrahaem cytochrome c_3 from *Desulfovibrio vulgaris*. *Eur J Biochem* **241**, 723-731.

51. Seeliger S, Cord-Ruwisch R & Schink B (1998) A periplasmic and extracellular *c*-type cytochrome of *Geobacter sulfurreducens* acts as a ferric iron reductase and as an electron carrier to other acceptors or to partner bacteria. *J Bacteriol* **180**, 3686-3691.

52. Dixon M (1971) The acceptor specificity of flavins and flavoproteins. I. Techniques for anaerobic spectrophotometry. *Biochim Biophys Acta* **226**, 241-258.

53. Pettersen EF, Goddard TD, Huang CC, Couch GS, Greenblatt DM, Meng EC & Ferrin TE (2004) UCSF Chimera-a visualization system for exploratory research and analysis. *J Comput Chem* **25**, 1605-1612.

54. van Zundert GC, Rodrigues JP, Trellet M, Schmitz C, Kastritis PL, Karaca E, Melquiond AS, van Dijk M, de Vries SJ & Bonvin AM (2016) The HADDOCK2.2 Web server: User-friendly integrative modeling of biomolecular complexes. *J Mol Biol* **428**, 720-725.

4

NMR INTERACTION STUDIES BETWEEN INNER MEMBRANE-ASSOCIATED AND PERIPLASMIC CYTOCHROMES[1]

---

[1] Partially reproduced from Dantas JM, Brausemann A, Einsle O, Salgueiro CA (2017) NMR studies of the interaction between inner membrane-associated and periplasmic cytochromes from *Geobacter sulfurreducens*, FEBS lett 591, 1657-1666 (doi: 10.1002/1873-3468.12695), in accordance with the Editors' Copyright Policy.

4. NMR interaction studies between inner membrane-associated and periplasmic cytochromes

MacA from *G. sulfurreducens* is a 35 kDa inner membrane-associated diheme cytochrome *c* (see Chapter 1 - Section 1.4). Genetic and proteomics studies showed that this cytochrome is important for the reduction of Fe(III) and U(VI) oxides [1-3]. This phenotype is also shared with triheme periplasmic cytochrome PpcA, and for that reason it was proposed that MacA is involved in the electron transfer between the reduced quinone pool and periplasmic electron transfer components. In more recently studies, Siedel and co-workers [4] suggested that MacA is a peroxidase and the previous proposed role for MacA was readdressed.

The MacA crystal structure is available for different redox states [4] showing that the two heme groups have different axial coordination and are located in opposite sides of the polypeptide chain: the heme placed at the C-terminal domain is axially coordinated by His-Met, whereas the other at the N-terminal domain, is axially coordinated by His-His (see Fig 1.5). The hemes also have quite distinct midpoint redox potentials and were designated as high- (HP) and low-potential (LP) hemes, respectively. As previously described, the catalytic and the redox reactions occur at the LP and HP hemes, respectively [4].

In the periplasm of *G. sulfurreducens*, a pool of several *c*-type cytochromes, among which PpcA is found, is considered to mediate electron transfer reactions at near isopotential values (see Table 1.2), serving as a source of electrons not only for enzymes, such as MacA, but also to a variety of terminal reductases. Electrochemical experiments showed that MacA can exchange electrons with the cytochrome PpcA suggesting the formation of a low-affinity complex between the two proteins [4], however, the interface region between the two cytochromes could not be established. The electrochemical results provided important information that prompted us to study the molecular interaction between the two proteins in detail. In this Chapter, the main goal was to probe the molecular interface region between MacA and PpcA by NMR chemical shift perturbation experiments.

4.1 Results and discussion

The molecular interface region between the periplasmic triheme PpcA and the inner membrane-associated diheme MacA cytochromes was investigated using NMR spectroscopy. The dispersion of heme NMR signals in the oxidized state are in less crowded regions, particularly in the case of the heme methyl substituents, and makes the analysis of the chemical shifts more straightforward. Thus, in the present study, NMR chemical shift perturbation experiments were performed with cytochromes PpcA and MacA in the oxidized state. In this redox state, PpcA is paramagnetic and all heme irons are in the low spin state (S = 1/2). In the case of MacA, the HP heme iron is axially coordinated by histidine and methionine residues and is in a rapid low spin - high spin equilibrium at room temperature, due to the long Fe-S bond of the distal methionine [4]. On the other hand, the LP heme, coordinated by two histidine residues, is in the low spin state. For these reasons, the heme methyl signals of each heme are in distinct regions of the NMR spectra. The HP heme methyls are strongly downfield shifted to the region above 50 ppm and are much broader compared to those of the LP heme, which are found at lower chemical shifts.

The 1D ^{1}H NMR spectra of PpcA and MacA are indicated in Fig 4.1. The comparison of the oxidized spectra of the two cytochromes shows that the heme methyl signals of both proteins are in distinct spectral regions. The MacA spectrum shows three HP (63.2, 67.2 and 75.6 ppm) and two LP (32.7 and 25.5 ppm) heme methyl signals shifted from the crowded region of the spectrum. However, these signals cover a distinct spectral region compared to those of PpcA. The structures of PpcA and MacA indicated that the heme groups are considerable exposed [9, 11, 12]. Thus, when a protein redox complex is formed we expect to observe chemical shift perturbations and/or broadening of heme methyl signals. Therefore, these signals are excellent candidates to probe any modification in the chemical environment upon complex formation. Consequently, the molecular interaction between PpcA and MacA was monitored by probing the chemical shift perturbation of their heme methyl signals with the addition of increasing amounts of PpcA to a MacA sample (Figs 4.1 B and 4.2).

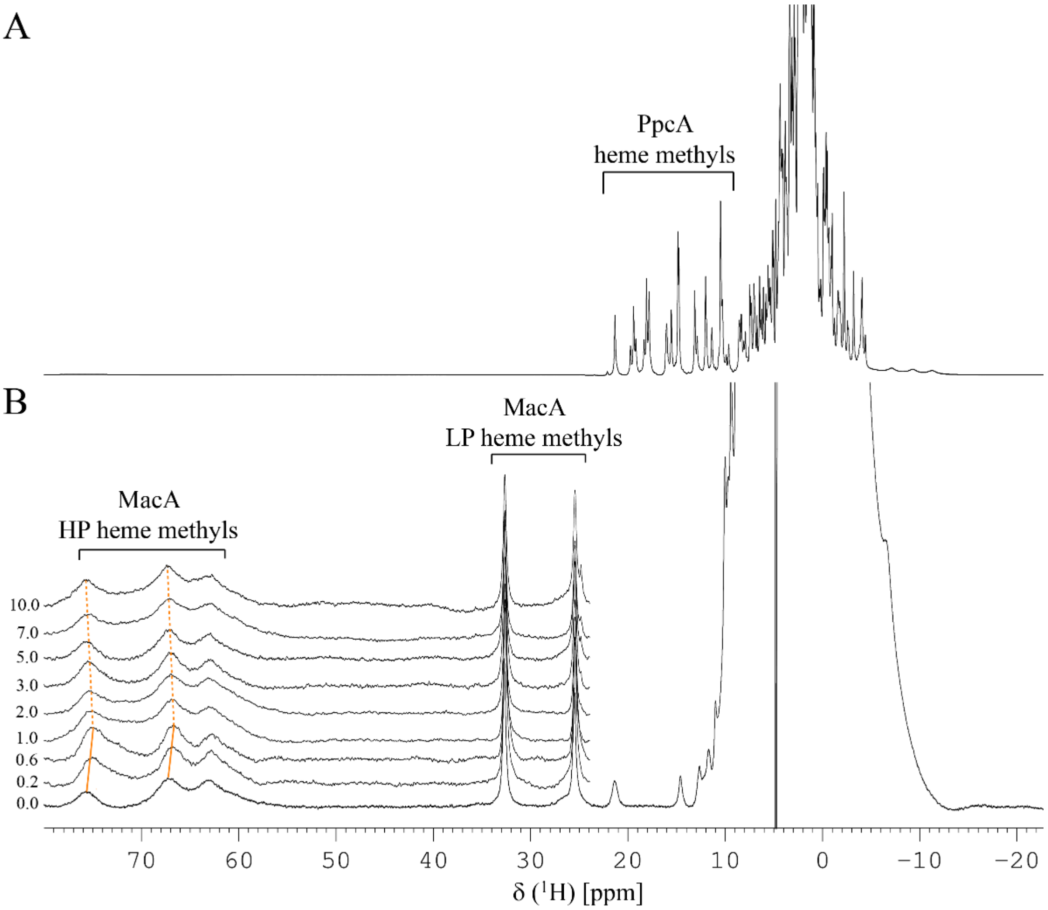

Fig 4.1 1D ^{1}H NMR spectra of cytochromes PpcA and MacA in the oxidized state (298 K, pH 7 and 20 mM final ionic strength). The typical chemical shift regions of the heme methyl signals from PpcA and MacA are indicated in panels A and B, respectively. The chemical shift perturbation on the MacA heme methyl signals in the presence of increasing amounts of PpcA is also indicated in panel B. A 180 µM sample of MacA was titrated with increasing amounts of a 6.5 mM PpcA sample and the [PpcA]/[MacA] ratios are indicated on the left side of each spectrum. The orange lines highlight the HP heme methyl signals that experienced chemical shift variation during the titration.

The low-field region of the 1D ^{1}H NMR spectra of MacA acquired with increasing amounts of PpcA is depicted in Fig 4.1 B and shows that the LP heme methyl signals are unaffected during the titration. On the other hand, the two more downfield-shifted HP heme methyl signals at 67.2 and 75.6 ppm are clearly affected upon addition of PpcA. These two signals show a similar behavior during the experiment, shifting to higher field in a straight line up to roughly 0.6 equivalents of PpcA, and then in the opposite direction until the maximum addition of PpcA. Such behavior is typical of two molecular binding events, resulting in distinct effects on the heme methyl chemical shifts from a primary and a secondary interaction [5].

The analysis of the chemical shift perturbation experiments for the PpcA heme methyl signals is depicted in Fig 4.2 B. In this spectral region, all the PpcA heme methyl signals, except for the one of $18^1CH_3^{III}$, can be observed. The most affected signal is the heme methyl $12^1CH_3^{IV}$ (Fig 4.2 B).

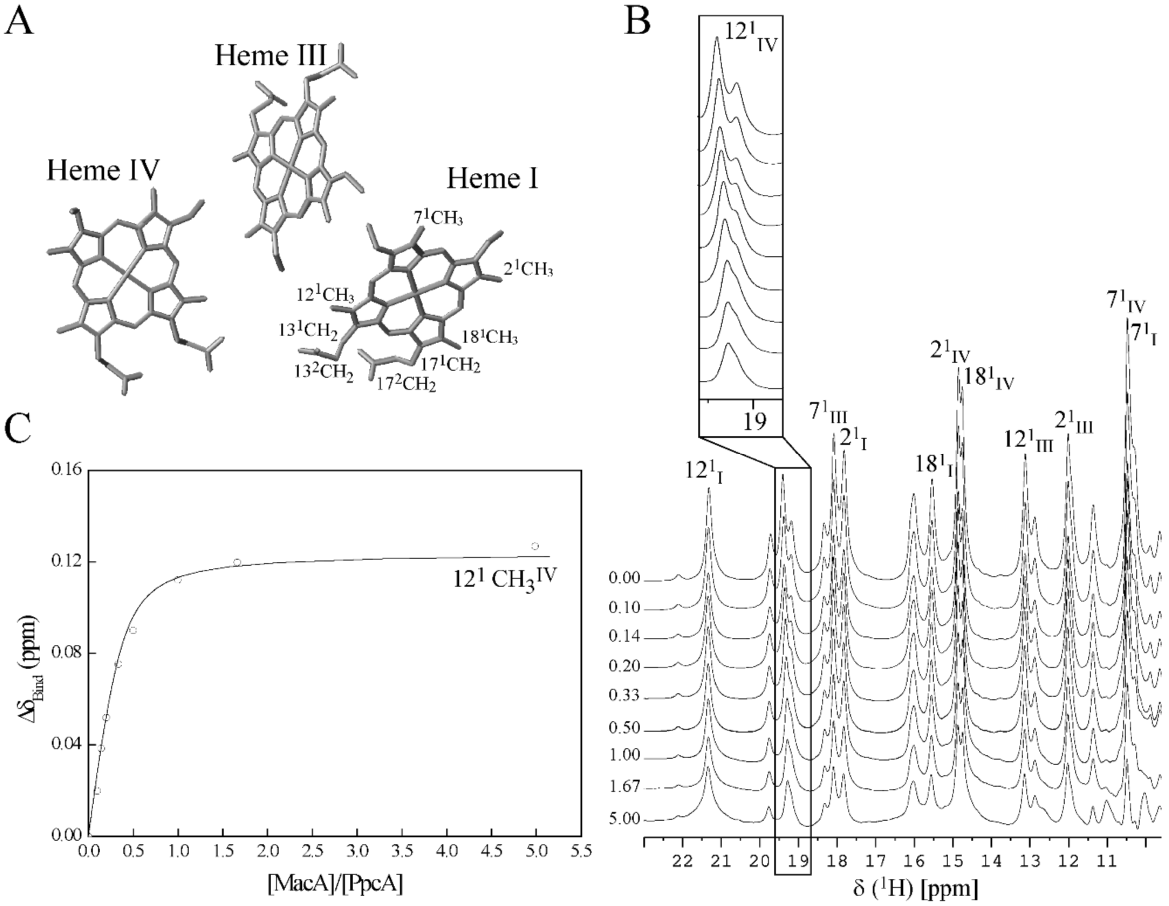

Fig 4.2 1D ^{1}H chemical shift changes of the heme methyls of PpcA. (A) PpcA heme core and the IUPAC nomenclature for tetrapyrroles [6]. (B) Expansions of the low-field region of 1D ^{1}H NMR spectra obtained for PpcA in presence of increasing amounts of MacA. The heme methyl signals (2^1CH_3, 7^1CH_3, 12^1CH_3 and 18^1CH_3) are labeled, except heme methyl $18^1CH_3^{III}$ whose signal appears at a chemical shift of approximately 1 ppm. The [MacA]/[PpcA] ratios are indicated on the left side of each spectrum. For clarity, the region containing the heme methyl signal $12^1CH_3^{IV}$ was expanded. (C) Binding curve for PpcA and MacA interaction monitored by the heme methyl signal $12^1CH_3^{IV}$. The fitting curve was simulated for the molar proportion of 2:1 PpcA/MacA with K_d of 32±8 μM and Δδ of 0.15 ppm.

To also evaluate the effect of the presence of MacA on the heme methyl $18^1CH_3^{III}$, whose signal appears at a chemical shift of approximately 1 ppm, 2D $^1H,^{13}C$ HMQC NMR spectra were recorded in the absence and in the presence of MacA (Fig 4.3).

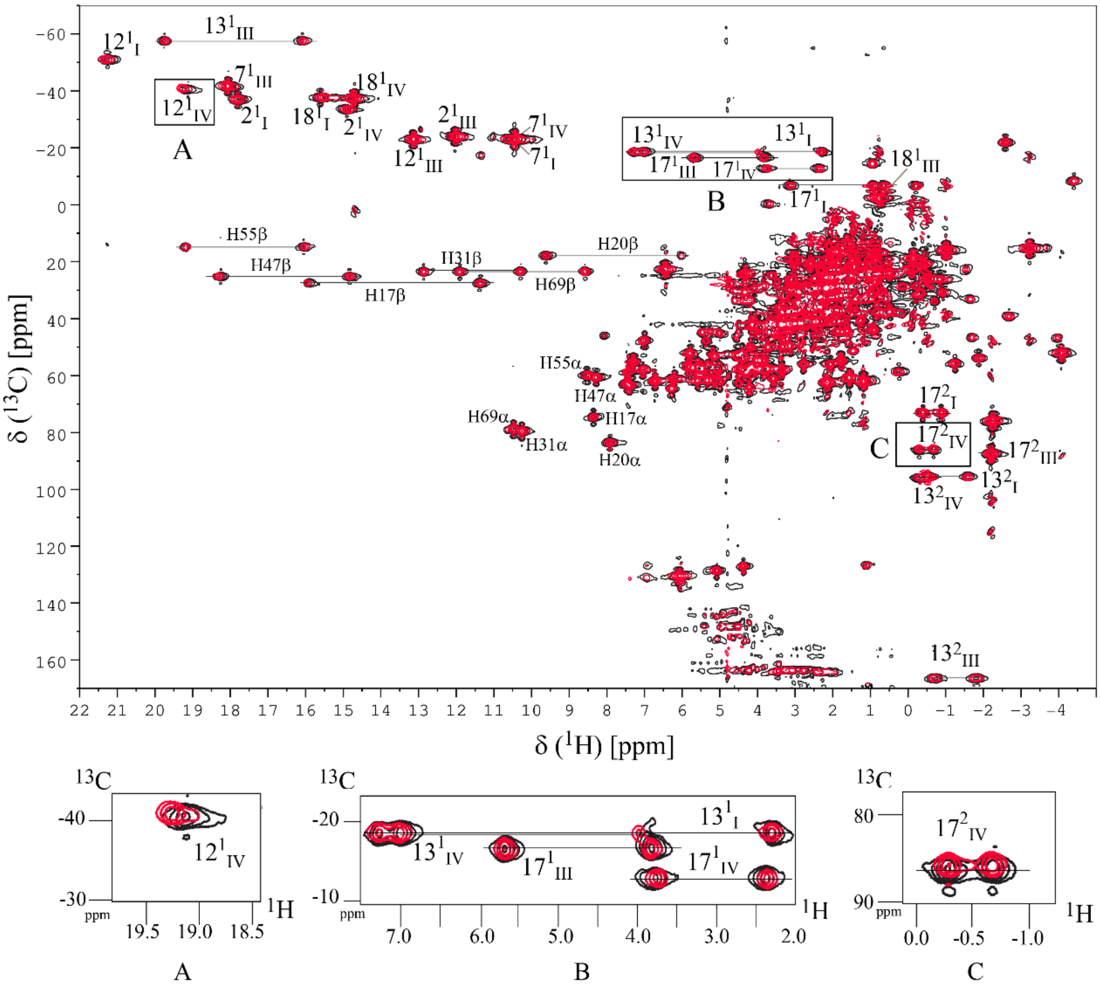

Fig 4.3 Overlay of the 2D ^{1}H,^{13}C HMQC NMR spectra of PpcA (1.8 mM) obtained in the absence and in the presence of MacA (0.18 mM) at 298 K, pH 7 and 20 mM final ionic strength. The signal contours in the reference spectrum and in the presence of MacA are shown in black and red, respectively. The assignments of the heme methyl signals (2^1CH_3, 7^1CH_3, 12^1CH_3 and 18^1CH_3), heme propionates (13^1CH_2, 13^2CH_2, 17^1CH_2 and 17^2CH_2) and Hα/Hβ protons from the heme axial histidines are indicated. The signals of the protons connected to the same carbon atom (CH_2 groups) are linked by a straight line. For clarity, the regions of the spectra boxed (A-C) were expanded to show the most affected PpcA signals in the presence of MacA.

In these spectra, the heme propionate (13^1CH_2, 13^2CH_2, 17^1CH_2 and 17^2CH_2) and the aliphatic protons (Hα and Hβ) of the six axial histidines that coordinated the three heme groups, His^{17}/His^{31} (heme I), His^{20}/His^{55} (heme III) and His^{47}/His^{69} (heme IV), are found in very typical regions, and therefore we further extended the chemical shift perturbation study to these signals. This analysis confirmed that the most affected PpcA heme methyl signal, by the presence of MacA, is $12^1CH_3^{IV}$ (Fig 4.4). In addition, other PpcA signals near heme IV also show important differences, namely the propionate 17 from heme IV (P_{17}^{IV}), followed by P_{13}^{IV} and P_{13}^{I}. Also, the chemical shift variation of all the aliphatic protons of the six axial histidines showed that the most affected signals are those from His^{47}, which axially coordinates PpcA heme IV, followed by His^{17} and His^{20} that coordinate hemes I and III, respectively (Fig 4.4 B).

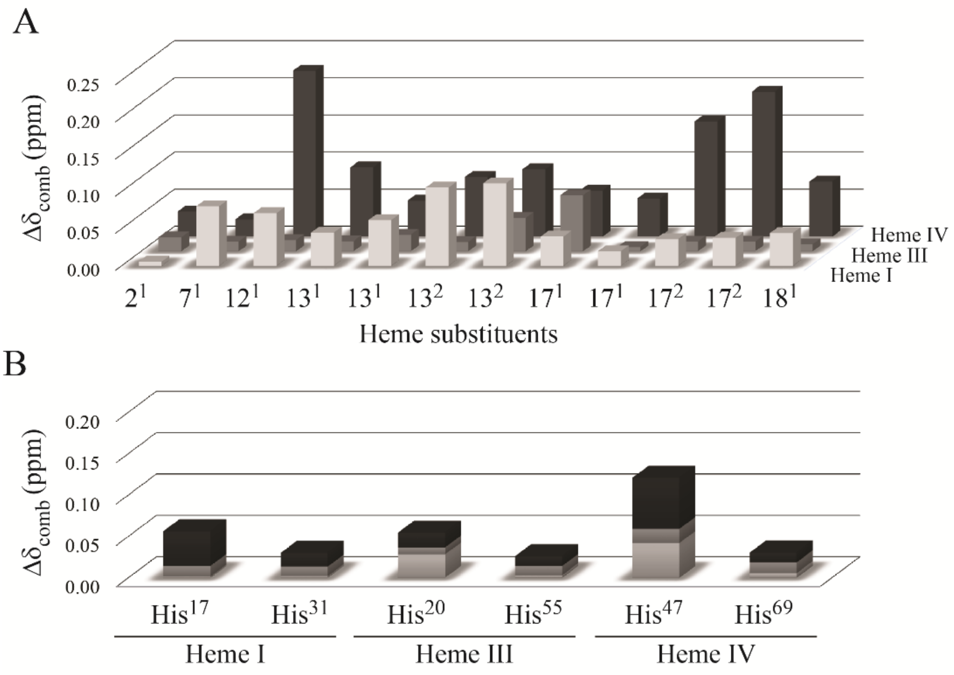

Fig 4.4 Variation of the combined chemical shift changes determined from the ^{1}H and ^{13}C signals of the PpcA heme substituents and heme axial ligands. The shifts were taken from the 2D ^{1}H,^{13}C HMQC NMR spectra (see Fig 4.3), acquired in the absence and in the presence of MacA. A) The bars represent the chemical shift variations of the heme substituents in the following order: 2^1CH_3, 7^1CH_3, 12^1CH_3, 13^1CH_2, 13^2CH_2, 17^1CH_2, 17^2CH_2, 18^1CH_3. The signals of hemes I, III and IV are represented in light gray, gray and black, respectively. B) The bars represent the chemical shift variations of the six heme axial histidine aliphatic protons. The histidine α and β protons are indicated in light gray, gray and black, respectively.

In the present study, we further extended the analysis of the NMR chemical shift perturbation measurements to the PpcA backbone NH signals. The NH signals were previously assigned [7] and were re-assigned in the present work for 20 mM ionic strength. The chemical shift perturbations on the PpcA backbone NH signals in the presence of MacA were monitored by 2D ^{1}H, ^{15}N HSQC NMR spectra (Fig 4.5 A). The NH signals showing highest chemical shift perturbation are from residues Lys^{18} and His^{20}, located between hemes I and III, and residues Lys^{43} and His^{47}, located near heme IV (Fig 4.5 B).

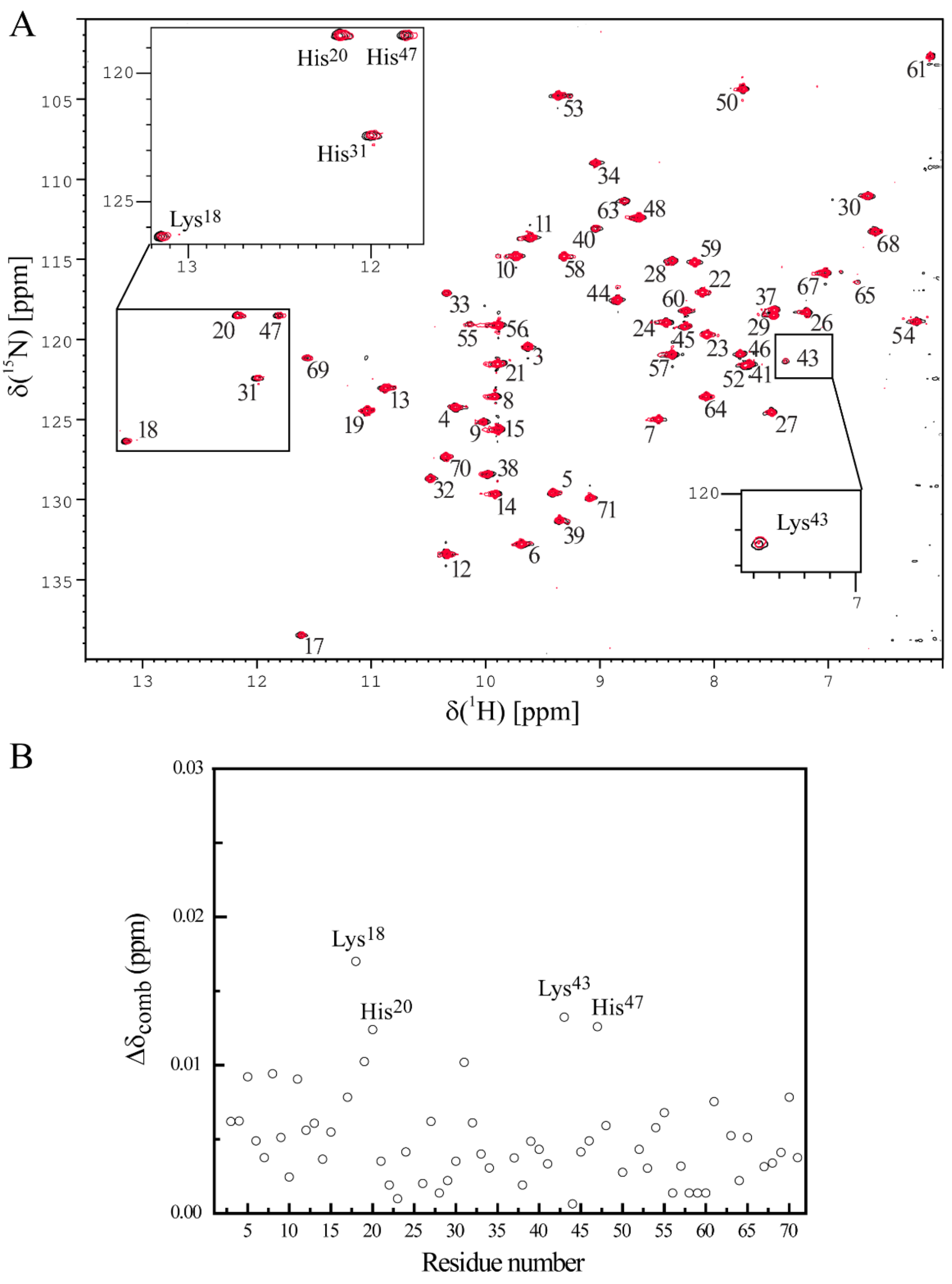

Fig 4.5 Chemical shift perturbation on PpcA backbone NH signals. (A) Overlay of the 2D ^{1}H, ^{15}N HSQC NMR spectra of ^{15}N-enriched PpcA (1.8 mM) in the presence of MacA (0.18 mM). The contours of the signals in the reference spectrum are shown in black, whereas in the presence of MacA are shown in red. The assignments of NH signals are indicated. For clarity, the regions of the spectra with the most affected PpcA signals in the presence of MacA are shown. (B) Combined chemical shift changes determined from the directly observed ^{1}H and ^{15}N chemical shifts.

Overall, the results obtained from the analysis of the NMR chemical shift perturbation experiments suggested that MacA interacts with PpcA in the protein cleft defined by hemes I and IV in an orientation that favors the closer contact between MacA HP heme and PpcA heme IV. These conclusions are also supported by the docking calculations (see Fig 4.6).

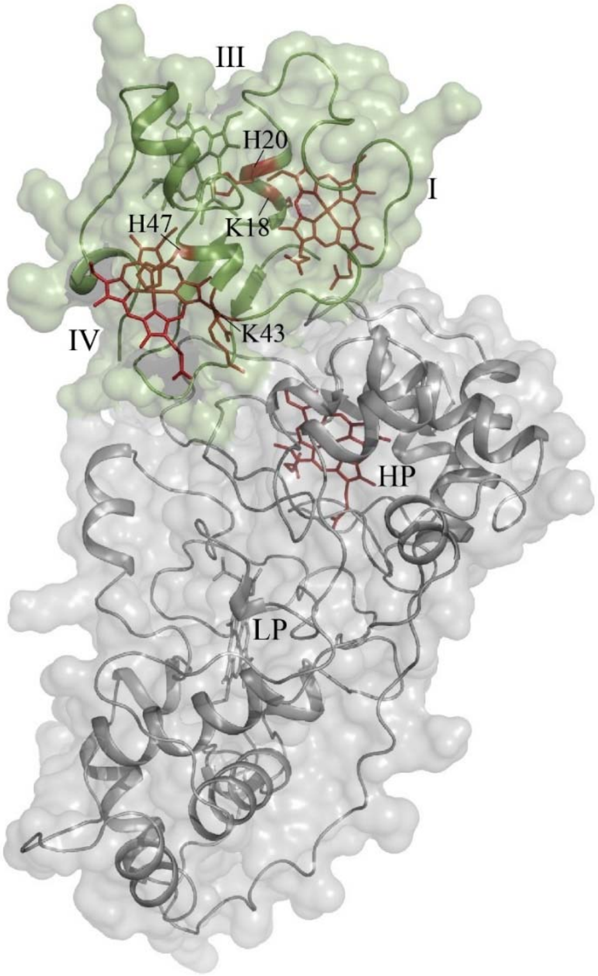

Fig 4.6 PpcA-MacA docked complex calculated using the HADDOCK2.2 Web server. The low-energy binding conformation for PpcA (green) and MacA monomer (gray) complex is illustrated as a ribbon diagram with the heme groups shown in green and gray sticks, respectively. The active residues for PpcA (Lys^{18}, His^{20}, Lys^{43}, His^{47}, heme I and IV) and for MacA (Heme HP) are shown in red.

Using the equations described in the Section 4.3.2 the dissociation constants (K_d) were determined from the chemical shift of the most affected heme methyls in PpcA and MacA (Table 4.1). Changes in chemical shifts of PpcA heme methyl were analyzed using a two-site binding model for the molar proportion of 2:1 PpcA/MacA, and changes in chemical shifts of MacA heme methyls were analyzed using an independent two-site binding model, in which the primary site is occupied with higher affinity than the secondary site. For the two HP methyl signals from MacA the K_d value of the first binding event is one order of magnitude lower compared to the second one. Therefore, PpcA initially binds almost exclusively to the primary site, but once most of the primary site is occupied, the protein will start to bind to a slightly different place (for a review see [5]). Two molecular binding events have also been described for the interaction between cytochrome *c* peroxidase from *Paracoccus pantotrophus* and two redox partners, cytochrome *c* and pseudoazurin [8]. The values are within the μM range suggesting the formation of a low affinity complex between the redox partners. These values are consistent with other K_d values previously reported for the interactions between cytochromes [8, 9].

Table 4.1 Equilibrium dissociation constants (K_d) for the complex formed between MacA and PpcA at 298 K, pH 7 and 20 mM final ionic strength. The K_d values were calculated as described in the Section 4.3.2 for the selected heme methyl signals. The ^1H chemical shift difference between the free form and the complex form (Δδ) is also indicated.

	δ (ppm)	K_d (μM)	Δδ (ppm)
MacA heme methyls			
HP heme methyl	67.2	87 ±16	1.49
		260 ± 33	1.91
HP heme methyl	75.6	43 ± 9	1.25
		235 ± 43	1.48
PpcA heme methyls			
$12^1CH_3^{IV}$	19.4	32 ± 8	0.15

The analysis of the SDS-PAGE obtained before and after removal of MacA by molecular exclusion chromatography confirmed that the interaction between the two cytochromes is fully reversible (Fig 4.7).

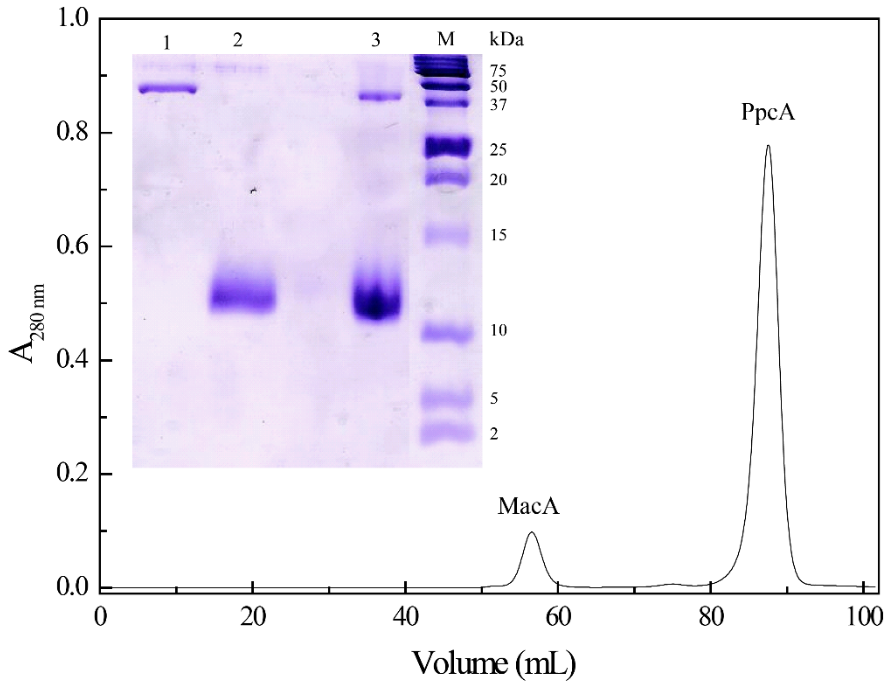

Fig 4.7 Elution profile for the molecular exclusion chromatography (100 mM sodium phosphate buffer, pH 8) of PpcA and MacA after the NMR chemical shift perturbation experiments. The inset shows the SDS-PAGE analysis before (Lane 3) and after the Ppca (Lane 2) and MacA (Lane 1) separation. Lane M corresponds to the molecular weight markers (Precision Plus Protein from Bio-Rad). The numbers on the left refer to molecular weight in kDa. The gel was stained with Coomassie Brilliant blue.

To rationalize the results obtained in structural and functional terms, we analyzed the electrostatic surface potential distribution of the two proteins. The analysis of the electrostatic surface of MacA showed a negative electrostatic region near the heme groups and showed that the HP heme is the most exposed and directly accessible from the surface (Fig 4.8). In PpcA the heme IV shows a significantly positive environment, due to the presence of several neighboring lysine residues (Fig 4.8).

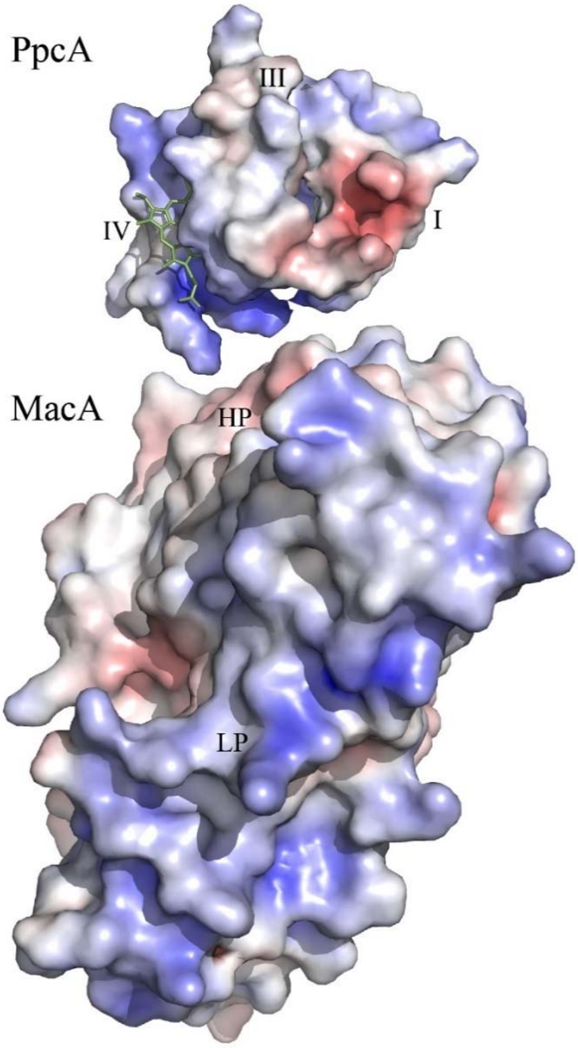

Fig 4.8 Electrostatic properties of MacA monomer and PpcA. The molecular surfaces were produced by PyMOL [10] and are colored accordingly to the electrostatic potential (from -7 k_BT in red to +7 k_BT in blue) calculated with APBS [11]. The heme groups are represented by green sticks and the PDB code files were 4AAL [4] and 2MZ9 [7] for MacA and PpcA, respectively. Both structures are in the same orientation as in the Fig 4.6.

Due to this surface complementarity, electrostatic interactions are expected to contribute favorably to the formation of the PpcA-MacA electron transfer complex. To test this hypothesis, we further analyzed the heme methyl chemical shift perturbation at higher ionic strength (100 mM). The comparison of the chemical shift perturbation of the ^{1}H chemical shift of the heme substituents of PpcA in the absence and in the presence of MacA at 20 mM and 100 mM ionic strength are indicated in Fig 4.9.

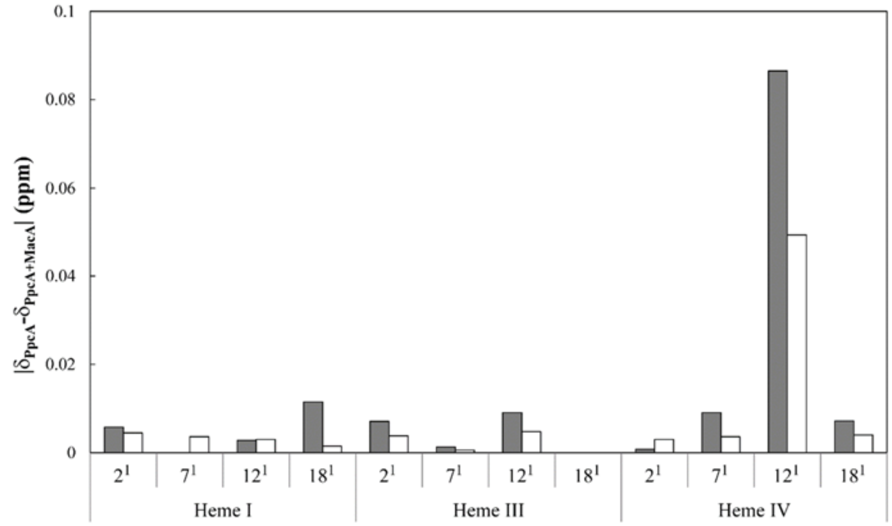

Fig 4.9 Variation of the PpcA ^{1}H heme methyl chemical shifts. The shifts were measured from 1D ^{1}H NMR spectra acquired in the absence (δ_{PpcA}) and in the presence of MacA ($\delta_{PpcA+MacA}$) at 20 mM (gray bars) and 100 mM (white bars).

The results obtained showed that the most strongly affected signals in both conditions are the same and that the magnitude of the chemical shift perturbation is higher at lower ionic strength. This was also observed for interaction studies described for other cytochromes [12, 13], suggesting that the interaction between PpcA and MacA is electrostatic driven. The reduction potential values of each heme group in MacA and PpcA have been previously determined [4, 14]. For MacA the midpoint redox potentials are -237 and -241 mV for heme LP in the His-bound and -free form, respectively. The heme HP showed a less negative redox potential (-138 mV). In the case of PpcA, the heme reduction potentials are of the same order of magnitude (-154, -138 and -125 mV for hemes I, III and IV, respectively), which indicates that the electron transfer between PpcA heme IV and MacA HP heme group have low thermodynamic barriers in either direction. Therefore, the structural and thermodynamic properties of the two proteins could facilitate the complex formation, redirecting the two proteins to the binding interface.

4.2 Conclusions

Many structural and functional studies have been carried out to understand the importance and the role of some proteins involved in the different electron transfer pathways in *G. sulfurreducens*. The next step to clarify the electron transfer networks is to map the redox partners and their complex interface region. In the present work, the molecular interaction between the diheme cytochrome MacA and the triheme cytochrome PpcA was investigated at atomic level using NMR chemical shift perturbation experiments. The MacA HP heme and a cleft defined by PpcA hemes I and IV were the most strongly affected regions. Our results also show that the complex between MacA and PpcA is supported by electrostatic interactions and that the electron transfer between PpcA heme IV and MacA HP heme group have a low thermodynamic barrier. Thus, in addition to the reduction of PpcA by MacA, the relative small difference in the redox potentials of the interacting heme groups and the high cellular abundance of PpcA suggests that, under oxidative stress conditions, PpcA might supply electrons to the peroxidase activity of MacA that protects the bacterial cell from oxidative damage caused by the formation of hydrogen peroxide as a by-product of the single-electron reduction of Fe(III) oxyhydroxide [15].

The results are in agreement with a previous study performed for a cytochrome *c* peroxidase from *Paracoccus pantotrophus* and two redox partners, cytochrome *c* and pseudoazurin, that competitively bind to the same site located in the region of the HP heme [8]. Other interaction studies carried out with a cytochrome peroxidase from *Paracoccus denitrificans* and its natural redox partner, cytochrome c_{550}, showed that the LP heme signals did not display any chemical shift perturbation [16]. Altogether, these results are consistent with the data obtained in the present work, which showed no chemical shift perturbation of the signals of the MacA LP heme in the presence of increasing amounts of PpcA. The K_d values obtained for the complex formed between the two proteins are in the μM range suggesting the formation of a low affinity complex between the redox partners, which is crucial for rapid protein-protein recognition and electron transfer.

4.3 Materials and methods

4.3.1 NMR samples preparation and experiments

For NMR studies, samples were prepared in 8 and 45 mM phosphate buffer, pH 7.1, and NaCl (20 and 100 mM final ionic strength). Samples were prepared in 92% H_2O/8% ^2H_2O or ^2H_2O (99% atom), to observe protein NH or heme substituent signals, respectively. For the 1D ^1H NMR chemical shift perturbation experiments, a MacA sample (180 µM) was titrated with a PpcA solution (6.5 mM) prepared in the same buffer.

The NMR spectra were acquired at 298 K, on a Bruker Avance 600 MHz spectrometer equipped with a triple-resonance cryoprobe. ^1H chemical shifts are reported in parts per million (ppm) calibrated using the water signal as internal reference and the ^{15}N and ^{13}C chemical shifts calibrated through indirect referencing [17]. Before and after all 2D experiments, 1D ^1H NMR spectra were acquired to verify the protein integrity. The pH of the samples was measured before and after each set of NMR experiments to confirm that pH of the solution is maintained. Spectra were processed using TOPSPIN software (Bruker Biospin, Karlsruhe, Germany) and analyzed with program Sparky (T. D. Goddard and D. G. Kneller, SPARKY 3, University of California, San Francisco).

The backbone NH and heme proton signals of PpcA were previously assigned at 298 K, pH 7 and 100 mM ionic strength [7, 18], and were reassigned in this work at 20 mM ionic strength. To measure the impact of the interaction on NMR signals, a series of 1D ^1H NMR spectra of MacA, in the presence of increasing amounts of PpcA, were first acquired to monitor the effect on the downfield-shifted heme methyl signals. Each 1D ^1H NMR spectra were acquired with at least 1024 scans and a sweep width of 96 kHz. To analyze the chemical shift perturbation of heme substituent signals, 2D $^1H,^{13}C$ HMQC and 2D ^1H, ^1H NOESY spectra were acquired for PpcA in the presence and absence of unlabeled MacA. 2D $^1H,^{13}C$ HMQC were acquired with a sweep width of 24 kHz in F_2 and 45 kHz in F_1, and 2D ^1H, ^1H NOESY spectra, with 80 ms mixing-time and a sweep width of 24 kHz in both dimensions. To analyze the chemical shift perturbation on the NH signals, 2D $^1H,^{15}N$ HSQC spectra were acquired for ^{15}N-labeled PpcA in the presence and absence of unlabeled MacA, with a sweep width of 11 kHz in F_2 and 2 kHz in F_1.

To investigate the binding reversibility between PpcA and MacA, 1D ^1H NMR spectra were acquired for PpcA in the absence of MacA and after separation of the proteins by gel filtration chromatography. The mixture was loaded into a XK 16/70 column (GE Healthcare) packed with Superdex 75 (GE Healthcare) connected to an AKTA Prime Plus Chromatography System (GE Healthcare). The efficiency of separation was first analyzed by the inspection of the obtained chromatogram and further confirmed by SDS-PAGE stained with Coomassie blue.

4.3.2 Complex interface and binding affinity

Changes in chemical shifts were analyzed with a two-parameter non-linear least squares fit using a two-site binding model corrected for the dilution effect. The K_d for the molar proportion of 2:1 PpcA/MacA was estimated under fast exchange conditions by fitting the observed chemical shift perturbations of the PpcA heme methyl signal with the Equation 4.1, previously described by Kannt and co-workers [19].

$$\Delta\delta_{Bind} = 0.5\Delta\delta\left(A - \sqrt{A^2 - 4/R}\right) \text{, with } A = 1 + 1/R + K_d\frac{[MacA]+1/R[PpcA]}{[MacA][PpcA]} \tag{4.1}$$

$\Delta\delta_{Bind}$ is the chemical shift perturbation at a given protein ratio; $\Delta\delta$ is the ^{1}H chemical shift difference between the PpcA free form and the complex form; R is the [*PpcA*]/[*MacA*] ratio at a given point; [*MacA*] and [*PpcA*] are the concentrations of MacA and PpcA, respectively. $\Delta\delta$ and K_d were the fitted parameters.

The most affected signals of MacA heme methyls in the presence of PpcA showed a typical behavior of two-site molecular binding. In this analysis, was assumed an independent two-site binding model, described by Equation 4.2, where MacA exists in the free form (F), the singly bound forms (B1 and B2) in which only the primary (high affinity) site or the secondary (low affinity) site is occupied, respectively, and the doubly bound form (B12) [20].

$$\Delta\delta_{Bind} = \frac{[PpcA]}{K_{d1}+[PpcA]}\Delta\delta_{FB1} + \frac{[PpcA]}{K_{d2}+[PpcA]}\Delta\delta_{FB2} \tag{4.2}$$

K_{d1} and K_{d2} are the dissociation constants for the primary and secondary binding, respectively, [*PpcA*] is the concentrations of PpcA, $\Delta\delta_{FB1}$ and $\Delta\delta_{FB2}$ are the ^{1}H chemical shift difference between the free form and the B1 or B2 form, respectively [20].

4.3.3 Molecular docking calculations

The molecular interaction simulations were performed using the easy interface from HADDOCK2.2 Web server [21] using the atomic coordinates of PpcA (PDB ID 2MZ9 [7]) and MacA (PDB ID 4AAL [4]) as a monomer. From NMR experimental data, the active residues were selected as Lys^{18}, His^{20}, Lys^{43}, His^{47}, heme I and IV for PpcA and high potential heme for MacA. The calculated binding interface of MacA is not coincident with the dimer interface.

4.4 References

1. Shelobolina ES, Coppi MV, Korenevsky AA, DiDonato LN, Sullivan SA, Konishi H, Xu H, Leang C, Butler JE, Kim BC, *et al.* (2007) Importance of *c*-type cytochromes for U(VI) reduction by *Geobacter sulfurreducens*. *BMC Microbiol* **7**, 16.

2. Kim BC & Lovley DR (2008) Investigation of direct *vs*. indirect involvement of the *c*-type cytochrome MacA in Fe(III) reduction by *Geobacter sulfurreducens*. *FEMS Microbiol Lett* **286**, 39-44.

3. Ding YH, Hixson KK, Aklujkar MA, Lipton MS, Smith RD, Lovley DR & Mester T (2008) Proteome of *Geobacter sulfurreducens* grown with Fe(III) oxide or Fe(III) citrate as the electron acceptor. *Biochim Biophys Acta* **1784**, 1935-1941.

4. Seidel J, Hoffmann M, Ellis KE, Seidel A, Spatzal T, Gerhardt S, Elliott SJ & Einsle O (2012) MacA is a second cytochrome *c* peroxidase of *Geobacter sulfurreducens*. *Biochemistry* **51**, 2747-2756.

5. Williamson MP (2013) Using chemical shift perturbation to characterise ligand binding. *Prog Nucl Magn Reson Spectrosc* **73**, 1-16.

6. Moss GP (1988) Nomenclature of tetrapyrroles. Recommendations 1986 IUPAC-IUB Joint Commission on Biochemical Nomenclature (JCBN). *Eur J Biochem* **178**, 277-328.

7. Morgado L, Bruix M, Pokkuluri PR, Salgueiro CA & Turner DL (2017) Redox- and pH-linked conformational changes in triheme cytochrome PpcA from *Geobacter sulfurreducens*. *Biochem J* **474**, 231-246.

8. Pauleta SR, Cooper A, Nutley M, Errington N, Harding S, Guerlesquin F, Goodhew CF, Moura I, Moura JJ & Pettigrew GW (2004) A copper protein and a cytochrome bind at the same site on bacterial cytochrome *c* peroxidase. *Biochemistry* **43**, 14566-14576.

9. Meschi F, Wiertz F, Klauss L, Blok A, Ludwig B, Merli A, Heering HA, Rossi GL & Ubbink M (2011) Efficient electron transfer in a protein network lacking specific interactions. *J Am Chem Soc* **133**, 16861-16867.

10. DeLano WL (2002) The PyMOL molecular graphics system. In http://wwwpymolorg.

11. Baker NA, Sept D, Joseph S, Holst MJ & McCammon JA (2001) Electrostatics of nanosystems: application to microtubules and the ribosome. *Proc Natl Acad Sci USA* **98**, 10037-10041.

12. Diaz-Moreno I, Diaz-Quintana A, Ubbink M & De la Rosa MA (2005) An NMR-based docking model for the physiological transient complex between cytochrome *f* and cytochrome c_6. *FEBS Lett* **579**, 2891-2896.

13. Crowley PB, Diaz-Quintana A, Molina-Heredia FP, Nieto P, Sutter M, Haehnel W, De La Rosa MA & Ubbink M (2002) The interactions of cyanobacterial cytochrome c_6 and cytochrome *f*, characterized by NMR. *J Biol Chem* **277**, 48685-48689.

14. Morgado L, Bruix M, Pessanha M, Londer YY & Salgueiro CA (2010) Thermodynamic characterization of a triheme cytochrome family from *Geobacter sulfurreducens* reveals mechanistic and functional diversity. *Biophys J* **99**, 293-301.

15. Aklujkar M, Coppi MV, Leang C, Kim BC, Chavan MA, Perpetua LA, Giloteaux L, Liu A & Holmes DE (2013) Proteins involved in electron transfer to Fe(III) and Mn(IV) oxides by *Geobacter sulfurreducens* and *Geobacter uraniireducens*. *Microbiology* **159**, 515-535.

16. Pettigrew GW, Prazeres S, Costa C, Palma N, Krippahl L, Moura I & Moura JJ (1999) The structure of an electron transfer complex containing a cytochrome *c* and a peroxidase. *J Biol Chem* **274**, 11383-11389.

17. Wishart DS, Bigam CG, Yao J, Abildgaard F, Dyson HJ, Oldfield E, Markley JL & Sykes BD (1995) ^{1}H, ^{13}C and ^{15}N chemical shift referencing in biomolecular NMR. *J Biomol NMR* **6**, 135-140.

18. Dantas JM, Morgado L, Catarino T, Kokhan O, Pokkuluri PR & Salgueiro CA (2014) Evidence for interaction between the triheme cytochrome PpcA from *Geobacter sulfurreducens* and anthrahydroquinone-2,6-disulfonate, an analog of the redox active components of humic substances. *Biochim Biophys Acta* **1837**, 750-760.

19. Kannt A, Young S & Bendall DS (1996) The role of acidic residues of plastocyanin in its interaction with cytochrome *f*. *Biochim Biophys Acta* **1277**, 115-126.

20. Arai M, Ferreon JC & Wright PE (2012) Quantitative analysis of multisite protein-ligand interactions by NMR: binding of intrinsically disordered p53 transactivation subdomains with the TAZ2 domain of CBP. *J Am Chem Soc* **134**, 3792-3803.

21. van Zundert GC, Rodrigues JP, Trellet M, Schmitz C, Kastritis PL, Karaca E, Melquiond AS, van Dijk M, de Vries SJ & Bonvin AM (2016) The HADDOCK2.2 Web server: User-friendly integrative modeling of biomolecular complexes. *J Mol Biol* **428**, 720-725.

5

SOLUTION STRUCTURE AND DYNAMICS OF THE OUTER MEMBRANE CYTOCHROME OMCF[1]

---

[1] Partially reproduced from Dantas JM, Silva MSE, Salgueiro CA, Bruix M (2015) Backbone, side chain and heme resonance assignments of cytochrome OmcF from *Geobacter sulfurreducens*, Biomol NMR Assign 9, 365-368 (doi: 10.1007/s12104-015-9611-5) and Dantas JM, Silva MA, Pantoja-Uceda D, Turner DL, Bruix M, Salgueiro CA (2017) Solution structure and dynamics of the outer membrane cytochrome OmcF from *Geobacter sulfurreducens*, Biochim Biophys Acta 1858, 733–741 (doi: 10.1016/j.bbabio.2017.03.007), in accordance with the Editors' Copyright Policy.

5. Solution structure and dynamics of the outer membrane cytochrome OmcF

OmcF is associated to the OM of *G. sulfurreducens* by a small anchor encompassing residues 1-19 [1]. The amino acid sequence of OmcF is indicated in Fig 5.1, showing both the signal peptide/transmembrane helix and soluble polypeptide chain. Only the soluble portion of the protein was cloned into the expression vector and further studied in this Thesis.

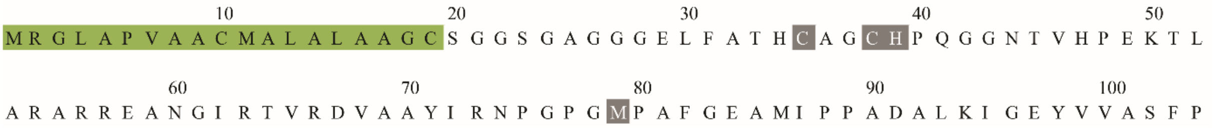

Fig 5.1 Amino acid sequence of OmcF. The signal peptide/transmembrane helix is highlighted in green. The heme binding residues are boxed in gray.

The crystal structure of the soluble region of OmcF was previously determined in the oxidized form and the global fold of OmcF shares similarities with cytochrome c_6 from the green alga, *Monoraphidium braunii* [2, 3]. The midpoint redox potential of OmcF was determined at pH 7 and 8, yielding the values +180 mV and +127 mV *versus* NHE, respectively [2]. The increase in the reduction potential values with pH decreasing leads to a progressive stabilization of the reduced form. Such modulation of the heme reduction potential with the pH (redox-Bohr effect) can be explained in a pure electrostatic basis since the progressive protonation of an acid/base group(s) near the heme is expected to increase its affinity for electrons with the concomitant increase of the reduction potential values. The notable redox-Bohr effect observed at physiological pH range for *G. sulfurreducens* cellular growth might be functionally relevant. This is in clear contrast with the data obtained for cytochrome c_6 from the green alga *M. braunii,* which shows essentially no redox-Bohr effect in the same pH range and a much higher reduction potential value (+358 mV at pH 7), regardless of the high structural similarity between the two cytochromes.

To obtain structural insights into the functional mechanism of OmcF the solution structure of this cytochrome was determined in the fully reduced state by NMR spectroscopy. The data obtained were also used to study the dynamic properties of the polypeptide backbone, to map the structural origin of the redox-Bohr effect and identify the redox-linked conformational changes in OmcF.

5.1 Results and discussion

5.1.1 Heme spin state and axial ligands of OmcF

1D ^{1}H NMR spectra of cytochromes provide valuable information about the heme spin-state and axial ligand coordination. The 1D ^{1}H NMR spectrum of cytochrome OmcF display quite distinct features in the reduced and oxidized states (Fig 5.2).

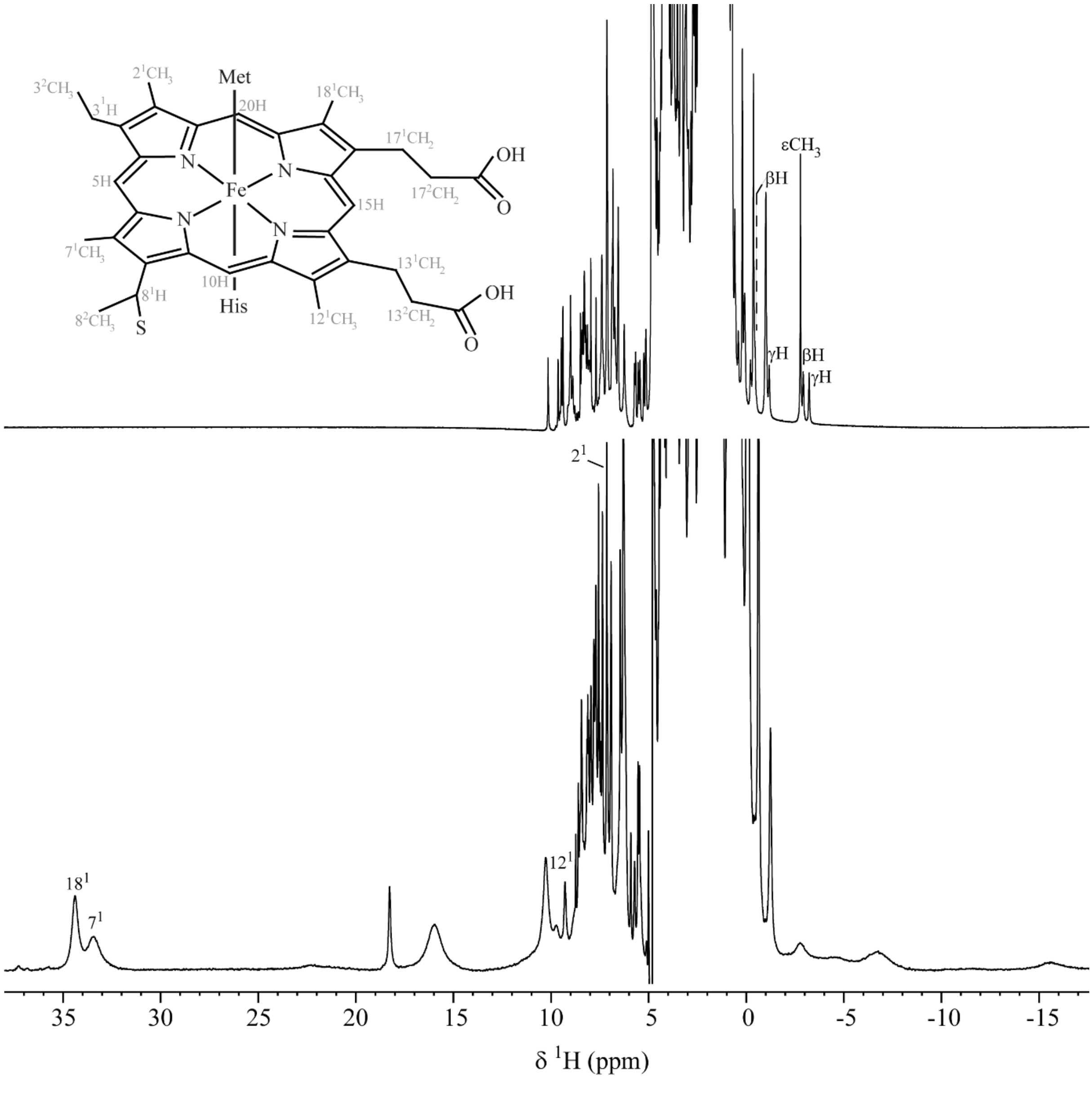

Fig 5.2 1D ^{1}H NMR spectra of the reduced (upper) and oxidized (lower) OmcF obtained at 298 K, pH 7 and final ionic strength 100 mM. Signals corresponding to the side chain of the heme axial methionine protons are indicated in the reduced spectrum. The signals of the heme methyls are labeled in the oxidized spectrum. The inset shows a diagram of a heme *c* showing the axial ligands His and Met. The IUPAC nomenclature for tetrapyrroles is indicated in gray [4].

In the reduced state, the signals are sharp and spread over the 10 to -5 ppm region. Due to the paramagnetic effect of the heme iron unpaired electron in the oxidized state the signals are broader and span a wider spectral region ranging from 35 to -18 ppm. Moreover, the presence of a relatively intense signal in a low-frequency region of the NMR spectra in the reduced protein (-2.84 ppm) suggests that a methionine residue coordinates the heme iron. In fact, the typical pattern of heme axial methionine signals includes a three-proton intensity peak at approximately -3 ppm, and up to four resolved one-proton intensity peaks in the low-frequency region of the spectrum due to the heme ring current effects [5]. Such a pattern is clearly observable in the reduced spectrum of cytochrome OmcF, confirming that the heme group is axially coordinated by a methionine (Fig 5.2).

Thus, from the NMR studies it can be concluded that the heme iron is hexacoordinated, diamagnetic (Fe(II), S=0) and paramagnetic (Fe(III), S=1/2) in the reduced and oxidized forms, respectively. To further investigate the spin state of OmcF, we analyzed the temperature dependence of the heme methyl proton chemical shifts in the range of 278 to 308 K, in the oxidized form. These signals were assigned as previously described [6]. Two of the heme methyls (18^1CH_3 and 7^1CH_3) are more downfield shifted (34.2 and 33.0 ppm, respectively) than the other two (12^1CH_3 and 2^1CH_3, 9.1 and 7.1 ppm, respectively). These chemical shifts are similar to those observed for the horse cytochrome *c* at 303 K: 34.6 (18^1CH_3), 31.8 (7^1CH_3), 10.1 (12^1CH_3) and 7.1 ppm (2^1CH_3) [7]. The heme methyl pairs $18^1CH_3/7^1CH_3$ and $2^1CH_3/12^1CH_3$ are attached to diametrically opposed pyrrole rings of the porphyrin (see inset in Fig 5.2), and the pattern of chemical shifts results from the asymmetry in the distribution of the delocalized unpaired electron on the molecular orbitals of the porphyrin [7].

The OmcF heme methyl signals follow Curie law behavior as their chemical shifts decrease with increasing temperature (Fig 5.3). Nonetheless, heme methyls 7^1CH_3 and 18^1CH_3 showed a small curvature above 296 K, suggesting some high-spin character, possibly caused by weakening of the Met-Fe bond.

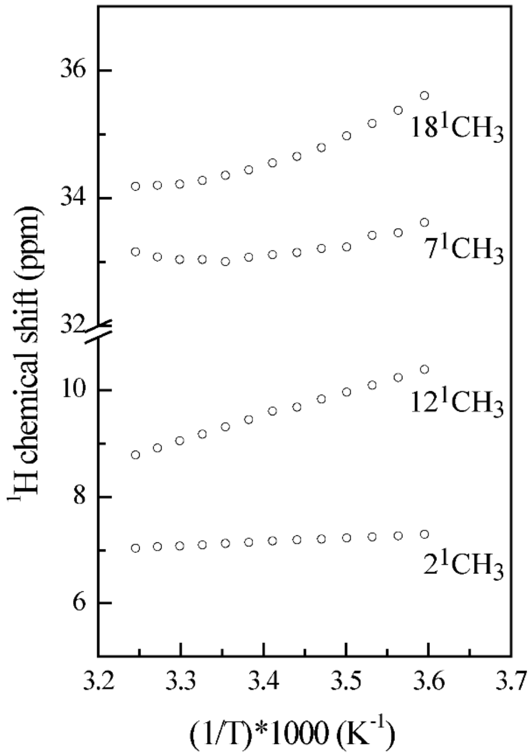

Fig 5.3 Temperature dependence of the OmcF heme methyl signals in the oxidized form at pH 7 and 100 mM ionic strength.

5.1.2 Sequential assignment and structure calculations

To facilitate the assignment of the OmcF NMR signals in the reduced state, in particular those of ^{1}H, ^{13}C, ^{15}N backbone and side chain signals, spectra were acquired at pH 5.3 and 308 K. The combined analysis of 2D ^{1}H,^{15}N HSQC and a series of 3D NMR spectra (3D CBCANH, 3D CBCA(CO)NH, 3D HNCA, 3D HN(CO)CA) led to the near-complete assignment of backbone signals ^{15}N (99 %), ^{1}HN (100 %), ^{13}Cα (100 %) and for ^{13}Cβ (100 %).

The 2D ^{1}H,^{15}N HSQC NMR spectrum of labeled reduced OmcF is indicated in Fig 5.4 with the backbone nitrogen resonances assigned as well as those of the side chains of arginine (Arg^{54}, Arg^{56}, Arg^{63}, Arg^{66}, Arg^{73}), asparagine (Asn^{44}, Asn^{60}, Asn^{74}), glutamine (Gln^{41}) and histidine (His^{39}) residues. To extend the assignment to aliphatic protons such as ^{1}Hα, ^{1}Hβ, ^{1}Hγ, ^{1}Hδ and ^{1}Hε and aliphatic carbons ^{13}Cγ, ^{13}Cδ and ^{13}Cε the 2D ^{1}H,^{13}C HSQC and a series of 3D spectra namely HCC(H)-TOCSY, HC(C)H-TOCSY, ^{13}C NOESY-HSQC and ^{15}N NOESY-HSQC were analyzed. The confirmation of the assignment and the aromatic ring protons were assigned based on 2D ^{1}H, ^{1}H COSY (correlation spectroscopy), 2D ^{1}H, ^{1}H TOCSY and 2D ^{1}H, ^{1}H NOESY NMR spectra.

Compared to the ring-current effects generated by the amino acid aromatic side chains in non-heme proteins, those produced by the heme group are much stronger. Therefore, the chemical shifts of the nuclei located in the proximities of heme groups differ significantly from equivalent residues in non-heme proteins, in particular the heme axial ligands (His^{39} and Met^{79}). In fact, the ring proton Hε_1 and Hδ_2 signals are strongly up-field shifted and are observed at 1.13 ppm and 0.52 ppm, respectively. This clearly contrasts with the typical positions found for these signals in non-heme proteins (around 7–8 ppm). Also, the signals correspondent to Hβ of heme axial histidines are typically up-field shifted by at least 2 ppm compared to a non-heme bound axial histidine. The effect of the ring current shifts is also extended to the nitrogen atom Nδ_1 of the axial histidine side chain, which appear in very characteristic positions (162.2 ppm) in the 2D ^{1}H,^{15}N HSQC spectrum (Fig 5.4 A). Similarly, for the axial methionine Met^{79}, the side chain protons closely located to the heme iron are strongly upfield shifted compared to non-axial methionine residues: Hβ's (-0.52 and -3.01 ppm); Hγ's (-1.27 and -3.32 ppm) and Hε (-2.86 ppm). Interestingly, in the 2D ^{1}H,^{15}N HSQC NMR spectrum of OmcF some of the NH signals of residues in the region 52-58, 63-69 and 99-103 showed considerable broadness (Fig 5.4 A). This effect is observed in both dimensions, for example in the ^{15}N dimension for the NH signal of residue Arg^{54} and in the ^{1}H dimension for the NH signal of residue Arg^{56}.

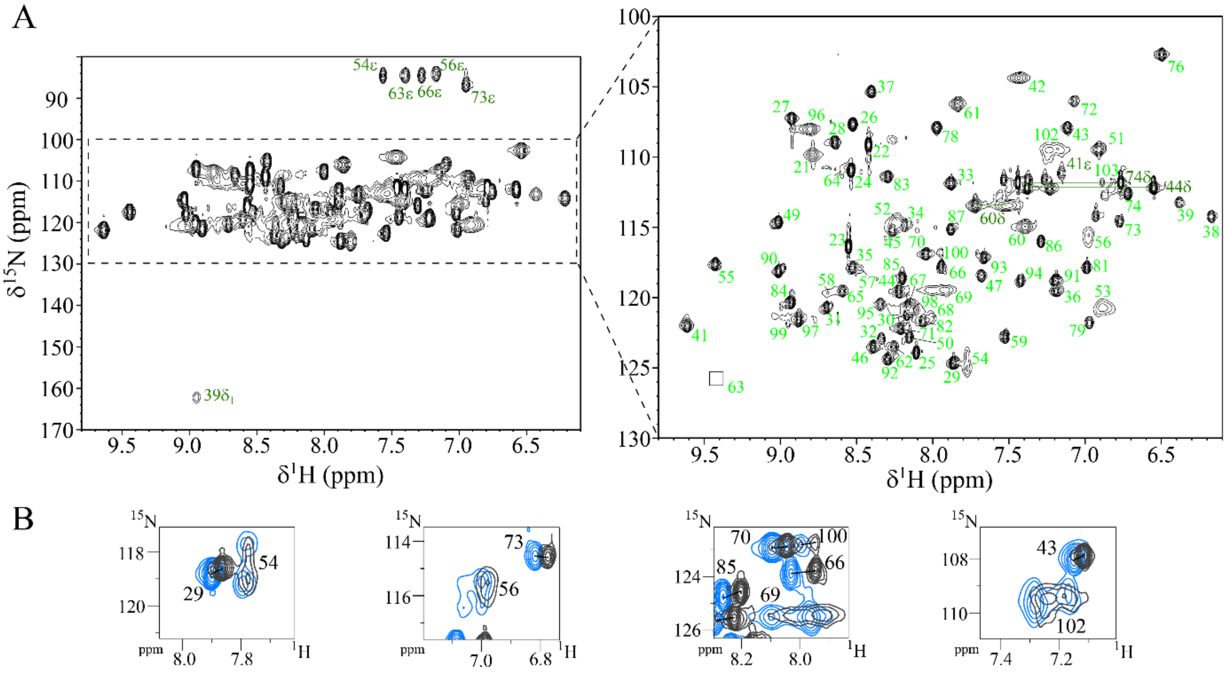

Fig 5.4 2D ^{1}H,^{15}N HSQC spectra of OmcF in the fully reduced state. (A) NMR spectra of ^{15}N-enriched OmcF (2 mM, 45 mM sodium phosphate buffer pH 5.3, 100 mM ionic strength, 308 K, 800 MHz). Light green and dark green labels represent ^{1}H–^{15}N connectivities for backbone and side-chains groups (Nε of Gln^{41}; Nε of Arg^{54}, Arg^{56}, Arg^{63}, Arg^{66} and Arg^{73}; Nδ of Asn^{44}, Asn^{60} and Asn^{74}; and Nδ_1 of His^{39}), respectively. The right-handed spectrum was acquired with a smaller spectral window in ^{15}N dimension (35 *versus* 130 ppm) to enhance the resolution compared to the left-handed one. The empty box corresponds to the position of the weak signal of NH signal of Arg^{63} only visible at lower contour levels. (B) Overlay of selected regions of 2D ^{1}H,^{15}N HSQC NMR spectra of ^{15}N-enriched OmcF in the fully reduced form (as in a) at 308 K (black contours) and 298 K (blue contours).

To evaluate the features of these NH signals, 2D ^{1}H,^{15}N HSQC NMR spectra were acquired at different temperature (298–313 K) and pH (4.6–9.3) ranges. The observed line-broadening dependence with temperature suggests that these group of signals are in slow to intermediate exchange rate between two conformations, on the NMR time scale (Fig 5.4 B). This might be relevant towards the recognition of OmcF physiological partners.

The ^{1}H, ^{13}C and ^{15}N chemical shifts have been deposited in the BMRB (http://www.bmrm.wisc.edu) under the accession number 25455 (Table A.5, Appendix). These signals were reassigned at pH 7 and 298 K for the determination of OmcF solution structure (BMRB accession number 34064), matching the physiological conditions for *G. sulfurreducens* growth. A summary of the sequential connectivities between HN, Hα and Hβ protons is shown in Fig 5.5.

Fig 5.5 Sequential NOE connectivities involving NH, Hα and Hβ protons observed in the 2D ^{1}H,^{1}H NOESY spectrum for reduced cytochrome OmcF.

For structure calculations, distance restraints of OmcF were obtained from the 2D ^{1}H,^{1}H NOESY spectrum acquired in 92% H_2O /8% ^2H_2O with a mixing time of 50 ms. The assigned cross-peaks were integrated and converted into volume restraints, resulting in 1056 lower limits for volumes (lov) and 1486 upper limits (upv) (Table 5.1).

Table 5.1 Summary of restraint violations and quality analysis for the final family of solution structures for cytochrome OmcF from *G. sulfurreducens*.

Parameter	
Type of distance restraint	
Intra-residue	724
Sequential	639
Medium range ($2 \leq \|i - j\| < 5$)	550
Long range ($\|i - j\| \geq 5$)	629
Total	2542 *(1056 lov + 1486 upv)*
Upper distance limit violations	
Average maximum	0.16 ± 0.05
Number of consistent violations (> 0.2Å)	0
Lower distance limit violations	
Average maximum	0.22 ± 0.02
Number of consistent violations (> 0.2Å)	0
Van der Waals violations	
Average maximum	0.18 ± 0.00
Number of consistent violations (> 0.2Å)	0
Ramachandran Plot (%) [a]	
Most favored regions	61
Additionally allowed regions	32
Generously allowed regions	7
Disallowed regions	0
Stereospecific Assignments [b]	24
Precision	
Average pairwise rmsd backbone (Å)	0.37 ± 0.08
Average pairwise rmsd heavy atoms (Å)	0.98 ± 0.11

[a] Values obtained with iCing
[b] Analysis with GLOMSA

These values were used as input for the program PARADYANA [8] together with a set of 43 fixed upper limit distances (associated with ring closure in the flexible proline residues and heme groups, and the attachment of His and Met ligands). During the calculations, the structures were analyzed using the program GLOMSA modified to take NOE volumes as input [9] and 24 stereospecific assignments were made for diastereotopic pairs of protons or methyl groups. The effect of spin diffusion introduces an uncertainty into the conversion of experimental data to distance constraints. These effects were simulated by complete relaxation matrix calculations based on the initial protein structures and, accordingly, a parameter was set in the program PARADYANA to loosen all distance restraints by 5%. An average of 32 NOE restraints per amino acid residue (13 lovs and 19 upvs) and 508 per heme residue (211 lovs and 297 upvs) were used for the final calculation. The distribution of the number of constraints is not uniform along the protein sequence, as the heme group attached to positions 38 shows many long-distance contacts (Fig 5.6).

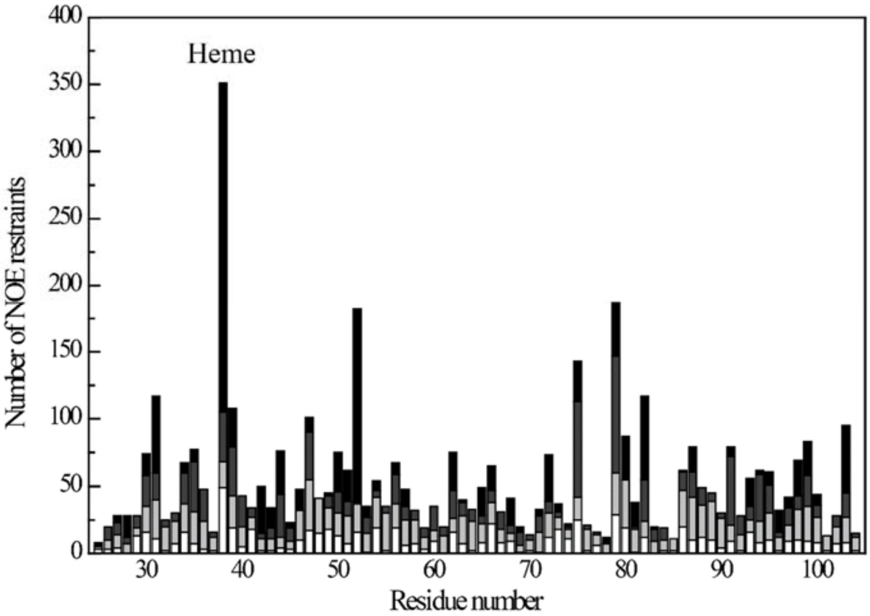

Fig 5.6 Number of restraints per residue used for the calculation of the cytochrome OmcF solution structure. Bars are white, light gray, dark gray and black for intra residue, sequential, medium and long-range restraints, respectively. Residue 38 also includes restraints to the heme group.

Despite the conformation of the axial methionine being *R* in the oxidized structure [2], calculations were carried out in parallel using methionine ligand to the heme iron with *R* or *S* configurations of the sulphur atom. This allowed us to investigate the redox-dependent configuration of the axial methionine, since a few cases have shown dependence of heme axial methionine on redox state (*e.g.* cytochrome c_{552} from *Nitrosomonas europaea* and cytochrome c_{552} from *Hydrogenobacter thermophilus*) [10, 11]. In the case of OmcF the methionine ligand with sulphur in the *R* configuration resulted in significantly lower target functions and was therefore used in the final family of structures. This result indicates that the coordination geometry of the sulphur is conserved regardless the redox state of the protein indicating that the protein is designed to minimize reorganization energy and optimize electron transfer rates.

5.1.3 Quality and analysis of the structures

The NMR solution structure was determined for cytochrome OmcF in the reduced form, excluding the highly flexible N-terminus region between the residues Ser^{20} to Gly^{24} due to the lack of NOE information. The relaxation studies confirm this flexibility, since the ^{1}H-^{15}N NOE spectrum showed negative signals for the N-terminal residues, which correlates with rapid large-amplitude internal motions (see section 5.1.5). Furthermore, Pokkuluri and co-workers [2] determined the crystal structure of the cytochrome in the oxidized form and only observed electron density between residues Gly^{26} and Pro^{104}.

In this Thesis, twenty structures with the lowest target function values (from 1.35Å^2 to 1.55Å^2, average value 1.46Å^2, 15 % range from the lowest value) were selected as being representative of the solution structures of the reduced cytochrome. The structures superimpose with an average backbone (NH-Cα-CO) rmsd of 0.37Å and a heavy atom rmsd of 0.98Å with respect to the mean structure (Fig 5.7).

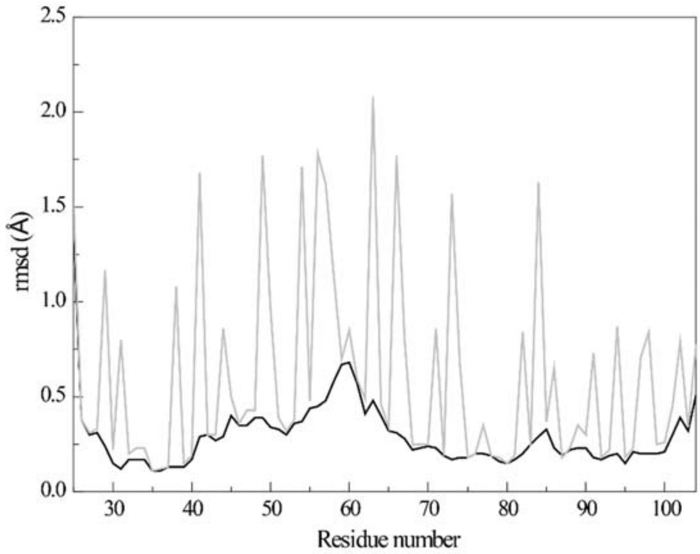

Fig 5.7 Average pairwise backbone (black) and heavy atom (gray) rmsd values per residue of the family of 20 conformers obtained for the cytochrome OmcF solution structure.

The backbone is very well defined and the amino acid side-chains showing larger conformational variability correspond to regions with higher solvent exposure. The N- and the C-terminus are more disordered showing higher rmsd values, but besides that, the region between residues Ala^{53} and Thr^{64} also shows high conformational variability for the backbone atoms in agreement with the dynamic data described below. The statistics for this family of structures are shown in Table 5.1. The Ramachandran plot shows 61% of the residues in the most favored regions, 32% in the additionally allowed and 7% in the generously allowed regions. A total of 62 hydrogen bonds were identified in the family of 20 structures with the program MOLMOL [12], 22 of which were present in at least 50% of the structures.

5.1.4 Comparison of cytochrome OmcF reduced and oxidized structures

The OmcF solution structure (Fig 5.8) displays five α-helices in the following regions Gly^{27}-His^{34}, Pro^{40}-Gly^{42}, Arg^{54}-Asn^{60}, Asp^{67}-Arg^{73}, Pro^{89}-Tyr^{98} (Fig 5.8 B) and the heme group is axially coordinated by His^{39} and Met^{79}. The secondary elements previously predicted by the program TALOS-N based on the OmcF assigned chemical shifts [13, 14], are in agreement with the secondary elements shown by the solution structure.

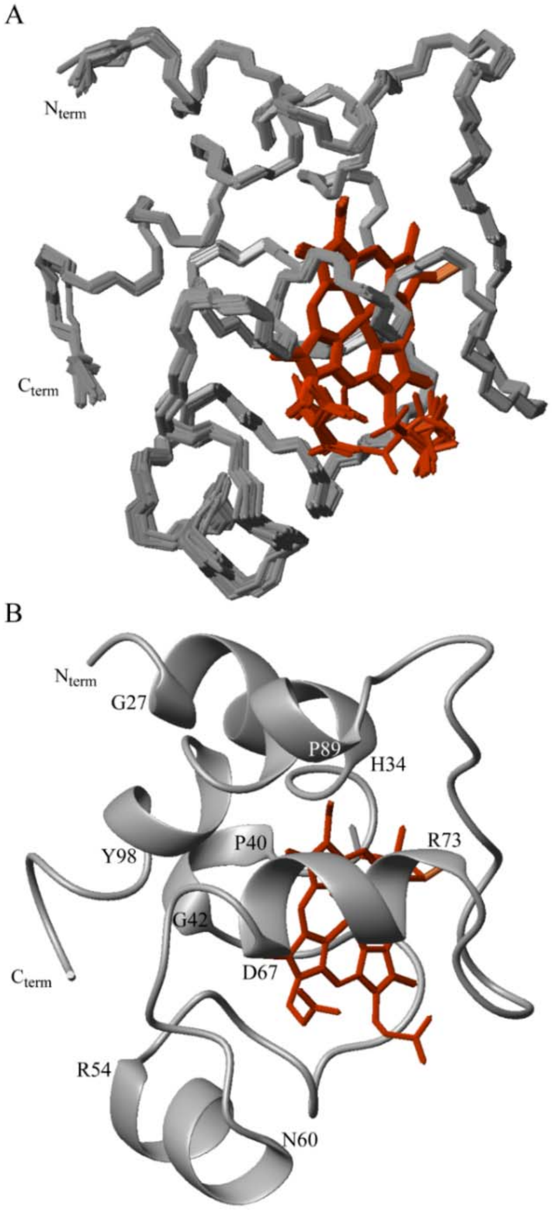

Fig 5.8 Solution structure of OmcF in the reduced state. (A) Overlay of the 20 lowest energy NMR structures of cytochrome OmcF at pH 7 and 298K. Superimposition was performed using all the heavy-atoms. The peptide chain and the hemes are color-coded gray and red, respectively. (B) Ribbon diagram of OmcF solution structure. Figures were produced using MOLMOL [12].

The lowest-energy NMR structure was compared with the oxidized one previously determined by X-ray crystallography (Fig 5.9) [2]. The comparison between the structures showed that the global rmsd value is 1.39 Å for backbone atoms. Overall, the structures are quite similar but some differences are observed in the polypeptide region of the residues Ala^{53}-Ile^{62}, Asn^{74}-Gly^{78}, Glu^{84}-Ala^{90}, the N-terminus (residue Gly^{26}) and C-terminus (residues Val^{100}-Pro^{104}). Interestingly some of these regions have the lower values of the dynamic S^2 order factor (see section 5.1.5). The structural differences observed between the oxidized and reduced structures suggest that the more affected regions are probably involved in the fine-tuning of the protein local structure for effective interaction with electron donors and acceptors. This information can be explored in the future to rational engineering OmcF by site-directed mutagenesis to maximize electron transfer effectiveness when the protein meets its redox partners and therefore contribute to the optimization of OmcF dependent EET processes.

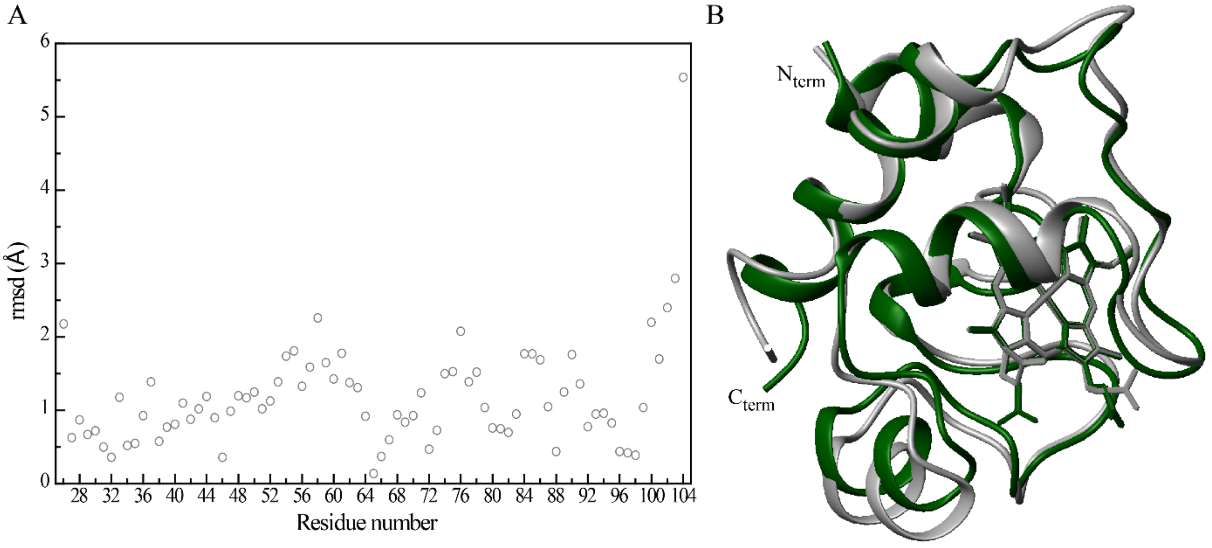

Fig 5.9 Comparison of OmcF lowest-energy solution structure with OmcF crystal structure (PDB ID: 3CU4 [2]). Structures were superimposed in MOLMOL using backbone atoms. (A) Average rmsd between each pair of structures. (B) OmcF solution structure superimposed on the crystal structure. OmcF solution and crystal structures are colored gray and green, respectively. Figure was produced using MOLMOL [12].

5.1.5 Backbone dynamics

^{15}N NMR relaxation was used to characterize the dynamic properties of OmcF in solution. The relaxation parameters T_1, T_2 and NOE were determined at 600 and 800 MHz (Fig 5.10). Relaxation data were obtained for the NH signals of all residues, except for proline residues (positions 40, 48, 75, 77, 80, 88, 89 and 104), the two first residues (Ser^{20} and Gly^{21}) and Arg^{54}, Glu^{58}, Arg^{63}, Thr^{64}, Val^{68}, Val^{100}, Ala^{101} and Phe^{103} that showed considerable broadness in the spectra (see section 5.1.2).

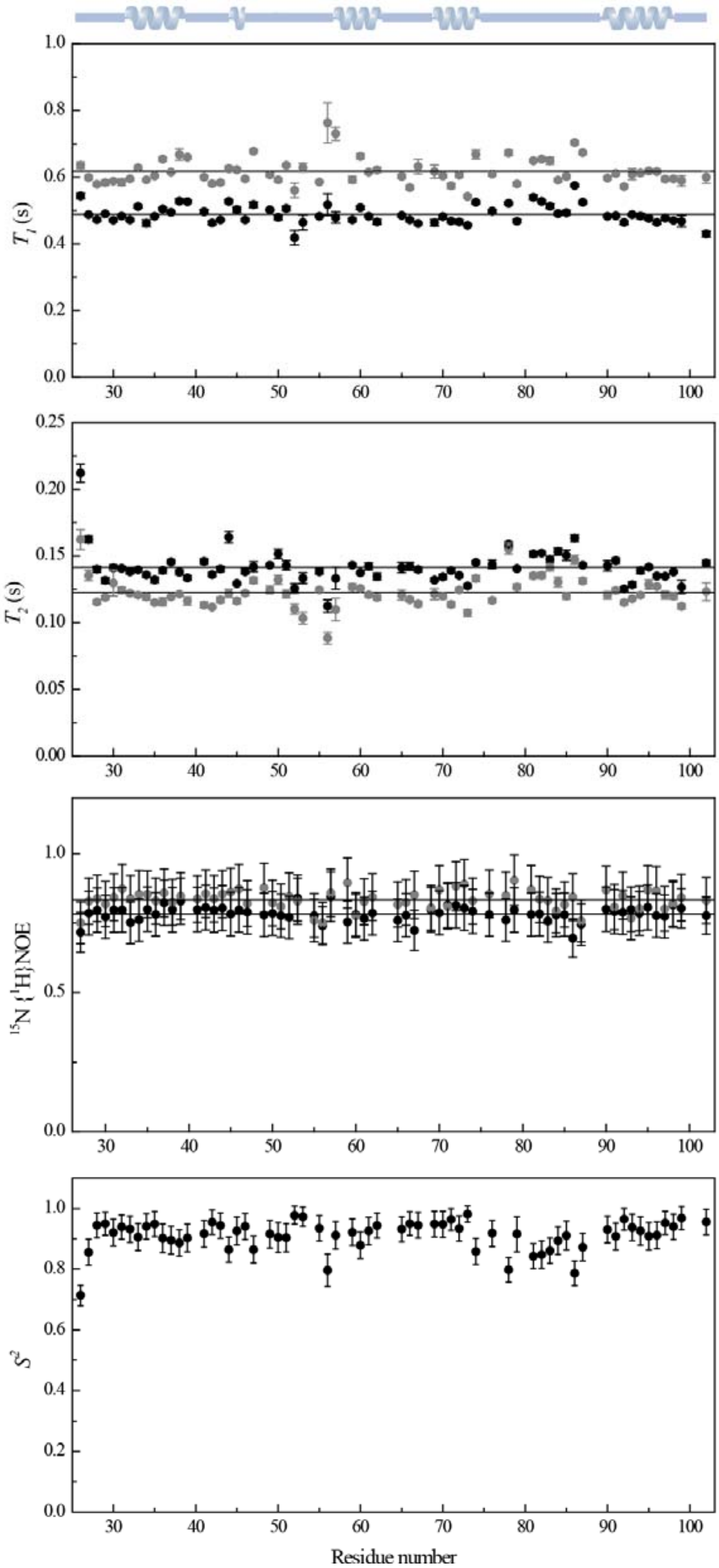

Fig 5.10 ^{15}N relaxation parameters for the cytochrome OmcF backbone in the reduced state. (A) longitudinal T_1 relaxation times (B) transverse T_2 relaxation times, (C) Heteronuclear ^{15}N{^{1}H} NOEs and (D) order parameter, S^2, calculated from the solution NMR OmcF structure [15, 16]. Gray circles 800 MHz and black circles 600 MHz; solid straight lines represent the average T_1, T_2 and NOE at the respective magnetic field; open circles 800 MHz and closed circles 600 MHz. Secondary-structure elements are shown on the top of the figure.

To calculate the average values for T_1, T_2 and NOE only the data from residue Gly^{26} up to the C-terminal region were considered, since the region of N-terminal is highly flexible and the values for relaxation parameters in this region are very different from the remaining values. The average values for T_1 are 488 ± 27 and 617 ± 40 ms and for T_2 values are 141 ± 12 and 123 ± 11 ms; the average NOE value is 0.78 ± 0.04 and 0.83 ± 0.04, measured at 600 and 800 MHz, respectively. Good correlation was observed between structure and experimental relaxation data. Most residues in regular secondary structure elements exhibited heteronuclear NOE values close to the theoretical maximum indicating high rigidity in these regions (Fig 5.10).

The overall differences in the T_1 values are not significant. Therefore, greater variability was clearly observed in the NOE and T_2 data. High T_2 values correlate with a decrease in the NOE ratio in the region between Gly^{78} and Ile^{87}, and the six residues at the N-terminus (positions Gly^{22}, Ser^{23}, Gly^{24}, Ala^{25}, Gly^{26} and Gly^{27}) indicating motions on the ps-ns time scale. These two regions are the more flexible ones and have, correspondingly, low S^2 values (see below). On the other hand, the region between Leu^{52} and Arg^{57} located in the third α-helix of OmcF showed lower NOE and T_2 values with respect to the mean, which indicates that this region is affected by conformational exchange processes in the μs-ms time scale.

The average value of the order parameter, S^2, is 0.91± 0.05 (Fig 5.10) showing that, globally, OmcF in solution has a high degree of order on the ps-ns time scale. In general, residues in loop regions have slightly lower values. The calculated global rotational diffusion correlation time (τ_m) was 4.83 ± 0.05 ns. This value is in good agreement with the shape and the small size of the protein. The principal components of the inertia tensor, calculated for the NMR structure, have relative values of 1.00, 0.98, and 0.71. These values indicate that the shape deviates from that of a sphere and approaches a prolate ellipsoid. In agreement with these findings, the diffusion tensor that better explained the NMR relaxation data was anisotropic, with different values for the two components (parallel and orthogonal) of the tensor giving a value of $D_{\|}/D_{\perp}$ of 0.87±0.07. Based on all these results, a subset of measured relaxation data for the amide ^{1}H-^{15}N pairs (64 of a total of 81) was analyzed using the model-free formalism to calculate the corresponding dynamical parameters. Most data could be satisfactorily described by the simplest dynamical model, which describes the internal dynamics of the ^{1}H-^{15}N pair in terms of a generalized order parameter, S^2, without any internal correlation time corresponding to fast motions. For residue Arg^{56} only, it was necessary to include a contribution of slow motions to the transverse relaxation time, on the microsecond to μs-ms time scale. This fact, together with the observation that some of the backbone NH signals of this region showed considerable broadness in the 2D ^{1}H,^{15}N HSQC NMR spectra, impairing the measurement of the relaxation data, suggest that this region could be a hub for interactions with other protein or compounds.

5.1.6 pH-linked conformational changes

The pH titration of the OmcF backbone NH signals is indicated in Fig 5.11. The most affected signals ($\Delta\delta_{avg} > 0.2$ ppm) are Thr^{33}, His^{34}, His^{47}, Glu^{49}, Leu^{52} and Gly^{76} , which are in two distinct regions. Residues Thr^{33} and His^{34} are in the N-terminal α-helix and the other four residues are in the region of the heme propionates. Analysis of the pH dependence of the NH chemical shifts showed that Thr^{33} and His^{34} have two distinct pK_a values: 5.6 and 7.9 for Thr^{33} and 5.5 and 8.0 for His^{34}. In contrast, all the other residues display only one pK_a value: 7.0, 7.4, 7.7 and 7.8 for His^{47}, Glu^{49}, Leu^{52} and Gly^{76}, respectively. Therefore, the data obtained for the two sets of residues indicates that their pH-linked conformational changes have different origins.

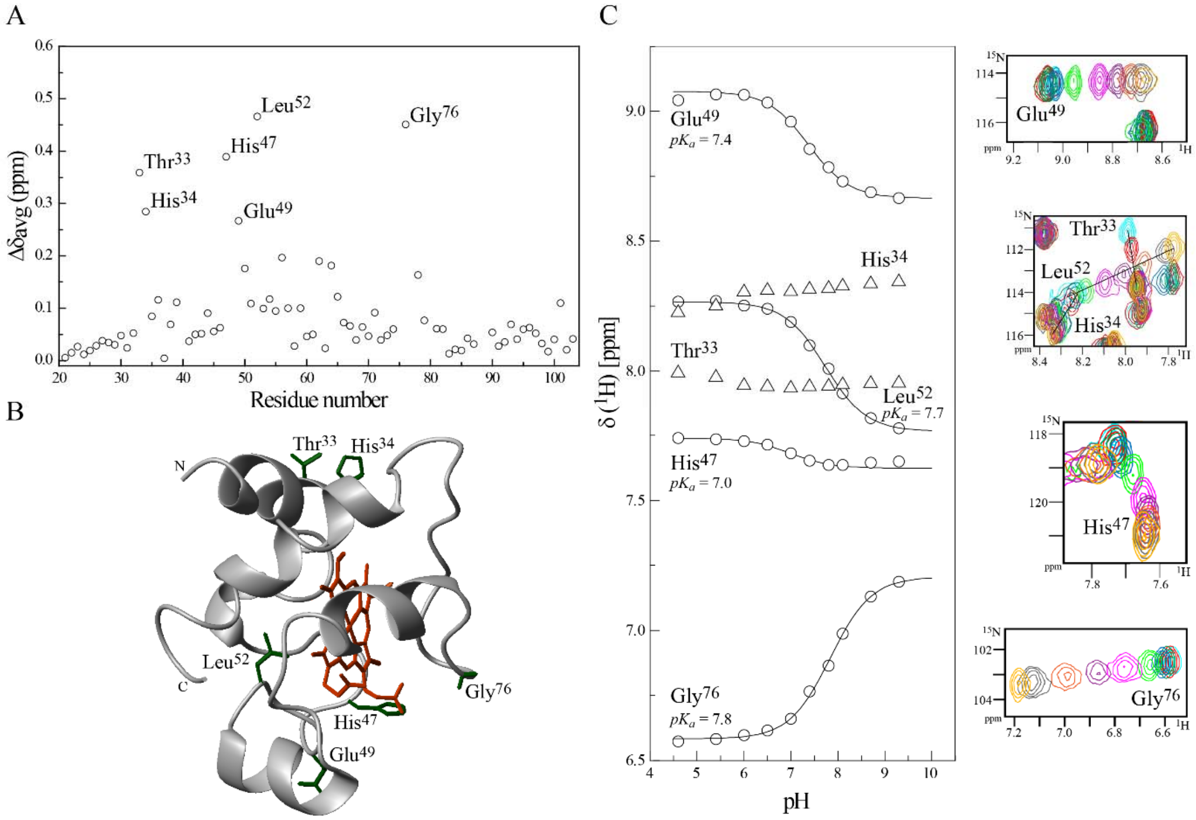

Fig 5.11 pH-linked conformational changes in cytochrome OmcF. (A) Average chemical shift differences ($\Delta\delta_{avg}$) between pH 4.6 and 9.3. (B) Mapping of the residues showing large pH-dependent shifts (green) on the OmcF solution structure. The OmcF backbone and the heme group is colored gray and red, respectively. Figure was produced using MOLMOL [12]. (C) pH titration data of the most affected OmcF amide signals. In the expansion of each 2D ^{1}H,^{15}N HSQC NMR spectrum pH increases from light blue to yellow.

Potentiometric redox titrations followed by visible spectroscopy previously measured at pH 7 and 8 for OmcF [2] showed a significant pH dependence of the reduction potential values. The significant redox-Bohr effect observed, seen as a 53 mV change in the reduction potential values (+180 mV and +127 mV *versus* NHE for pH 7 and 8, respectively) correlates with the pK_a values obtained for the amide residues of His^{47}, Glu^{49}, Leu^{52} and Gly^{76} in this study (Fig 5.11 C). The fact that all backbone NH signals of these residues displayed pK_a values in the pH range from 7 to 8, for which a significant redox-Bohr effect was also observed, indicates that they are near the redox-Bohr center of OmcF whose protonation/deprotonation affect their chemical shifts. Surprisingly, despite the high structural similarity observed between OmcF and cytochrome c_6 from *M. braunii*, essentially no redox-Bohr effect was observed between pH 7 and 8 for the latter [17].

In the crystal structure of OmcF the side chain of His^{47} is disordered but it is well defined in the family of the structures obtained for the fully reduced protein in solution (Fig 5.11 B). Interestingly, the equivalent residue in cytochrome c_6 from *M. braunii* is Ile^{27}. The extra histidine near the heme propionate groups in OmcF (His^{47}), and the typical pK_a value of its side chain close to the circumneutral pH, suggests that it is likely to be the redox-Bohr center. Therefore, the protonation/deprotonation of the His^{47} side chain modulates the redox potential of the heme group and could implicate OmcF protein in electron and proton transfer processes. On the other hand, the strong dependence of the heme midpoint reduction potential, in the physiological pH range, indicates that the protein can be redox active in wider environmental pH and redox potential windows, a feature particularly relevant as OmcF was shown to participate in EET to various terminal acceptors [1, 18, 19].

5.2 Conclusions

The structure of cytochrome OmcF determined in this study constitutes the first solution structure of an outer membrane cytochrome from *G. sulfurreducens*. The polypeptide segment formed by residues from Leu^{52} to Arg^{57} was identified as the most dynamic segment in the μs-ms time scale by analysis of the ^{15}N relaxation parameters obtained for the backbone NH signals. This segment may be involved in interaction with other molecules. The analysis of the chemical shift variation of the backbone and side chain NH signals with pH allowed mapping of the pH-linked conformational changes caused by protonation/deprotonation of the redox-Bohr center. The backbone and heme signal assignment together with the solution structure of OmcF will be used to assist in the rational design of mutants and in the mapping of interaction sites with redox partners, an essential step to the understanding of EET in *G. sulfurreducens*.

5.3 Materials and methods

5.3.1 NMR samples preparation and experiments

NMR samples (2 mM) were prepared in 45 mM sodium phosphate buffer pH 5 and 7 with 100 mM NaCl and 0.04 % sodium azide. For the sequence-specific assignment uniformly ^{13}C,^{15}N-labeled OmcF was prepared in 92%H_2O/8%^2H_2O. For the assignment of heme protons and structure calculations unlabeled OmcF was prepared in ^2H_2O (99 % atom) and in 92% H_2O/8%^2H_2O, respectively. For the experiments in the reduced state samples were fully reduced directly in the NMR tube with gaseous hydrogen in the presence of catalytic amounts of the enzyme hydrogenase from *Desulfovibrio vulgaris* (Hildenborough), as previously described [20, 21]. The pH values of the samples were checked with a glass micro electrode and were not corrected for isotope effects.

The NMR spectra were acquired on a Bruker Avance 800 MHz or 600 MHz spectrometer equipped with a triple-resonance cryoprobe. ^1H chemical shifts are reported in parts per million (ppm) ad were calibrated using the water signal as internal reference and the ^{15}N and ^{13}C chemical shifts were calibrated through indirect referencing [22]. Before and after all 2D and 3D experiments, 1D ^1H NMR spectra were acquired to verify the protein integrity. The pH of the samples was measured before and after each set of NMR experiments to confirm that pH of the solution is maintained. Spectra were processed using TOPSPIN software (Bruker Biospin, Karlsruhe, Germany) and analyzed with program Sparky (T. D. Goddard and D. G. Kneller, SPARKY 3, University of California, San Francisco).

For the assignment of the OmcF heme proton signals in the reduced state, 2D ^1H,^1H NOESY (100 ms, mixing-time) and 2D ^1H,^1H TOCSY (45 ms) experiments were acquired with 2048 (F_2) x 128 (F_1) data points for a sweep width of 10823 Hz with 64 scans per increment in a Bruker Avance III 600 spectrometer. The assignment of the heme substituent signals was further confirmed during the structure calculations. On the other hand, for the assignment of the heme signals in oxidized state, 2D ^1H,^1H NOESY (25 ms) was acquired with 4096 (F_2) x 512 (F_1) data points for a sweep width of 41667 Hz with 136 scans per increment and 2D ^1H,^{13}C HMQC was acquired with 4096 (F_2) x 256 (F_1) data points for a sweep width of 41667 (^1H) Hz and 30181 (^{13}C) Hz, with 320 scans per increment. These last experiments were acquired for the unlabeled sample prepared in ^2H_2O.

The temperature dependence of OmcF heme methyl signals of OmcF was probed by acquiring a series of 1D ^1H NMR spectra in the oxidized state, in the range 278 – 308 K. 1D ^1H NMR spectra were acquired with 65536 data points for a sweep width of 39683 Hz with 512 scans per increment, in a Bruker Avance 400 MHz spectrometer.

For backbone and side chain assignments the following spectra were acquired: (i) 2D ^1H, ^{13}C and ^1H, ^{15}N HSQC, 3D CBCANH, CBCA(CO)NH, HNCA, HN(CO)CA, HCC(H)-TOCSY, HC(C)H-TOCSY, ^1H, ^{13}C NOESY-HSQC and ^1H, ^{15}N NOESY-HSQC (80 ms) for labeled sample and (ii) 2D ^1H, ^1H COSY, ^1H, ^1H TOCSY (60 ms) and ^1H, ^1H NOESY (50 ms) for the unlabeled sample. NMR acquisition parameters and experiments acquired for the backbone assignment of OmcF protein are summarized in Table 5.2.

Table 5.2 NMR experiments and acquisition details for OmcF backbone resonance assignment in the reduced state. The NMR experiments acquired in (A) Bruker Avance III 600 MHz spectrometer, at 298 K and pH 7 or (B) Bruker Avance III 800 MHz, 308 K and pH 5 are indicated. ‘ns’ stands for the number of scans.

	NMR experiments	**Complex points**			**Spectral width (Hz)**			**Frequency offset (Hz)**			**ns**
		^{1}H	^{15}N	^{13}C	^{1}H	^{15}N	^{13}C	^{1}H	^{15}N	^{13}C	
A	2D ^{1}H,^{15}N HSQC	2048	256	-	10823	4865	-	2801	6689	-	40
	2D ^{1}H,^{15}N HSQC	2048	256	-	10823	2740	-	2801	7176	-	40
	2D ^{1}H,^{13}C HSQC	2048	-	256	10823	-	15152	2801	-	7545	40
	3D HNCA	2048	64	128	8418	2740	5291	2801	7176	7847	16
	3D HN(CO)CA	2048	64	128	8418	2740	5291	2801	7176	7847	16
	3D CBCANH	2048	64	128	8418	2740	12195	2801	7176	5885	16
	3D CBCA(CO)NH	2048	64	128	8418	2740	12195	2801	7176	5885	16
B	2D ^{1}H,^{15}N HSQC	2048	128	-	14368	10542	-	3801	9446	-	16
	2D ^{1}H,^{15}N HSQC	2048	128	-	9615	2190	-	3801	9244	-	8
	2D ^{1}H,^{13}C HSQC	2048	-	400	13889	-	15099	3801	-	7847	16
	3D HNCA	2048	26	100	9615	2190	7043	3801	9244	10463	8
	3D HN(CO)CA	2048	26	100	9615	2190	7043	3801	9244	10463	8
	3D CBCANH	2048	26	128	9615	2190	14085	3801	9244	7847	16
	3D CBCA(CO)NH	2048	26	128	9615	2190	14085	3801	9244	7847	16

2D ^{1}H, ^{1}H NOESY (50 ms) was acquired in a in Bruker Avance III 800 spectrometer with 2048 (F_2) x 512 (F_1) data points for a sweep width of 10822 Hz with 80 scans per increment, to determine the OmcF solution structure.

5.3.2 Assignment of the heme proton signals

In the particular case of the cytochromes, in addition to the polypeptide signals the heme substituent signals also need to be assigned. This is particularly important for small heme proteins, as it is the case of OmcF: In fact, the heme substituent signals display a considerable amount of NOE to the polypeptide chain, which are crucial to assist in the solution structure determination.

5.3.2.1 Reduced state

In the diamagnetic reduced form, the proton chemical shifts of the heme substituents are strongly affected by the heme ring-current effects. Thus, for fully reduced proteins typical regions for the signals of the heme substituents can be easily identified in 2D ^{1}H, ^{1}H NOESY spectra: 8 to 10 ppm, meso protons (H5, H10, H15 and H20); 6 to 8 ppm, thioether methines (3^1H and 8^1H); 3 to 5 ppm methyl groups (2^1CH$_3$, 7^1CH$_3$, 12^1CH$_3$, 18^1CH$_3$) and 3 to -1 ppm, thioether methyls (3^2CH$_3$ and 8^2CH$_3$). The first step to assign the heme proton signals in the reduced state is the analysis of scalar connectivities between a thioether methine ($3^1\mathrm{H}$ or $8^1\mathrm{H}$) and a thioether methyl group ($3^2\mathrm{CH}_3$ or $8^2\mathrm{CH}_3$) in 2D $^1\mathrm{H}$, $^1\mathrm{H}$ TOCSY spectra. In fact, as shown in Fig 5.12, these are the only protons that are in the same spin system.

2D $^1\mathrm{H},^1\mathrm{H}$ NOESY NMR spectra detect spatial correlation between protons that are typically closer than 5 Å and are used to conclude the fully assignment of the heme proton signals. As depicted in Fig 5.12 meso protons present a characteristic pattern of short-range intraheme connectivities observed 2D $^1\mathrm{H},^1\mathrm{H}$ NOESY spectra: protons H15 are not correlated to either methyl groups or thioether substituents; protons H20 are correlated to two heme methyls ($2^1\mathrm{CH}_3$ and $18^1\mathrm{CH}_3$); and the only ambiguity arises from H5 and H10 protons, which both present connectivities with a thioether methine, a thioether methyl and one heme methyl group. This ambiguity was solved by observing the correlation between one of the heme methyls near the H20 protons ($2^1\mathrm{CH}_3$ and $18^1\mathrm{CH}_3$) with the closest tioether methyl ($3^2\mathrm{CH}_3$) which were unequivocally assigned in the 2D $^1\mathrm{H},^1\mathrm{H}$ TOCSY. This allowed connecting H20 and H5 faces of each heme. The heme methyls $7^1\mathrm{CH}_3$ are part of H5 faces and show correlations with thioether groups ($8^1\mathrm{H}$ and $8^2\mathrm{CH}_3$), which are in H10 faces. After the identification of these heme faces, H15 protons are identified by observing the connectivities between cross-peaks that correlate H15 and $12^1\mathrm{CH}_3$ or $18^1\mathrm{CH}_3$ protons (Fig 5.12).

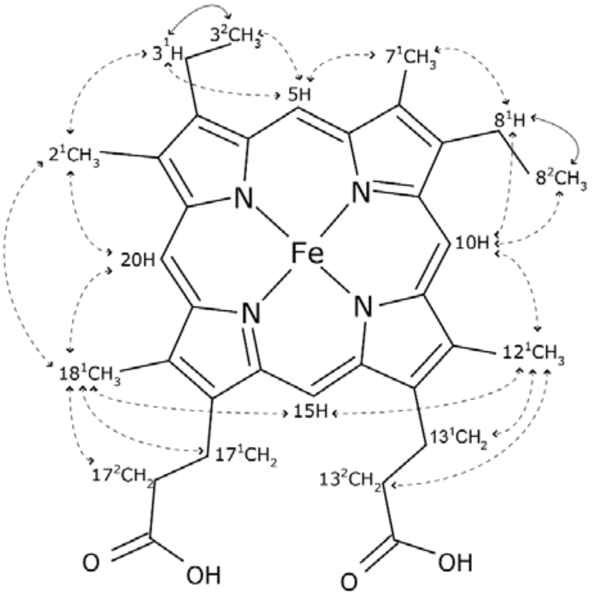

Fig 5.12 Diagram of heme *c* numbered according to the IUPAC-IUB nomenclature [4]. Dashed arrows indicate the correlations observed in 2D $^1\mathrm{H},^1\mathrm{H}$ NOESY spectra and solid lines the correlations observed in 2D $^1\mathrm{H},^1\mathrm{H}$ TOCSY spectra.

5.3.2.2 Oxidized state

In the paramagnetic oxidized state in addition to the ring-current, paramagnetic contribution due to the presence of unpaired electrons strongly contributes to the final observed chemical shift of the heme substituents, making their assignment more complex. Indeed, in the oxidized form, the same type of signals is differently affected by the paramagnetic centers, show different levels of broadness and are spread all over the NMR spectral width. Therefore, the chemical shifts of the heme substituents in the oxidized form are completely different in comparison with those observed in the fully reduced proteins. Consequently, a different NMR assignment strategy is used to assign the heme signals in the oxidized form. In this case, 2D $^{1}H,^{13}C$ HMQC experiments are very useful to assist in the heme substituent signals because typical $^{1}H,^{13}C$ regions can be identified. The propionates (αCH_2 protons (17^1CH_2 and 13^1CH_2) are identified in 2D $^{1}H,^{13}C$ HMQC spectrum, whereas the intraheme correlations with the propionates βCH_2 (17^2CH_2 and 13^2CH_2) are obtained from the analysis of 2D $^{1}H,^{1}H$ TOCSY spectrum and then confirmed in 2D $^{1}H,^{13}C$ HMQC spectrum at the typical region of propionates βCH_2. Afterwards, 2D $^{1}H,^{1}H$ NOESY spectra are used to identify the cross-peaks between each propionate proton with those of the closest heme methyl group (18^1CH_3 and 12^1CH_3).

5.3.3 Solution structure determination

The determination of a cytochrome solution structure requires the assignment of polypeptide and heme signals and distance information that can be obtained in the 2D ^{1}H, ^{1}H NOESY experiment. In this spectrum, signals are integrated using the program Sparky (T. D. Goddard and D. G. Kneller, SPARKY 3, University of California, San Francisco). The measured NOEs were used to provide upper distance limits (upls) and lower distance limits (lols) to the program PARADYANA [8], which uses automatic calibration of the conversion from volumes to distance constraints.

The assignment of the signals and the volumes are used as input for the structure calculation. At the end of the calculation the output structures are evaluated using the program CHIMERA 1.10.2 [23] and refined considering additional distance information. The precision of the calculations can be assessed by the tightness of the fit between the ensemble of the resulting conformers. Usually hundreds of conformers are calculated and a small sub-group (~20) with the lowest target function and small root mean square deviation (RMSD) are selected to represent the NMR structure of the protein. The process continues in an iterative fashion, adjusting the input parameters until a well-defined final ensemble of structures is achieved. The quality of the ensemble of structures is then validated using iCing webserver [24]. Finally, the program MOLMOL [12] is used to superimpose, identify elements of secondary structure and calculate H-bonds in the final set of conformers.

5.3.4 Data Bank accession number

The structure of OmcF has been deposited in the Protein Data Bank (PDB) with accession number 5MCS.

5.3.5 Backbone dynamics

To study the OmcF dynamic properties, a series of ^{1}H-^{15}N correlation spectra were measured at 600 and 800 MHz to obtain the T_1, T_2 and NOE parameters. For the longitudinal relaxation rate, a set of eight experiments was acquired with relaxation delays from 5 to 1200 ms, and for the transverse relaxation rate, eight experiments were recorded with relaxation delays between 16 and 130 ms. T_1 and T_2 values were determined from fitting the data for each backbone NH signal to an exponential decay, as a function of the relaxation delay. Heteronuclear {^{15}N} NOE were determined from the ratio of two experiments in the presence and absence of proton saturation. These were carried out with an overall recycling delay of 10 s to ensure the maximal development of NOEs before acquisition and to allow solvent relaxation. Results from the different spectra were treated as peak heights. We estimate an uncertainty as about 10% at both magnetic fields. Furthermore, the experimental relaxation and structural data of reduced cytochrome OmcF determined in this work was used to determine the values of the order parameter, S^2, for this cytochrome, which reflects the amplitude of internal motion on a ns–ps time scale. The principal components of the inertia tensor were calculated with the Pdbinertia program (A. G. Palmer III, Columbia University, New York, NY) using the NMR structure determined in this work. The overall correlation time from the ratio of the mean T_1 and T_2 values was estimated in the usual manner. The diffusion tensor, which describes rotational diffusion anisotropy, was determined by standard approaches using r2r1_diffusion and quadric diffusion programs (A. G. Palmer III, Columbia University, New York, NY). The ^{15}N relaxation was analyzed assuming dipolar coupling with the directly attached proton (with a bond length of 1.02 Å), and a contribution from the ^{15}N chemical shift anisotropy evaluated as -160 ppm. The internal order parameters for most residues were determined from the fits of several extensions of the Lipari and Szabo model to the experimental relaxation data [25, 26].

5.3.6 pH-linked conformational changes probed by NMR

To estimate the effect of the pH change on OmcF solution structure in the reduced state, a series of 2D ^{1}H,^{15}N HSQC NMR spectra were acquired in the pH range of 4.6-9.3. The pH was adjusted inside an anaerobic chamber (MBraun, LABstar) to avoid sample oxidation. The pH titration data were analyzed following the same strategy proposed by Garret and co-workers [27]. Briefly, the average chemical shift difference ($\Delta\delta_{avg}$) of each backbone and side chain amide signals were calculated using the Equation 5.1.

$$\Delta\delta_{avg} = \sqrt{\frac{\frac{\Delta\delta^2 N}{25}+\Delta\delta^2 H}{2}} \tag{5.1}$$

ΔδH and ΔδN are the differences in the ^{1}H and ^{15}N chemical shifts, respectively.

5.4 References

1. Kim BC, Leang C, Ding YHR, Glaven RH, Coppi MV & Lovley DR (2005) OmcF, a putative *c*-type monoheme outer membrane cytochrome required for the expression of other outer membrane cytochromes in *Geobacter sulfurreducens*. *J Bacteriol* **187**, 4505-4513.

2. Pokkuluri PR, Londer YY, Wood SJ, Duke NE, Morgado L, Salgueiro CA & Schiffer M (2009) Outer membrane cytochrome *c*, OmcF, from *Geobacter sulfurreducens*: high structural similarity to an algal cytochrome c_6. *Proteins* **74**, 266-270.

3. Lukat P, Hoffmann M & Einsle O (2008) Crystal packing of the c_6-type cytochrome OmcF from *Geobacter sulfurreducens* is mediated by an N-terminal Strep-tag II. *Acta Crystallogr D Biol Crystallogr* **64**, 919-926.

4. Moss GP (1988) Nomenclature of tetrapyrroles. Recommendations 1986 IUPAC-IUB Joint Commission on Biochemical Nomenclature (JCBN). *Eur J Biochem* **178**, 277-328.

5. Moore GR & Pettigrew GW (1990) *Cytochromes c : evolutionary, structural and physicochemical aspects*. Springer-Verlag, Berlin.

6. Keller RM & Wuthrich K (1978) Assignment of the heme *c* resonances in the 360 MHz H NMR spectra of cytochrome *c*. *Biochim Biophys Acta* **533**, 195-208.

7. Turner DL (1993) Evaluation of ^{13}C and ^{1}H Fermi contact shifts in horse cytochrome *c*. The origin of the anti-Curie effect. *Eur J Biochem* **211**, 563-568.

8. Turner DL, Brennan L, Chamberlin SG, Louro RO & Xavier AV (1998) Determination of solution structures of paramagnetic proteins by NMR. *Eur Biophys J* **27**, 367-375.

9. Guntert P, Braun W & Wuthrich K (1991) Efficient computation of three-dimensional protein structures in solution from nuclear magnetic resonance data using the program DIANA and the supporting programs CALIBA, HABAS and GLOMSA. *J Mol Biol* **217**, 517-530.

10. Kaur R & Bren KL (2013) Redox state dependence of axial ligand dynamics in *Nitrosomonas europaea* cytochrome c_{552}. *J Phys Chem B* **117**, 15720-15728.

11. Zhong L, Wen X, Rabinowitz TM, Russell BS, Karan EF & Bren KL (2004) Heme axial methionine fluxionality in *Hydrogenobacter thermophilus* cytochrome c_{552}. *Proc Natl Acad Sci USA* **101**, 8637-8642.

12. Koradi R, Billeter M & Wuthrich K (1996) MOLMOL: a program for display and analysis of macromolecular structures. *J Mol Graph* **14**, 51-55, 29-32.

13. Dantas JM, Silva ESM, Salgueiro CA & Bruix M (2015) Backbone, side chain and heme resonance assignments of cytochrome OmcF from *Geobacter sulfurreducens*. *Biomol NMR Assign* **9**, 365-368.

14. Shen Y & Bax A (2013) Protein backbone and sidechain torsion angles predicted from NMR chemical shifts using artificial neural networks. *J Biomol NMR* **56**, 227-241.

15. Zhang F & Bruschweiler R (2002) Contact model for the prediction of NMR N-H order parameters in globular proteins. *J Am Chem Soc* **124**, 12654-12655.

16. Ming D & Bruschweiler R (2004) Prediction of methyl-side chain dynamics in proteins. *J Biomol NMR* **29**, 363-368.

17. Campos AP, Aguiar AP, Hervas M, Regalla M, Navarro JA, Ortega JM, Xavier AV, De La Rosa MA & Teixeira M (1993) Cytochrome c_6 from *Monoraphidium braunii*. A cytochrome with an unusual heme axial coordination. *Eur J Biochem* **216**, 329-341.

18. Aklujkar M, Coppi MV, Leang C, Kim BC, Chavan MA, Perpetua LA, Giloteaux L, Liu A & Holmes DE (2013) Proteins involved in electron transfer to Fe(III) and Mn(IV) oxides by *Geobacter sulfurreducens* and *Geobacter uraniireducens*. *Microbiology* **159**, 515-535.

19. Kim BC, Postier BL, Didonato RJ, Chaudhuri SK, Nevin KP & Lovley DR (2008) Insights into genes involved in electricity generation in *Geobacter sulfurreducens* via whole genome microarray analysis of the OmcF-deficient mutant. *Bioelectrochemistry* **73**, 70-75.

20. Morgado L, Bruix M, Orshonsky V, Londer YY, Duke NE, Yang X, Pokkuluri PR, Schiffer M & Salgueiro CA (2008) Structural insights into the modulation of the redox properties of two *Geobacter sulfurreducens* homologous triheme cytochromes. *Biochim Biophys Acta* **1777**, 1157-1165.

21. Morgado L, Bruix M, Pessanha M, Londer YY & Salgueiro CA (2010) Thermodynamic characterization of a triheme cytochrome family from *Geobacter sulfurreducens* reveals mechanistic and functional diversity. *Biophys J* **99**, 293-301.

22. Wishart DS, Bigam CG, Yao J, Abildgaard F, Dyson HJ, Oldfield E, Markley JL & Sykes BD (1995) ^{1}H, ^{13}C and ^{15}N chemical shift referencing in biomolecular NMR. *J Biomol NMR* **6**, 135-140.

23. Pettersen EF, Goddard TD, Huang CC, Couch GS, Greenblatt DM, Meng EC & Ferrin TE (2004) UCSF Chimera-a visualization system for exploratory research and analysis. *J Comput Chem* **25**, 1605-1612.

24. Doreleijers JF, da Silva AWS, Krieger E, Nabuurs SB, Spronk CAEM, Stevens TJ, Vranken WF, Vriend G & Vuister GW (2012) CING: an integrated residue-based structure validation program suite. *J Biomol NMR* **54**, 267-283.

25. Cole R & Loria JP (2003) FAST-Modelfree: a program for rapid automated analysis of solution NMR spin-relaxation data. *J Biomol NMR* **26**, 203-213.

26. Lipari G & Szabo A (1982) Model-free approach to the interpretation of nuclear magnetic resonance relaxation in macromolecules. 2. Analysis of experimental results. *J Am Chem Soc* **104**, 4559–4570.

27. Garrett DS, Seok YJ, Peterkofsky A, Clore GM & Gronenborn AM (1997) Identification by NMR of the binding surface for the histidine-containing phosphocarrier protein HPr on the N-terminal domain of enzyme I of the *Escherichia coli* phosphotransferase system. *Biochemistry* **36**, 4393-4398.

6

BIOCHEMICAL AND STRUCTURAL CHARACTERIZATION OF PCCH[1]

---

[1] Partially reproduced from Dantas JM, Tomaz DM, Morgado L, Salgueiro CA (2013) Functional characterization of PccH, a key cytochrome for electron transfer from electrodes to the bacterium *Geobacter sulfurreducens*, FEBS Lett 587, 2662-2668 (doi: 10.1016/j.febslet.2013.07.003) and Dantas JM, Campelo LM, Duke NE, Salgueiro CA, Pokkuluri PR (2015) The structure of PccH from *Geobacter sulfurreducens* - a novel low reduction potential monoheme cytochrome essential for accepting electrons from an electrode, FEBS J 282, 2215-2231 (doi: 10.1111/febs.13269), in accordance with the Editors' Copyright Policy.

6. Biochemical and structural characterization of PccH

Comparative microarray analysis of gene transcript abundance in current-consuming *versus* current-producing *G. sulfurreducens* biofilms showed that electrode-dependent fumarate reduction was independent of major OM cytochromes required for electron transfer out of the cell [1]. Instead, the fumarate reduction was dependent upon a monoheme *c*-type cytochrome (GSU3274) designated PccH [1]. Deletion of gene *pccH* completely inhibited electron transfer from electrodes but had no influence on electron transfer to electrodes, suggesting different routes for electron transfer into and out of the cell in *G. sulfurreducens* [1]. Apparently, none of these other genes encoded OM redox-active proteins. Therefore, to date only cytochrome PccH was unequivocally identified as crucial for *G. sulfurreducens* cells to be able to accept electrons from electrodes. PccH was proposed to serve as an intermediary in electron transfer between the outer cell surface and the inner membrane on *G. sulfurreducens* cells [1].

This cytochrome has a polypeptide chain length of 129 amino acids that contains a typical heme-binding CXXCH sequence close to the N-terminus (Fig 6.1).

```
                  10                  20                  30                  40                  50                  60
G E V T Y R K D I K P I F D V R C A G C H G A D A A P E Y H A F K A E K E K W L A K G Q G M R M D T Y S H L I F Y T A W P D T G A
        70                  80                  90                  100                 110                 120
L M R R L D D G K N S K D A K P G N M Y R H L G A T E E E R Q R N L A V F K A W V G V W N L K K W P D I T K E E L N A I T V T Y
```

Fig 6.1 Amino acid sequence of mature cytochrome PccH. The *c*-type heme binding motif (CXXCH sequence) is indicated with gray boxes.

In this Chapter will be addressed the biochemical and structural characterization of cytochrome PccH. This cytochrome was heterologously produced, isolated and characterized by complementary biophysical techniques, including CD, UV-visible and NMR spectroscopies. The preliminary characterization of PccH included the evaluation of protein stability, determination of secondary structure elements and heme spin-state, as well as the identification of the heme axial ligands by NMR and site-directed mutagenesis. The X-ray crystal structure of cytochrome PccH is also reported. Structural information for this cytochrome is important in interpreting the physicochemical data, such as thermodynamic and kinetic properties, becoming essential for determining the electron transport events and molecular mechanisms involved in *G. sulfurreducens* current-consuming biofilms [1].

6.1 Results and discussion

The analysis of the amino acid sequence of PccH (Fig 6.1) indicates that the histidine present in the heme binding motif (His^{21}) is the natural candidate for the heme proximal ligand. However, up to four methionine residues (Met^{46}, Met^{48}, Met^{67} and Met^{84}) can putatively bind the PccH heme group at the distal position. To identify the sixth ligand of PccH heme group, each methionine was replaced by alanine by Site-Directed mutagenesis. These mutants were designated PccHM46A, PccHM48A, PccHM67A and PccHM84A.

6.1.1 Purification of cytochrome PccH and PccH mutants

After the construction of the expression vectors and the confirmation of the PccH and PccH mutants gene sequences by DNA sequencing, all proteins were expressed and purified by cation exchange chromatography and molecular exclusion chromatography (see Chapter 2). Since the elution profiles for the proteins were similar, the results obtained are illustrated below only for the wild-type cytochrome (Fig 6.2).

The only difference between the wild-type and mutated proteins is the substitution of residue methionine by alanine. Both residues have non-ionizable side chains and for this reason, the isoelectric point is maintained in all proteins. The isoelectric point determined for PccH was 8.84 (see section 2.4). Therefore, PccH is a considerably basic protein that strongly binds to the cation exchange column at pH 8. After application of the NaCl gradient, the major peak fractions were eluted at approximately 180 mM NaCl (Fig 6.2A) and then pooled together before loading in the XK 16/70 molecular exclusion column packed with Superdex 75, with molecular weight range between 3 and 70 kDa.

The elution profile of the molecular exclusion chromatogram for PccH is indicated in Fig 6.2B. The molecular weight of PccH and mutants is approximately 15.4 kDa (see section 2.4) and proteins were eluted at approximately 70 mL of the elution buffer (Fig 6.2 B).

The purity of the proteins and the presence of heme groups were evaluated by SDS-PAGE stained with Coomassie brilliant blue and TMBZ, respectively. As depicted in Fig 6.2 C and D, one intense band was obtained in the region of the expected molecular weight (~15 kDa).

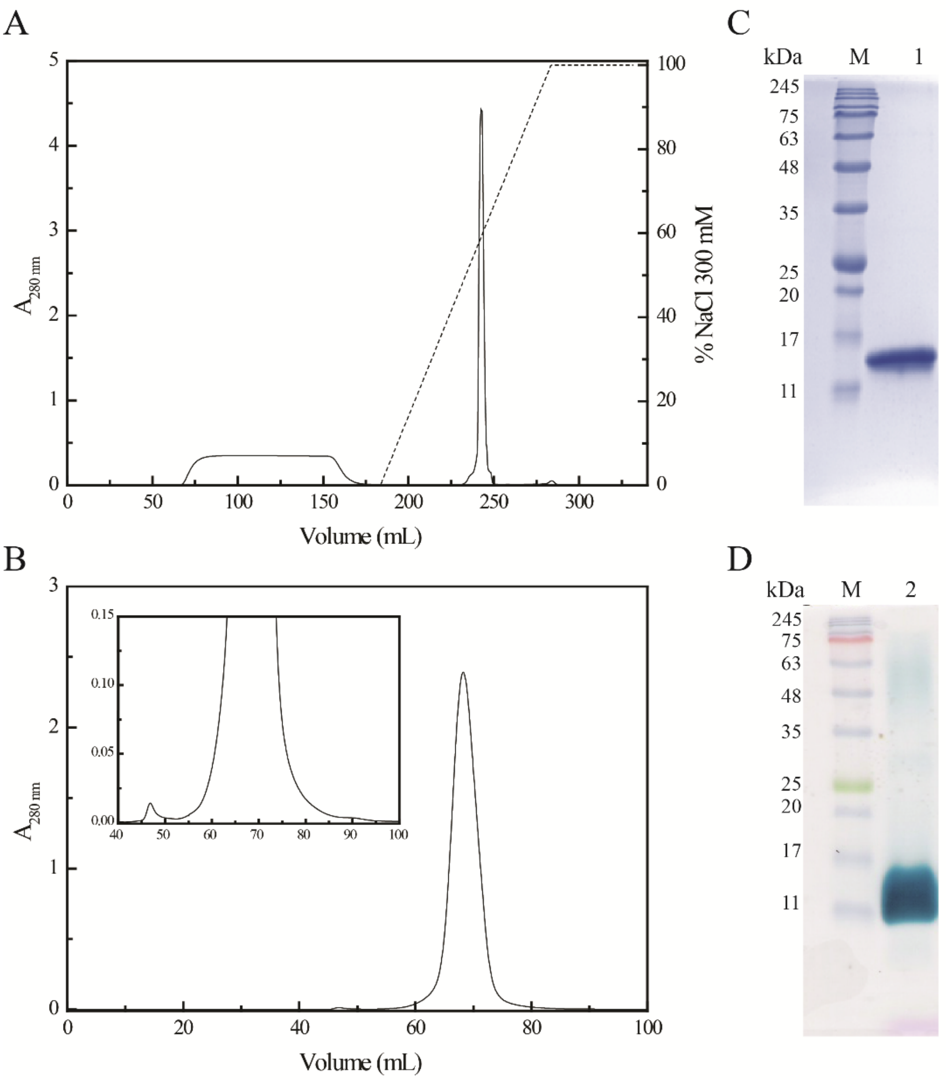

Fig 6.2 Purification of cytochrome PccH. (A) Elution profile for the cation exchange chromatography using a column equilibrated with 10 mM Tris-HCl, pH 8 and eluted at a flow rate of 1 mL/min. Primary and second y-axis, report the variation of absorbance at 280 nm (solid line) and the NaCl gradient profile (dashed line), respectively. (B) Elution profile for the molecular exclusion chromatography using a column equilibrated with 100 mM sodium phosphate buffer, pH 8. The inset shows an expanded view of the chromatogram. (C) and (D) correspond to SDS-PAGE analysis of pure cytochrome (lanes 1 and 2). The gels were stained with Coomassie Brilliant blue and TMBZ, respectively. Lane M corresponds to the molecular weight markers (NZYColour Protein Marker II). The numbers on the left refer to the molecular weight of the markers in kDa.

The molecular weight of PccH was confirmed by MALDI-TOF-MS (Fig 6.3). The peak of the pure cytochrome in the mass spectrum corresponds to a molecular mass of 15452.05 Da (±0.02%), which is in excellent agreement with the predicted MW for mature PccH (15452.91 Da, resulting from 14836.91 Da from the apo-protein plus 616 Da of one heme group [2]). The similarity between the predicted and experimental values also indicates that PccH contains one heme group, which was further confirmed by the pyridine hemochrome assay.

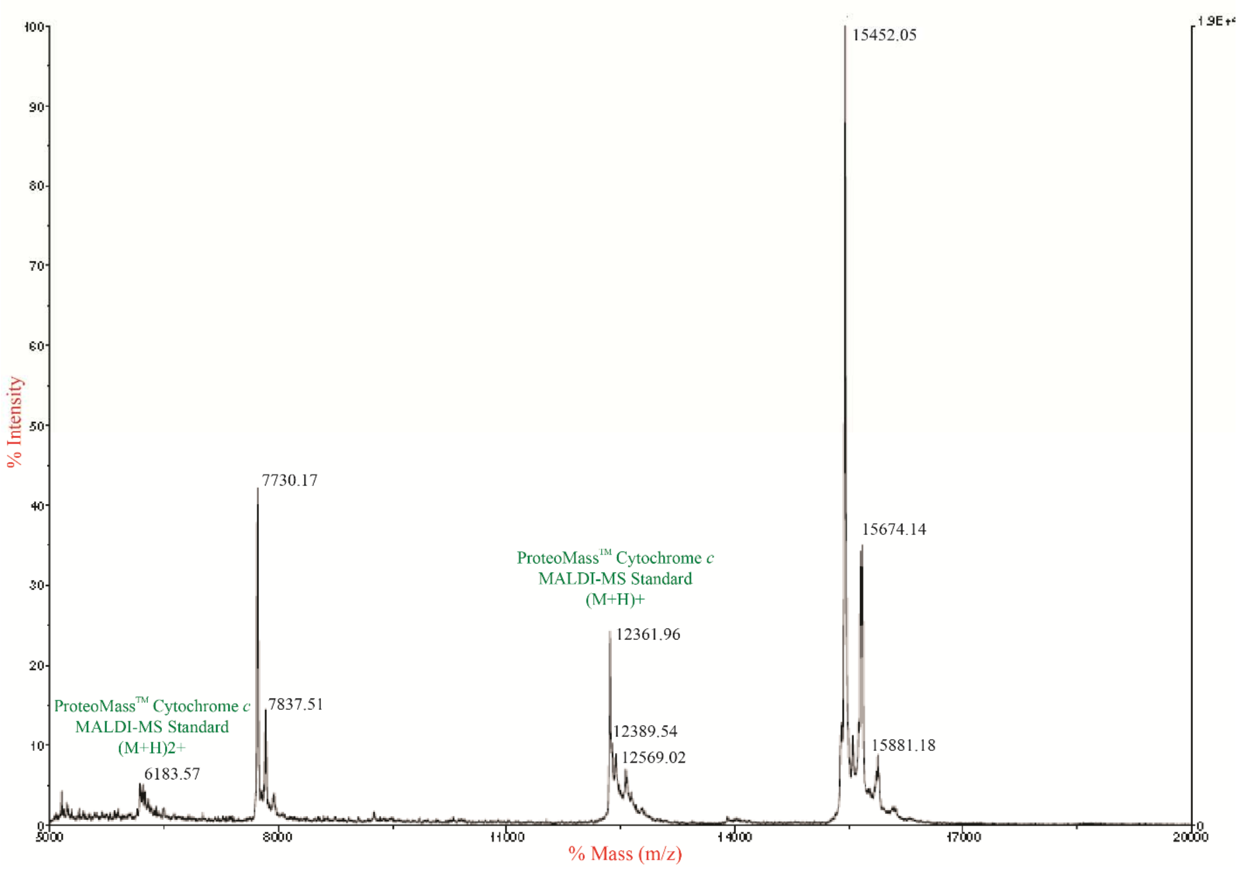

Fig 6.3 MALDI-TOF mass spectrum of PccH. A matrix solution of sinapinic acid in 70:30 water/acetonitrile with 0.1% TFA (final concentration) was used. The measurements were performed in triplicates in positive ion mode using ProteoMassTM cytochrome *c* (MW 12361.96 Da) as internal calibration.

Protein yields were determined by UV-visible spectroscopy using the PccH molar extinction coefficient of the α band (552 nm) characteristic of the protein reduced form (ε_{552} = 32.5 $mM^{-1}cm^{-1}$) determined in this Thesis (see section 6.1.2). The protein yields for PccH, PccHM46A, PccHM48A, PccHM67A and PccHM84A were 4.70, 11.70, 1.26, 8.61 and 0.03 mg per liter of cell culture, respectively.

6.1.2 Spectroscopic characterization

CD, UV-visible and NMR spectroscopies were used to probe the protein stability, secondary structural elements, heme spin-state and the nature of the heme axial ligands of cytochrome PccH. The far-UV CD spectrum obtained for cytochrome PccH is indicated in Fig 6.4. In the native state, the spectrum is typical of a folded protein with high α-helix content, featuring intense negative bands at 208 nm and 220 nm (Fig 6.4 A, solid line). An additional negative band at 233 nm in the CD spectrum is attributed to aromatic residues [3], for which the five tryptophan residues of PccH (Fig 6.4) contribute the most. To monitor the thermal stability of the protein, a characterization of the temperature-induced unfolding followed by far-UV CD spectroscopy was also carried out (Fig 6.4 B). Increasing the temperature resulted in a progressive α-helix to random coil transition with loss of the folded spectral features (Fig 6.4 A, dotted line). The value of midpoint thermal unfolding (T_m) was 78 ± 1 ºC (Fig 6.4 B). At the end of the thermal denaturation a notable protein precipitation was observed, suggesting the occurrence of nonreversible modifications at high temperature.

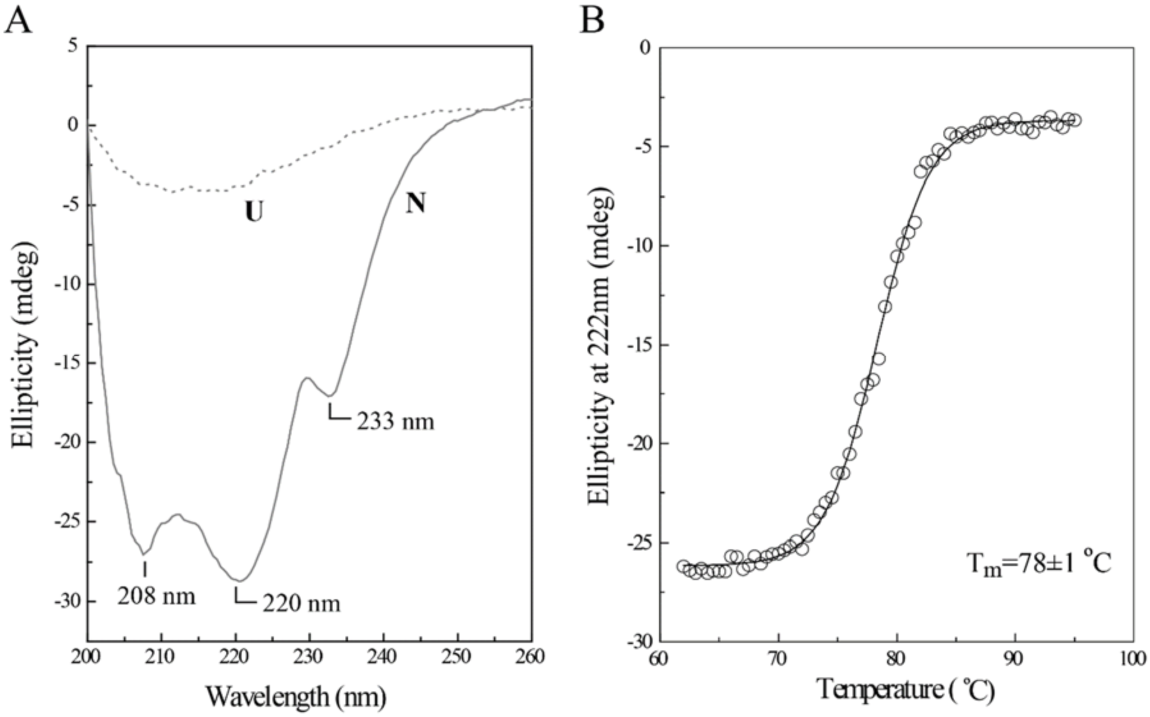

Fig 6.4 Spectroscopic characterization of PccH by circular dichroism. (A) Far UV-CD spectra of PccH in the native (N, solid line) and after incubation at 95°C (U, dotted line). (B) Thermal unfolding of cytochrome PccH. The solid line corresponds to the sigmoidal fitting of the data, from which T_m was determined.

The heme spin-state and the nature of the heme axial ligands of cytochrome PccH were probed by UV–visible spectroscopy. The optical absorption spectrum of PccH as purified has maxima at 525, 411, 352 and 280 nm (Fig 6.5). Upon reduction, the protein shows the Soret, β and α bands at 417, 523 and 552 nm, respectively (Fig 6.5).

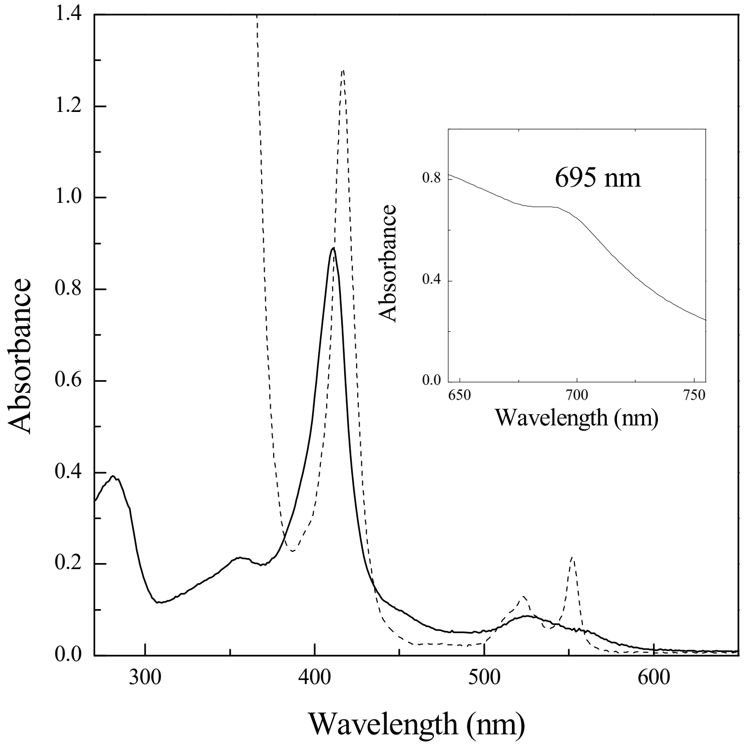

Fig 6.5 UV-visible spectral features of cytochrome PccH as purified (solid line) and in the reduced state (dashed line). A more concentrated PccH sample was used to probe the region of 695 nm band (see inset), which is indicative of an axial methionine coordinated to the ferric heme.

This spectral pattern is typical of low spin hexacoordinated hemes [4]. The band at 695 nm observed in the UV–visible spectrum (see inset in Fig 6.5) is indicative of His–Met axial coordination [4] in the oxidized form. The molar extinction coefficients of the UV-visible absorption bands are summarized in Table 6.1.

Table 6.1 UV-visible absorption bands and molar extinction coefficient of cytochrome PccH.

	Bands in the electronic absorption spectra (nm)		**Molar extinction coefficient ($mM^{-1}cm^{-1}$)**
Oxidized	Soret	411	134.2
	Others	280	58.7
		352	31.5
		525	13.0
Reduced	Soret	417	193.3
	β-band	523	19.4
	α-band	552	32.5

The proper folding of PccH and the heme spin-state were also corroborated by the well-dispersed and narrow signals observed in the 1D ^{1}H NMR spectra of the protein in the reduced and oxidized states

(Fig 6.6). The line widths of the NMR signals (<10 Hz and <60 Hz in the reduced and oxidized states, respectively) are typical of a monomeric protein in solution [5].

The NMR spectral regions are quite distinct for cytochromes containing high- or low spin hemes. In the oxidized state, the 1D ^{1}H NMR spectra of high-spin cytochromes shows extremely broad signals above 40 ppm, which typically correspond to the heme methyl substituents. In contrast, in low-spin cytochromes, the methyl signals are mainly found in the region 8–35 ppm. Similarly, in the reduced form, 1D ^{1}H NMR spectra in both cases are also quite distinct [6]. The reduced NMR spectra of high-spin cytochromes show wider spectral regions (typically from 15 up to 30 ppm) compared to low-spin ones (typically from 5 to 11 ppm).

In the case of PccH, the 1D ^{1}H NMR signals cover the regions 3 to 30 ppm and 5 to 12 ppm in the oxidized and reduced forms, respectively and, hence, are typical of a low-spin cytochrome (Fig 6.6). Thus, from the NMR studies it can be concluded that PccH is diamagnetic when reduced (Fe(II), S = 0) and paramagnetic when oxidized (Fe(III), S = 1/2). The reduced 1D ^{1}H NMR spectrum of a low-spin cytochrome is also very helpful in identification of the heme axial ligands, particularly in the case of a methionine residue. On the contrary, the signals correspondent to the aliphatic αCH and βCH$_2$ groups of an axial histidine are typically shifted to low-field region in the oxidized spectra and in this case, is not possible to distinguish that signals in the 1D ^{1}H NMR spectrum.

As mentioned in the Chapter 5, the typical pattern of heme axial methionine signals includes a three-proton intensity peak at approximately 3 ppm, and up to four resolved one-proton intensity peaks in the low-frequency region of the spectrum [4]. Such pattern is clearly observed in the reduced spectrum of cytochrome PccH indicating that the heme group is axially coordinated by a methionine (see upper spectrum in Fig 6.6), as similarly observed for the monoheme cytochrome OmcF described in the Chapter 5.

The side chain signals of the heme axial methionine are also expected to be observed in the upfield region of the oxidized 1D ^{1}H NMR spectrum. However, due to their proximity to the unpaired electron of the heme iron, the signals are extremely broad to be detected. The only exception is for the three-proton intensity εCH$_3$ group, which despite its broadness is still observed, in the oxidized spectrum in the region 9 to 25 ppm, as reported in the BMRB (http://www.bmrb.wisc.edu/) for *c*-type cytochromes with His–Met axial coordination. Therefore, the signal with three-proton intensity at -11.48 ppm in the oxidized spectrum of PccH can be tentatively assigned to axial methionine εCH$_3$ group (see bottom spectrum in Fig 6.6).

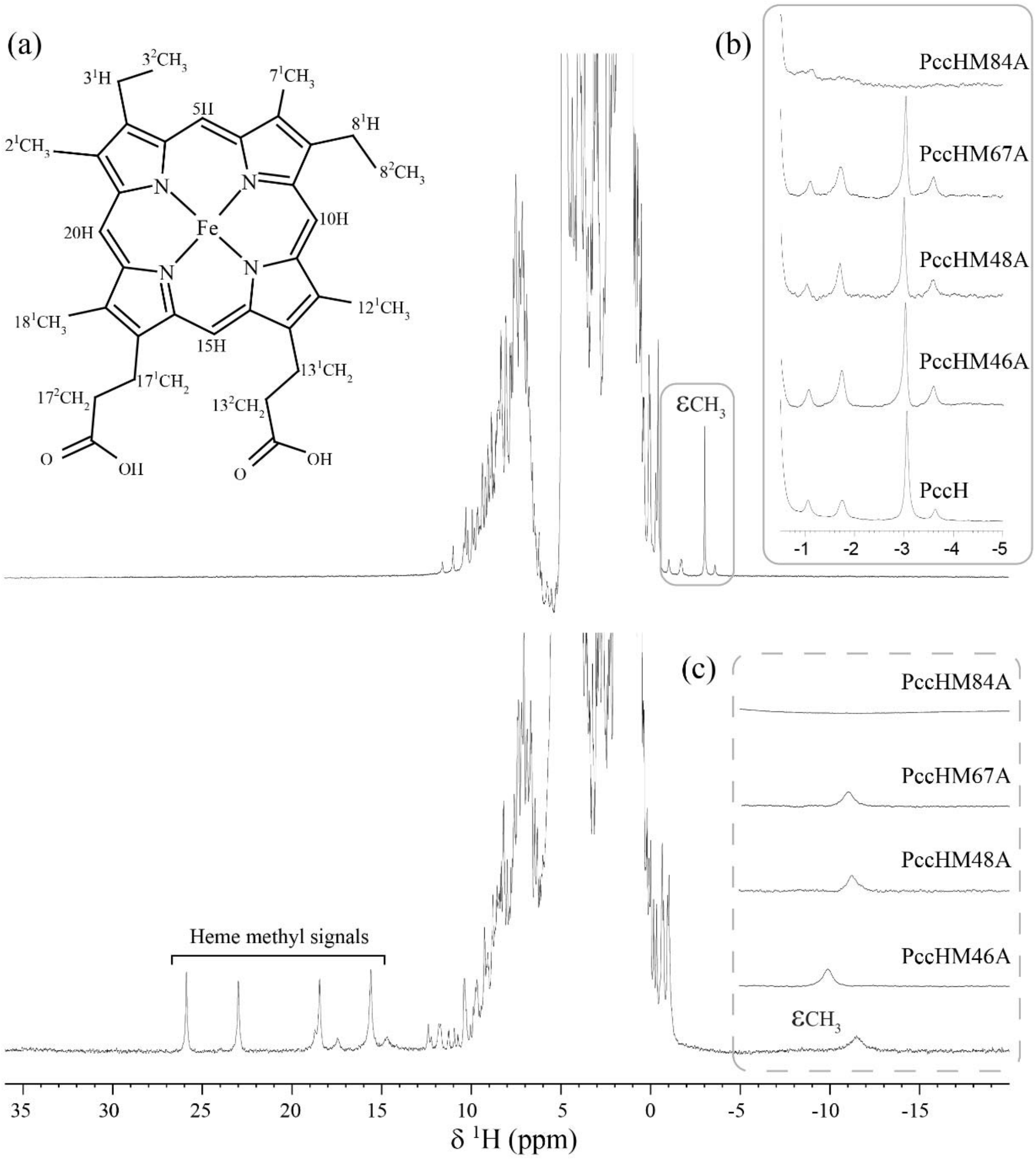

Fig 6.6 1D ^{1}H NMR spectra of the reduced (upper) and oxidized (lower) PccH obtained at 298K and pH 7. Signals correspondent to the heme axial methionine εCH_3 protons are indicated in each spectrum. The signals of the heme methyls are labeled in the oxidized spectrum. The inset (a) shows a diagram of a heme *c*. The spectral regions containing the typical signals for the heme axial methionine in the wild-type cytochrome are compared with those for PccH mutants in insets (b) and (c).

To further confirm this, a 2D ^{1}H, ^{1}H EXSY NMR spectrum was acquired for a partially oxidized PccH sample. In this spectrum, the signal between the εCH_3 proton signal at 3.06 ppm, with proton signal at 11.48 ppm further confirms that the latter can be assigned to an axial methionine εCH_3 group (Fig 6.7).

The 1D ^{1}H NMR spectra acquired in both oxidized and reduced PccH mutants were compared to those obtained for the wild-type cytochrome. With exception of mutant PccHM84A, in all other mutants the typical signal of the methionine εCH_3 proton is clearly observed (see insets (b) and (c) in Fig 6.6) showing that Met[84] binds axially to PccH heme group. Therefore, the heme binding motif CXXCH is placed at N-terminus region and the sixth ligand, provided by a methionine residue, about 40 residues further on towards the C-terminus constitute a typical feature of the class I cytochromes [4].

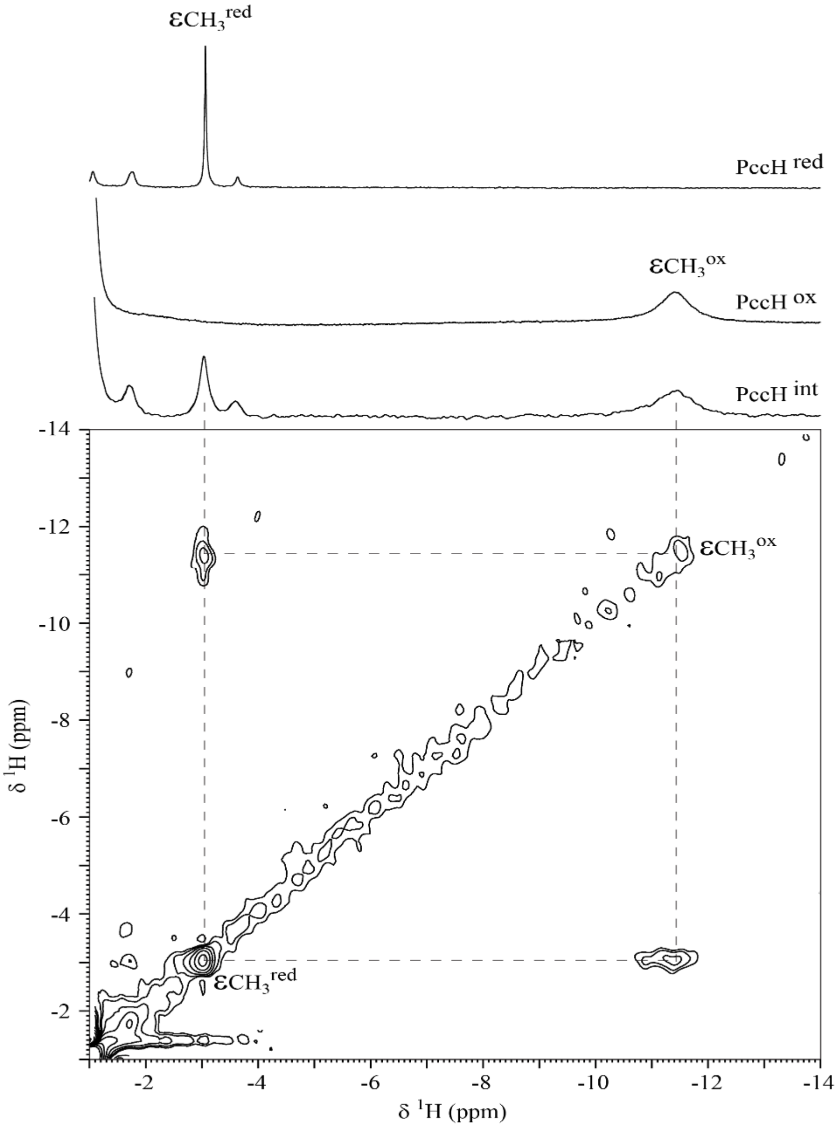

Fig 6.7 Portion of a 2D ^1H, ^1H EXSY NMR spectrum of cytochrome PccH (298K and pH 7) obtained for a partially oxidized sample. Cross peaks connecting the signals of the axial methionine εCH_3 protons in the reduced and oxidized forms are indicated. The correspondent regions in the 1D ^1H NMR spectra of fully reduced (PccH^{red}), fully oxidized (PccH^{ox}) and partial oxidized (PccH^{int}) PccH samples are indicated.

6.1.3 Specific assignment of PccH heme axial ligands

The combined used of 2D ^1H, ^{13}C HMQC, 2D ^1H, ^1H TOCSY and 2D ^1H, ^1H NOESY NMR spectra acquired in the oxidized form of several mono- and multiheme *c*-type cytochromes are reported in the literature and established typical regions for heme methyl, heme propionate and axial His βCH_2 and αCH groups in the 2D ^1H, ^{13}C HMQC [7]. Therefore, this methodology was used to assign these signals for the monoheme cytochrome PccH (Fig 6.8). The assignment of the heme substituents was crucial to perform the temperature- and pH- dependence studies, presented in the sections below.

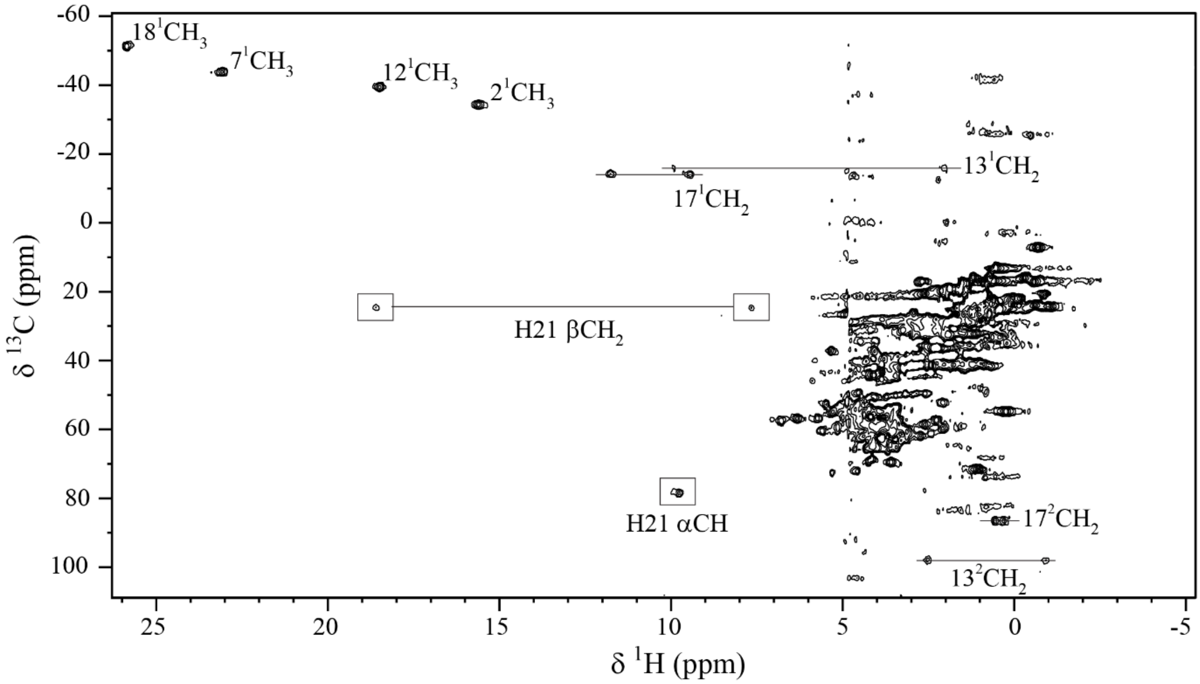

Fig 6.8 2D ^{1}H, ^{13}C HMQC NMR spectrum of cytochrome PccH in the oxidized state (298K and pH 7). Labels relate with the heme methyl signals according to IUPAC-IUB nomenclature [8] and with αCH and βCH_2 signals of heme axial histidine (H21). The peaks of the protons connected to the same carbon atom (CH_2 groups) are linked by a straight line.

6.1.4 Temperature dependence of PccH heme methyl signals

The heme spin-state in solution was studied by analyzing the temperature dependence of the heme methyl proton chemical shifts of oxidized PccH in range 290–309 K. As can be observed in Fig 6.9, two of the heme methyls (18^1CH_3 and 7^1CH_3) are more downfield shifted (25.7 and 23.0 ppm, respectively, at 303 K) compared to the other two (2^1CH_3 at 18.5 ppm and 12^1CH_3 at 15.6 ppm). Each pair of heme methyls is in diametrically opposed pyrrole rings of the porphyrin and therefore the chemical shifts pattern results from an asymmetry in the distribution of the delocalized unpaired electron on the molecular orbitals of the porphyrin [9]. However, in the case of PccH, the NMR spectra did not reflect a very strong asymmetry in the distribution of the delocalized unpaired electron *(e.g.* compared to the chemical shift pattern of the same heme methyls in the horse heart cytochrome). The chemical shift of the first pair of signals in the latter cytochrome at 303 K are observed at 34.6 ppm (18^1CH_3) and 31.8 ppm (7^1CH_3), whereas those of the second pair are observed at 10.1 ppm (12^1CH_3) and 7.1 ppm (2^1CH_3) [9].

The dependence of the PccH heme methyl proton chemical shifts with the temperature shows that for all methyls the shifts decrease with increasing temperature, therefore indicating a Curie law behavior, a feature that is observed in low-spin hemes. Nonetheless, the signals of heme methyls 2^1CH_3 and 12^1CH_3 show an increase of the chemical shifts at above 290 K, whereas a small curvature is observed for the chemical shift of heme methyls 18^1CH_3 and 7^1CH_3. This suggests some high-spin character, possibly caused by weakening of the Met-Fe bond. Therefore, the chemical shift dependence of the heme methyls with temperature indicates that the heme is in the low-spin state in the oxidized form, which is compatible with the PccH X-ray structure (section 6.1.5).

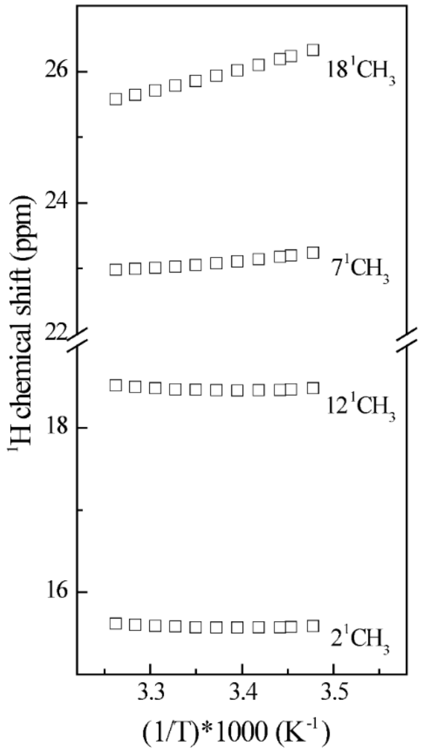

Fig 6.9 Temperature dependence of the four PccH heme methyl ^{1}H signals.

6.1.5 Crystal structure

The crystal structure of cytochrome PccH was determined in the oxidized state by the collaborative group from the Argonne National Laboratory, Argonne, Illinois, USA. Crystallization and structure determination details are presented in [10].

The final refined structure of PccH contains residues 1–74 and 78–129 with a heme (protophorphyrin IX) covalently bound to Cys^{17} and Cys^{20} via thioether bonds. In addition to 177 water molecules, the final model included three Zn ions. Other unexplained peaks in the difference electron density map were modeled as a cacodylate ion, phosphate ion and acetate ion. The quality of electron density in the region of residues 75–77 was very poor and multiple attempts to build these residues were not successful. The final coordinates and structure factor data were deposited in the PDB under accession code 4RLR.

As is typical for cytochromes, the secondary structure of PccH is composed mostly of helical segments connected by turns and loops. The structural fold of PccH can be described as forming two lobes: one N-lobe approximately consisting of residues 1–63 and 125–129, as well as one C-lobe approximately consisting of residues 64–124. The heme is sandwiched in a cleft between the two lobes (Fig 6.10). This is unique for PccH because monoheme cytochromes in general form one globular domain with the polypeptide chain wrapping around the heme with helices, turns and loops, with the heme being the central part of the hydrophobic core. An approximately 10-residue segment, residues 72–81, extends away from the rest of the protein. Residues 75–77 within this segment are not visible in the electron density map. Typically, in monoheme cytochromes, the heme forms an essential and central part of the hydrophobic core of the protein. This is interesting because PccH contains many hydrophobic residues; in the structure, the two protein lobes have their own hydrophobic cores and the heme forms a bridge between the two lobes. Residues Tyr^{5}, Ile^{9}, Ile^{12}, Phe^{13}, Ala^{18}, Ala^{25}, Ala^{26}, Tyr^{29}, Phe^{32}, Trp^{39}, Leu^{40}, Met^{46}, Met^{48}, Tyr^{51}, Leu^{54}, Ile^{55}, Phe^{56}, Val^{127} and Tyr^{129} form hydrophobic interactions in the N-terminal lobe, whereas residues Ala^{59}, Met^{67}, Leu^{70}, Leu^{88}, Tyr^{85}, Leu^{99}, Phe^{102}, Val^{106}, Trp^{109}, Leu^{111}, Leu^{122} and Ile^{125} form hydrophobic interactions in the C-terminal lobe.

The hydrophobic residues that interact with the heme in the interface are Phe^{13}, Tyr^{29}, Phe^{32}, Leu^{40}, Met^{46}, Met^{48} and Tyr^{57} from the N-lobe and Ala^{65}, Leu^{66}, Leu^{70}, Leu^{88} and Phe^{102} from the C-lobe. The heme group is attached through thioether bonds to Cys^{17} and Cys^{20}, whereas His^{21} and Met^{84} form the fifth and sixth axial ligands, respectively (Fig 6.10). Therefore, the heme Fe ion is hexacoordinated and low-spin. The heme porphyrin ring is not planar, the distortion is similar to the cytochrome c_6-like protein, OmcF from *G. sulfurreducens* reported previously [11] and less distorted compared to the multiheme cytochromes from *G. sulfurreducens* [12, 13]. The axial methionine residue Met^{84} has an *S* configuration. The crystal structure of cytochrome PccH confirms the preliminary data that have been presented in the previous sections of this Chapter.

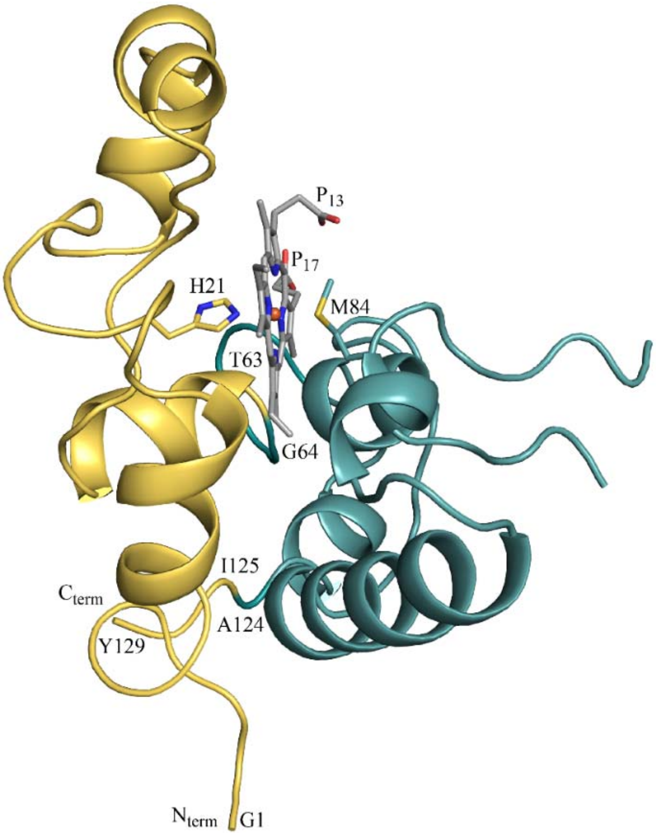

Fig 6.10 Crystal structure of cytochrome PccH from *G. sulfurreducens* (PDB ID 4RLR). The N-lobe (residues 1–63 and 125–129) and C-lobe (residues 64–124) are colored gold and blue, respectively. The heme is colored gray and the side chains of the axial ligands (His^{21} and Met^{84}) are shown in stick representation with atom type colors. Figure was produced using the program PyMOL [14].

6.1.6 Redox-Bohr center

Redox titrations of PccH followed by UV-visible spectroscopy were performed at pH 4, 5, 6, 7, 8 and 9. The redox titration curves for pH 6 and 8 are represented in Fig 6.11. No hysteresis was observed, as the reductive and oxidative curves are superimposable, indicating that the redox process is fully reversible.

The reduction potential values obtained were +54 ± 5 mV (pH 4), +42 ± 5 mV (pH 5), +1 ± 5 mV (pH 6), -24 ± 5 mV (pH 7), -35 ± 5 mV (pH 8) and -40 ± 5 mV (pH 9) *versus* NHE (Fig 6.12). The decrease in the reduction potential values with pH leads to a progressive stabilization of the oxidized form.

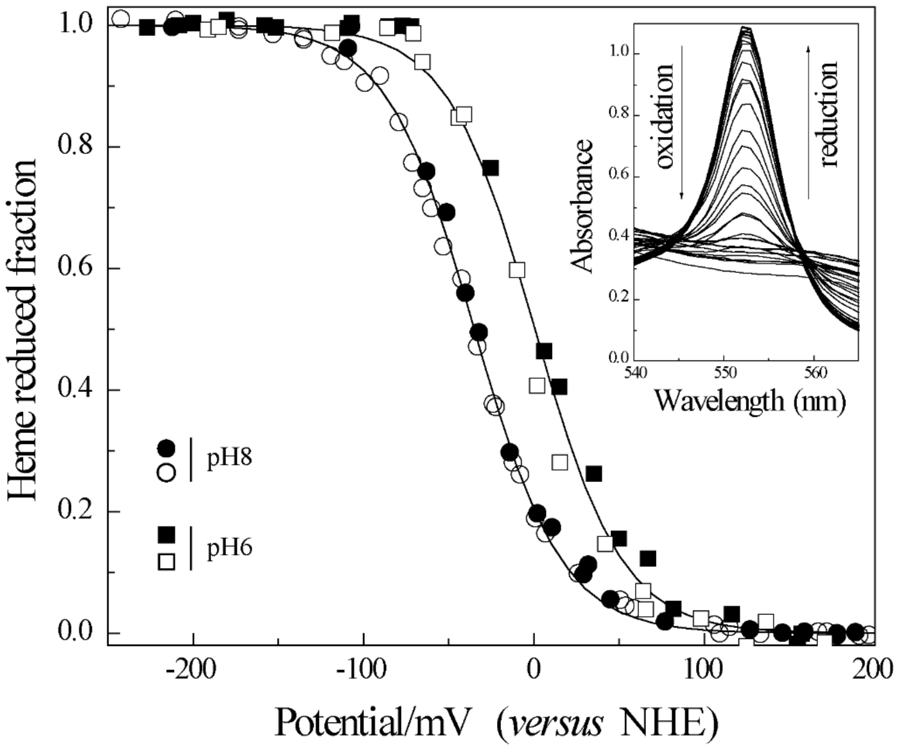

Fig 6.11 Redox titrations followed by visible spectroscopy for PccH at pH 8 (circles) and pH 6 (squares). The open and filled symbols represent the data points in oxidative and reductive titrations, respectively. The continuous lines indicate the results of the fits to the Nernst curves for one-electron reduction with -35 ± 5 mV (pH 8) and +1 ± 5 mV (pH 6). As an example, the inset illustrates the α-band region of the visible spectra acquired in the redox titration at pH 8.

As previously described for cytochrome OmcF (see Chapter 5), the influence of the pH on the heme reduction potential (redox-Bohr effect) can be explained in a pure electrostatic basis since the progressive deprotonation of an acid/base group near the heme is expected to lower its affinity for electrons with the concomitant decrease of the reduction potential values. Also, on a pure electrostatic basis, the pK_{red} value of the protonatable group responsible for the redox-Bohr effect is expected to be higher compared to its value in the fully oxidized protein (pK_{ox}). The pH dependence of the reduction potential in the pH range 4 to 9 was used to determine the pK_{red} (6.6) and pK_{ox} (5.0) values of PccH (Fig 6.12).

Indeed, PccH shows significant redox-Bohr effect in the physiological pH range of growth of *G. sulfurreducens*. The variation in reduction potential with pH clearly exceeds the experimental error and the decrease in the reduction potential with pH indicates that the oxidized form of PccH is stabilized more at higher pH values. The pH dependence of the reduction potential also suggests that protonation/deprotonation events occur near the heme group within this pH range.

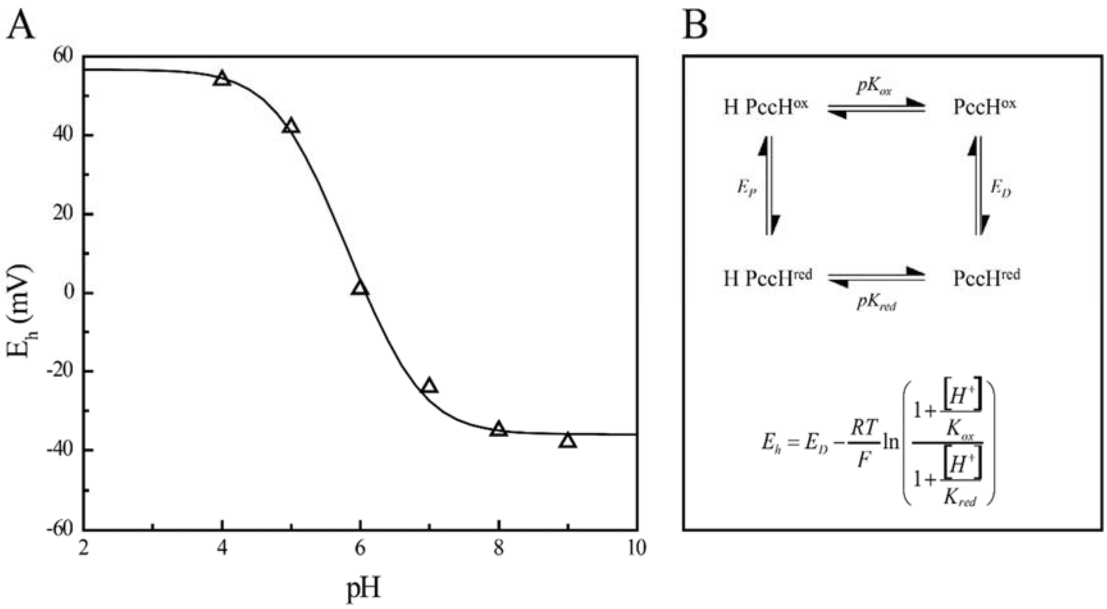

Fig 6.12 Effect of the pH on the heme reduction potential values of cytochrome PccH. (A) pH dependence of the reduction potential (E_h) of cytochrome PccH. Data points are represented by triangles. The solid line is the result of the fit to the Nernst equation for the transfer of one electron coupled to one proton according to the model and equation indicated in panel B [15]. E_P (57 mV) and E_D (-36 mV) correspond to the reduction potential values of cytochrome PccH in the protonated and deprotonated forms, respectively. pK_{ox} (5.0) and pK_{red} (6.6) are the pK_a values of the fully oxidized and fully reduced protein, respectively.

The methyl substituents at the periphery of the heme can be used to monitor such changes occurring in the heme vicinity. In addition, the heme propionate substituents (P_{13} and/or P_{17}) are potential candidates for the redox-Bohr center(s) via protonation/deprotonation of their carboxylic groups, as shown for several mono- and multiheme cytochromes [16-21]. Therefore, the 2D ^1H, ^{13}C HMQC chemical shift pH dependences of the four heme methyls and propionate groups in pH range 5–8 were measured (Fig 6.13). From the analysis, the chemical shifts of the $P_{17}{}^1CH_2$ protons are the most affected, indicating that these signals are sensing a protonation in its close vicinity.

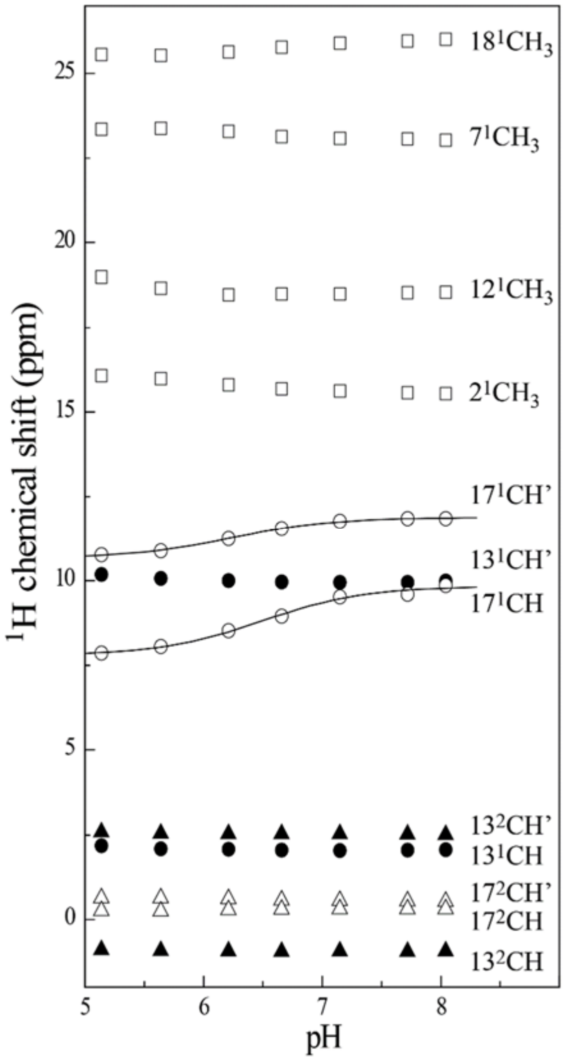

Fig 6.13 pH dependence of the heme propionate and methyl ^{1}H chemical shifts. Solid lines were obtained by using the least-squares fitting to Henderson-Hasselbalch equation $\delta_{obs} = \delta_A + (\delta_B - \delta_A)\frac{10^{pH-pKa}}{1+10^{pH-pKa}}$, where δ_{obs}, δ_A, and δ_B are the observed, protonated, and deprotonated chemical shifts, respectively.

An examination of the structure of PccH provided clues for the origin of redox-Bohr effect in this protein (Fig 6.14). The propionate P_{13} forms salt bridge with Arg^{69}, which very likely lowers the pK_a of the carboxylate group of this propionic acid. By contrast, the propionate P_{17} is found within hydrogen bonding distance (2.6 Å) to negatively charged Asp^{62}.

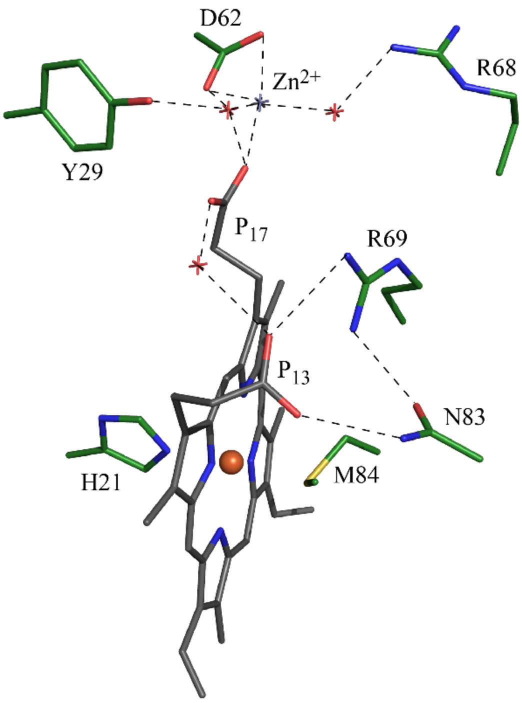

Fig 6.14 Polar interactions involving the heme propionates including a zinc ion. The propionates are labeled in accordance with IUPAC nomenclature [8].

In solution and in the absence of Zn^{2+}, the negative charge present on Asp^{62} is likely to increase the pK_a of the propionic acid P_{17}, pushing it into the pH 6–8 region. The side chain conformation of Asp^{62} is restricted in the structure of PccH. Asp^{62} OD2 is 3.5 Å from CD1 of Tyr^{57} with a close to linear geometry at the aromatic hydrogen (C-H$^{\cdots}$O) and may be regarded as a weak hydrogen bond. In addition, the side chain conformation of Asp^{62} is sterically constrained by the side chains of Tyr^{29}, Phe^{56} and Ala^{65} and therefore could not assume a side chain conformation (rotamer), which will place the carboxylate group away from the propionic acid. This suggests that the propionic acid A (P_{17}) of the heme could be responsible for the observed redox-Bohr effect of PccH. The pK_a values calculated from the measured pH dependence of the ^{1}H chemical shifts of propionate 17^1CH_2 protons in pH range 5–8 also reinforces this hypothesis (Fig 6.13, solid lines). pK_a values of 6.2 and 6.5 were obtained, which are significantly higher than those of free carboxylic acids (pK_a ~ 3–4), and correlates well with the fact that propionate P_{17} is partially shielded from the solvent by the structural environment described above. The propionate P_{17} ionizes with a pK_a similar to the transition pK_a for the heme reduction potential and therefore is most likely the candidate responsible for the redox-Bohr effect observed in PccH.

Most of the class I cytochromes have reduction potentials in the range of +150 to +350 mV [22]. The factors responsible for the modulation of cytochrome *c* reduction potentials over a large range has been a subject of considerable research [23, 24] and yet it is difficult to identify one major determining factor for large differences among closely related structural homologs. For a monoheme cytochrome, PccH has the lowest reduction potential observed to date (-24 mV at pH 7). Positive reduction potentials, such as +240 mV in the case of horse heart cytochrome *c*, have been attributed to the heme being largely buried in the protein core. The solvent accessible surface area of the heme in PccH calculated by SURFACE [25] is 112 Å^2. For comparison, the heme exposures of various other bacterial monoheme cytochromes are presented in Table 6.2. Clearly, the surface exposure of the heme in PccH is much higher, which could be one of the factors contributing to the lower reduction potential observed for the heme in this protein.

Table 6.2 Heme accessibility and reduction potential for representative bacterial class I *c*-type cytochromes. The values reported for *G. sulfurreducens* cytochrome PccH were obtained in the present study.

Protein	PDB ID	Heme surface area exposed (Å^2)	Reduction potential (mV)
Geobacter sulfurreducens cyt PccH	4RLR	112	−24
Pseudomonas aeruginosa cyt c_{551}	451C	37	+276 [26]
Chlorobaculum tepidum cyt c_{554}	4J20	37	+148 [27]
Desulfovibrio vulgaris cyt c_{553}	2DVH	44	+37 [28]
Arthrospira maxima cyt c_6	1F1F	42	+314 [29]
Paracoccus denitrificans cyt c_2	1COT	37	+250 [30]
Azotobacter vinelandii cyt c_5	1CC5	58	+312 [31]

The electrostatic surface of PccH as calculated by GRASP [32] is shown in Fig 6.15. There are no significant positively or negatively charged regions on the surface of PccH. Therefore, it is not clear how the electrostatic potential of the protein affects the reduction potential of the heme in PccH.

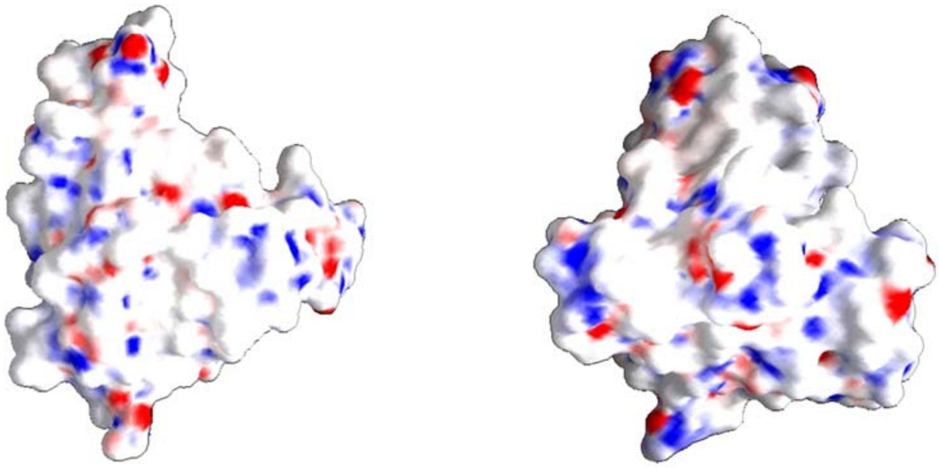

Fig 6.15 Electrostatic potential displayed on surface representation of PccH. The left panel is approximately in the same orientation as in Fig 6.10. The view in the right panel is that following a rotation of about 180° around a vertical axis.

6.1.7 Analysis of PccH protein sequence and comparison with other cytochromes

Using the amino acid sequence of the mature PccH, we searched the non-redundant amino acid data base of NCBI using the basic local alignment search tool (BLAST) [33]. This cytochrome shows the highest homology with putative monoheme cytochrome *c* family proteins isolated from the following bacteria: *Pelobacter propionicus* (70%, sequence identity), *Thioalkalivibrio nitratireducens* (54%), *Thioalkalivibrio sulfidophilus* (51%), *Leptothrix cholodnii* (51%), *Rhodoferax ferrireducens* (49%), and *Polaromonas* sp. (47%). The sequence alignment of these proteins is depicted in Fig 6.16. For all cytochromes, the heme binding motif CXXCH is placed at the N-terminus region, a typical feature of cytochrome *c* class I members [4]. Ambler's class I cytochromes include the subclasses of monoheme cytochromes c_2, c_5, c_6, $c_{551/552}$, c_{553}, c_{554} [34, 35]. More recently, Stelter and co-authors [36] proposed a new subclass of class I cytochromes for *c*-type cytochromes from the bacteria of *Bacteroidetes phylum*.

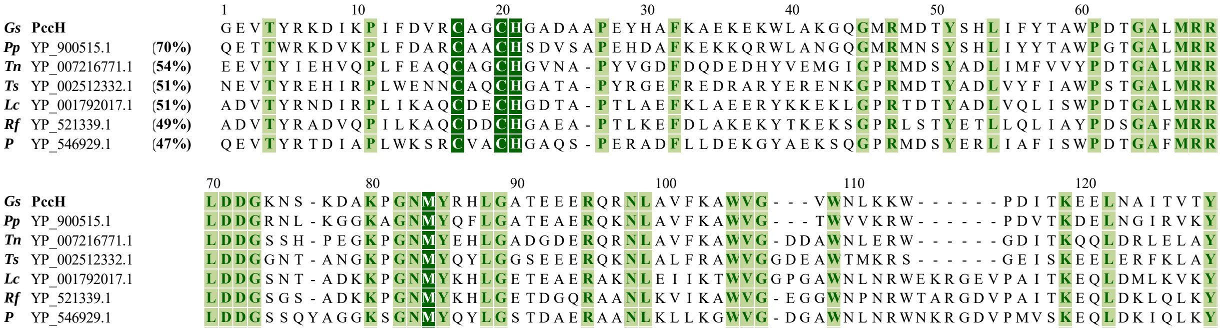

Fig 6.16 Sequence alignment of the top six hits returned for the amino acid sequence of the mature PccH using the basic local alignment search tool (BLAST). *Pp*, *Pelobacter propionicus*; *Tn*, *Thioalkalivibrio nitratireducens*; *Ts*, *Thioalkalivibrio sulfidophilus*; *Lc*, *Leptothrix cholodnii*; *Rf*, *Rhodoferax ferrireducens*; *P*, *Polaromonas* sp.. The sequence accession codes and the percentage identity with PccH are indicated. The conserved residues in the proteins are boxed: heme binding residues (green) and other residues (light green).

Representative sequences from the cytochromes above mentioned were used together with the top six hits returned for the BLAST search with PccH sequence to produce the dendrogram presented in Fig 6.17.

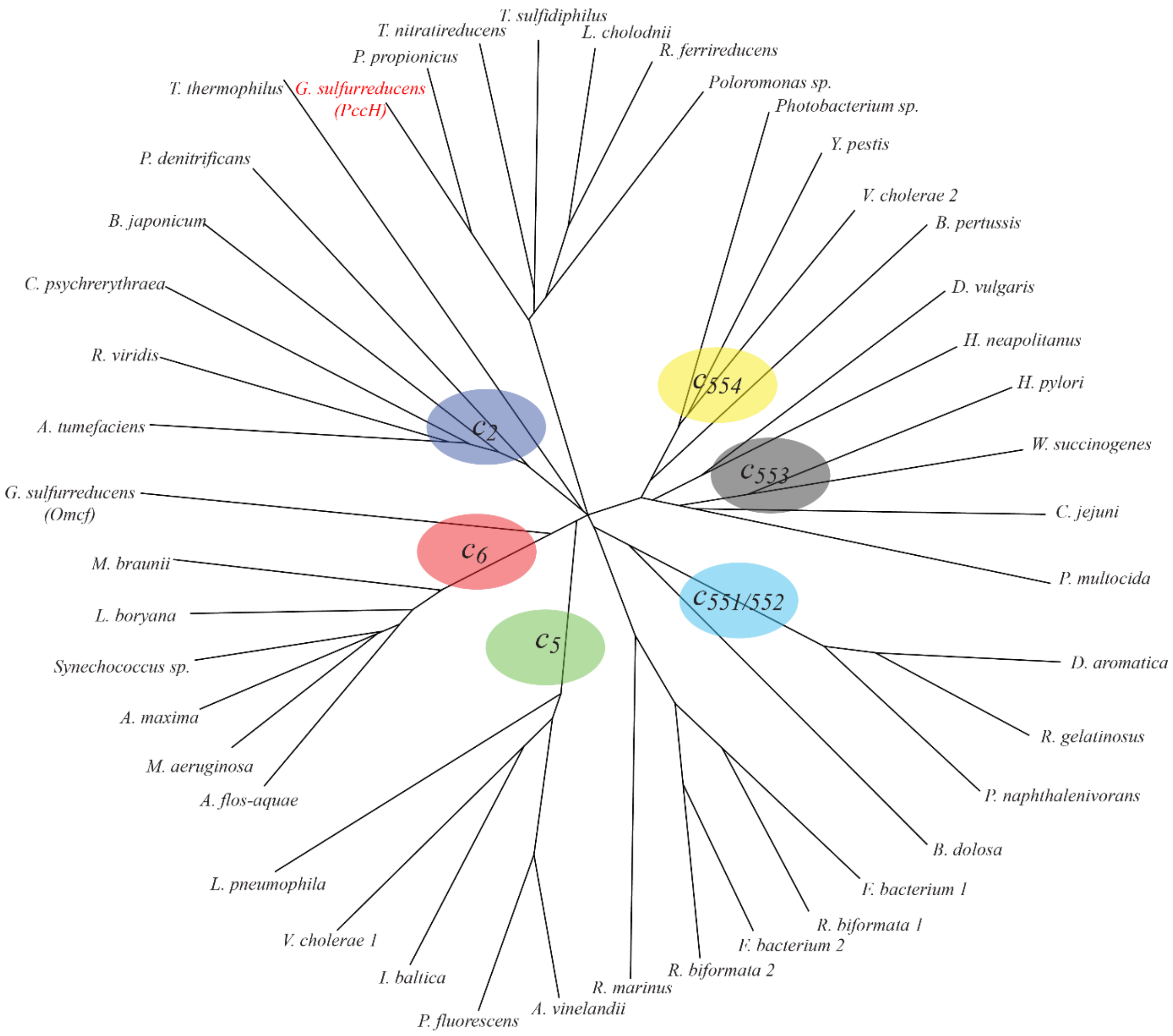

Fig 6.17 Amino acid sequence comparison of *G. sulfurreducens* PccH cytochrome *c* with prokaryotic *c*-type monoheme cytochromes (accession number in parenthesis): *Agrobacterium tumefaciens* (P00081); *Aphanizomenon flos-aquae* (P00116); *Arthrospira maxima* (P00118); *Azotobacter vinelandii* (AAC45922); *Bordetella pertussis* (Q7VVZ0); *Bradyrhizobium japonicum* (Q89SL2); *Burkholderia dolosa* (ZP_00982883); *Campylobacter jejuni* (NP_282300); *Colwellia psychrerythraea* (YP_270114); *Dechloromonas aromatica* (AAZ45778); *Desulfovibrio vulgaris* (YP_012252); *Flavobacteroides bacterium* 1 (ZP_01105921); *Flavobacteroides bacterium* 2 (ZP_01105294); *G. sulfurreducens* PccH (GSU3274); *G. sulfurreducens* OmcF (NP_953478); *Halothiobacillus neapolitanus* (P25938); *Helicobacter pylori* (WP_000756023); *Idiomarina baltica* (ZP_01041945); *Legionella pneumophila* (YP_096733); *Leptolyngbya boryana* (P00117); *L. cholodnii* (YP_001792017); *Microcystis aeruginosa* (P00112); *Paracoccus denitrificans* (P00096); *Pasteurella multocida* (NC_002663); *P. propionicus* (YP_900515); *Photobacterium* sp. (ZP_01162384); *Polaromonas* sp. (YP_546929); *Polaromonas naphthalenivorans* (ZP_01020507); *Pseudomonas fluorescens* (YP_351250); *Rhodothermus marinus* (ACA83734); *Rhodopseudomonas viridis* (M59302); *Robiginitalea biformata* 1 (ZP_01120248); *Robiginitalea biformata* (ZP_01119795); *R. ferrireducens* (YP_521339); *Rubrivivax gelatinosus* (ZP_00243317); *Synechococcus* sp. (P00115); *Thermus thermophilus* (M93437); *T. nitratireducens* (YP_007216771); *T. sulfidiphilus* (YP_002512332); *Vibrio cholerae* 1 (NP_229825); *Vibrio cholerae* 2 (NP_231872); *Wolinella succinogenes* (NP_906926); *Yersinia pestis* (CAC89905). The Ambler's class I monoheme cytochromes subclasses c_2, c_5, c_6, $c_{551/552}$, c_{553}, c_{554} are labeled. The two unlabeled groups correspond to the *c*-type cytochromes from the bacteria of *Bacteroidetes phylum* and *G. sulfurreducens* PccH cytochrome (highlighted in red) and top six hits returned for the BLAST search with PccH (see Fig 6.14).

From this analysis, a separate group is formed by PccH and its most homologous sequences (Figs 6.16 and 6.17) suggesting that they are representatives of a new subclass within the class I cytochromes.

Further structural evidence discussed below emphasizes this proposal. The proteins of PccH family contain the largest monoheme cytochromes observed to date with around 129 amino acids. For comparison, the mitochondrial cytochromes have ~104 amino acids whereas the other subclasses of class I cytochromes are even smaller (~80 amino acids). PccH is structurally quite different from any of the other class I cytochromes. A Dali search [37] with PccH structure did not reveal any meaningful structural homologs in the PDB. The Dali search returned non-heme containing proteins with very low Z-scores. For example, the top hit with a Z-score of 2.4 (rmsd 4.1 Å for 70 residues aligned) was a helical protein from *Bordetella bacteriophage* (PDB ID: 4DWL). Structural alignment with secondary structure matching [38] also did not reveal any significant structural homologs; cytochrome c_{554} from *Cholorobaculum tepidum* (PDB ID: 4J20) is the top hit in this search with Z-score of 2.7 (rmsd 3.8 Å for 69 residues aligned) and 50% of sequence identity. The most striking feature of the heme binding site in PccH is that the methionine axial ligand comes from a very different part of the protein structure as compared to other monoheme cytochromes. This is illustrated by using the overlap of PccH and the *C. tepidum* cytochrome c_{554} (PDB ID: 4J20) in Fig 6.18.

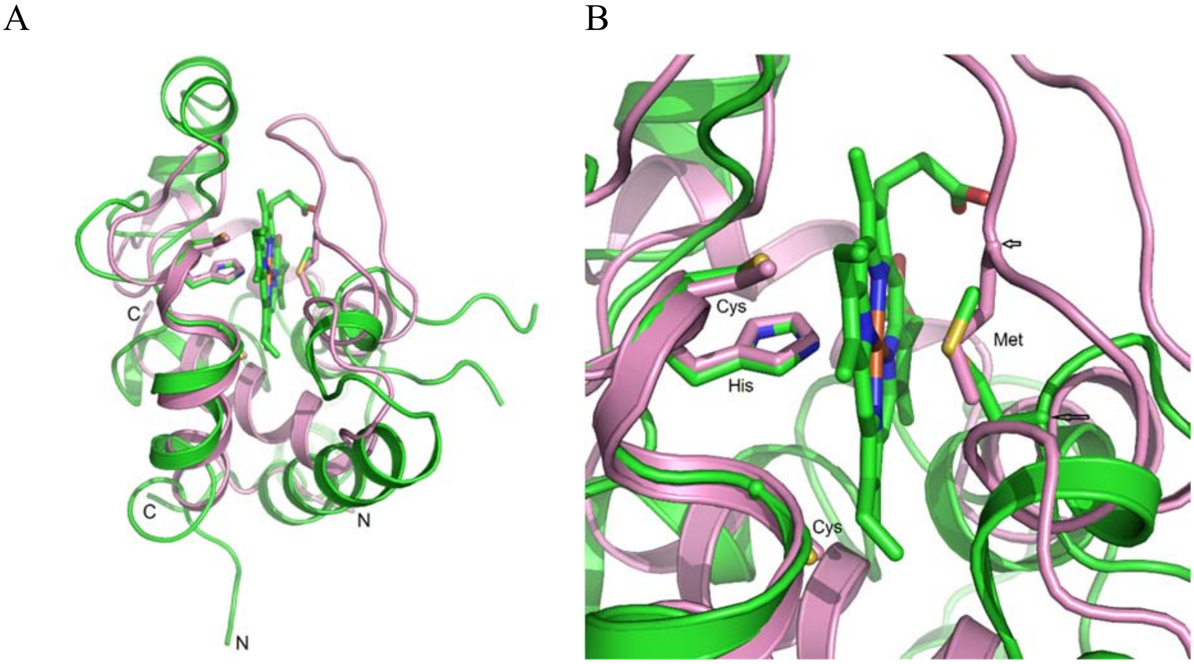

Fig 6.18 Comparison between PccH and *Chlorobaculum tepidum* cytochrome c_{554} (PDB ID: 4J20) structures. (A) A cartoon view of the overlap of both cytochromes. The proteins were manually overlapped using their heme porphyrin ring atoms. For clarity purposes, only heme from PccH is shown. Cα ribbon of PccH is in green and that of cytochrome c_{554} is in pink. The side chains of cysteines, histidines and methionines are shown in pink for cytochrome c_{554}; heme and side chains for PccH are shown in atom type colors. Respective N and C termini are indicated. (B) A closer view of the heme binding residues to illustrate the difference in the positions of the axial methionine residues between the two cytochromes. Note that the cysteine and histidine side chains overlap quite well, whereas the methionine side chains binding the heme originate from different parts in each of the two proteins (the Cα position of the methionine in each case is pointed by an arrow).

When the hemes are aligned in these proteins, the heme binding cysteine residues and the axial histidine residues align quite well (left side of the heme in Fig 6.18A), whereas the methionine side chains do not overlap even though the sulfur atoms of the methionine binding the heme iron do align well. It is worth noting that upon overlapping the two proteins using only heme porphyrin ring atoms, the N-terminal helices up until the heme binding motif (cysteines and histidines) of the two proteins overlap well. Beyond the axial histidine, the two structures differ greatly. The Cα of the axial methionine in case of PccH comes from below the plane of the histidine ring, whereas the same for axial methionine in case of *C. tepidum* cytochrome c_{554} comes from above the plane of the histidine ring (indicated by arrows in Fig 6.18B). The Cα of axial methionine in PccH and that in horse heart cytochrome *c* are separated by 5.3 Å. The axial methionine side chain points toward the surface of the protein in case of PccH whereas to the best of our knowledge, it points to the interior of the protein in all other monoheme cytochromes.

The structure of PccH is unique among all the monoheme cytochromes of class I known to date [34, 35]. For comparison, a gallery of structures of bacterial monoheme *c*-type cytochrome representatives from each of the subclasses is shown in Fig 6.19. There are a significant number of amino acids strictly conserved in the PccH family of cytochromes (Fig 6.16). Thirty-four of 129 residues (29%) including the two cysteines and the axial ligands histidine and methionine residues are conserved. Therefore, it seems likely that the structural fold of this family of cytochromes will be conserved. We propose that PccH together with the cytochromes with similar sequences from other species (Fig 6.16) forms a new subclass within the class I cytochromes.

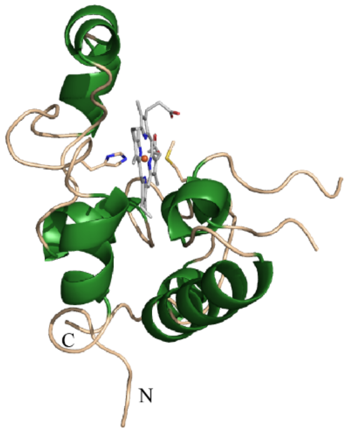

Geobacter sulfurreducens
cytochrome PccH
PDB ID: 4RLR

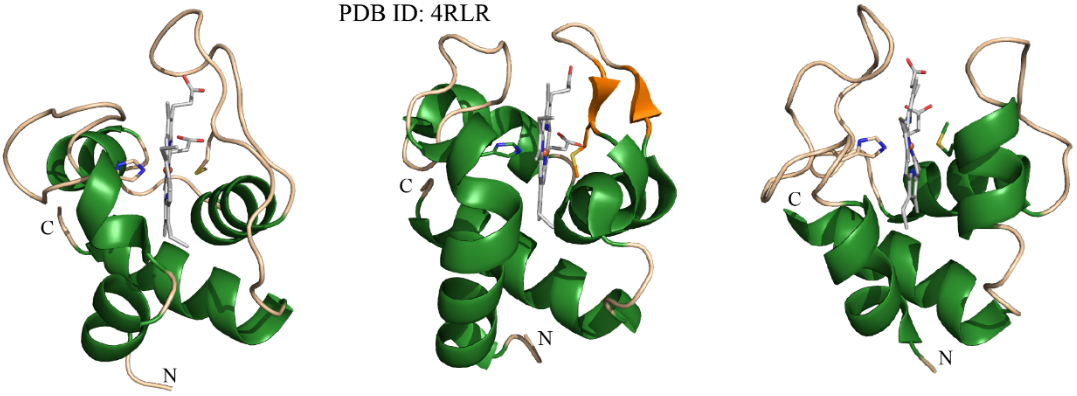

Pseudomonas aeruginosa
cytochrome c_{551}
PDB ID: 451C

Chlorobaculum tepidum
cytochrome c_{554}
PDB ID: 4J20

Desulfovibrio vulgaris
cytochrome c_{553}
PDB ID: 2DVH

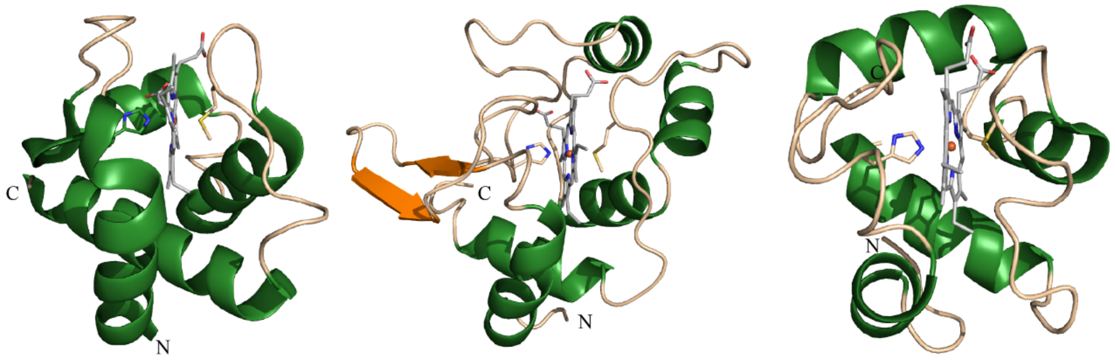

Arthrospira maxima
cytochrome c_6
PDB ID: 1F1F

Paracoccus denitrificans
cytochrome c_2
PDB ID: 1COT

Azotobacter vinelandii
cytochrome c_5
PDB ID: 1CC5

Fig 6.19 A gallery of representative bacterial class I monoheme cytochromes including PccH shown as Cα cartoons. The heme orientation is approximately the same in each case with the respective N- and C-termini labeled; the helical regions are shown in green, β-strands in orange and loops in light brown.

6.1.8 Functional clues for PccH

An examination of the immediate neighbors of PccH in the genome of *G. sulfurreducens* did not reveal any obvious clues regarding a more detailed functional information for this cytochrome. Bacterial localization prediction tool PSORTB (http://www.psort.org/psortb) suggests that PccH is located at the periplasm of *G. sulfurreducens*; therefore, this cytochrome could not be involved in the first step of accepting electrons from the electrode. This it is very likely involved in the downstream electron transport events in the periplasm. However, it is not clear what the interacting partners of this cytochrome may be. Because the transcripts of both PccH and a periplasmic triheme cytochrome, PpcD, have a higher expression in *G. sulfurreducens* growing on an electrode [1], we have examined the potential for interaction between these two cytochromes using NMR spectroscopy. The heme methyl signals have been assigned for both PccH and PpcD and can therefore be used to map the potential interaction sites between the two proteins [39]. Fig 6.20 illustrates the region of the 1D ^{1}H NMR spectra containing the heme methyl signals of PpcD in the presence of increasing amounts of PccH. Analysis clearly shows that the heme methyl signals of both proteins are unperturbed both in terms of chemical shift and line broadening, indicating that these proteins do not interact under the experimental conditions tested.

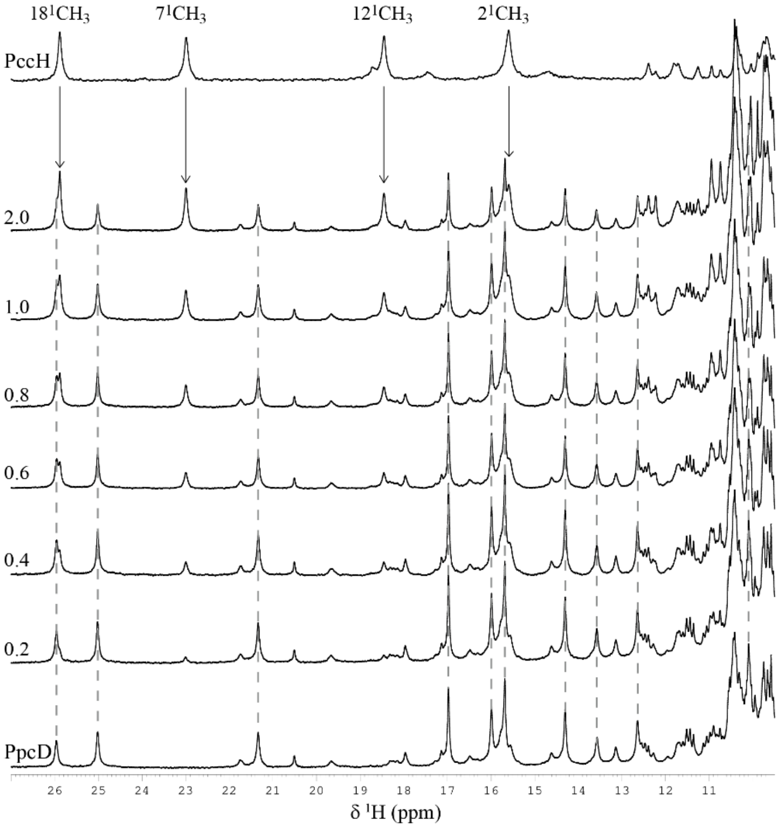

Fig 6.20 Expansions of the low-field region of 1D ^{1}H NMR spectra obtained for cytochrome PpcD in the oxidized form (lower spectrum) in the presence of increasing amounts of PccH at 298 K, pH 7, 100 mM final ionic strength. The molar ratio of [PccH]/[PpcD] is indicated on the left side of each spectrum. The dashed lines indicate the heme methyl signals of PpcD in the following order from left to right: $2^1CH_3^{I}$, $18^1CH_3^{I}$, $12^1CH_3^{I}$, $18^1CH_3^{IV}$, $12^1CH_3^{III}$, $7^1CH_3^{III}$, $7^1CH_3^{IV}$, $12^1CH_3^{IV}$, $2^1CH_3^{IV}$, $7^1CH_3^{III}$. The heme methyl $7^1CH_3^{I}$ and $18^1CH_3^{III}$, whose signals appear in crowded regions at chemical shift of approximately 4 and -1 ppm, respectively are not indicated. The 1D ^{1}H NMR spectrum of free PccH is indicated in the top of the figure and the arrows indicate the heme methyl signals of this cytochrome throughout the titration of PpcD.

To further confirm the absence of interaction between the two cytochromes, the chemical shift perturbations on the backbone NH signals of PpcD with increasing amounts of PccH were also monitored by recording a series of two-dimensional 2D ^{1}H,^{15}N HSQC spectra (Fig 6.21). As for the heme methyl signals, no perturbation on the NH backbone signals of PpcD was observed in presence of PccH, further confirming that the two proteins are not direct physiological redox partners in the electron transfer chain from graphite electrodes (poised at -300 mV *versus* NHE) to the terminal electron acceptor fumarate.

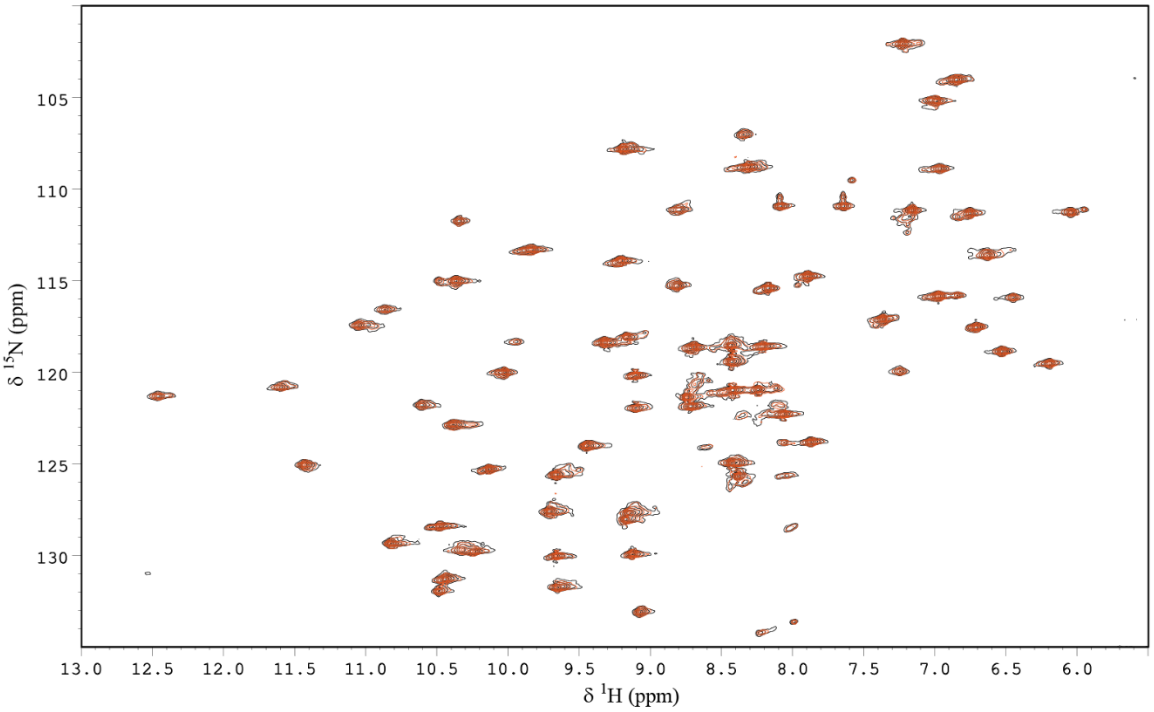

Fig 6.21 Overlay of the 2D ^{1}H,^{15}N HSQC spectra of ^{15}N-enriched PpcD (0.5 mM, pH 7, 100 mM final ionic strength) in the presence of PccH in a 1:1 molar ratio. The contours of the signals in the PpcD and PpcD:PccH spectra are shown in black and orange, respectively.

6.2 Conclusions

The discovery that *G. sulfurreducens* cells can accept electrons directly from electrodes for the reduction of terminal electron acceptors, led to the investigation of a wide-range of applications. This work reports the first biochemical characterization of the cytochrome PccH, a key protein in this process.

The data obtained by CD spectroscopy suggested that cytochrome PccH has a high helical content. In addition, UV-visible and NMR spectroscopy studies showed the presence of a hexacoordinated low-spin Fe ion axially bound to His and Met residues. These axial ligands were assigned to His^{21} and Met^{84}. The crystal structure of PccH determined at a resolution of 2.0 Å, confirms this information and shows that the heme cofactor is wedged between two lobes formed by the protein chain. The unique structure of PccH, taken together with the sequence phylogenetic analysis, suggests that this cytochrome forms a new subclass of class I monoheme *c*-type cytochromes.

The cytochrome PccH was previously suggested to function as an intermediary in electron transfer between the outer cell surface and the inner membrane. Gene knockout studies revealed that the absence of PccH inhibited the capacity of *G. sulfurreducens* cells to accept electrons from electrodes. Also, microarray analysis revealed that *pccH* was the gene showing the highest transcript abundance when *G. sulfurreducens* cells use a graphite cathode (poised at -293 mV *versus* NHE) as the sole electron donor to reduce fumarate (+30 mV *versus* NHE) to succinate [1] (Fig 6.22).

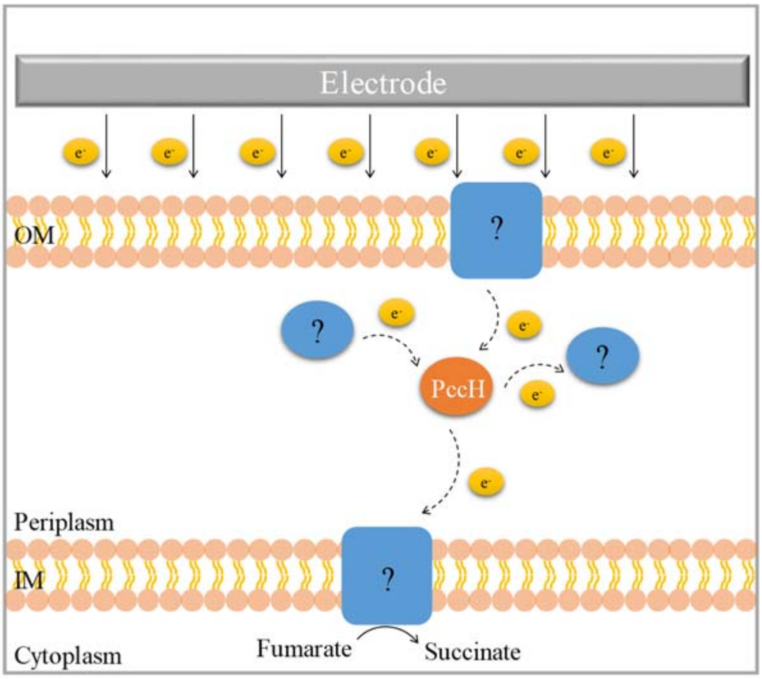

Fig 6.22 Schematic representation of possible electron transfer pathways that involve PccH in *G. sulfurreducens* cells grown using graphite cathode (poised at -293 mV *vs* NHE) as a sole electron donor and fumarate (E^0 = 30 mV *vs* NHE) as terminal electron acceptor [1]. The dashed arrows indicate possible electron flow from/to still unknown redox partners of PccH (E^0 = - 24 mV *vs* NHE). Adapted from [40].

The thermodynamic studies performed in the present work are relevant for the understanding of the electron transfer mechanism from graphite cathodes to *G. sulfurreducens* cells. The reduction potential values of PccH determined in the physiological pH range for *G. sulfurreducens* growth show that this periplasmic cytochrome is thermodynamically suitable to bridge the electron transfer from biocathodes to more electro-positive electron acceptors, such as fumarate. Since outer membrane cytochromes are abundant in *G. sulfurreducens* cells, it is conceivable that a yet unknown cell-surface associated redox component accepts electrons from the biocathode, which are then transferred to more electro-positive electron acceptors within the periplasm, such as PccH, to cytoplasmic-associated redox components and, finally, to the terminal electron acceptor fumarate. The observation that the current-consuming capacity of *G. sulfurreducens* cells increased over time with the repeated addition of fumarate, suggests that energy might be conserved to support growth from direct electron transfer from electrodes [41]. The redox-Bohr effect observed in the pH range 6 to 8 indicates that PccH can also couple proton to electron transfer in the *G. sulfurreducens* physiological pH range and may be involved in these energy-conserving mechanisms. To the best of our knowledge, PccH is the first *c*-type monoheme cytochrome showing a negative reduction potential value (-24 mV *versus* NHE, pH 7) within the physiological pH range of growth for *G. sulfurreducens*. This feature permits the protein to be redox active at the typically negative working potential ranges encountered by this bacterium [42-44].

6.3 Materials and methods

6.3.1 Molecular mass determination and heme quantification

The molecular mass of cytochrome PccH was determined by matrix-assisted laser desorption−ionization time-of-flight mass spectrometry (MALDI-TOF-MS) using a Voyager-DETM PRO Biospectrometry workstation equipped with a nitrogen laser radiating at 337 nm from Applied Biosystems (Foster City, United States). A matrix solution of sinapinic acid in 70:30 water/acetonitrile with 0.1% TFA (final concentration) was used. The measurements were performed in triplicates in positive ion mode using ProteoMassTM cytochrome *c* MALDI-MS from Sigma-Aldrich (MW 12361.96 Da) as internal calibration.

The quantification of the *c*-type hemes present in PccH was obtained by the pyridine hemochrome method, as described by Berry and Trumpower [45]. Purified protein (5 μM final concentration) was initially incubated with 50 mM NaOH and 20% v/v pyridine in aqueous solution at room temperature for 15 min. Two separated aliquots of the resulting solution were then prepared by adding the reductant sodium dithionite (pyridine ferrohemochrome form) and the oxidant potassium ferricyanide (pyridine ferrihemochrome form). UV-visible spectra of both pyridine hemochrome forms were recorded between 350-700 nm and the heme content was determined using the difference absorption coefficient of 21.84 $mM^{-1}cm^{-1}$ at 550 nm for the pyridine ferrohemochrome and the pyridine ferrihemochrome spectrum [45].

6.3.2 Circular dichroism analysis

The protein PccH (0.2 mg/mL prepared in 20 mM NaCl at pH 7) was analyzed by circular dichroism (CD) spectroscopy and its spectra were recorded at 25ºC in the far UV region using a JASCO J-810 spectropolarimeter with a Peltier-thermostated cell support using a 0.1 cm path-length cell quartz. The conformational stability of PccH was assessed by performing temperature denaturation, monitored by far-UV CD at 220 nm, which reports on the stability of the secondary structural elements. For thermal-induced denaturation, a heating rate of $3ºC.min^{-1}$ was used, and temperature was increased from 25ºC to 95ºC. The fraction of unfolded protein (f_U) was monitored by CD spectroscopy and calculated with the expression $f_U = (\theta_N-\theta)/(\theta_N-\theta_U)$, with θ_N corresponding to the ellipticity at 220 nm of the protein in the native folded state, θ the ellipticity at a defined temperature, and θ_U the ellipticity at 220 nm of the completely unfolded state.

CD spectroscopy measures the difference in absorption between left (L) and right (R) handed circularly polarized light in chiral molecules. The two polarizations are differently absorbed, and the difference in absorption is detected, yielding the CD spectrum. This is an established biophysical method probing the secondary structure (α-helices, β-sheets or turns) of peptides, proteins and nucleic acids which have distinct CD bands in the far UV (~200-260 nm) and near UV (~300-400 nm) regions [46]. Additionally, the protein secondary structure is sensitive to its environment (*e.g.* temperature, pH) circular dichroism can be used to observe how secondary structure changes with environmental conditions or on interaction with other molecules.

6.3.3 Redox titrations followed by UV-visible spectroscopy

Redox titrations of PccH were followed by visible spectroscopy at 15 ºC inside an anaerobic LABstar glove box (MBraun) kept at <1 ppm oxygen, with argon circulation, as previously described [47]. The solution potentials were measured using a combined Pt/Ag/AgCl electrode, calibrated with two quinhydrone saturated solutions at different pH values. The visible spectra were recorded in Evolution 300 (Thermo Scientific) spectrophotometer. To check for hysteresis, each redox titration was performed in both reductive and oxidative directions, using sodium dithionite and potassium ferricyanide solutions as reductant and oxidant, respectively. Each UV-visible spectrum is correlated with a measured electric potential after each addition of reductant or oxidant agent. The reduced fraction of the proteins was determined by integrating the area of the α band at 552 nm, connecting the flanking isobestic points to subtract the optical contribution of the redox mediators. The measured solution potentials were corrected to NHE. The experiments were performed at least two times, and the reduction potentials (relative to NHE) were found to be reproducible within ± 5 mV.

The redox titrations of PccH samples with 30 μM protein concentration were prepared in the pH range 4–9 using sodium acetate, sodium phosphate and Tris–HCl buffer solution adjusted with NaCl to a final ionic strength of 100 mM. To ensure a good equilibrium between the redox centers and the working electrode, a mixture of the following redox mediators (~2 μM final concentration) was added to the protein solution: p-benzoquinone, tetramethyl 1,4-phenylenediamine, 1,2-naphtoquinone-4-sulfonic acid, 1,2-naphtoquinone, trimethylhydroquinone, phenazine methosulphate, phenazine ethosulphate, methylene blue, indigo tetrasulphonate, indigo trisulphonate, and indigo disulphonate. These mediators cover the potential range of +280 to -120 mV *versus* NHE, in the first and second case, respectively.

6.3.4 NMR samples preparation and experiments

Cytochrome PccH samples with ~140 μM for 1D NMR studies and 2 mM for 2D NMR studies were prepared in 45 mM phosphate buffer pH 7 with NaCl (100 mM final ionic strength) in 92% H_2O/8% ^2H_2O or in ^2H_2O (99.9%). To prepare the samples in ^2H_2O, the protein was previously lyophilized twice and then resuspended in the phosphate buffer. NMR spectra were obtained before and after the lyophilization to confirm that the protein integrity was not affected. Reduction of the samples was achieved by first flushing out the air from the oxidized sample with argon and then by adding sodium dithionite in small aliquots from a degassed 2 M stock solution to the NMR tube with a gas-tight syringe through the rubber septum. NMR spectra were obtained before the addition of sodium dithionite and after its removal by ultrafiltration methods (Amicon Ultra) to confirm that the protein integrity was not affected.

For NMR interaction studies, ^{15}N PpcD and natural abundance PccH samples (2 mM and 0.5 mM concentration, respectively) were prepared in 45 mM phosphate buffer, pH 7, with NaCl (100 mM final ionic strength), in 92% H_2O/8% ^2H_2O and in ^2H_2O (99.9%), respectively.

All the NMR experiments were acquired in a Avance III 600 spectrometer equipped with a triple-resonance cryoprobe at 298 K. ^{1}H and ^{15}N chemical shifts were calibrated using the water signal as internal reference and through indirect referencing, respectively. Spectra were processed using TOPSPIN (Bruker BioSpin, Karlsruhe, Germany) and analyzed with SPARKY (T. D. Goddard and D. G. Kneller, SPARKY 3, University of California, San Francisco).

For 1D ^{1}H NMR spectra, a total of 64k data points was collected to cover a sweep width of 42 kHz. The following set of 2D NMR experiments was acquired: fully oxidized protein: 2D ^{1}H, ^{13}C HMQC; 2D ^{1}H, ^{1}H TOCSY (45 ms, mixing-time) and 2D ^{1}H, ^{1}H NOESY (80 ms); sample with a mixture of reduced and oxidized protein: 2D ^{1}H, ^{1}H EXSY (25 ms). 2D NMR spectra were acquired with a sweep with of 26 kHz in ^{1}H dimension and 45 kHz in ^{13}C dimension.

To measure the impact of PccH on the chemical shifts of PpcD signals, a series of 1D ^{1}H NMR and 2D ^{1}H, ^{15}N HSQC NMR spectra in the presence of increasing amounts of PccH were acquired. The last spectra were acquired with a sweep width of 11 kHz in F_2 and 22 kHz in F_1. 1D ^{1}H NMR spectra were acquired by collecting 16k data points with 128 scans.

The temperature dependence of heme methyl signals of PccH was probed by acquiring a series of 1D ^{1}H NMR spectra in the range 290–309 K. 1D ^{1}H NMR spectra were acquired with 32k data points for a sweep width of 41667 Hz with 64 scans per increment. Analysis of the temperature dependence of heme signals by NMR can be used to study the cytochrome heme spin-states in solution.

The effect of pH on the chemical shifts of the PccH heme propionates and heme methyl groups were evaluated by a series of 2D ^{1}H, ^{1}H NOESY spectra acquired in pH range 5–9. The spectra were collected with a mixing-time of 80 ms and a sweep width of 26 kHz in both dimensions. The pH dependence of NMR signals can be used to search for protonation centers and to describe proton association-dissociation equilibriums.

6.4 References

1. Strycharz SM, Glaven RH, Coppi MV, Gannon SM, Perpetua LA, Liu A, Nevin KP & Lovley DR (2011) Gene expression and deletion analysis of mechanisms for electron transfer from electrodes to *Geobacter sulfurreducens*. *Bioelectrochemistry* **80**, 142-150.

2. Thony-Meyer L (1997) Biogenesis of respiratory cytochromes in bacteria. *Microbiol Mol Biol Rev* **61**, 337-376.

3. de Prat Gay G & Fersht AR (1994) Generation of a family of protein fragments for structure-folding studies. 1. Folding complementation of two fragments of chymotrypsin inhibitor-2 formed by cleavage at its unique methionine residue. *Biochemistry* **33**, 7957-7963.

4. Moore GR & Pettigrew GW (1990) *Cytochromes c : evolutionary, structural and physicochemical aspects*. Springer-Verlag, Berlin.

5. Teng Q (2005) *Structural Biology: Practical NMR Applications*. Springer Science+Business Media, Inc., Boston, MA.

6. Bertini I & Luchinat C (1986) NMR of paramagnetic molecules in biological systems. In *Physical bioinorganic chemistry series*. pp. 336. Benjamin-Cummings Pub Co, Menlo Park, Calif.

7. Salgueiro CA, Turner DL & Xavier AV (1997) Use of paramagnetic NMR probes for structural analysis in cytochrome c_3 from *Desulfovibrio vulgaris*. *Eur J Biochem* **244**, 721-734.

8. Moss GP (1988) Nomenclature of tetrapyrroles. Recommendations 1986 IUPAC-IUB Joint Commission on Biochemical Nomenclature (JCBN). *Eur J Biochem* **178**, 277-328.

9. Turner DL (1993) Evaluation of ^{13}C and ^{1}H Fermi contact shifts in horse cytochrome *c*. The origin of the anti-Curie effect. *Eur J Biochem* **211**, 563-568.

10. Dantas JM, Campelo LM, Duke NE, Salgueiro CA & Pokkuluri PR (2015) The structure of PccH from *Geobacter sulfurreducens* - a novel low reduction potential monoheme cytochrome essential for accepting electrons from an electrode. *FEBS J* **282**, 2215-2231.

11. Pokkuluri PR, Londer YY, Wood SJ, Duke NE, Morgado L, Salgueiro CA & Schiffer M (2009) Outer membrane cytochrome *c*, OmcF, from *Geobacter sulfurreducens*: high structural similarity to an algal cytochrome c_6. *Proteins* **74**, 266-270.

12. Campos AP, Aguiar AP, Hervas M, Regalla M, Navarro JA, Ortega JM, Xavier AV, De La Rosa MA & Teixeira M (1993) Cytochrome c_6 from *Monoraphidium braunii*. A cytochrome with an unusual heme axial coordination. *Eur J Biochem* **216**, 329-341.

13. Pokkuluri PR, Londer YY, Yang X, Duke NE, Erickson J, Orshonsky V, Johnson G & Schiffer M (2010) Structural characterization of a family of cytochromes c_7 involved in Fe(III) respiration by *Geobacter sulfurreducens*. *Biochim Biophys Acta* **1797**, 222-232.

14. DeLano WL (2002) The PyMOL molecular graphics system. In http://wwwpymolorg.

15. Dutton PL (1978) Redox potentiometry: determination of midpoint potentials of oxidation-reduction components of biological electron-transfer systems. *Methods Enzymol* **54**, 411-435.

16. Morgado L, Bruix M, Orshonsky V, Londer YY, Duke NE, Yang X, Pokkuluri PR, Schiffer M & Salgueiro CA (2008) Structural insights into the modulation of the redox properties of two *Geobacter sulfurreducens* homologous triheme cytochromes. *Biochim Biophys Acta* **1777**, 1157-1165.

17. Moore GR, Pettigrew GW, Pitt RC & Williams RJ (1980) pH dependence of the redox potential of *Pseudomonas aeruginosa* cytochrome c_{551}. *Biochim Biophys Acta* **590**, 261-271.

18. Leitch FA, Moore GR & Pettigrew GW (1984) Structural basis for the variation of pH-dependent redox potentials of *Pseudomonas cytochromes* c_{551}. *Biochemistry* **23**, 1831-1838.

19. Park JS, Ohmura T, Kano K, Sagara T, Niki K, Kyogoku Y & Akutsu H (1996) Regulation of the redox order of four hemes by pH in cytochrome c_3 from *D. vulgaris* Miyazaki F. *Biochim Biophys Acta* **1293**, 45-54.

20. Saraiva LM, Salgueiro CA, da Costa PN, Messias AC, LeGall J, van Dongen WM & Xavier AV (1998) Replacement of lysine 45 by uncharged residues modulates the redox-Bohr effect in tetraheme cytochrome c_3 of *Desulfovibrio vulgaris* (Hildenborough). *Biochemistry* **37**, 12160-12165.

21. Brennan L, Turner DL, Messias AC, Teodoro ML, LeGall J, Santos H & Xavier AV (2000) Structural basis for the network of functional cooperativities in cytochrome c_3 from *Desulfovibrio gigas*: solution structures of the oxidised and reduced states. *J Mol Biol* **298**, 61-82.

22. Reedy CJ, Elvekrog MM & Gibney BR (2008) Development of a heme protein structure-electrochemical function database. *Nucleic Acids Res* **36**, 307-313.

23. Schnackenberg J, Than ME, Mann K, Wiegand G, Huber R & Reuter W (1999) Amino acid sequence, crystallization and structure determination of reduced and oxidized cytochrome c_6 from the green alga *Scenedesmus obliquus*. *J Mol Biol* **290**, 1019-1030.

24. Mao J, Hauser K & Gunner MR (2003) How cytochromes with different folds control heme redox potentials. *Biochemistry* **42**, 9829-9840.

25. Lee B & Richards FM (1971) The interpretation of protein structures: estimation of static accessibility. *J Mol Biol* **55**, 379-400.

26. Taniguchi VT, Sailasuta-Scott N, Anson FC & Gray HB (1980) Thermodynamics of metalloprotein electron transfer reactions. *Pure Appl Chem* **52**, 2275-2281.

27. Itoh M, Seo D, Sakurai H & Setif P (2002) Kinetics of electron transfer between soluble cytochrome c_{554} and purified reaction center complex from the green sulfur bacterium *Chlorobium tepidum*. *Photosynth Res* **71**, 125-135.

28. Bertrand P, Mbarki O, Asso M, Blanchard L, Guerlesquin F & Tegoni M (1995) Control of the redox potential in *c*-type cytochromes: importance of the entropic contribution. *Biochemistry* **34**, 11071-11079.

29. Cho YS, Wang QJ, Krogmann D & Whitmarsh J (1999) Extinction coefficients and midpoint potentials of cytochrome c_6 from the cyanobacteria *Arthrospira maxima*, *Microcystis aeruginosa*, and *Synechocystis* 6803. *Biochim Biophys Acta* **1413**, 92-97.

30. Meyer TE, Przysiecki CT, Watkins JA, Bhattacharyya A, Simondsen RP, Cusanovich MA & Tollin G (1983) Correlation between rate constant for reduction and redox potential as a basis for systematic investigation of reaction mechanisms of electron transfer proteins. *Proc Natl Acad Sci USA* **80**, 6740-6744.

31. Carter DC, Melis KA, O'Donnell SE, Burgess BK, Furey WR, Jr., Wang BC & Stout CD (1985) Crystal structure of *Azotobacter cytochrome* c_5 at 2.5 A resolution. *J Mol Biol* **184**, 279-295.

32. Nicholls A, Sharp KA & Honig B (1991) Protein folding and association: insights from the interfacial and thermodynamic properties of hydrocarbons. *Proteins* **11**, 281-296.

33. Altschul SF, Madden TL, Schaffer AA, Zhang J, Zhang Z, Miller W & Lipman DJ (1997) Gapped BLAST and PSI-BLAST: a new generation of protein database search programs. *Nucleic Acids Res* **25**, 3389-3402.

34. Ambler RP (1991) Sequence variability in bacterial cytochromes *c*. *Biochim Biophys Acta* **1058**, 42-47.

35. Bertini I, Cavallaro G & Rosato A (2006) Cytochrome *c*: occurrence and functions. *Chem Rev* **106**, 90-115.

36. Stelter M, Melo AM, Pereira MM, Gomes CM, Hreggvidsson GO, Hjorleifsdottir S, Saraiva LM, Teixeira M & Archer M (2008) A novel type of monoheme cytochrome *c*: biochemical and structural characterization at 1.23 A resolution of *rhodothermus marinus* cytochrome *c*. *Biochemistry* **47**, 11953-11963.

37. Holm L & Rosenstrom P (2010) Dali server: conservation mapping in 3D. *Nucleic Acids Res* **38**, 545-549.

38. Krissinel E & Henrick K (2004) Secondary-structure matching (SSM), a new tool for fast protein structure alignment in three dimensions. *Acta Crystallogr D Biol Crystallogr* **60**, 2256-2268.

39. Dantas JM, Saraiva IH, Morgado L, Silva MA, Schiffer M, Salgueiro CA & Louro RO (2011) Orientation of the axial ligands and magnetic properties of the hemes in the cytochrome c_7 family from *Geobacter sulfurreducens* determined by paramagnetic NMR. *Dalton Trans* **40**, 12713-12718.

40. Silveira CM, Castro MA, Dantas JM, Salgueiro C, Murgida DH & Todorovic S (2017) Structure, electrocatalysis and dynamics of immobilized cytochrome PccH and its microperoxidase. *Phys Chem Chem Phys* **19**, 8908-8918.

41. Lovley DR (2011) Powering microbes with electricity: direct electron transfer from electrodes to microbes. *Environ Microbiol Rep* **3**, 27-35.

42. Liu Y, Kim H, Franklin RR & Bond DR (2011) Linking spectral and electrochemical analysis to monitor *c*-type cytochrome redox status in living *Geobacter sulfurreducens* biofilms. *Chemphyschem* **12**, 2235-2241.

43. Srikanth S, Marsili E, Flickinger MC & Bond DR (2008) Electrochemical characterization of *Geobacter sulfurreducens* cells immobilized on graphite paper electrodes. *Biotechnol Bioeng* **99**, 1065-1073.

44. Marsili E, Rollefson JB, Baron DB, Hozalski RM & Bond DR (2008) Microbial biofilm voltammetry: direct electrochemical characterization of catalytic electrode-attached biofilms. *Appl Environ Microbiol* **74**, 7329-7337.

45. Berry EA & Trumpower BL (1987) Simultaneous determination of hemes *a*, *b*, and *c* from pyridine hemochrome spectra. *Anal Biochem* **161**, 1-15.

46. Kelly SM, Jess TJ & Price NC (2005) How to study proteins by circular dichroism. *Biochim Biophys Acta* **1751**, 119-139.

47. Paquete CM, Turner DL, Louro RO, Xavier AV & Catarino T (2007) Thermodynamic and kinetic characterisation of individual haems in multicentre cytochromes c_3. *Biochim Biophys Acta* **1767**, 1169-1179.

7

FUTURE PERSPECTIVES[1]

---

[1] Partially reproduced from Dantas JM, Salgueiro CA, Bruix M (2015) Backbone, side chain and heme resonance assignments of the triheme cytochrome PpcD from *Geobacter sulfurreducens*, Biomol NMR Assign 9, 211-214 (doi: 10.1007/s12104-014-9576-9), in accordance with the Editors' Copyright Policy.

7. Future perspectives

This Chapter describes the work that were also developed during the time course of this Thesis, but still not completely concluded. The future focus of the research group will be the functional and structural characterization of OM cytochromes. In this context, genes encoding some OM cytochromes that are involved in EET, in particular those clearly affecting *G. sulfurreducens* growth in presence of extracellular iron compounds (OmcE, OmcS and OmaB) were cloned (see Table 1.1). In addition, the NMR signal fingerprints of periplasmic cytochromes PpcB, PpcD and PpcE in the reduced form were also obtained and can now be explored to assist to their solution structure determination and to probe interface interacting regions with periplasmic components of OM cytochromes. Overall, it is expected that these studies will pave the way to further understand the EET mechanisms in *G. sulfurreducens*.

7.1 Periplasmic triheme cytochromes

The NMR backbone and side chain assignment of PpcA were previously determined in oxidized and reduced states [1-3]. This assignment was used to assist the protein solution structure in both redox states [2, 3] and to probe interaction regions with putative redox partners (Chapters 3 and 4). Under the scope of this Thesis, with exception of PpcC, NMR fingerprints were also obtained for the other members of the PpcA-family in the oxidized state (see Chapter 3) and in the reduced state (this Chapter). This assignment can be used to explore the folding, aggregation, dynamic and stability of these proteins. Moreover, it can be also used to probe their pH- and redox-linked conformational changes, as well as to assist the solution structure determination and the mapping of interacting interface regions with redox partners.

7.1.1 Backbone NMR signals assignment in the reduced state

2D ^{1}H,^{15}N HSQC and the series of 3D NMR experiments (3D CBCANH, 3D CBCA(CO)NH, 3D HNCA, 3D HNCACO) were acquired for PpcB, PpcD and PpcE in the reduced state at pH values that warrant the fully protonation of the redox-Bohr center (see Table 1.4). This is an important issue to allow the appropriate mapping of the redox-linked conformational changes since it excludes any contributions due to different protonation levels of the redox-Bohr center. The assigned signals of PpcB, PpcD and PpcE are indicated in Figure 7.1, except for the two fist residues.

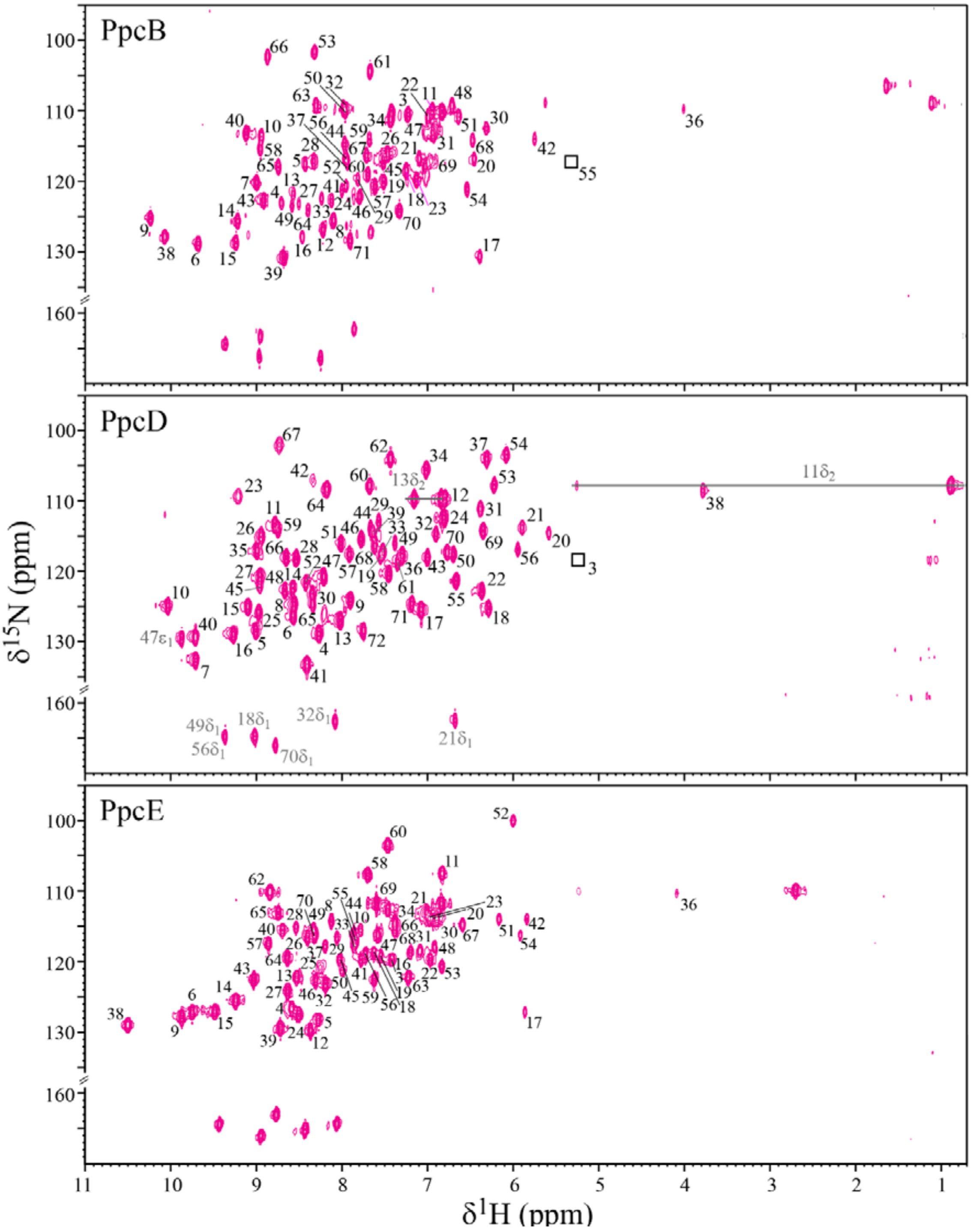

Fig 7.1 2D ^{1}H,^{15}N HSQC spectra of reduced PpcB (1.0 mM, pH 6.5, 600 MHz), PpcD (2.0 mM, pH 7.1, 800 MHz) and PpcE (0.7 mM, pH 6.5, 600 MHz), acquired in 45 mM sodium phosphate buffer with NaCl to 100 mM ionic strength, 298 K. Black and gray labels represent ^{1}H-^{15}N connectivities for backbone and side-chains groups, respectively.

The full list of the chemical shift of the assigned signals is provided in Tables A.6-8 in the Appendix and the assignment percentage is shown in Table 7.1.

Table 7.1 Percentage of NH backbone signal assignment of PpcB, PpcD and PpcE in reduced state.

	Backbone assignment (%)			
Protein	**^{15}N**	**^{1}HN**	**^{13}Cα**	**^{13}Cβ**
PpcB	99	99	97	95
PpcD	99	99	100	98
PpcE	98	98	97	97

Comparing the 2D ^{1}H,^{15}N HSQC NMR spectra obtained for the reduced and oxidized samples (*cf.* Figs 7.1 and 3.1, respectively), the NH signals appear in different spectral regions, which illustrates the effect of the spin state of the heme groups in the protein signals. Additionally, the signals of the axial histidines are observed in the reduced state, but are not observed in the oxidized state, due to the excessive line broadening caused by heme unpaired electrons.

7.1.2 Solution structure determination of PpcD in the reduced state

The detailed thermodynamic characterization of the periplasmic PpcA-family cytochromes showed that PpcA and PpcD have an important redox-Bohr effect that might implicate these proteins in the e^-/H^+ coupling mechanisms to sustain cellular growth [4]. This functional mechanism requires control of both the redox state and the protonation state. The comparative analysis of the solution structure obtained for PpcA in the oxidized and reduced state provided insights in to redox-linked conformational changes, as well as on the pH-linked conformational rearrangements observed in the vicinity of the redox-Bohr center [2, 3]. Such studies established the structural basis for the differences observed in the redox-Bohr center pK_a values (see Table 1.4), providing insights into the e^-/H^+ coupling molecular mechanisms driven by PpcA in *G. sulfurreducens*. Compared to PpcA, PpcD has a similar dependence for the pK_a values of the redox-Bohr center (Table 1.4). However, the proposed functional mechanisms for the two proteins differ considerably [4]. Indeed, the route for the electrons from the fully reduced to the fully oxidized protein involved quite different microstates. For PpcA is $P_{0H} \rightarrow P_{1H} \rightarrow P_{14} \rightarrow P_{134}$, whereas for PpcD is $P_{0H} \rightarrow P_{14} \rightarrow P_{134}$ (see Fig. 1.6). In order to collect structural information that might explain these functional differences it is necessary to compare the structure of PpcD in the reduced and oxidized states. In contrast with the oxidized state ([5], see also Fig 1.5), the structure of PpcD is not available for the reduced state. Therefore, during the time course of this Thesis the assignment of PpcD backbone signals was extended to the side chains to assist its solution structure determination in the reduced state (for PpcD amino acid sequence details see Fig 3.1, Chapter 3).

The side chains of Asn^{11}, Asn^{13}, Trp^{47} and the six axial histidines (His^{18}, His^{21}, His^{32}, His^{49}, His^{56} and His^{70}) were assigned (Fig 7.1), as well as the aliphatic protons such as ^{1}Hα, ^{1}Hβ, ^{1}Hγ, ^{1}Hδ and ^{1}Hε and the aliphatic carbons ^{13}Cγ, ^{13}Cδ and ^{13}Cε. These signals were assigned based on 2D ^{1}H,^{13}C HSQC, 3D HCC(H)-TOCSY, 3D HC(C)H-TOCSY, as well as 2D ^{1}H, ^{1}H COSY, 2D ^{1}H, ^{1}H TOCSY and 2D ^{1}H, ^{1}H NOESY NMR spectra.

Compared to those ring-current effects produced by the amino acid aromatic side chains in non-heme proteins, produced by the three hemes in PpcD are much stronger. Therefore, the chemical shifts of the nuclei located in the proximities of heme groups differ significantly from equivalent residues in non-heme proteins. The more affected nuclei are those of axial histidines. In fact, the ring proton signal (Hδ_1) is strongly up-field to the 1.60–0.60 ppm range. This contrasts clearly with the typical positions found for this signal in non-heme proteins (around 7–8 ppm). Also, the signals correspondent to Hβ of heme axial histidines are typically up-field shifted by at least 2 ppm compared to a non-heme bound histidines. The effect of the ring-current shifts is also extended to the nitrogen atoms (Nδ_1) of the axial histidine side chains, which appear in very characteristic positions (160–170 ppm) in the 2D ^{1}H,^{15}N HSQC spectrum (Fig 7.1).

The chemical shifts of other nuclei located in the neighborhoods of the heme groups are also significantly affected, as it is the case of the Asn^{11} Hδ_{21} (0.79 ppm), Lys^{20} HN (5.55 ppm), Gly^{37} Hα (1.50 and -0.84 ppm), Gly^{38} HN (3.77 ppm), Lys^{45} Hγ (-0.82 and -1.65 ppm); Gly^{62} Hα (2.51 and 1.16 ppm) and Pro^{63} Hδ (-0.70 ppm). Therefore, because of the strong heme ring-current effects, the observed chemical shifts of the nuclei located in the proximities of the heme group(s) are differently affected, depending upon their relative orientation to the closest heme(s). The total extent of the assignment for the ^{1}H, ^{13}C and ^{15}N, excluding carboxyl, amino and hydroxyl groups, is 91, 99 and 99 %, respectively. The ^{1}H, ^{13}C and ^{15}N chemical shifts have been deposit in the BMRB (http://www.bmrm.wisc.edu) under the accession number 19985.

The solution structure of PpcD in the reduced form is under final refinement and its current status in represented Fig 7.2.

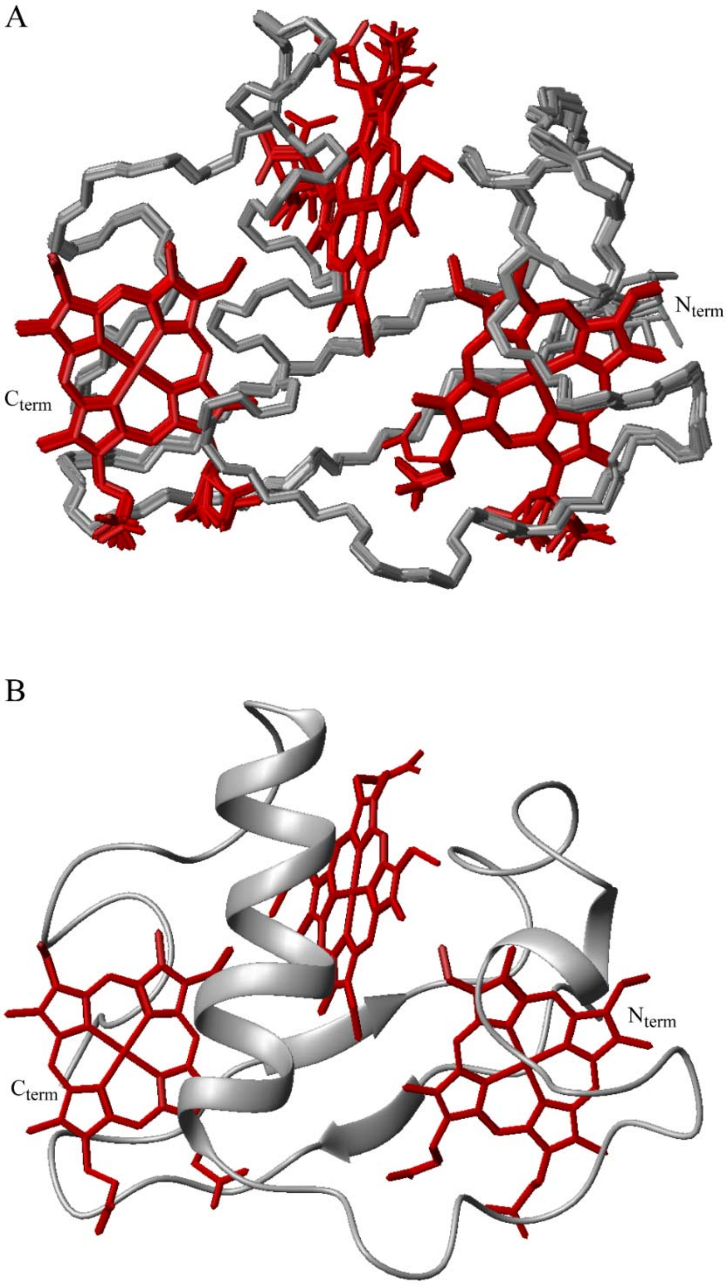

Fig 7.2 Status for the solution structure of PpcD in the reduced state. (A) Overlay of the 20 lowest energy NMR structures of cytochrome PpcD at pH 7 and 298 K. Superimposition was performed using all atoms. The peptide chain and the hemes are color-coded gray and red, respectively. (B) Ribbon diagram of PpcD solution structure. Figures were produced using MOLMOL [6].

7.2 Outer membrane cytochromes

To fully understand the EET pathways in *G. sulfurreducens*, namely those involved in iron reduction, it will be crucial to focus on OM cytochromes, namely OmcE, OmcS and OmaB. In general, OM cytochromes from *G. sulfurreducens* are still very poorly characterized. In fact, with exception of OmcF (Chapter 5) there is no structural data for any other OM cytochrome. Also in terms of functional properties only OmcF, and partially OmcS, were characterized to date. Expression vectors carrying the gene sequence encoding for OmcE, OmcS and OmaB proteins were constructed. OmcE (26 kDa) and

OmcS (47 kDa) are tetraheme and hexaheme *c*-type cytochromes, respectively that are predicted to be located at the exterior of the bacterium OM. OmaB is a component of a trans-outer membrane protein complex that was proposed to connect the periplasm to the cell exterior. This membrane complex is composed by three proteins (OmaB-OmbB-OmcB). OmcB is a dodecaheme cytochrome *c* located in the exterior of the OM, OmbB is in the outer membrane and OmaB is a periplasmic octaheme cytochrome *c* [7].

7.2.1 Transmembrane helices and signal peptide prediction

Genomic DNA from *G. sulfurreducens* was provided by Prof. D.R. Lovley (University of Massachusetts, Amherst). Sequence data for *omcE, omcS* and *omaB* genes (GenBank accession number AAR33949, AAR35877 and AAR36110, respectively) were obtained from Kyoto Encyclopedia of Genes and Genomes Web site, under the accession number T00155. The automatic servers, TMHMM (http://www.cbs.dtu.dk/services/TMHMM/) and HMMTOP (http://www.enzim.hu/hmmtop/) were used to predict transmembrane helices and the signal peptide cleavage site of the three proteins. The *omcE, omcS* and *omaB* genes were cloned including only the gene sequence encoding for the soluble regions of the proteins. For OmcE, OmcS and OmaB, the predicted soluble residues started at Lys^{27}, His^{27} and Asp^{24}, respectively (Table 7.2).

Table 7.2 Amino acid sequences of OmcE, OmcS and OmaB proteins. The predicted sequence of transmembrane helices/signal peptide is underlined and the sequence of a *c*-type heme binding motifs are indicated in red boldface.

Protein	Amino acid sequence
OmcE	MRSEVKIGLALTALLVAVTAAGAASIKNTKHDLSSGSTGATFKATNTDQI**CVFCH**TPHN AQQDIPLWNRGNPTASTFTLYSSSSMNNVPVKQGFTADSISLF**CMSCH**DGATGLGGAVH NDPNGAAIAMVGGNDLITGEANLGTDLSNDHPVNFEVTPAGIAADGNLGALDTGTNPPT MKTGDVTNGLPLFKSARGATTLE**CGSCH**KVHDNTDAPFLRTTMAGSKL**CLGCH**KK
OmcS	MKKGMKVSLSVAAAALLMSAPAAFAFHSGGVAE**CEGCH**TMHNSLGGAVMNSATAQF TTGPMLLQGATQSSS**CLNCH**QHAGDTGPSSYHISTAEADMPAGTAPLQMTPGGDFGWV KKTYTWNVRGLNTSEGERKGHNIVAGDYNYVADTTLTTAPGGTYPANQLH**CSSCH**DPH GKYRRFVDGSIATTGLPIKNSGSYQNSNDPTAWGAVGAYRILGGTGYQPKSLSGSYAFA NQVPAAVAPSTYNRTEATTQTRVAYGQGMSEW**CANCH**TDIHNSAYPTNLRHPAGNGA KFGATIAGLYNSYKKSGDLTGTQASAYLSLAPFEEGTADYTVLKGHAKIDDTALTGADA TSNVN**CLSCH**RAHASGFDSMTRFNLAYEFTTIADASGNSIYGTDPNTSSLQGRSVNEMT AAYYGRTADKFAPYQRAL**CNKCH**AKD
OmaB	MKKWFIALLLLTVSAFTVQMALADKMSHKEYATTPIGE**CNACH**KGEGIAPNHDADWV RGHRVVASRAGKN**CADCH**VQQF**CLDCH**QGGGIEADLSTRTFMRDYVPKSHRSNFLSIH PTKALDNPQT**CTRCH**DQSY**CNECH**ARFPKGSLRIKSHLMLGPNGQKYSFGLGEHAIEAR RNLQS**CQTCH**PEGDV**CIQCH**SSGKTSPHPRNWNSIKNNYKDRAGSRV**CTKCH**LPGTY

7.2.2 Construction of the expression vectors

The genes encoding OmcE and OmcS were cloned using restriction enzymes, whereas the construction of the expression vector encoding for OmaB was cloned using the Gibson Assembly method. In cloning method using restriction enzymes, the pair of primers was designed with the restriction enzymes *NotI* and *EcoRI* sequences and used to amplify the gene sequence encoding for each protein. Then, both fragments and vectors were independently digested with the same restriction enzymes and T4 DNA ligase was used to join cohesive ends, as well as, repair single stranded nicks in each vector construction (Fig 7.2A). On the other hand, in the molecular cloning method using the Gibson Assembly (Fig 7.2B), two pairs of primers were designed. One pair of primers was used to amplify the sequence encoding for the protein from the genomic DNA and containing homology sequences with the destined vector. The other pair of primers was used to amplify the vector, that becomes linear and with the homology sequence regions in the 3' and 5' end. After these two PCR cycles, the products were purified and mixed together with the Master Mix Assembly.

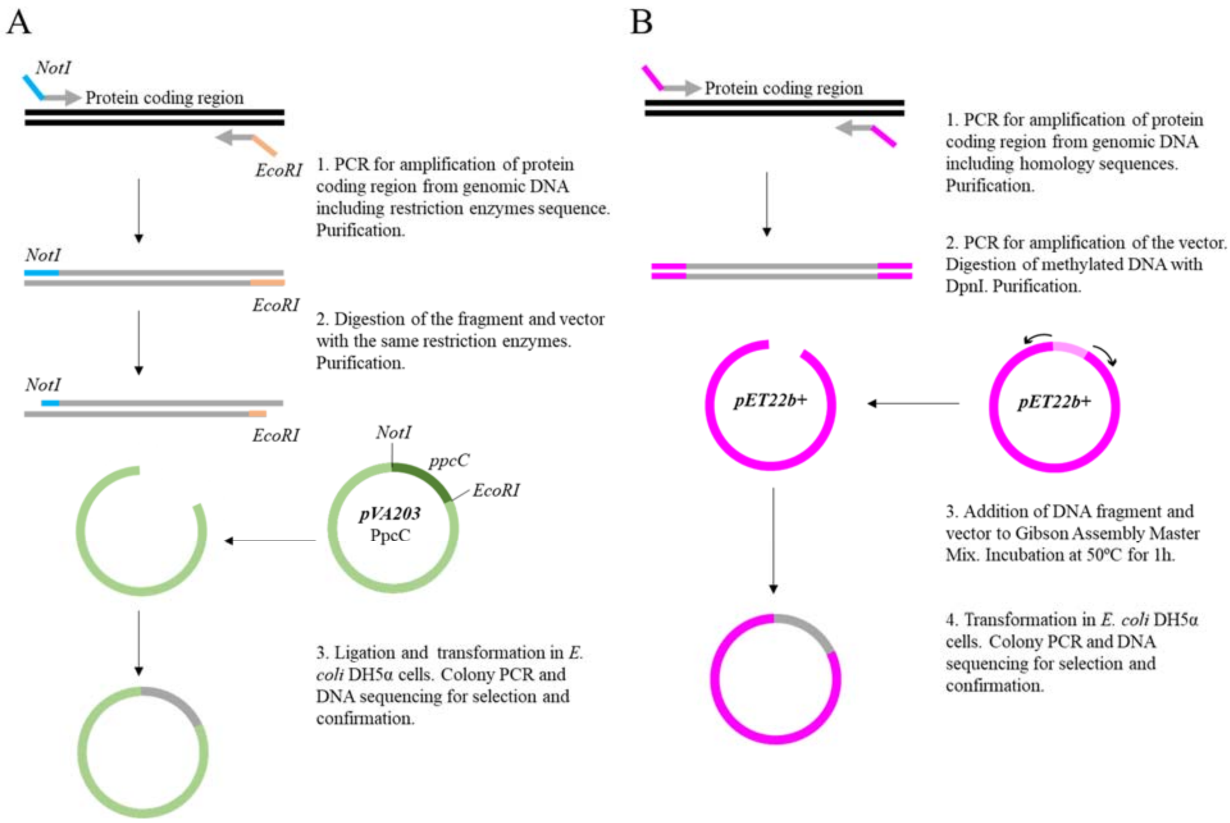

Fig 7.2 Overview of the two molecular cloning methods using to clone the soluble regions of OmcE, OmcS and OmaB proteins. (A) Cloning with restriction enzymes. The restriction enzymes *NotI* and *EcoRI* are represented in blue and orange, respectively. The vector pVA203, containing the encoding sequence for PpcC are indicated in green. (B) Gibson Assembly. The homology regions between the DNA fragments and the cloning vector are indicated in magenta. Genomic DNA and the protein coding region are in black and gray, respectively. Primers used to amplify the fragment and vector are in gray/magenta and black, respectively.

The Gibson Assembly cloning method allows insertion of one or more DNA fragments into virtually any position of the linearized vector and does not rely on the presence of restriction sites within a sequence to be synthesized or cloned. Furthermore, the Gibson Assembly method is faster compared to the cloning with restriction enzymes.

The melting temperatures (T_m) were calculated from thermo scientific web tool (https://www.thermofisher.com/). The primers used for the cloning of the expression vectors encoding for the three proteins are in Table 7.3. Primers were designed to amplify the fragments of *omcE* and *omcS* using the *G. sulfurreducens* genomic DNA as template and including the sequence of the restriction enzymes *NotI*/*EcoRI*. Both fragments were cloned into the vector ppcC-pVA203. For cloning of *omaB* two pair of primers were designed to amplify i) *omaB* fragment and with homology sequences for their assembly into the cloning vector pET22b+, and ii) vector pET22b+.

Table 7.3 DNA templates and primers used to clone the genes encoding for OmcE, OmcS and OmaB. The temperatures of melting (T_m) for each primer were calculated from thermo scientific web tool (https://www.thermofisher.com/). Restriction enzymes *NotI* and *EcoRI* sequences are highlighted in blue and orange, respectively. The homology sequences between the DNA fragments and the cloning vector are highlighted in magenta.

Gene		Sequence	T_m (ºC)	DNA template
omcE	fw	5’CGGGAGCCGGCGGCCGCCAAGAATACCAAG	87	Genomic
	Rv	5’CCACCCTTTTCCCGGAGAATTCCCCCCTACTTCTTGTGGC	85	
omcS	fw	5’GTTCGCGGCCGCCTCCGGCGGCGTTG	91	Genomic
	Rv	5’GGCGGACCCCGGCGGAATCACAGAATTCCAGATTGTGGC	90	
omaB	fw	5’CAGCCGGCGATGGCCGTCCAGATGGCACTG	89	Genomic
	Rv	5’CGGGCTTTGTTAGCAGCCGGTTAGTACGTACCAGGAAGGTG	83	
	fw	5’CCGGCTGCTAACAAAGCCCGAAAGG	77	pET22b+
	Rv	5’GGCCATCGCCGGCTGGGC	80	

For the cloning method using restriction enzymes, the digested vector and plasmids (Invitrogen) were purified using E-gel Electrophoresis System (Invitrogen) and NZYMiniprep kit (NZYTech), respectively. Phusion High-Fidelity DNA polymerase (Finnzymes) was used for amplification from genomic DNA and Taq DNA polymerase (VWR) for colony PCR. For the Gibson Assembly cloning method, the vector was incubated with the restriction endonuclease, DpnI, for 1h at 37ºC, to digest the methylated DNA. The reaction was then stopped after incubation period of 20 min at 80˚C. Both PCR products were purified using the wizard PCR Preps DNA purification system (Promega). Both fragment and vector were mixed together with the Assembly Mater Mix containing T5 exonuclease (New England BioLabs), Phusion High-Fidelity DNA polymerase (Finnzymes) and T4 DNA ligase (Fermentas), and then incubated 1h at 50ºC.

The electrophoretic result after amplification of the gene sequences of *omcE* (621 bp), *omcS* (1222 bp), *omaB* (680 bp) and for the vector pET22b+ (5403 bp) are depicted in Fig 7.3. A negative control was also performed.

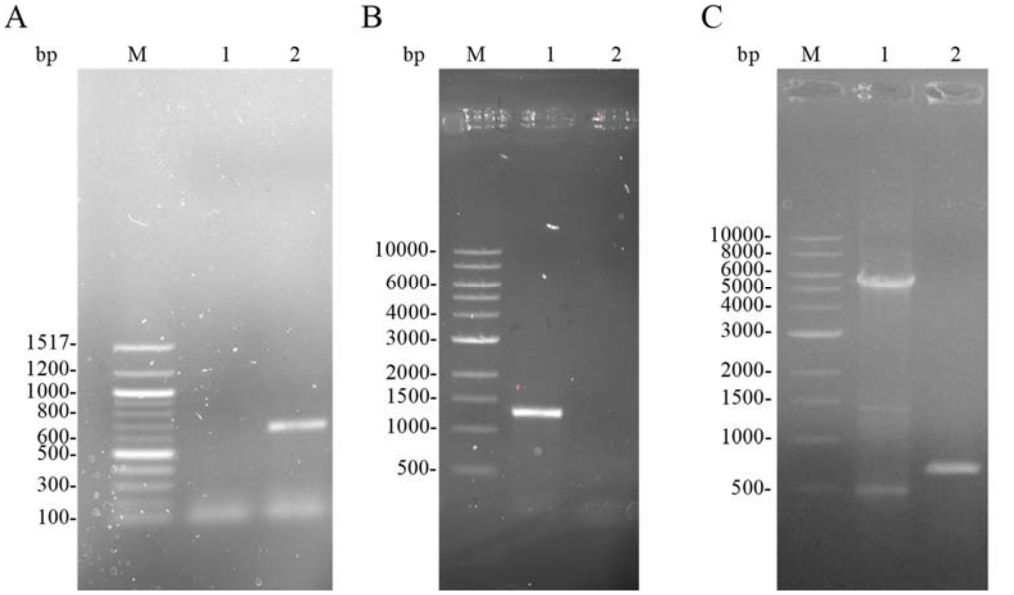

Fig 7.3 Gel electrophoresis of PCR products in 0.8% agarose gel in TAE (Tris-acetate-EDTA) buffer. A) lane M: 100 bp DNA ladders (New England BioLabs), lane 1: negative control, lane 2: amplification result of omcE gene sequence (621 bp). B) lane M: 1000 bp DNA ladders (New England BioLabs), lane 1: amplification result of omcS gene sequence (1222 bp), lane 2: negative control. C) Lane M: 1000 bp DNA ladders (New England BioLabs), lane 1: amplification result of pET22b+ (5403 bp), lane 2: amplification result of *omaB* gene sequence (680 bp).

After both cloning methods, the constructed vectors were transformed in *E. coli* DH5α competent cells and plated for selection in LB medium supplemented with ampicillin (100 µg/mL). The resulting colonies were screened by colony PCR, and those with a PCR product of the correct size were grown in liquid LB supplemented with ampicillin for plasmid extraction and sequencing. In Table 7.4, the quantity of each expression vector containing the correct gene sequence of the three membrane proteins is shown. The production of these three proteins is planning to be carried out in the Laboratory.

Table 7.4 Quantity of each expression vector containing the gene sequence encoding for OmcE, OmcS and OmaB, measured in the NanoDrop.

Expression vector	Quantity (ng/µL)
omcE-pVA203	223.6
omcS-pVA203	227.1
omaB-pET22b+	53.7

7.3 Materials and methods

7.3.1 NMR samples preparation and experiments

Samples (1-2 mM) were prepared in 45 sodium phosphate buffer with NaCl, 100 mM ionic strength, at pH 6.5 (PpcB and PpcE) and 7.1 (PpcD). All NMR samples were prepared in 92%H_2O/ 8%^2H_2O. The pH of the samples was adjusted by the addition of small amounts of NaO^{2}H or ^{2}HCl and checked with a glass micro electrode. The pH values were not corrected for isotope effects. Protein samples for solution structure determination were prepared with 0.04% sodium azide to avoid bacterial growth. To observe proteins in the reduced state, the NMR tubes were sealed with a gas-tight serum cap and the air was flushed out form the sample. The samples were reduced directly in the NMR tube with gaseous hydrogen in the presence of catalytic amounts of hydrogenase from *Desulfovibrio vulgaris* (Hildenborough), as previously described [4, 8].

The NMR experiments were acquired on Bruker Avance III 600 and 800 spectrometers, equipped with a triple-resonance cryoprobe (TCI). ^{1}H chemical shifts are reported in parts per million (ppm) calibrated using the water signal as internal reference and the ^{15}N and ^{13}C chemical shifts calibrated through indirect referencing [9]. Before and after all 2D and 3D experiments, 1D ^{1}H NMR spectra were acquired to verify the protein integrity. The pH of the samples was measured before and after each set of NMR experiments to confirm that pH of the solution is maintained. Spectra were processed using TOPSPIN software (Bruker Biospin, Karlsruhe, Germany) and analyzed with program Sparky (T. D. Goddard and D. G. Kneller, SPARKY 3, University of California, San Francisco).

NMR acquisition parameters and experiments acquired for the backbone assignment of PpcB, PpcD and PpcE proteins are summarized in Table 7.5.

Table 7.5 NMR experiments and acquisition details for the PpcB, PpcD and PpcE backbone resonance assignment in the reduced state, at 298 K. The NMR experiments acquired in Bruker Avance III 600 (PpcB and PpcE) or 800 (PpcD) spectrometers are indicated. 'ns' stands for the number of scans.

Protein	**NMR Experiments**	**Complex points**			**Spectral width (Hz)**			**Frequency offset (Hz)**			**ns**
		^{1}H	**^{15}N**	**^{13}C**	**^{1}H**	**^{15}N**	**^{13}C**	**^{1}H**	**^{15}N**	**^{13}C**	
PpcB	2D ^{1}H,^{15}N HSQC	2048	128	-	7212	4257	-	2789	8149	-	8
	2D ^{1}H,^{15}N HSQC	2048	128	-	7212	2068	-	2789	7115	-	8
	2D ^{1}H,^{13}C HSQC	2048	-	256	7212	-	10564	2789	-	6036	8
	3D HNCA	2048	40	128	7212	2068	5282	2789	7115	7847	16
	3D HN(CO)CA	2048	40	128	7212	2068	5282	2789	7115	7847	16
	3D CBCANH	2048	40	128	7212	2068	10564	2789	7115	6036	24
	3D CBCA(CO)NH	2048	40	128	7212	2068	10564	2789	7115	6036	16
PpcD	2D ^{1}H,^{15}N HSQC	2048	128	-	9615	6487	-	3801	10945	-	8
	2D ^{1}H,^{15}N HSQC	2048	128	-	9615	2838	-	3801	9567	-	8
	2D ^{1}H,^{13}C HSQC	2048	-	256	9615	-	16095	3801	-	7646	8
	3D HNCA	2048	26	100	9615	2838	7042	3801	9567	10463	8
	3D HN(CO)CA	2048	26	100	9615	2838	7042	3801	9567	10463	8
	3D CBCANH	2048	26	128	9615	2838	14084	3801	9567	8047	16
	3D CBCA(CO)NH	2048	26	128	9615	2838	14084	3801	9567	8047	16
PpcE	2D ^{1}H,^{15}N HSQC	2048	128	-	7212	4866	-	2809	8149	-	8
	2D ^{1}H,^{15}N HSQC	2048	128	-	7212	2311	-	2809	7054	-	8
	2D ^{1}H,^{13}C HSQC	2048	-	256	8418	-	12073	2809	-	5734	8
	3D HNCA	2048	40	128	8418	2189	5282	2809	7054	7847	16
	3D HN(CO)CA	2048	40	128	8418	2189	5282	2809	7054	7847	16
	3D CBCANH	2048	40	128	8418	2189	12073	2809	7054	5734	24
	3D CBCA(CO)NH	2048	40	128	8418	2189	12073	2809	7054	5734	24

For backbone and side chain assignments of PpcD the following spectra were acquired: (i) 3D HCC(H)-TOCSY and 3D HC(C)H-TOCSY, acquired for the ^{13}C, ^{15}N labeled PpcD sample, and (ii) 2D ^{1}H, ^{1}H COSY, 2D ^{1}H, ^{1}H TOCSY (60 ms) and 2D ^{1}H, ^{1}H NOESY (50 ms) for the unlabeled one. The 3D experiments were acquired with 2048 (F_3) x 64 (F_2) x 128 (F_1) data points for a sweep width of 9615 (^{1}H) Hz and 14084 Hz (^{13}C) with 8 scans per increment. The 2D experiments were acquired with 2048 (F_2) x 512 (F_1) data points for a sweep width of 11161 Hz with 80, 40 and 64 scans per increment for the 2D ^{1}H, ^{1}H COSY, 2D ^{1}H, ^{1}H TOCSY and 2D ^{1}H, ^{1}H NOESY, respectively.

7.4 References

1. Morgado L, Paixão VB, Salgueiro CA & Bruix M (2011) Backbone, side chain and heme resonance assignments of the triheme cytochrome PpcA from *Geobacter sulfurreducens*. *Biomol NMR Assign* **5**, 113-116.

2. Morgado L, Paixão VB, Schiffer M, Pokkuluri PR, Bruix M & Salgueiro CA (2012) Revealing the structural origin of the redox-Bohr effect: the first solution structure of a cytochrome from *Geobacter sulfurreducens*. *Biochem J* **441**, 179-187.

3. Morgado L, Bruix M, Pokkuluri PR, Salgueiro CA & Turner DL (2017) Redox- and pH-linked conformational changes in triheme cytochrome PpcA from *Geobacter sulfurreducens*. *Biochem J* **474**, 231-246.

4. Morgado L, Bruix M, Pessanha M, Londer YY & Salgueiro CA (2010) Thermodynamic characterization of a triheme cytochrome family from *Geobacter sulfurreducens* reveals mechanistic and functional diversity. *Biophys J* **99**, 293-301.

5. Pokkuluri PR, Londer YY, Yang X, Duke NE, Erickson J, Orshonsky V, Johnson G & Schiffer M (2010) Structural characterization of a family of cytochromes c_7 involved in Fe(III) respiration by *Geobacter sulfurreducens*. *Biochim Biophys Acta* **1797**, 222-232.

6. Koradi R, Billeter M & Wuthrich K (1996) MOLMOL: a program for display and analysis of macromolecular structures. *J Mol Graph* **14**, 51-55, 29-32.

7. Liu Y, Wang Z, Liu J, Levar C, Edwards MJ, Babauta JT, Kennedy DW, Shi Z, Beyenal H, Bond DR*, et al.* (2014) A trans-outer membrane porin-cytochrome protein complex for extracellular electron transfer by *Geobacter sulfurreducens* PCA. *Environ Microbiol Rep* **6**, 776-785.

8. Morgado L, Bruix M, Orshonsky V, Londer YY, Duke NE, Yang X, Pokkuluri PR, Schiffer M & Salgueiro CA (2008) Structural insights into the modulation of the redox properties of two *Geobacter sulfurreducens* homologous triheme cytochromes. *Biochim Biophys Acta* **1777**, 1157-1165.

9. Wishart DS, Bigam CG, Yao J, Abildgaard F, Dyson HJ, Oldfield E, Markley JL & Sykes BD (1995) ^{1}H, ^{13}C and ^{15}N chemical shift referencing in biomolecular NMR. *J Biomol NMR* **6**, 135-140.

8

CONCLUSIONS

8. Conclusions

The work developed in this Thesis contributed to the structural and functional characterization of several electron transfer components that participate in *G. sulfurreducens* extracellular electron transfer pathways. The important outcomes associated with the biochemical characterization of *G. sulfurreducens* cytochromes, including those addressed in this Thesis, are indicated in Fig 8.1.

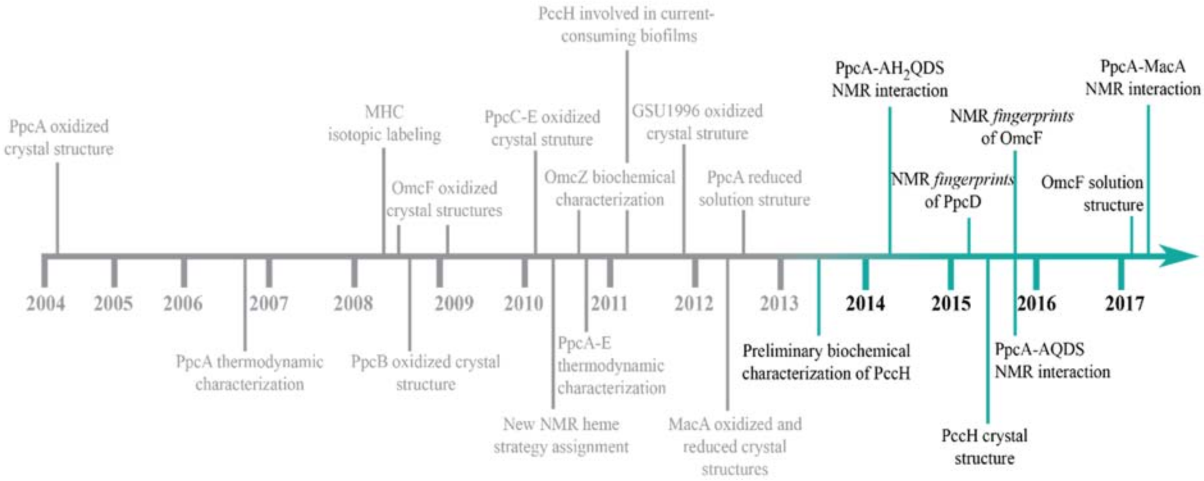

Fig 8.1 Time line of the important outcomes associated with the biochemical characterization of electron transfer components of *G. sulfurreducens*. This time line includes the outcomes obtained before and during the time course of this Thesis. The contributions obtained from the work developed in this Thesis are highlighted in green.

The backbone and heme NMR resonance assignment of the proteins studied in this work established the foundations to obtain high-resolution structures in solution, search for putative redox partners, map the redox- and pH-linked conformational changes, as well as to study the protein dynamics, which constitute important steps toward the rationalization of the *G. sulfurreducens* respiratory chains. The results obtained from the NMR interaction studies were also supported by molecular docking calculations.

Humic substances constitute a significant fraction of natural organic matter in terrestrial and aquatic environments and can act as terminal electron acceptors in anaerobic microbial respiration. *G. sulfurreducens* has a remarkable respiratory versatility and can utilize the humic substance analog anthraquinone-2,6-disulfonate (AQDS) as a terminal electron acceptor or its reduced form (AH_2QDS) as an electron donor. Using stopped-flow measurements we were able to demonstrate that PpcA, PpcB, PpcD and PpcE electron transfer proceeds in both directions at a similar rate but its extent is thermodynamically controlled, being more favorable in the case of the reduction of the cytochrome by the quinone. Such behavior might confer selective advantage to *G. sulfurreducens*, which can utilize the humic substances in any redox state available in the environment for its metabolic needs. The molecular interaction between the cytochromes PpcA, PpcB, PpcD and PpcE, with AQDS were probed by NMR chemical shift perturbation experiments in the oxidized state. Although the high sequence identity shared between this family of cytochromes, the charge distribution in these proteins surface is slightly different, particularly in the case of PpcE holding the positively charged residues equally distributed in the heme I and IV faces. Indeed, the results showed that only the region of heme IV, containing several positively charged lysines, is involved in the interaction between PpcA, PpcB and PpcD, with AQDS. On the other hand, the results demonstrate that the regions of heme I and heme IV are equally affected by the presence of AQDS. In addition, this study was also carried out for the PpcA in the reduced state and AH_2QDS, the reduced form of AQDS, showing that this molecule also interacts with reduced PpcA in the same region of the oxidized PpcA. These redox partners form reversible complexes with low binding affinity allowing a rapid and selective electron transfer, required for an efficient electron transfer reaction.

Besides the study of protein-ligand interaction complexes, the molecular interaction between the diheme cytochrome MacA and the triheme cytochrome PpcA, previously studied by electrochemical experiments, was also investigated in this work using NMR chemical shift perturbation experiments. These experiments allowed mapping the specific interacting regions of the redox complex, including MacA high-potential heme and a cleft defined by hemes I and IV of PpcA. The complex between these two proteins has a low binding affinity, is reversible and supported by electrostatic interactions, which are crucial for rapid protein–protein recognition and electron transfer.

Moreover, the solution structure of cytochrome OmcF was determined in the reduced state and constitutes the first solution structure of an outer membrane cytochrome from *G. sulfurreducens.* The most dynamic regions analyzed by ^{15}N relaxation parameters obtained for the backbone NH signals were identified. The analysis of the chemical shift variation of the backbone and side chain NH signals with pH allowed mapping of the pH-linked conformational changes caused by protonation/deprotonation of the redox-Bohr center.

In addition to the study of these proteins involved in electron transfer pathways towards extracellular terminal acceptors, the recent discovery that the periplasmic cytochrome PccH is crucial for the electron accepting mechanism from electrodes aroused our interest. Complementary biophysical techniques including CD, UV-visible and NMR spectroscopy were used to characterize PccH. This preliminary biochemical characterization anticipated the information about the number of heme groups, its axial coordination and the amino acids that are involved in the heme axial coordination. The protein stability was evaluated and the secondary structural elements were probed by circular dichroism. The determined structure of PccH is unique among the monoheme cytochromes described to date. The structural fold of PccH can be described as forming two lobes with the heme sandwiched in a cleft between the two lobes.

The PccH crystal structure determined confirmed all preliminary results and taken together with the sequence phylogenetic analysis, it was proposed that this cytochrome is the first representative of a new subclass of class I monoheme *c*-type cytochromes. The low solvent exposure of the heme group in PccH might explain its unusual reduction potential values (-35 to +1 mV in the physiological pH range), which may enable the protein to be redox active at the typically negative potential ranges encountered by *G. sulfurreducens*. Because PccH is predicted to be located in the periplasm, it could not be involved in the first step of accepting electrons from the electrode but is very likely involved in the downstream electron transport events in the periplasm. Indeed, the reduction potential values of PccH show that the cytochrome is thermodynamically suitable to bridge the electron transfer from biocathodes to more electro-positive electron acceptors, such as fumarate.

A

APPENDIX

A. Appendix

A.1 Supplementary Figures

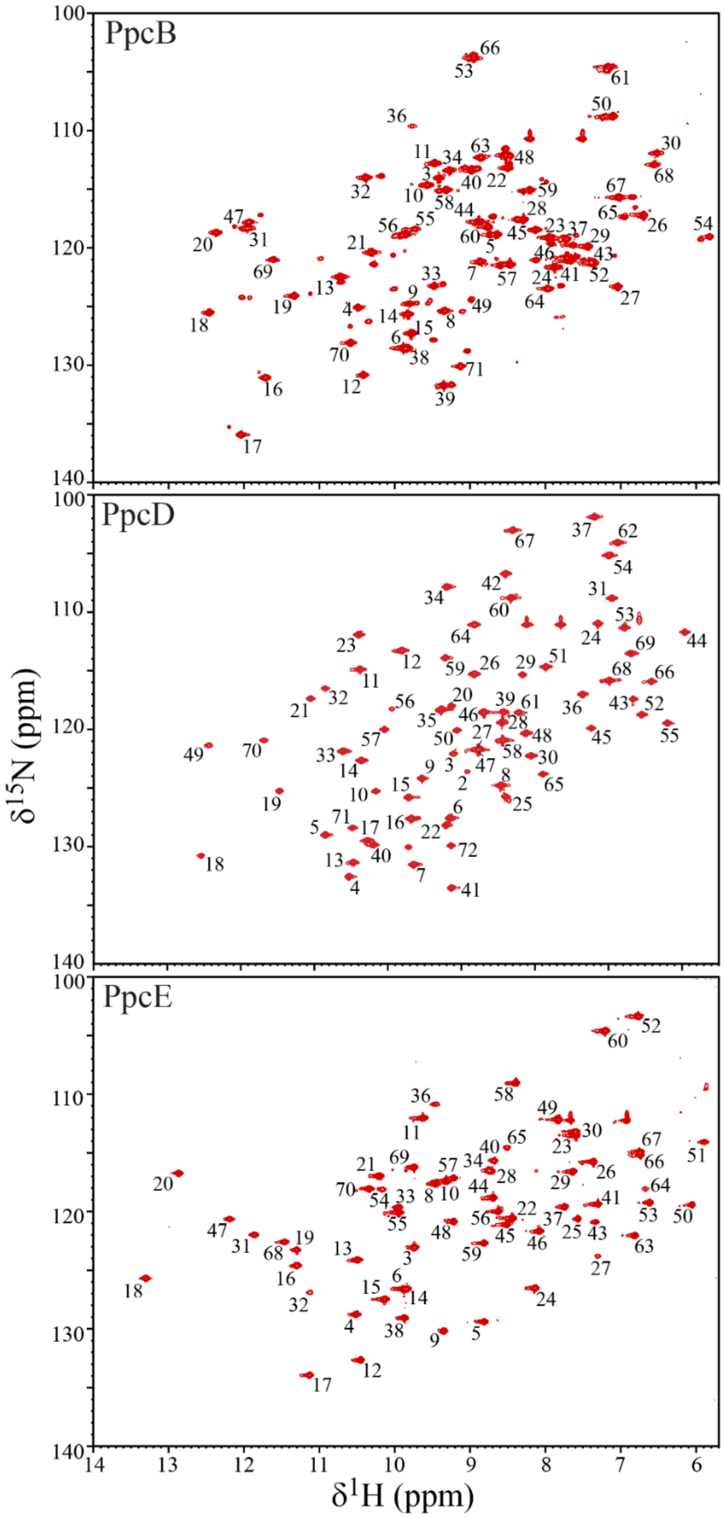

Fig A.1 2D ^{1}H,^{15}N HSQC spectra of oxidized PpcB (1.0 mM, pH 5.5), PpcD (1.0 mM, pH 5.9) and PpcE (0.7 mM, pH 6.5). All samples were prepared in 45 mM sodium phosphate buffer, 100 mM ionic strength. The experiments were acquired in a Bruker Avance 600 at 298K. Black labels represent ^{1}H-^{15}N connectivities for protein backbone.

A.2 Supplementary Tables

A.2.1 NMR assignment of PpcB, PpcD and PpcE proteins in the oxidized state

Table A.1 Backbone assignment (^{15}N, ^{1}HN, ^{13}Cα and ^{13}Cβ) of PpcB from *G. sulfurreducens* in the oxidized state (1.0 mM, 45 mM sodium phosphate buffer pH 5.5, 100 mM ionic strength, 298 K, Bruker Avance III 600). The abbreviations RN and RT indicate residue number and residue type, respectively.

Backbone chemical shift (ppm) of oxidized PpcB											
RN	**RT**	^{15}N	^{1}HN	^{13}Cα	^{13}Cβ			^{15}N	^{1}HN	^{13}Cα	^{13}Cβ
1	A	-	-	-	-	**37**	K	119.4	7.821	56.72	31.8
2	D	-	-	58.79	43.01	**38**	I	128.1	9.504	61.57	39.64
3	T	114.2	9.413	62.57	71.88	**39**	E	131.7	9.388	58.44	29.25
4	M	125	10.49	55.7	36.76	**40**	G	113.2	8.974	45.15	-
5	T	118.2	8.776	61.99	70.89	**41**	F	121	7.642	61.46	37.97
6	F	128	9.868	56.26	39.71	**42**	G	-	-	43.34	-
7	T	120.4	8.888	62.55	69.78	**43**	K	121	7.38	59.04	32.24
8	A	125.8	9.506	52.5	24.16	**44**	E	117.6	8.913	61.55	29.24
9	K	124.9	9.824	59.07	31.76	**45**	M	118.5	8.214	59.68	33.29
10	N	114.6	9.626	53.82	35.82	**46**	A	120.6	7.673	55.22	15.77
11	G	112.8	9.449	47.42	-	**47**	H	117.9	11.94	60.86	24.97
12	N	131	10.47	56.19	39.62	**48**	G	112.1	8.57	44.93	-
13	V	122.3	10.66	62.2	36.91	**49**	K	124.6	9.016	59.13	32.6
14	T	125.8	9.853	63.68	69.85	**50**	S	108.8	7.15	60.31	61.75
15	F	127.2	9.752	55.87	43.98	**51**	C	-	-	53	38.85
16	D	131.1	11.73	55.48	41.61	**52**	K	121.4	7.435	61.65	34.38
17	H	135.8	12.05	76.63	27.01	**53**	G	103.9	8.993	47.35	-
18	K	125.5	12.4	62.37	34.26	**54**	C	119.1	5.878	57.44	27.88
19	K	124.1	11.34	61.23	33.85	**55**	H	118.5	9.781	60.19	17.29
20	H	118.6	12.36	84.03	20.09	**56**	E	118.9	9.888	60.44	30.68
21	Q	120.5	10.33	58.1	28.15	**57**	E	121.4	8.509	59.75	30.07
22	T	113.3	8.529	65.31	69.79	**58**	M	115.2	9.351	57.8	32.88
23	I	119.2	7.982	63.16	39.5	**59**	K	115.2	8.243	57.49	29.22
24	V	121.6	7.914	58.77	30.57	**60**	K	118.9	8.68	56.24	38.25
25	P	-	-	64.02	31.51	**61**	G	104.7	7.183	40.64	-
26	D	117.2	6.734	52.18	41.3	**62**	P	-	-	63.49	33.96
27	C	123.3	7.066	55.35	32.42	**63**	T	112.3	8.873	62.33	71.22
28	A	117.7	8.325	54.48	19.6	**64**	K	123.6	7.99	54.95	33.15
29	V	119.9	7.472	66.05	31.22	**65**	C	116.7	6.793	56	34.27
30	C	111.8	6.57	55.49	37.1	**66**	G	103.4	8.522	45.79	-
31	H	118.5	11.94	84.49	27.54	**67**	E	115.8	7.046	56.73	30.4
32	G	114	10.39	47.48	-	**68**	C	113	6.615	57.46	39.34
33	K	123.3	9.48	59.35	33.75	**69**	H	121.2	11.67	80.95	23.31
34	T	113.5	9.282	59.74	71.46	**70**	K	128.1	10.57	56.72	34.94
35	P	-	-	65.59	-	**71**	K	130.1	9.15	59.07	34.21
36	G	109.7	9.794	46.84	-						

Table A.2 Backbone assignment (^{15}N, ^{1}HN, ^{13}Cα and ^{13}Cβ) of PpcD from *G. sulfurreducens* in the oxidized state (1.0 mM, 45 mM sodium phosphate buffer pH 5.9, 100 mM ionic strength, 298 K, Bruker Avance III 600). The abbreviations RN and RT indicate residue number and residue type, respectively.

Backbone chemical shift (ppm) of oxidized PpcD											
RN	**RT**	**^{15}N**	**^{1}HN**	**^{13}Cα**	**^{13}Cβ**			**^{15}N**	**^{1}HN**	**^{13}Cα**	**^{13}Cβ**
1	H	-	-	-	-	**37**	G	101.90	7.19	42.32	-
2	D	123.60	8.93	55.30	42.71	**38**	G	-	-	44.78	-
3	K	122.10	9.11	59.74	35.89	**39**	K	118.60	8.43	57.01	32.47
4	V	132.60	10.53	64.12	33.18	**40**	I	129.90	10.20	61.60	-
5	V	129.00	10.85	61.35	35.70	**41**	A	133.60	9.14	54.27	18.04
6	V	127.60	9.16	62.85	32.23	**42**	G	106.70	8.41	44.65	-
7	L	131.60	9.65	53.17	-	**43**	M	117.40	6.67	55.33	28.92
8	E	124.80	8.47	57.24	30.26	**44**	G	111.70	5.97	43.14	-
9	A	124.20	9.54	52.48	24.49	**45**	K	119.90	7.24	58.75	31.87
10	K	125.30	10.16	59.38	32.07	**46**	D	118.50	8.70	59.22	40.77
11	N	114.80	10.38	54.28	36.38	**47**	W	121.80	8.78	61.98	30.25
12	G	113.30	9.81	47.76	-	**48**	A	120.30	8.12	54.99	16.08
13	N	131.40	10.47	56.15	39.48	**49**	H	121.40	12.43	62.48	24.67
14	V	122.70	10.36	61.63	36.15	**50**	K	120.10	9.07	59.89	33.57
15	T	125.80	9.72	64.28	69.19	**51**	T	114.70	7.86	65.06	67.39
16	F	127.60	9.69	58.47	40.39	**52**	C	118.80	6.55	53.95	34.51
17	D	129.50	10.28	54.33	43.88	**53**	T	111.30	6.79	67.09	67.84
18	H	130.80	12.54	85.41	17.40	**54**	G	105.20	7.00	47.87	-
19	K	125.30	11.47	61.92	32.43	**55**	C	119.50	6.21	57.44	28.50
20	K	118.00	9.14	57.76	33.12	**56**	H	118.30	9.94	60.04	13.09
21	H	117.40	11.05	80.08	18.26	**57**	K	120.00	10.05	60.46	33.18
22	A	128.20	9.22	54.66	19.81	**58**	E	121.00	8.44	59.69	29.92
23	G	112.00	10.40	46.12	-	**59**	M	113.90	9.22	57.07	33.52
24	V	111.00	7.15	60.55	32.33	**60**	G	108.80	8.33	46.66	-
25	K	125.70	8.41	58.42	31.51	**61**	K	118.60	8.22	55.02	37.32
26	G	115.40	8.82	44.83	-	**62**	G	104.10	6.88	40.07	-
27	E	121.60	8.78	57.51	28.57	**63**	P	-	-	63.03	33.92
28	C	119.40	8.45	56.96	31.69	**64**	T	111.10	8.83	62.08	71.19
29	K	115.40	8.17	57.56	31.17	**65**	K	123.80	7.90	54.60	33.17
30	A	122.30	8.06	54.37	17.74	**66**	C	115.90	6.42	55.22	32.62
31	C	108.90	6.96	54.05	40.63	**67**	G	103.00	8.31	45.69	-
32	H	116.50	10.85	91.31	14.22	**68**	E	115.80	6.99	56.74	30.47
33	E	121.90	10.62	60.01	30.95	**69**	C	113.60	6.69	57.66	39.89
34	T	107.90	9.21	59.54	72.79	**70**	H	121.00	11.68	79.81	23.67
35	E	118.30	9.28	58.47	28.81	**71**	K	128.40	10.48	56.63	34.46
36	A	117.10	7.35	51.47	18.35	**72**	K	130.00	9.14	59.03	34.23

Table A.3 Backbone assignment (^{15}N, ^{1}HN, ^{13}Cα and ^{13}Cβ) of PpcE from *G. sulfurreducens* in the oxidized state (0.7 mM, 45 mM sodium phosphate buffer pH 6.5, 100 mM ionic strength, 298 K, Bruker Avance III 600). The abbreviations RN and RT indicate residue number and residue type, respectively.

Backbone chemical shift (ppm) of oxidized PpcE											
RN	**RT**	**^{15}N**	**^{1}HN**	**^{13}Cα**	**^{13}Cβ**	**RN**	**RT**	**^{15}N**	**^{1}HN**	**^{13}Cα**	**^{13}Cβ**
1	A	-	-	-	-	**36**	G	110.90	9.50	48.34	-
2	D	-	-	59.43	42.28	**37**	K	119.70	7.75	56.26	31.54
3	V	123.10	9.74	63.36	35.73	**38**	I	129.10	9.84	61.59	39.83
4	I	128.80	10.51	61.47	42.49	**39**	R	130.30	9.25	58.62	29.65
5	L	129.40	8.81	53.35	43.66	**40**	N	115.70	8.67	52.87	36.73
6	F	126.60	9.87	54.64	39.36	**41**	F	119.40	7.29	61.37	38.07
7	P	-	-	63.16	31.50	**42**	G	-	-	43.17	-
8	S	117.40	9.31	59.46	67.98	**43**	K	120.90	7.33	59.14	31.73
9	K	130.20	9.38	59.29	31.62	**44**	D	118.80	8.69	59.28	40.64
10	N	117.50	9.46	54.63	38.05	**45**	Y	121.20	8.51	61.50	38.86
11	G	112.00	9.61	47.13	-	**46**	A	121.70	8.07	54.75	15.49
12	A	132.70	10.45	55.60	20.66	**47**	H	120.70	12.19	62.84	23.54
13	V	124.10	10.50	62.13	37.24	**48**	K	120.90	9.22	59.97	33.51
14	T	126.60	9.83	64.06	68.96	**49**	T	112.10	7.82	63.98	67.61
15	F	127.50	10.12	54.65	42.06	**50**	C	119.50	6.06	54.04	35.05
16	T	124.60	11.29	61.92	68.48	**51**	K	114.10	5.89	60.35	33.04
17	H	133.90	11.12	80.59	25.07	**52**	G	103.40	6.76	47.75	-
18	K	125.70	13.28	63.29	34.24	**53**	C	119.30	6.61	57.58	27.05
19	R	123.30	11.29	61.56	31.39	**54**	H	118.10	10.16	59.89	16.36
20	H	116.80	12.87	83.81	20.25	**55**	E	120.10	9.94	60.41	30.65
21	S	117.00	10.22	61.42	62.91	**56**	V	120.00	8.62	66.10	32.07
22	E	120.60	8.43	58.20	29.84	**57**	R	117.20	9.22	57.32	30.31
23	F	113.50	7.60	57.20	38.80	**58**	G	109.10	8.38	46.86	-
24	V	126.60	8.13	61.96	29.82	**59**	A	122.70	8.81	52.40	23.09
25	R	120.80	7.57	58.80	29.70	**60**	G	104.60	7.19	40.58	-
26	E	115.70	7.36	54.61	30.45	**61**	P	-	-	-	-
27	C	123.80	7.29	55.92	31.53	**62**	T	-	-	61.89	69.91
28	R	116.60	8.70	57.32	29.65	**63**	K	122.10	6.80	55.28	33.13
29	S	116.60	7.63	61.93	-	**64**	C	118.10	6.66	55.71	35.14
30	C	113.30	7.61	55.32	38.90	**65**	K	114.60	8.49	57.40	31.37
31	H	122.00	11.87	79.62	25.81	**66**	L	115.20	6.73	54.50	41.25
32	E	126.90	11.12	60.12	31.23	**67**	C	114.90	6.73	56.52	37.44
33	K	119.60	9.94	56.71	33.67	**68**	H	122.60	11.47	79.40	22.16
34	T	116.50	8.74	61.76	70.58	**69**	T	116.20	9.74	64.09	70.99
35	P	-	-	66.35	30.80	**70**	G	118.10	10.34	47.82	-

Table A.4 Percentage of the backbone assignment of PpcB, PpcD and PpcE in oxidized state. All backbone NH resonances were assigned except the Ala[1], Asp[2], Gly[42] and Cys[51], in the case of PpcB; His[1], Gly[38], for PpcD; and for PpcE Ala[1], Asp[2], Gly[42] and Thr[62] (Fig A.1 and Tables A.1-A.3).

	Backbone assignment (%)			
Protein	**^{15}N**	**^{1}HN**	**^{13}Cα**	**^{13}Cβ**
PpcB	96	96	99	97
PpcD	99	99	99	95
PpcE	95	95	97	95

A.2.2 NMR assignment of the OmcF, PpcB, PpcD and PpcE proteins in the reduced state

Table A.5 Assignment of ^{1}H, ^{13}C and ^{15}N signals of OmcF from *G. sulfurreducens* in the reduced state (2.0 mM, 45 mM sodium phosphate buffer pH 5.0, 100 mM ionic strength, 298 K, Bruker Avance III 800). The abbreviations RN and RT indicate residue number and residue type, respectively. The chemical shifts were deposited in the Biological Magnetic Resonance Data Bank (BMRB, http://www.bmrb.wisc.edu) under accession number 25455.

RN	RT	Atom	Chemical shift (ppm)
20	SER	HA	4.67
		HB3	4.30
		CA	60.06
		CB	62.01
21	GLY	H	8.83
		HA2	3.97
		CA	43.83
		N	109.86
22	GLY	H	8.45
		HA2	4.03
		HA3	4.04
		CA	45.32
		N	109.16
23	SER	H	8.59
		HA	4.53
		HB2	3.96
		HB3	3.99
		CA	58.86
		CB	64.20
		N	116.38
24	GLY	H	8.56
		HA2	4.05
		HA3	3.99
		CA	45.57
		N	110.96
25	ALA	H	8.12
		HA	4.39
		HB	1.41
		CA	52.47
		CB	19.86
		N	123.98
26	GLY	H	8.56
		HA2	4.30
		HA3	4.27
		CA	44.81
		N	107.68
27	GLY	H	8.94
		HA2	3.96
		HA3	3.61
		CA	47.83
		N	107.27
28	GLY	H	8.66
		HA2	3.39
		HA3	2.23
		CA	46.90
		N	108.96
29	GLU	H	7.87
		HA	4.15
		HB2	2.08
		HB3	2.19
		HG2	2.33
		HG3	2.30
		CA	59.47
		CB	29.28
		CG	36.84
		N	124.71
30	LEU	H	8.18
		HA	4.20
		HB2	1.48
		HB3	2.18
		HD1	1.06
		HD2	1.05
		HG	1.83
		CA	58.17
		CB	43.17
		CD1	23.70
		CD2	26.97
		CG	26.86
		N	121.19
31	PHE	H	8.71
		HA	4.25
		HB2	2.95
		HD1	7.32
		HE1	6.81
		HZ	6.68
		CA	62.13
		CB	40.77
		N	120.75
32	ALA	H	8.34
		HA	4.11
		HB	1.58
		CA	55.21
		CB	18.00
		N	122.95
33	THR	H	7.87
		HA	3.97
		HB	3.99
		HG2	0.70
		CA	66.25
		CB	69.93
		CG2	20.73
		N	111.89

***Table A.5** (cont.)*

RN	RT	Atom	Chemical shift (ppm)
34	HIS	H	8.24
		HA	5.22
		HB2	3.46
		HB3	3.55
		HD2	7.12
		HE1	8.06
		CA	59.04
		CB	34.11
		N	114.87
35	CYS	H	8.51
		HA	5.65
		HB2	0.96
		HB3	2.06
		CA	55.50
		CB	37.36
		N	117.91
36	ALA	H	7.23
		HA	3.11
		HB	1.46
		CA	54.70
		CB	19.28
		N	119.56
37	GLY	H	8.40
		HA2	3.78
		HA3	3.67
		CA	46.60
		N	105.35
38	CYS	H	6.21
		HA	4.56
		HB2	0.62
		HB3	1.69
		CA	53.57
		CB	36.61
		N	114.26
39	HIS	H	6.42
		HA	3.50
		HB2	1.00
		HB3	1.29
		HD1	8.93
		HD2	0.52
		HE1	1.13
		CA	51.07
		CB	28.00
		N	113.26
		ND1	162.23
40	PRO	HA	4.19
		HB2	1.78
		HB3	1.99
		HD2	2.57
		HD3	2.69
		HG2	1.67
		HG3	1.78
		CA	64.06
		CB	30.15
		CD	50.59
		CG	27.71
41	GLN	H	9.63
		HA	3.83
		HB2	1.98
		HB3	2.26
		HE21	7.46
		HE22	6.79
		HG2	2.30
		HG3	2.34
		CA	57.06
		CB	27.06
		CG	34.64
		N	122.05
		NE2	111.85
42	GLY	H	7.46
		HA2	2.43
		HA3	1.76
		CA	44.92
		N	104.40
43	GLY	H	7.13
		HA2	3.70
		HA3	3.25
		CA	43.41
		N	107.94
44	ASN	H	8.24
		HA	3.98
		HB2	1.44
		HB3	2.39
		HD21	7.24
		HD22	5.05
		CA	53.13
		CB	37.83
		N	119.60
		ND2	112.27
45	THR	H	8.29
		HA	4.00
		HB	4.33
		HG2	0.90
		CA	62.72
		CB	68.31
		CG2	22.64
		N	115.23

***Table A.5** (cont.)*

RN	RT	Atom	Chemical shift (ppm)	RN	RT	Atom	Chemical shift (ppm)
46	VAL	H	8.36	**50**	LYS	H	8.16
		HA	4.25			HB2	2.24
		HB	2.49			HB3	2.45
		HG1	1.18			HD2	1.96
		HG2	1.39			HD3	2.02
		CA	64.99			HE2	3.32
		CB	34.17			HE3	3.34
		CG1	21.32			HG2	1.82
		CG2	21.91			HG3	1.92
		N	123.54			CA	53.36
47	HIS	H	7.69			CB	31.89
		HA	5.68			CD	29.54
		HB2	3.51			CE	42.76
		HB3	3.57			CG	24.25
		HD2	7.69			N	122.86
		HE1	8.60	**51**	THR	H	6.93
		CA	50.82			HA	3.47
		CB	31.01			HB	4.65
		N	118.47			HG2	1.07
48	PRO	HA	4.66			CA	60.85
		HB2	2.07			CB	68.98
		HB3	2.40			CG2	22.47
		HD2	3.68			N	109.48
		HD3	3.84	**52**	LEU	H	8.24
		HG2	2.06			HA	3.96
		HG3	1.90			HB2	0.84
		CA	65.10			HB3	1.31
		CB	32.84			HD1	-0.51
		CD	51.29			HD2	-0.81
		CG	27.21			HG	0.02
49	GLU	H	9.02			CA	54.02
		HA	4.33			CB	40.13
		HB2	2.07			CD1	21.50
		HB3	2.17			CD2	25.57
		HG2	2.32			CG	26.12
		HG3	2.46			N	114.65
		CA	57.63	**53**	ALA	H	6.89
		CB	29.48			HA	4.03
		CG	36.57			HB	1.35
		N	114.66			CA	52.77
						CB	19.14
						N	120.76

***Table A.5** (cont.)*

RN	RT	Atom	Chemical shift (ppm)	RN	RT	Atom	Chemical shift (ppm)
54	ARG	H	7.78	**58**	GLU	H	8.71
		HA	3.68			HA	3.78
		HB2	1.90			HB2	2.01
		HB3	2.00			HB3	2.09
		HD2	3.23			HG2	2.90
		HD3	3.26			HG3	2.85
		HE	7.55			CA	60.55
		HG2	1.44			CB	28.78
		HG3	1.64			CG	38.37
		CA	61.27			N	119.71
		CB	30.96	**59**	ALA	H	7.54
		CD	43.71			HA	4.30
		CG	26.94			HB	1.65
		N	124.74			CA	54.68
		NE	84.71			CB	17.87
55	ALA	H	9.44			N	122.85
		HA	4.09	**60**	ASN	H	7.40
		HB	1.43			HA	5.10
		CA	55.47			HB2	2.91
		CB	18.27			HB3	3.31
		N	117.66			HD21	7.54
56	ARG	H	7.00			HD22	7.74
		HA	4.26			CA	52.63
		HB2	1.89			CB	40.29
		HD2	3.33			N	114.98
		HD3	3.41			ND2	113.48
		HE	7.17	**61**	GLY	H	7.85
		HG2	1.77			HA2	4.29
		HG3	1.86			HA3	3.76
		CA	56.96			CA	46.09
		CB	29.18			N	106.22
		CD	42.31	**62**	ILE	H	8.27
		CG	26.10			HA	4.22
		N	115.58			HB	1.93
		NE	84.25			HD1	0.79
57	ARG	H	8.51			HG12	1.01
		HA	4.11			HG13	1.49
		HB2	1.72			HG2	0.91
		HB3	1.76			CA	60.42
		HD2	2.95			CB	37.74
		HD3	2.99			CD1	15.26
		HG2	1.44			CG1	27.14
		HG3	1.46			CG2	19.45
		CA	60.48			N	123.56
		CB	29.21				
		CD	42.29				
		CG	24.91				
		N	117.99				

Table A.5 *(cont.)*

RN	RT	Atom	Chemical shift (ppm)	RN	RT	Atom	Chemical shift (ppm)
63	ARG	H	9.36	**67**	ASP	H	8.18
		HA	3.31			HA	4.58
		HB2	2.05			HB2	2.90
		HB3	1.95			HB3	3.31
		HD2	3.28			CA	57.37
		HD3	7.39			CB	41.14
		HE	1.49			N	120.69
		HG2	1.61	**68**	VAL	H	8.06
		HG3	57.82			HA	3.71
		CA	33.46			HB	2.56
		CB	43.31			HG1	1.20
		CD	28.79			HG2	1.52
		CG	125.94			CA	67.52
		N	84.70			CB	31.66
64	ARG	NE	8.50			CG1	22.55
		H	4.86			CG2	22.21
		HA	4.86			N	121.45
		HB	1.32	**69**	ALA	H	7.95
		CA	59.78			HA	4.01
		CB	73.18			HB	1.43
		N	21.82			CA	55.46
		H	111.03			CB	18.28
65	ARG	HA	8.61			N	119.51
		HB2	3.46	**70**	ALA	H	8.06
		HD2	2.17			HA	4.14
		HD3	1.14			HB	1.51
		HE	1.16			CA	54.12
		HG2	67.52			CB	18.63
		HG3	32.19			N	116.94
		CA	21.95	**71**	TYR	H	8.22
		CB	23.22			HA	3.70
		CD	119.58			HB2	2.99
66	ARG	CG	7.96			HB3	3.27
		N	3.94			HD1	6.85
		NE	1.87			HE1	6.36
		H	1.90			CA	61.98
		HA	3.25			CB	38.94
		HB2	7.28			N	122.26
		HB3	1.81	**72**	ILE	H	7.09
		HD2	1.69			HA	2.63
		HD3	59.66			HB	1.53
		HG2	29.54			HD1	0.70
		HG3	43.48			HG12	1.61
		CA	28.71			HG13	1.19
		CB	117.83			HG2	0.82
		CD	84.66			CA	64.05
						CB	37.14
						CD1	13.83
						CG1	25.10
						CG2	16.84
						N	106.03

Table A.5 *(cont.)*

RN	RT	Atom	Chemical shift (ppm)
73	ARG	H	6.78
		HA	3.88
		HB2	1.84
		HB3	1.81
		HD2	3.11
		HD3	3.25
		HE	6.94
		HG2	1.83
		CA	55.55
		CB	30.45
		CD	43.28
		CG	26.57
		N	114.62
		NE	87.06
74	ASN	H	6.74
		HA	4.48
		HB2	2.31
		HB3	2.37
		HD21	6.57
		HD22	7.40
		CA	51.33
		CB	38.97
		N	112.64
		ND2	112.22
75	PRO	HA	2.74
		HB2	-0.27
		HB3	0.03
		HD2	2.50
		HD3	2.65
		HG2	0.33
		HG3	0.48
		CA	62.17
		CB	32.30
		CD	47.61
		CG	24.64
76	GLY	H	6.53
		HA2	4.03
		HA3	3.87
		CA	44.36
		N	102.71
77	PRO	HA	4.05
		HB2	2.14
		HB3	2.12
		HD2	3.53
		HD3	3.66
		HG2	2.04
		HG3	2.24
		CA	63.39
		CB	31.82
		CD	49.69
		CG	28.01
78	GLY	H	7.99
		HA2	4.28
		HA3	3.53
		CA	44.81
		N	107.90
79	MET	H	6.99
		HA	3.81
		HB2	-3.01
		HB3	-0.51
		HE	-2.86
		HG2	-3.32
		HG3	-1.25
		CA	50.99
		CB	29.73
		CE	15.18
		CG	27.02
		N	121.86
80	PRO	HA	3.68
		HB2	0.94
		HB3	1.70
		HD2	2.73
		HD3	3.56
		HG2	1.71
		HG3	1.87
		CA	61.50
		CB	31.00
		CD	51.63
		CG	27.05
81	ALA	H	7.01
		HA	3.42
		HB	0.86
		CA	50.62
		CB	18.92
		N	117.90
82	PHE	H	8.07
		HA	4.36
		HB2	2.23
		HB3	2.43
		HD1	6.77
		HE1	7.06
		HZ	8.22
		CA	56.82
		CB	39.72
		N	121.72
83	GLY	H	8.31
		HA2	4.20
		HA3	3.87
		CA	44.61
		N	111.42

***Table A.5** (cont.)*

RN	RT	Atom	Chemical shift (ppm)
84	GLU	H	8.95
		HA	3.94
		HB2	1.94
		HB3	1.98
		HG2	2.20
		HG3	2.31
		CA	59.31
		CB	29.54
		CG	37.31
		N	120.37
85	ALA	H	8.21
		HA	4.19
		HB	1.39
		CA	53.89
		CB	18.23
		N	118.65
86	MET	H	7.30
		HA	4.43
		HB2	2.11
		HB3	2.16
		HE	2.26
		HG2	2.59
		HG3	2.70
		CA	57.31
		CB	34.47
		CE	17.73
		CG	32.00
		N	116.03
87	ILE	H	7.89
		HA	4.57
		HB	1.47
		HD1	0.14
		HG12	1.19
		HG13	0.76
		HG2	0.72
		CA	58.06
		CB	39.87
		CD1	13.15
		CG1	26.92
		CG2	17.75
		N	115.18
88	PRO	HA	5.05
		HB2	2.03
		HB3	2.67
		HD2	3.59
		HD3	4.07
		HG2	2.16
		HG3	2.03
		CA	62.60
		CB	31.12
		CD	51.38
		CG	27.70
89	PRO	HA	4.05
		HB2	2.50
		HB3	2.04
		HD2	3.72
		HD3	3.94
		HG2	2.15
		HG3	2.15
		CA	67.21
		CB	32.17
		CD	50.63
		CG	27.67
90	ALA	H	9.02
		HA	4.16
		HB	1.48
		CA	55.57
		CB	18.47
		N	118.16
91	ASP	H	7.21
		HA	4.50
		HB2	2.63
		HB3	2.75
		CA	56.64
		CB	41.04
		N	118.85
92	ALA	H	8.30
		HA	3.88
		HB	1.46
		CA	55.66
		CB	17.96
		N	124.43
93	LEU	H	7.67
		HA	4.05
		HB2	1.67
		HB3	1.88
		HD1	0.96
		HD2	0.89
		HG	1.79
		CA	58.23
		CB	41.44
		CD1	25.27
		CD2	23.28
		CG	26.99
		N	117.20

Table A.5 *(cont.)*

RN	RT	Atom	Chemical shift (ppm)
94	LYS	H	7.43
		HA	4.23
		HB2	1.75
		HB3	2.18
		HD2	1.75
		HD3	1.89
		HE2	3.03
		HE3	3.08
		HG2	1.63
		HG3	1.91
		CA	60.19
		CB	33.00
		CD	30.24
		CE	42.74
		CG	25.72
		N	118.85
95	ILE	H	8.34
		HA	3.92
		HB	2.26
		HD1	1.12
		HG12	1.64
		HG13	0.90
		HG2	1.57
		CA	66.51
		CB	38.52
		CD1	15.17
		CG1	29.20
		CG2	19.71
		N	120.49
96	GLY	H	8.81
		HA2	4.05
		HA3	3.94
		CA	48.66
		N	108.03
97	GLU	H	8.90
		HA	4.04
		HB2	2.16
		HB3	2.36
		HG2	2.50
		HG3	2.52
		CA	59.66
		CB	29.63
		CG	36.64
		N	121.62
98	TYR	H	8.15
		HA	4.09
		HB2	3.09
		HB3	3.19
		HD1	6.67
		HE1	6.16
		CA	62.46
		CB	38.45
		N	120.93
99	VAL	H	8.94
		HA	3.46
		HB	2.64
		HG1	1.27
		HG2	1.66
		CA	66.37
		CB	32.50
		CG1	21.80
		CG2	24.79
		N	121.90
100	VAL	H	7.98
		HA	3.66
		HB	2.08
		HG1	0.97
		HG2	1.01
		CA	65.60
		CB	31.54
		CG1	21.01
		CG2	22.32
		N	116.82
101	ALA	H	7.73
		HA	4.11
		HB	1.31
		CA	54.19
		CB	19.63
		N	116.89
102	SER	H	7.23
		HA	3.78
		HB2	1.64
		HB3	2.29
		CA	60.89
		CB	62.68
		N	109.52
103	PHE	H	6.86
		HA	5.36
		HB2	2.78
		HB3	2.85
		HD1	7.06
		HE1	6.50
		HZ	6.53
		CA	53.69
		CB	38.52
		N	111.87

Table A.5 *(cont.)*

RN	RT	Atom	Chemical shift (ppm)
104	PRO	HA	4.58
		HB2	2.11
		HB3	2.17
		HD2	3.45
		HD3	3.76
		HG2	1.88
		HG3	1.91
		CA	64.96
		CB	32.52
		CD	50.99
		CG	26.71
	HEME	2^1CH_3	3.63
		3^1H	5.48
		3^2CH_3	1.13
		5H	10.08
		7^1CH_3	4.05
		8^1H	6.16
		8^2CH_3	2.48
		10H	9.38
		12^1CH_3	3.12
		13^1 CH_2	4.18
			4.45
		13^2 CH_2	2.87
			3.29
		15H	9.58
		17^1CH_2	2.62
			4.15
		17^2CH_2	1.96
			3.06
		18^1CH_3	3.01
		20H	9.32

Table A.6 Backbone assignment (^{15}N, ^{1}HN, ^{13}Cα and ^{13}Cβ) of PpcB from *G. sulfurreducens* in the reduced state (1.0 mM, 45 mM sodium phosphate buffer pH 6.5, 100 mM ionic strength, 298 K in a Bruker Avance III 600). The abbreviations RN and RT indicate residue number and residue type, respectively.

Backbone chemical shift (ppm) of reduced PpcB											
		^{15}N	^{1}HN	^{13}Cα	^{13}Cβ			^{15}N	^{1}HN	^{13}Cα	^{13}Cβ
1	A	-	-	-	-	**37**	K	117.40	7.94	56.69	32.69
2	D	-	-	56.19	40.4	**38**	I	127.80	10.01	60.90	39.15
3	T	110.60	7.23	60.21	70.62	**39**	E	130.90	8.69	58.35	29.05
4	M	123.00	8.71	54.64	36.39	**40**	G	113.30	9.12	45.33	-
5	T	117.60	8.43	61.58	70.43	**41**	F	121.30	8.00	62.36	39.07
6	F	128.80	9.68	56.12	40.02	**42**	G	114.00	5.76	44.55	-
7	T	120.10	9.01	62.25	69.49	**43**	K	122.60	8.92	59.25	33.43
8	A	125.60	8.13	51.65	20.63	**44**	E	114.70	7.98	59.34	28.07
9	K	125.20	10.24	58.97	32.01	**45**	M	117.30	7.54	59.38	33.65
10	N	113.70	8.97	52.63	34.67	**46**	A	122.10	7.80	54.74	18.92
11	G	110.00	6.94	44.13	-	**47**	H	113.10	6.94	53.47	26.91
12	N	126.90	8.23	53.69	38.08	**48**	G	109.30	6.72	43.71	-
13	V	121.60	8.56	60.69	34.97	**49**	K	123.50	8.59	59.00	32.78
14	T	125.60	9.22	63.42	69.06	**50**	S	110.10	7.97	62.90	-
15	F	128.70	9.23	54.68	43.82	**51**	C	110.90	6.64	57.82	36.98
16	D	127.90	8.46	51.55	38.87	**52**	K	120.70	7.96	59.67	32.83
17	H	130.70	6.39	56.75	28.23	**53**	G	101.60	8.32	46.75	-
18	K	118.50	7.25	57.89	31.01	**54**	C	121.10	6.54	58.27	29.32
19	K	120.10	7.51	58.50	31.17	**55**	H	117.60	5.28	55.07	27.35
20	H	116.80	6.46	61.33	26.31	**56**	E	116.60	7.96	59.12	29.78
21	Q	116.80	7.10	57.67	27.48	**57**	E	120.80	7.62	59.29	30.04
22	T	111.00	6.99	64.34	69.33	**58**	M	115.40	8.95	57.41	32.92
23	I	119.90	7.13	63.53	39.11	**59**	K	114.20	7.68	57.17	28.94
24	V	122.70	8.12	60.02	32.18	**60**	K	119.00	7.70	55.90	37.65
25	P	-	-	64.95	32.14	**61**	G	104.40	7.68	42.58	-
26	D	116.20	7.47	53.35	42.95	**62**	P	-	-	63.08	34.55
27	C	123.20	8.50	56.91	34.17	**63**	T	109.30	8.30	61.76	70.70
28	A	117.10	8.33	53.37	18.92	**64**	K	124.10	8.40	55.69	33.83
29	V	119.80	7.82	66.56	32.34	**65**	C	118.00	8.75	58.25	33.60
30	C	112.60	6.31	54.82	37.17	**66**	G	102.30	8.87	45.33	-
31	H	113.70	6.94	56.15	29.04	**67**	E	116.40	7.71	57.09	30.71
32	G	109.70	7.98	45.87	-	**68**	C	114.20	6.48	57.00	36.78
33	K	122.50	8.24	57.82	32.94	**69**	H	117.90	7.03	54.85	26.06
34	T	111.40	7.44	58.03	70.32	**70**	K	124.20	7.32	54.94	33.46
35	P	-	-	-	-	**71**	K	128.40	7.91	57.97	33.34
36	G	109.80	4.03	43.94	-						

Table A.7 Assignment of ^{1}H, ^{13}C and ^{15}N signals of PpcD from *G. sulfurreducens* in the reduced state (2.0 mM, 45 mM sodium phosphate buffer pH 7.1, 100 mM ionic strength, 298 K, Bruker Avance III 800). The abbreviations RN and RT indicate residue number and residue type, respectively. The chemical shifts were deposited in the Biological Magnetic Resonance Data Bank (BMRB, http://www.bmrb.wisc.edu) under accession number 19985.

RN	RT	Atom	Chemical shift (ppm)
1	HIS	CA	56.00
		CB	33.11
		HA	3.17
		HB2	1.45
		HB3	2.39
2	ASP	CA	52.21
		CB	40.99
		HA	3.75
		HB2	1.99
		HB3	2.14
3	LYS	CA	56.18
		CB	33.21
		CD	28.33
		CE	41.89
		CG	24.14
		HA	3.40
		HB2	0.16
		HB3	0.56
		HD2	1.18
		HD3	1.26
		HE2	2.77
		HG2	0.69
		HG3	0.74
		HN	5.16
		N	118.36
4	VAL	CA	61.82
		CB	31.43
		CG1	21.25
		HA	4.02
		HB	1.55
		HN	8.33
		N	128.92
		QG1	0.41
5	VAL	CA	60.60
		CB	34.83
		CG1	21.72
		CG2	20.23
		HA	4.21
		HB	2.02
		HN	9.02
		N	128.43
		QG1	1.16
		QG2	0.56
6	VAL	CA	62.19
		CB	31.79
		CG1	20.99
		CG2	21.00
		HA	4.51
		HB	1.91
		HN	8.57
		N	126.26
		QG1	0.80
		QG2	0.68
7	LEU	CA	53.90
		CD1	24.61
		CD2	26.77
		HA	4.80
		HB3	2.37
		HG	2.13
		HN	9.70
		N	132.66
		QD1	1.55
		QD2	1.69
8	GLU	CA	56.70
		CB	29.80
		CG	37.02
		HA	4.04
		HB2	1.88
		HB3	1.95
		HG2	2.01
		HG3	2.30
		HN	8.58
		N	124.70
9	ALA	CA	51.13
		CB	20.83
		HA	4.73
		HN	7.98
		N	124.11
		QB	0.77

Table A.7 *(cont.)*

RN	RT	Atom	Chemical shift (ppm)
10	LYS	CA	58.79
		CB	31.80
		CD	29.18
		CE	42.01
		CG	24.70
		HA	3.87
		HB2	1.77
		HB3	1.79
		HD2	1.71
		HD3	1.75
		HE2	3.00
		HG2	1.48
		HG3	1.52
		HN	10.03
		N	124.91
11	ASN	CA	52.33
		CB	34.41
		HA	4.13
		HB2	1.83
		HB3	1.98
		HD21	0.78
		HD22	5.33
		HN	8.84
		N	113.53
		ND2	107.95
12	GLY	CA	44.04
		HA1	2.94
		HA2	3.33
		HN	6.80
		N	109.79
13	ASN	CA	53.61
		CB	38.00
		HA	4.33
		HB2	2.29
		HB3	2.56
		HD21	6.84
		HD22	7.16
		HN	8.03
		N	126.96
		ND2	109.87
14	VAL	CA	60.59
		CB	34.76
		CG1	21.34
		CG2	18.41
		HA	4.23
		HB	2.17
		HN	8.55
		N	122.45
		QG1	1.59
		QG2	-0.94
15	THR	CA	63.35
		CB	68.85
		CG	21.51
		HA	4.66
		HB	3.97
		HN	9.11
		N	125.03
		QG2	0.83
16	PHE	CA	56.97
		CB	41.66
		HA	4.29
		HB2	2.69
		HB3	2.92
		HN	9.26
		N	128.98
17	ASP	CA	50.55
		CB	41.75
		HA	3.72
		HB2	1.65
		HB3	1.83
		HN	7.08
		N	125.45
18	HIS	CA	61.47
		CB	26.55
		HA	1.30
		HB2	0.71
		HB3	1.12
		HD1	9.03
		HD2	0.91
		HE1	1.50
		HN	6.31
		N	125.24
		ND1	164.61
19	LYS	CA	58.79
		CB	30.25
		CD	28.16
		CE	40.48
		CG	23.97
		HA	3.36
		HB2	1.22
		HD2	1.30
		HD3	1.33
		HE2	2.64
		HG2	0.86
		HG3	0.94
		HN	7.59
		N	118.03

Table A.7 *(cont.)*

RN	RT	Atom	Chemical shift (ppm)
20	LYS	CA	55.09
		CB	31.11
		CD	28.35
		CE	42.00
		CG	24.38
		HA	3.40
		HB2	0.30
		HB3	0.55
		HD2	1.29
		HD3	1.45
		HE2	2.78
		HG2	0.72
		HG3	0.84
		HN	5.54
		N	114.74
21	HIS	CA	56.38
		CB	27.55
		HA	2.91
		HB2	0.49
		HB3	2.16
		HD1	6.67
		HD2	0.98
		HE1	1.16
		HN	5.87
		N	113.88
		ND1	162.42
22	ALA	CA	53.41
		CB	18.23
		HA	4.13
		HN	6.37
		N	122.80
		QB	1.14
23	GLY	CA	45.51
		HA1	3.85
		HA2	4.17
		HN	9.30
		N	109.47
24	VAL	CA	61.69
		CB	33.27
		CG1	22.79
		CG2	18.55
		HA	4.52
		HB	2.84
		HN	6.77
		N	112.47
		QG1	1.14
		QG2	1.23
25	LYS	CA	58.76
		CB	32.00
		CD	29.50
		CE	42.14
		CG	24.84
		HA	4.19
		HB2	2.01
		HB3	2.04
		HD2	1.83
		HE2	3.07
		HG2	1.49
		HG3	1.64
		HN	8.99
		N	125.85
26	GLY	CA	45.02
		HA1	3.57
		HA2	4.19
		HN	8.94
		N	115.24
27	GLU	CA	57.89
		CB	28.41
		CG	37.31
		HA	4.04
		HB2	2.50
		HB3	2.71
		HG2	2.64
		HG3	2.68
		HN	8.98
		N	120.82
28	CYS	CA	56.37
		CB	33.83
		HA	5.43
		HB2	2.25
		HB3	2.38
		HN	8.55
		N	118.19
29	LYS	CA	56.68
		CB	30.54
		CD	28.78
		CE	41.29
		CG	25.35
		HA	4.24
		HB2	1.60
		HB3	1.84
		HD2	1.49
		HE2	2.83
		HE3	2.86
		HG2	0.75
		HG3	1.18
		HN	7.57
		N	112.98

Table A.7 *(cont.)*

RN	RT	Atom	Chemical shift (ppm)	RN	RT	Atom	Chemical shift (ppm)
30	ALA	CA	55.35	**36**	ALA	CA	51.79
		CB	19.14			CB	19.05
		HA	4.23			HA	4.18
		HN	8.33			HN	7.29
		N	123.25			N	117.90
		QB	2.09			QB	1.07
31	CYS	CA	54.65	**37**	GLY	CA	42.23
		CB	39.33			HA1	-0.84
		HA	4.48			HA2	1.50
		HB2	0.87			HN	6.27
		HB3	2.34			N	104.05
		HN	6.38	**38**	GLY	CA	43.14
		N	111.25			HA1	3.31
32	HIS	CA	53.75			HA2	3.89
		CB	29.71			HN	3.77
		HA	3.09			N	108.64
		HB2	1.12	**39**	LYS	CA	55.97
		HB3	1.37			CB	31.81
		HD1	8.09			CD	27.97
		HD2	0.70			CE	42.04
		HE1	1.54			CG	24.30
		HN	6.92			HA	3.90
		N	114.85			HB2	1.53
		ND1	162.48			HD2	1.75
33	GLU	CA	58.30			HE2	3.09
		CB	30.04			HG2	1.44
		CG	36.39			HG3	1.48
		HA	3.67			HN	7.63
		HB2	1.64			N	114.78
		HB3	1.69	**40**	ILE	CA	60.93
		HG2	1.98			CB	38.58
		HG3	2.02			CD1	11.80
		HN	7.52			CG1	27.88
		N	117.38			CG2	15.05
34	THR	CA	58.59			HA	3.40
		CB	72.62			HB	0.94
		CG	20.79			HG12	-0.65
		HA	4.34			HG13	0.38
		HB	4.13			HN	9.68
		HN	7.01			N	129.37
		N	105.55			QD1	-1.06
		QG2	0.84			QG2	-0.43
35	GLU	CA	58.00	**41**	ALA	CA	53.98
		CB	28.60			CB	17.82
		CG	36.32			HA	3.83
		HA	3.57			HN	8.43
		HB2	1.95			N	133.23
		HB3	2.02			QB	1.13
		HG2	2.20				
		HG3	2.26				
		HN	8.95				
		N	117.15				

***Table A.7** (cont.)*

RN	RT	Atom	Chemical shift (ppm)
42	GLY	CA	44.82
		HA1	3.50
		HA2	3.76
		HN	8.35
		N	107.06
43	MET	CA	56.30
		CB	30.05
		CE	18.02
		CG	32.09
		HA	3.87
		HB2	1.88
		HB3	2.01
		HG2	2.73
		HG3	2.85
		HN	6.98
		N	118.11
		QE	2.17
44	GLY	CA	44.50
		HA1	4.52
		HA2	4.51
		HN	7.65
		N	113.99
45	LYS	CA	59.45
		CB	33.29
		CD	29.32
		CE	41.75
		CG	22.52
		HA	2.56
		HB2	1.33
		HB3	1.75
		HD2	1.10
		HD3	1.14
		HE2	2.18
		HE3	2.31
		HG2	-1.65
		HG3	-0.82
		HN	9.00
		N	121.95
46	ASP	CA	57.06
		CB	39.60
		HA	3.42
		HB2	2.24
		HB3	2.27
		HN	7.78
		N	115.52
47	TRP	CA	61.95
		CB	30.95
		HA	3.68
		HB2	3.17
		HB3	3.19
		HD1	7.01
		HE1	9.87
		HE3	7.54
		HH2	7.40
		HN	8.26
		HZ2	7.56
		HZ3	7.54
		N	120.82
		NE1	129.58
48	ALA	CA	55.10
		CB	19.38
		HA	4.37
		HN	8.63
		N	122.73
		QB	1.42
49	HIS	CA	54.83
		CB	26.17
		HA	2.79
		HB2	1.34
		HB3	1.47
		HN	7.39
		N	116.11
50	LYS	CA	58.51
		CB	32.64
		CD	28.85
		CE	41.82
		CG	24.31
		HA	3.58
		HB2	1.37
		HD2	1.25
		HD3	1.31
		HE2	2.62
		HG2	0.88
		HG3	1.01
		HN	6.69
		N	117.70
51	THR	CA	66.50
		CB	69.56
		CG	21.32
		HA	3.55
		HB	3.12
		HN	7.99
		N	116.14
		QG2	1.25

Table A.7 *(cont.)*

RN	RT	Atom	Chemical shift (ppm)
52	CYS	CA	58.43
		CB	35.21
		HA	4.25
		HB2	2.24
		HB3	2.91
		HN	8.44
		N	121.68
53	THR	CA	64.66
		CB	66.19
		CG	23.40
		HA	2.42
		HB	3.52
		HN	6.22
		N	107.83
		QG2	0.68
54	GLY	CA	46.85
		HA1	3.23
		HA2	3.63
		HN	6.07
		N	103.44
55	CYS	CA	58.01
		CB	28.96
		HA	4.30
		HB2	2.32
		HB3	3.61
		HN	6.67
		N	121.36
56	HIS	CA	55.38
		CB	27.67
		HA	3.60
		HB2	1.26
		HD1	9.36
		HD2	0.94
		HE1	1.42
		HN	5.94
		N	116.97
		ND1	164.67
57	LYS	CA	59.27
		CB	32.07
		CD	29.07
		CE	41.66
		CG	25.69
		HA	3.54
		HB2	1.47
		HB3	1.53
		HD2	1.33
		HE2	2.61
		HG2	1.09
		HG3	1.20
		HN	7.91
		N	117.68
58	GLU	CA	59.19
		CB	29.69
		CG	36.08
		HA	3.88
		HB2	2.06
		HB3	2.07
		HG2	2.20
		HG3	2.25
		HN	7.45
		N	120.44
59	MET	CA	56.30
		CB	33.88
		CE	17.30
		CG	32.19
		HA	4.42
		HB2	2.97
		HB3	3.35
		HG2	2.27
		HN	8.74
		N	114.24
		QE	2.49
60	GLY	CA	45.97
		HA1	3.57
		HA2	3.89
		HN	7.67
		N	107.95
61	LYS	CA	54.98
		CB	37.15
		CD	29.70
		CE	42.45
		CG	24.72
		HA	4.26
		HB2	1.62
		HB3	2.02
		HD2	1.93
		HE2	3.16
		HG2	1.48
		HG3	1.52
		HN	7.34
		N	118.81
62	GLY	CA	42.12
		HA1	1.16
		HA2	2.52
		HN	7.43
	GLY	N	104.05

Table A.7 *(cont.)*

RN	RT	Atom	Chemical shift (ppm)
63	PRO	CA	62.71
		CB	34.13
		CD	48.39
		CG	28.92
		HA	3.87
		HB2	1.85
		HB3	1.89
		HD2	-0.70
		HD3	2.43
		HG2	0.96
		HG3	1.78
64	THR	CA	61.51
		CB	70.65
		CG	21.65
		HA	4.33
		HB	3.99
		HN	8.17
		N	108.44
		QG2	0.56
65	LYS	CA	55.66
		CB	33.51
		CD	28.96
		CE	42.06
		CG	25.12
		HA	5.02
		HB2	1.59
		HB3	2.00
		HD2	1.63
		HE2	2.90
		HG2	1.41
		HG3	1.47
		HN	8.34
		N	124.74
66	CYS	CA	57.89
		CB	33.40
		HA	4.81
		HB2	2.61
		HB3	2.72
		HN	8.65
		N	118.14
67	GLY	CA	45.23
		HA1	3.41
		HA2	3.87
		HN	8.74
		N	102.05
68	GLU	CA	57.07
		CB	30.65
		CG	37.72
		HA	4.05
		HB2	2.01
		HB3	2.28
		HG2	2.12
		HG3	2.21
		HN	7.61
		N	116.47
69	CYS	CA	56.75
		CB	36.42
		HA	4.57
		HB2	1.36
		HB3	2.00
		HN	6.35
		N	114.38
70	HIS	CA	54.71
		CB	25.68
		HA	2.53
		HB2	0.89
		HB3	1.11
		HD1	8.77
		HD2	0.60
		HE1	0.74
		HN	6.78
		N	117.43
		ND1	165.91
71	LYS	CA	54.66
		CB	33.05
		CD	28.69
		CE	42.41
		CG	24.23
		HA	4.17
		HB2	1.51
		HD2	1.42
		HE2	2.79
		HE3	2.83
		HG2	1.07
		HN	7.15
		N	124.62

***Table A.7** (cont.)*

RN	RT	Atom	Chemical shift (ppm)	RN	RT	Atom	Chemical shift (ppm)
72	LYS	CA	57.80	**III**	HEME	$2^1\mathrm{CH}_3$	4.36
		CB	33.25			$3^1\mathrm{H}$	6.49
		CD	28.95			$3^2\mathrm{CH}_3$	2.68
		CE	42.05			5H	9.54
		CG	24.71			$7^1\mathrm{CH}_3$	3.76
		HA	3.78			$8^1\mathrm{H}$	6.45
		HB2	1.39			$8^2\mathrm{CH}_3$	2.80
		HB3	1.51			10H	9.69
		HD2	1.35			$12^1\mathrm{CH}_3$	3.34
		HE2	2.70			$13^1\ \mathrm{CH}_2$	2.90
		HG2	1.08				4.06
		HN	7.74			$13^2\ \mathrm{CH}_2$	2.78
		N	128.46				3.55
						15H	9.21
I	HEME	$2^1\mathrm{CH}_3$	3.17			$17^1\mathrm{CH}_2$	3.10
		$3^1\mathrm{H}$	6.01				4.19
		$3^2\mathrm{CH}_3$	2.18			$17^2\mathrm{CH}_2$	3.85
		5H	9.67				-
		$7^1\mathrm{CH}_3$	3.37			$18^1\mathrm{CH}_3$	3.71
		$8^1\mathrm{H}$	5.33			20H	9.95
		$8^2\mathrm{CH}_3$	1.47				
		10H	7.94	**IV**	HEME	$2^1\mathrm{CH}_3$	3.52
		$12^1\mathrm{CH}_3$	2.74			$3^1\mathrm{H}$	5.82
		$13^1\ \mathrm{CH}_2$	2.42			$3^2\mathrm{CH}_3$	1.94
			3.68			5H	8.92
		$13^2\ \mathrm{CH}_2$	3.19			$7^1\mathrm{CH}_3$	2.82
			4.47			$8^1\mathrm{H}$	6.12
		15H	9.45			$8^2\mathrm{CH}_3$	1.34
		$17^1\mathrm{CH}_2$	3.90			10H	9.24
			4.14			$12^1\mathrm{CH}_3$	3.75
		$17^2\mathrm{CH}_2$	2.84			$13^1\ \mathrm{CH}_2$	3.01
			3.07				3.56
		$18^1\mathrm{CH}_3$	3.09			$13^2\ \mathrm{CH}_2$	2.56
		20H	8.72				4.16
						15H	9.39
						$17^1\mathrm{CH}_2$	2.97
							3.89
						$17^2\mathrm{CH}_2$	3.25
							4.40
						$18^1\mathrm{CH}_3$	3.23
						20H	9.31

Table A.8 Backbone assignment (^{15}N, ^{1}HN, ^{13}Cα and ^{13}Cβ) of PpcE from *G. sulfurreducens* in the reduced state (0.7 mM, 45 mM sodium phosphate buffer pH 6.5, 100 mM ionic strength, 298 K in a Bruker Avance III 600). The abbreviations RN and RT indicate residue number and residue type, respectively.

Backbone chemical shift (ppm) of reduced PpcE											
RN	**RT**	**^{15}N**	**^{1}HN**	**^{13}Cα**	**^{13}Cβ**	**RN**	**RT**	**^{15}N**	**^{1}HN**	**^{13}Cα**	**^{13}Cβ**
1	A	-	-	-	-	**36**	G	110.70	4.09	44.26	-
2	D	-	-	56.12	40.00	**37**	K	118.10	8.20	56.74	32.04
3	V	120.00	7.41	60.98	34.46	**38**	I	129.20	10.52	61.18	39.51
4	I	126.80	8.59	60.60	41.48	**39**	R	129.70	8.72	58.68	29.53
5	L	128.50	8.28	53.11	43.36	**40**	N	115.80	8.69	52.86	36.89
6	F	127.40	9.75	54.46	39.90	**41**	F	120.00	7.78	62.50	39.34
7	P	-	-	62.63	31.60	**42**	G	114.30	5.85	44.42	-
8	S	114.50	8.12	58.31	65.76	**43**	K	122.80	9.03	59.39	32.93
9	K	128.10	9.87	58.64	32.26	**44**	D	116.40	7.86	57.32	39.45
10	N	115.90	7.78	51.98	38.19	**45**	Y	120.10	8.03	61.39	39.25
11	G	107.90	6.83	43.25	-	**46**	A	122.90	8.31	54.80	19.06
12	A	130.00	8.37	53.19	19.42	**47**	H	116.50	7.58	55.32	26.17
13	V	122.50	8.53	60.68	36.10	**48**	K	118.30	6.92	58.58	32.95
14	T	125.80	9.24	63.64	68.76	**49**	T	115.80	8.33	66.63	69.96
15	F	127.40	9.49	54.33	42.44	**50**	C	121.50	8.00	59.10	34.86
16	T	120.00	7.43	58.07	65.51	**51**	K	114.30	6.17	58.71	31.67
17	H	127.40	5.87	59.04	27.28	**52**	G	100.50	6.01	46.83	-
18	K	118.90	7.63	58.79	30.97	**53**	C	121.00	6.83	58.11	29.06
19	R	119.50	7.55	58.84	29.07	**54**	H	116.60	5.92	55.06	27.64
20	H	114.40	6.94	58.22	26.62	**55**	E	117.40	7.84	59.17	29.78
21	S	113.30	7.01	61.09	62.40	**56**	V	119.20	7.73	65.55	32.09
22	E	119.90	6.97	57.87	29.44	**57**	R	117.70	8.86	57.64	30.55
23	F	114.20	6.98	57.65	38.89	**58**	G	108.00	7.70	46.32	-
24	V	127.80	8.51	64.02	31.77	**59**	A	122.80	7.63	51.85	22.60
25	R	121.10	8.26	59.77	30.01	**60**	G	103.90	7.47	42.45	-
26	E	116.80	8.40	55.58	31.51	**61**	P	-	-	62.87	33.52
27	C	124.50	8.63	57.39	33.39	**62**	T	110.50	8.84	61.40	69.41
28	R	115.40	8.54	56.32	29.19	**63**	K	122.50	7.23	56.09	33.73
29	S	116.90	8.06	63.01	63.72	**64**	C	119.80	8.64	58.02	34.62
30	C	114.50	6.89	54.63	39.02	**65**	K	113.50	8.73	56.55	31.02
31	H	118.80	7.09	54.08	27.14	**66**	L	115.80	7.38	55.01	42.23
32	E	123.50	8.20	58.41	30.00	**67**	C	115.00	6.59	57.01	35.69
33	K	118.00	7.86	55.07	32.67	**68**	H	118.90	7.20	53.87	24.73
34	T	114.80	7.38	60.58	70.11	**69**	T	112.90	7.47	62.43	70.30
35	P	-	-			**70**	G	116.60	8.32	46.52	-